Orbital-dependent exchange-correlation functionals in density-functional theory realized by the FLAPW method

Von der Fakultät für Mathematik, Informatik und Naturwissenschaften der RWTH Aachen University zur Erlangung des akademischen Grades eines Doktors der Naturwissenschaften genehmigte Dissertation

vorgelegt von

Dipl.-Phys. Markus Betzinger

aus Fröndenberg

Berichter:	Prof. Dr. rer. nat. Stefan Blügel
	Prof. Dr. rer. nat. Andreas Görling
	Prof. Dr. rer. nat. Carsten Honerkamp
Tag der mündlichen Prüfung:	14.12.2011

This document was typeset with LaTeX. Figures were created using Gnuplot, InkScape, and VESTA.

Das Unverständlichste am Universum ist im Grunde, dass wir es verstehen können.
Albert Einstein

Abstract

In this thesis, we extended the applicability of the full-potential linearized augmented-plane-wave (FLAPW) method, one of the most precise, versatile and generally applicable electronic structure methods for solids working within the framework of density-functional theory (DFT), to orbital-dependent functionals for the exchange-correlation (xc) energy. In contrast to the commonly applied local-density approximation (LDA) and generalized gradient approximation (GGA) for the xc energy, orbital-dependent functionals depend directly on the Kohn-Sham (KS) orbitals and only indirectly on the density.

Two different schemes that deal with orbital-dependent functionals, the KS and the generalized Kohn-Sham (gKS) formalism, have been realized. While the KS scheme requires a local multiplicative xc potential, the gKS scheme allows for a non-local potential in the one-particle Schrödinger equations.

Hybrid functionals, combining some amount of the orbital-dependent exact exchange energy with local or semi-local functionals of the density, are implemented within the gKS scheme. We work in particular with the PBE0 hybrid of Perdew, Burke, and Ernzerhof. Our implementation relies on a representation of the non-local exact exchange potential – its calculation constitutes the most time consuming step in a practical calculation – by an auxiliary mixed product basis (MPB). In this way, the matrix elements of the Hamiltonian corresponding to the non-local potential become a Brillouin-zone (BZ) sum over vector-matrix-vector products. Several techniques are developed and explored to further accelerate our numerical scheme. We show PBE0 results for a variety of semiconductors and insulators. In comparison with experiment, the PBE0 functional leads to improved band gaps and an improved description of localized states. Even for the ferromagnetic semiconductor EuO with localized $4f$ electrons, the electronic and magnetic properties are correctly described by the PBE0 functional.

Subsequently, we discuss the construction of the local, multiplicative exact exchange (EXX) potential from the non-local, orbital-dependent exact exchange energy. For this purpose we employ the optimized effective potential (OEP) method. Central ingredients of the OEP equation are the KS wave-function response and the single-particle density response function. A formulation in terms of a slightly modified MPB enables to solve the OEP integral

equation for the local potential without any shape approximations for the potential. We show that a balance between the LAPW and mixed product basis is mandatory for a smooth and physical local EXX potential. The LAPW basis must be converged to an accuracy which is far beyond that for LDA or GGA calculations. We demonstrate that this is necessary to lend the LAPW basis and thus the KS wave functions and density sufficient flexibility to react adequately to the changes of the effective potential, which are described in our formalism by the MPB. If both basis sets are properly balanced, our results for C, Si, SiC, Ge, GaAs as well as solid Ne and Ar are in favorable agreement with plane-wave pseudopotential results. Because of the exceedingly large LAPW basis sets the EXX-OEP approach is computationally expensive. We propose a correction, the finite basis-set correction (FBC), for the density and wave-function response, which explicitly considers the dependence of the LAPW basis on the effective potential and which vanishes in the limit of an infinite, complete basis. For the example of ScN, we demonstrate that the FBC leads to converged potentials at much smaller LAPW basis sets and thus turns the EXX-OEP approach into a practical method. Finally, we discuss a generalization of the formalism to metals and report results for the cubic perovskites $CaTiO_3$, $SrTiO_3$, and $BaTiO_3$, the transition-metal oxides MnO, FeO, and CoO as well as the metals Al, Na, and Cu.

Zusammenfassung

Im Rahmen dieser Arbeit wurde die full-potential linearized augmented-plane-wave (FLAPW) Methode, eine der präzisesten, vielseitigsten und allgemein anwendbarsten elektronischen Strukturmethoden der Dichtefunktionaltheorie (DFT) für Festkörper, um orbitalabhängige Funktionale für die Austausch-Korrelations (xc) Energie erweitert. Im Gegensatz zu den geläufigen Funktionalen, wie der lokalen Dichtenährung (LDA) und der verallgemeinerten Gradientennährung (GGA), hängen orbitalabhängige Funktionale direkt von den Kohn-Sham (KS) Orbitalen ab und sind damit nur indirekte Funktionale der Dichte.

Für die numerische Umsetzung orbitalabhängiger Funktionale haben sich zwei unterschiedliche Ansätze etabliert, der KS und der verallgemeinerte KS (gKS) Formalismus. Sie unterscheiden sich in der Behandlung des xc Potentials. Während der KS Formalismus ein lokales, multiplikatives xc Potential erfordert, lässt das gKS Schema auch ein nicht-lokales Potential zu. Im Rahmen dieser Arbeit werden beiden Ansätze diskutiert und untersucht.

Hybridfunktionale, die typischerweise im gKS Schema behandelt werden, kombinieren orbitalabhängigen exakten Austausch mit dichteabhängigen LDA oder GGA Funktionalen. Im Speziellen konzentrieren wir uns in dieser Arbeit auf das Hybridfunktional von Perdew, Burke und Ernzerhof (PBE0). Die entwickelte Implementierung des PBE0 Funktionales beruht auf einer Darstellung des nicht-lokalen Austauschpotentials durch eine Hilfsbasis, die gemischte Produktbasis (MPB). Mittels dieser werden die Matrixelemente des nicht-lokalen Austauschpotentials zum Hamiltonian eine Brillouin-Zone (BZ) Summe über Vektor-Matrix-Vektor Produkte. Zur beschleunigten Berechnung dieser Matrixelemente werden weitere Techniken entwickelt und erforscht. Im Vergleich zu LDA und GGA führt das PBE0 Funktional zu einer verbesserten Beschreibung der experimentellen Bandlücke und zu einer verbesserten Beschreibung von lokalisierten Zuständen, wie d- und f-Elektron Zuständen. Zum Beispiel beschreibt das PBE0 Funktional die elektronischen und magnetischen Eigenschaften des ferromagnetischen Halbleiters EuO mit seinen lokalisierten $4f$ Zuständen im Einklang mit dem Experiment.

Die Konstruktion eines lokalen, multiplikativen Austauschpotentials im Rahmen des KS Formalismus ausgehend von der nicht-lokalen, orbitalabhängigen, exakten Austauschenergie (EXX) erfordert hingegen die optimierte-effektive-Potential (OEP) Methode. Sie führt

zu einer Integralgleichung für das lokale Austauschpotential, deren zentrale Bestandteile die KS Wellenfunktionsresponse und die KS Dichteresponse sind. Eine Darstellung des lokalen Potentials durch eine leicht modifizierte MPB gestattet die Lösung der Integralgleichung. Wir zeigen, dass ein glattes und physikalisches Austauschpotential eine Balance zwischen LAPW und gemischter Produkt Basis erfordert, d.h. die LAPW Basis muss zu einer Genauigkeit konvergiert werden, die weit jenseits derer für LDA oder GGA Rechnungen liegt. Diese Genauigkeit der LAPW Basis ist notwendig, damit die KS Wellenfunktion und damit die Dichte adäquat auf die Potentialänderungen, welche in unserem Formalismus durch die MPB beschrieben werden, antworten können. Sofern beide Basen balanciert sind, finden wir eine gute Übereinstimmung zwischen unseren All-Elektronen FLAPW Resultaten für C, Si, SiC, Ge, GaAs, festes Ne und Ar und Pseudopotentialergebnissen der Literatur. Aufgrund der nötigen Balance beider Basen ist der EXX-OEP Ansatz numerisch sehr aufwendig. Wir haben eine finite Basissatzkorrektur (FBC) entwickelt, welche die Abhängigkeit der LAPW Basis vom Potential explizit berücksichtigt und im Grenzfall einer vollständigen LAPW Basis verschwindet. Anhand von ScN demonstrieren wir, dass die FBC zu konvergierten Austauchpotentialen bei kleinerer LAPW Basis führt, was eine EXX-OEP Rechnung auf der Basis der FLAPW-Methode erst praktisch ermöglicht. Desweiteren diskutieren wir eine Verallgemeinerung des Formalismus für Metalle und berichten Ergebnisse für die kubischen Perovskite $CaTiO_3$, $SrTiO_3$ und $BaTiO_3$, die Übergangsmetalloxide MnO, FeO und CoO, wie auch für die Metalle Al, Na und Cu.

Contents

1. Introduction

A description of the electronic structure of a material from first-principles requires to solve the quantum-mechanical Schrödinger equation for the electrons and atomic nuclei constituting the material. The large mass difference between the electrons and the atomic nuclei permits to separate the electronic motion from that of the nuclei [1], which finally results in a Schrödinger equation solely for the electrons. The electrons move in an external potential created by the atomic nuclei and interact among themselves via the electrostatic Coulomb interaction. As a consequence the motion of the electrons is correlated, i.e., the motion of an individual electron is influenced by all other electrons and, conversely, it affects the motion of all others. The Coulomb interaction impedes a direct solution of the many-electron Schrödinger equation, a partial differential equation for the many-electron wave function, except for a very limited number of (small) systems.

Density-functional theory (DFT) provides an ingenious reformulation of the many-electron problem and thus avoids the direct solution of the many-electron Schrödinger equation. The central quantity of DFT is the electron ground-state density, a function of the three spatial coordinates, which is much less complex than the many-electron wave function, which depends on $3N$ coordinates, where N denotes the number of electrons of the system. Despite this reduction in complexity, the electron ground-state density incorporates all information about the system, in principle. Hohenberg and Kohn [2] showed that the ground-state density uniquely determines the external potential (up to a constant) of the many-electron system so that the many-electron Hamiltonian, its ground state, and excited states can be regarded as functionals of the ground-state density. Ultimately, the expectation value of any observable becomes a functional of the density. However, the ground-state density of a material is unknown a priori and must be calculated. It can be determined by applying the variational principle for the total energy, which constitutes the second part of the Hohenberg and Kohn theorem [2] and states that the total energy becomes minimal for the ground-state density. Yet, the explicit functional dependence of the total energy on the density is unknown. Therefore, Kohn and Sham [3] proposed an indirect procedure to minimize the total energy and determine the ground-state density.

Kohn and Sham introduced an auxiliary system of non-interacting electrons, the Kohn-

Sham (KS) system, whose effective potential is adjusted such that its ground-state density coincides with that of the real interacting system. In order to determine the effective potential, they partitioned the total energy of the interacting system into the kinetic energy of non-interacting electrons, the classical Hartree energy, the energy arising from the external potential and an everything-else term, the so-called exchange-correlation (xc) energy. The latter comprises exchange and correlation effects of the many-electron system as well as a correction for the kinetic energy. Application of the variational principle then leads to the identification of the effective, local potential as the sum of three terms: external, Hartree, and xc potential, where the latter is defined as the functional derivative of the xc energy with respect to the density. In this way, Kohn and Sham mapped the complicated interacting electron problem onto an auxiliary system of non-interacting electrons with the same ground-state density.

This mapping is, in principle, exact. All complicated many-electron effects are hidden in the xc energy functional. However, its mathematical form is unknown, and we must resort to approximations for practical calculations. The local-density approximation (LDA) [4–6] and the generalized gradient approximation (GGA) [7, 8] are nowadays routinely employed approximations. While in the LDA the xc energy is approximated by a (direct) functional of the density, the GGA additionally incorporates the density gradient. Despite their success, they suffer from several shortcomings: (a) the Hartree potential contains an unphysical interaction of the electron with itself, which should be compensated exactly by the exchange potential. However, the only approximate treatment of exchange in the LDA and the GGA leads only to a partial compensation and a spurious self-interaction remains [9]. As a consequence, localized states are typically bound too loosely and appear too high in energy. (b) LDA and GGA do not exhibit a derivative discontinuity of the xc energy functional with respect to the particle number and, hence, underestimate the experimental fundamental band gap by 40% or even more [10–12]. (c) The inherent locality of LDA and GGA prohibits to describe van-der-Waals bonded systems [13].

Orbital-dependent xc functionals constitute a new and promising class of xc functionals [14, 15]. They are functionals of the KS orbitals and are only indirect functionals of the density. In contrast to the LDA and the GGA, orbital-dependent functionals can be improved systematically. They naturally arise from an expansion of the exact xc energy in powers of the electron-electron interaction [16]. In first order, this expansion gives the orbital-dependent exact exchange energy, which is formally identical to the Hartree-Fock (HF) exchange energy, but evaluated with the KS orbitals. The higher-order terms define an orbital-dependent correlation functional. Already, the first-order term, the exact exchange energy, cures the self-interaction problem of LDA and GGA and gives rise to a derivative discontinuity, whereas

the second-order term of the expansion enables a description of the van-der-Waals interaction [17].

A combination of density- and orbital-dependent functionals into one functional yields the hybrid functionals. They usually mix orbital-dependent exact exchange with LDA and GGA functionals and are motivated by the adiabatic-connection method [18–20]. The first hybrid functional has been proposed by Becke in the year 1993 [21] and consists of 50% exact exchange and 50% LDA exchange and correlation. Since then, many hybrid functionals have been developed. For example, Perdew, Burke, and Ernzerhof [22] proposed a hybrid, named PBE0, which combines 25% of exact exchange with 75% PBE exchange and 100% PBE correlation, where PBE [7] denotes one specific GGA functional. The amount of orbital-dependent exact exchange has been inferred from theoretical arguments. Typically, hybrid functionals are employed within the generalized Kohn-Sham (gKS) system [23], in which the orbital-dependent exact exchange energy is treated as a non-local HF-like potential in the one-particle Schrödinger equations.

In this thesis, we have developed an implementation of the PBE0 hybrid functional in the gKS system and of the exact exchange energy functional in the KS formalism, which in contrast to the gKS formalism demands a local instead of a non-local potential. Both approaches and functionals are realized within the all-electron full-potential linearized augmented-plane-wave (FLAPW) method [24–27], which treats core and valence electrons on an equal footing. The FLAPW method does not employ any shape approximations for the density and potential and allows a treatment of open as well as close-packed multicomponent systems including d- and f-electron states. Frequently, FLAPW results are considered as the "gold standard" for the problem at hand.

The first hybrid functional implementations and calculations for solids within the gKS system were reported in the late 1990s and the early 2000s [28–30]. They employed Gaussian-type functions or plane-waves in the pseudopotential or the projector augmented-wave (PAW) approach. In the all-electron FLAPW method, so far only an approximate scheme [31] has been proposed due to the methodological complexity involved in the implementation as well as the large computational demand required for the calculation of the non-local potential. In this approximation, the non-local exchange term is restricted to certain atoms and selected angular momenta l. We have developed an implementation of hybrid functionals, in particular of the PBE0 hybrid, without the limitations of Ref. 31. It relies on an additional auxiliary basis, the mixed product basis (MPB), which is constructed from products of LAPW basis functions. The MPB is suited for the representation of products of LAPW wave functions. It retains the all-electron character of the wave function product and can be converged in a systematic manner. The usage of the MPB turns the matrix elements

of the Hamiltonian corresponding to the non-local exchange potential into vector-matrix-vector products, where the matrix can be calculated once at the beginning of a calculation. Only the vectors are computed in each iteration. Due to the large computational demand for the calculation of the non-local exchange potential, we develop several techniques to accelerate our numerical scheme. In order to verify our implementation, we compare our results of PBE0 hybrid-functional calculations for prototype semiconductors and insulators with theoretical results from the literature. As an application we discuss and compare the structural, electronic, and magnetic properties of rock-salt EuO obtained with the PBE and PBE0 functional. While the PBE functional predicts EuO to be a metal in contradiction to experiment, the PBE0 hybrid opens a band gap and leads to a consistent description of the structural and magnetic properties of EuO.

A treatment of hybrid functionals and orbital-dependent functionals within the KS formalism, in contrast to the gKS formalism, requires a local, multiplicative xc potential. The only indirect dependence of orbital functionals on the density, however, does not allow for a direct differentiation of the xc energy with respect to the density. Instead one has to apply the optimized effective potential (OEP) method [32–34], which yields an integral equation for the local xc potential. For periodic systems and the exact exchange (EXX) functional, this integral equation was solved first by Kotani in 1994 [35]. He employed the linearized muffin-tin orbital (LMTO) method with the additional approximation that the potential is purely spherical around each atom (atomic sphere approximation). Implementations of the EXX-OEP approach within the pseudopotential plane-wave method followed [36–38]. The first all-electron full-potential implementation, realized within the FLAPW method, goes back to Sharma *et al.* [39] in 2005. However, their results deviated substantially from the pseudopotential values reported before, which initiated a controversy about the adequacy of the pseudopotential approximation in the context of the EXX-OEP approach. Engel [40] demonstrated that all-electron and pseudopotential EXX-OEP results for lithium and diamond differ only slightly. He mimicked the all-electron results by pushing the pseudopotential and plane-wave cutoffs to their all-electron limit. Reasonable agreement between all-electron and pseudopotential EXX-OEP calculations has also been observed by Makmal *et al.* [41] for the diatomic molecules BeO and CO employing a real-space grid approach. We have developed an alternative implementation of the EXX-OEP approach within the FLAPW method – different and independent from that in Ref. 39. It employs a slightly modified version of the MPB for the representation of the local exact exchange potential. So, the integral equation becomes an algebraic equation, which can be solved for the local potential by standard numerical techniques. We discuss and demonstrate the requirement of a balance between MPB and LAPW basis to obtain physical and stable EXX potentials. Only if both basis sets are properly

balanced, a favorable agreement between our all-electron full-potential and pseudopotential plane-wave EXX KS transition energies reported in literature is observed. This balance demands a very flexible LAPW basis set and, thus, leads to a high computational cost of EXX calculations in practice. In order to reduce the demand on the LAPW basis we develop and explore a finite basis correction (FBC) for the KS response function, which arises from the dependence of the LAPW basis functions on the spherical effective potential in the MT spheres. It leads to stable exchange potentials at much smaller LAPW basis sets. This FBC turns out to be a very general concept that paves the road to response quantities and density functional perturbation theory applicable to electronic structure methods with potential-dependent basis sets. We also report results for the cubic transition-metal perovskites $CaTiO_3$, $SrTiO_3$, and $BaTiO_3$ as well as the transition-metal monoxides MnO, FeO, and CoO. We will see that the EXX functional leads to an opening of the KS band gap. Most notably, antiferromagnetic FeO and CoO are correctly predicted to be insulating. Finally, we present a generalization of the EXX-OEP formalism for metals and show results for Na, Al, and Cu.

The thesis is organized as follows. The second chapter provides a short introduction to KS DFT, where the basic equations and quantities are defined. The xc energy functional is thoroughly discussed in the third chapter. Orbital-dependent as well as hybrid functionals are motivated and the basic concepts for the development of functionals are introduced. The FLAPW method is explained in chapter 4, where emphasis lies on the local-orbital extension of the LAPW approach and the construction of the MPB. Chapter 5 introduces the gKS system and discusses the implementation of the hybrid functionals within the gKS system. The OEP method and its numerical realization within the FLAPW approach for the EXX functional is described in chapter 6. The thesis is concluded in chapter 7.

Parts and results of chapter 5 and 6 have recently been published in *Physical Review* **B** [42, 43].

2. Basics of density-functional theory

The physical properties of a material, be they of mechanical, electrical or magnetic character, rest on the motion of the electrons under the influence of the ions constituting the material. This motion is governed by the time-dependent Schrödinger equation

$$H|\Psi\rangle = i\frac{\partial}{\partial t}|\Psi\rangle \tag{2.1}$$

with the many-body wave function $|\Psi\rangle$ and the Hamiltonian

$$H = -\frac{1}{2}\sum_i \nabla_i^2 - \sum_\alpha \frac{1}{2M_\alpha}\nabla_\alpha^2 + \frac{1}{2}\sum_{\substack{i,j\\ i\neq j}} \frac{1}{|\mathbf{r}_i - \mathbf{r}_j|} - \sum_{i,\alpha} \frac{Z_\alpha}{|\mathbf{r}_i - \mathbf{R}_\alpha|} + \frac{1}{2}\sum_{\substack{\alpha,\beta\\ \alpha\neq\beta}} \frac{Z_\alpha Z_\beta}{|\mathbf{R}_\alpha - \mathbf{R}_\beta|}, \tag{2.2}$$

where Z_α and M_α denote the atomic number and mass of the α-th atomic ion, $\mathbf{R}_\alpha$ its space coordinates and $\mathbf{r}_i$ the coordinates of the i-th electron.[1] In the time-independent case Eq. (2.1) becomes

$$H|\Psi\rangle = E|\Psi\rangle \tag{2.3}$$

with the total energy E. In 1929 Dirac [44] already noted that with Eqs. (2.1)–(2.3) "the laws necessary for [...] a large part of physics and the whole of chemistry are thus completely known, and the difficulty is only that exact application of these laws lead to equations which are to complicated too be soluble". Indeed, even 82 years after Dirac the exact solution of the Schrödinger equation for the enormous number of interacting electrons and atomic ions present in real materials is impossible. It is therefore necessary to develop models or approximations that are able to describe the main aspects of the physical problem under consideration. The density-functional theory (DFT) is such an approximation and has been proven to be very successful over the last decades. But before the DFT is introduced, the Born-Oppenheimer approximation, which allows to separate the electronic from the ionic motion, is discussed. It is essential for DFT, as well. In order to contrast DFT with wave function based approaches, we will also briefly discuss the Hartree and Hartree-Fock (HF) approach.

The enormous mass difference between the electrons and ions – the mass of the latter is at

[1] We use atomic units except where noted otherwise: $\hbar = m = e = 1$.

least a factor of 1000 larger than that of the electrons – causes the motion of the electrons and ions to take place in different time scales. On the time scale of the electron motion the ions appear fixed, which justifies to decouple the electronic from the ionic motion and to define an electronic Hamiltonian

$$H = \sum_i \left[-\frac{1}{2}\nabla_i^2 + V(\mathbf{r}_i) \right] + V_{ee} \,, \tag{2.4}$$

where we have introduced the external potential $V(\mathbf{r}_i) = -\sum_\alpha \frac{Z_\alpha}{|\mathbf{r}_i - \mathbf{R}_\alpha|} + \frac{1}{2}\sum_{\substack{\alpha,\beta \\ \alpha\neq\beta}} \frac{Z_\alpha Z_\beta}{|\mathbf{R}_\alpha - \mathbf{R}_\beta|}$ and the abbreviation $V_{ee} = \frac{1}{2}\sum_{\substack{i,j \\ i\neq j}} \frac{1}{|\mathbf{r}_i - \mathbf{r}_j|}$ for the electron-electron interaction. The ion positions enter in (2.4) solely as fixed parameters. This is the so-called Born-Oppenheimer approximation [1].

However, solving Eq. (2.3) with the Born-Oppenheimer Hamiltonian (2.4) is still too complex for systems with many electrons. Actually, a simple brute-force solution, which samples each coordinate direction of the wave function with only 10 grid points, requires for an atom with N electrons the storage of 10^{3N} numbers. For an iron atom ($N = 26$) this amounts to 10^{78} numbers. This 'gedankenexperiment' already indicates that from a practical point of view the many-body wave function $|\Psi\rangle$ might not be the optimal quantity to describe the many electron system with.

In the Hartree theory [45] the many-electron wave function $|\Psi\rangle$ is approximated by a product of one-particle wave functions

$$\Psi_{\mathrm{H}}(\mathbf{r}_1, \mathbf{r}_2, \ldots, \mathbf{r}_N) = \phi_{n_1}(\mathbf{r}_1)\phi_{n_2}(\mathbf{r}_2)\ldots\phi_{n_N}(\mathbf{r}_N) \tag{2.5}$$

where n_i denotes a set of quantum numbers. Due to the separation of the variables, the demand of storing 10^{3N} numbers in our 'gedankenexperiment' for the true many-electron wave functions is reduced to $N \cdot 10^3$ numbers. Using ansatz (2.5) in combination with the Hamiltonian (2.4) yields the total energy

$$E_{\mathrm{H}} = \langle \Psi_{\mathrm{H}} | H | \Psi_{\mathrm{H}} \rangle = \sum_{i=1}^{N} \langle \phi_{n_i} | -\frac{1}{2}\nabla^2 + V(\mathbf{r}) | \phi_{n_i} \rangle + \frac{1}{2} \sum_{\substack{i,j \\ i\neq j}} \iint \frac{|\phi_{n_i}(\mathbf{r})|^2 |\phi_{n_j}(\mathbf{r}')|^2}{|\mathbf{r} - \mathbf{r}'|} d^3r\, d^3r' \,. \tag{2.6}$$

Minimization of E_{H} with respect to the one-particle wave functions $\phi_{n_i}(\mathbf{r}_i)$ under the constraint that the latter are normalized leads to a Schrödinger equation for the one-particle wave functions

$$\left(-\frac{1}{2}\nabla^2 + V(\mathbf{r}) + V_i(\mathbf{r}) \right) \phi_{n_i}(\mathbf{r}) = \epsilon_i \phi_{n_i}(\mathbf{r}) \tag{2.7}$$

with the electrostatic potential $V_i(\mathbf{r}) = \sum_{j\,(j\neq i)} \int \frac{|\phi_{n_j}(\mathbf{r}')|^2}{|\mathbf{r}-\mathbf{r}'|} d^3r'$. The set of Eqs. (2.7) must be solved self-consistently, as the electrostatic potential already depends on the one particle wave functions and thus on the solution of Eq. (2.7). Starting with a guess of wave functions the electrostatic potential is calculated and a new set of orbitals is gained by solving Eqs. (2.7), which is then used to calculate a new electrostatic potential. This scheme is iterated until the orbitals do not alter anymore. According to the Ritz variational principle the total energy E_{H} constitutes an upper bound for the exact one.

In the Hartree approach the Pauli principle is only considered insofar that two one-particle wave functions are not allowed to agree in all quantum numbers. A rigorous consideration of the Pauli principle however requires that the electron wave function $|\Psi\rangle$ is antisymmetric under the exchange of two particles. A corresponding refinement of the Hartree-ansatz (2.5) leads to a single Slater determinant as an approximation for the many-electron wave function

$$\Psi_{\mathrm{HF}}(\mathbf{r}_1, \mathbf{r}_2, \ldots, \mathbf{r}_N) = \frac{1}{\sqrt{N!}} \det\left|\phi_{n_i}(\mathbf{r}_j)\right| . \tag{2.8}$$

This is the HF approach [46, 47]. The explicit anti-symmetrization of the wave function entails an additional energy contribution to the total energy, the so-called exchange energy or HF exchange energy E_{x}

$$E_{\mathrm{HF}} = E_{\mathrm{H}} + E_{\mathrm{x}} \tag{2.9}$$

with

$$E_{\mathrm{x}} = -\frac{1}{2} \sum_{\substack{i,j \\ i\neq j}} \iint \frac{\phi^*_{n_i}(\mathbf{r})\phi_{n_j}(\mathbf{r})\phi^*_{n_j}(\mathbf{r}')\phi_{n_i}(\mathbf{r}')}{|\mathbf{r}-\mathbf{r}'|} d^3r\, d^3r' . \tag{2.10}$$

In analogy to the Hartree approach minimization of E_{HF} with respect to the one-particle wave functions yields Schrödinger-type equations for the orbitals $\phi_{n_i}(\mathbf{r})$

$$\left(-\frac{1}{2}\nabla^2 + V(\mathbf{r}) + V_i(\mathbf{r})\right)\phi_{n_i}(\mathbf{r}) - \sum_{j\,(j\neq i)} \int \frac{\phi^*_{n_j}(\mathbf{r}')\phi_{n_i}(\mathbf{r}')}{|\mathbf{r}-\mathbf{r}'|} d^3r'\, \phi_{n_j}(\mathbf{r}) = \epsilon_i \phi_{n_i}(\mathbf{r}) , \tag{2.11}$$

where the HF exchange energy results in an additional non-local exchange potential.[2] The HF approach considers exchange exactly, but completely neglects correlation effects. A linear combination of Slater determinants [configuration interaction (CI)] is able to give the exact many-electron wave function in the limit of infinite many determinants. However, the computational demand scales exponentially with the system size. As a consequence, only small

[2] In Eq. (2.11) the diagonal term $j = i$ can be added to the local potential $V_i(\mathbf{r})$ and the non-local exchange potential as they cancel out mutually.

systems (atoms, molecules) can be treated.

In contrast to the Hartree, Hartree-Fock or CI approach, the DFT pursues a different approach. The electron density instead of the complex many-electron wave function is the central quantity. The density depends only on three spatial coordinates in contrast to the $3N$ coordinates of the many-electron wave function, where N denotes the number of electrons in the system. This is a tremendous simplification and DFT still represents an exact theory of the many-electron system, in principle. The central theorem of DFT is the Hohenberg and Kohn theorem and will be discussed in the next section.

2.1. Hohenberg-Kohn theorem

The Hohenberg and Kohn theorem [2] forms the foundation of DFT. It comprises the following two statements:

- The ground-state density of any electronic system $n_0(\mathbf{r})$ uniquely determines the external potential $V(\mathbf{r})$ (up to a constant) and, thus, with Eqs. (2.3) and (2.4) the ground-state wave function $\Psi(\mathbf{r})$. Consequently, the expectation value of any observable of a many-electron system can be regarded as a functional of its ground-state density, in particular the total energy.

- The total energy functional

$$E[n] = F[n] + \int V(\mathbf{r}) n(\mathbf{r}) d^3r \tag{2.12}$$

with the universal functional

$$F[n] = \min_{\Psi \to n} \langle \Psi | T + V_{ee} | \Psi \rangle \,, \tag{2.13}$$

where the minimization is over all N-electron wave functions yielding the density n, becomes equal to the exact ground-state energy E_0 for $n(\mathbf{r}) = n_0(\mathbf{r})$. For all other densities with $n(\mathbf{r}) \neq n_0(\mathbf{r})$

$$E[n] > E[n_0] \tag{2.14}$$

holds. This is the variational principle of DFT leading to the Euler-Lagrange equation

$$\frac{\delta}{\delta n(\mathbf{r})} \left[E[n] - \mu \left(\int n(\mathbf{r}) d^3r - N \right) \right] = 0 \,, \tag{2.15}$$

where the Lagrange multiplier μ ensures particle conservation.

$F[n]$ is universal in the sense that it is independent from the actual external potential. It is the same for all electronic systems.

These theorems alone are, however, of little practical use, as for a practical calculation of the ground-state density and energy the universal functional $F[n]$ has to be evaluated. So far, besides its formal definition in terms of the many-electron wave function no method has been given to find or approximate $F[n]$. A simple but crude approximation for the universal functional is given within the Thomas-Fermi approach.

2.2. Thomas-Fermi approach

The Thomas-Fermi approach [48, 49] goes back to the year 1927. This is 37 years before the rigorous fundament of DFT was laid by Hohenberg and Kohn. In retrospect, however, it can be understood as the first realization of DFT. In the following, the main ideas of the Thomas-Fermi method are discussed in the terminology of DFT.

The Thomas-Fermi method approximates the universal functional by an explicit functional of the density

$$F_{\mathrm{TF}}[n] = \frac{3}{10}(3\pi^2)^{\frac{2}{3}} \int n(\mathbf{r})^{\frac{5}{3}} d^3r + \frac{1}{2} \iint \frac{n(\mathbf{r})n(\mathbf{r}')}{|\mathbf{r}-\mathbf{r}'|} d^3r\, d^3r' \,. \tag{2.16}$$

The first term is an approximation to the kinetic energy assuming that it can be described locally by that of a homogeneous electron gas. The second term is the classical electrostatic Coulomb energy, which is in the context of DFT usually denoted by Hartree energy

$$U_{\mathrm{H}}[n] = \frac{1}{2} \iint \frac{n(\mathbf{r})n(\mathbf{r}')}{|\mathbf{r}-\mathbf{r}'|} d^3r\, d^3r' \,. \tag{2.17}$$

Application of the variational principle (2.15) leads to the Thomas-Fermi equation for the density $n(\mathbf{r})$

$$\frac{1}{2}(3\pi^2)^{\frac{2}{3}} n(\mathbf{r})^{\frac{2}{3}} + V_{\mathrm{H}}(\mathbf{r}) + V(\mathbf{r}) - \mu = 0 \,, \tag{2.18}$$

where we additionally introduced the Hartree potential

$$V_{\mathrm{H}}(\mathbf{r}) = \frac{\delta U_{\mathrm{H}}[n]}{\delta n(\mathbf{r})} = \int \frac{n(\mathbf{r}')}{|\mathbf{r}-\mathbf{r}'|} d^3r' \,. \tag{2.19}$$

Solution of the integral equation (2.18) results in the ground-state density and with Eqs. (2.16) and (2.12) the ground-state total energy can be calculated. But it turns out that the Thomas-Fermi approach is not able to describe the bonding of molecules or solids, because the ki-

netic energy functional is only a poor approximation for the true kinetic energy and essential physics like electron exchange and correlation are neglected. The decisive step for an accurate, practical realization of DFT is the Kohn-Sham approach [3].

2.3. Kohn-Sham system

The brilliant idea of Kohn and Sham [3] was to map the interacting many-electron system onto an auxiliary system of non-interacting electrons, the Kohn-Sham (KS) system. The independent electrons of the KS system move in an effective, local potential $V_{\text{eff}}(\mathbf{r})$, which is adjusted such that the ground-state density of the KS system equals the ground-state density of the interacting system.

The Hohenberg and Kohn theorem is independent of the particular form of the electron-electron interaction. Especially, it holds for the non-interacting KS system

$$H_{\text{s}} = \sum_i \left(-\frac{1}{2}\nabla_i^2 + V_{\text{eff}}(\mathbf{r}_i) \right) . \tag{2.20}$$

Consequently, $V_{\text{eff}}(\mathbf{r})$ is uniquely determined by the ground-state density, and the KS single Slater determinant Φ

$$H_{\text{s}}\Phi(\mathbf{r}_1, \ldots, \mathbf{r}_N) = E_{\text{KS}}\Phi(\mathbf{r}_1, \ldots, \mathbf{r}_N) \tag{2.21}$$

as well as its single-particle wave functions $\phi_i(\mathbf{r})$

$$[-\frac{1}{2}\nabla^2 + V_{\text{eff}}(\mathbf{r})]\phi_i(\mathbf{r}) = \epsilon_i \phi_i(\mathbf{r}) \tag{2.22}$$

can be regarded as functionals of the density. The total energy of the KS system is given by

$$E_{\text{KS}}[n] = T_{\text{s}}[n] + \int V_{\text{eff}}(\mathbf{r}) n(\mathbf{r}) d^3r \tag{2.23}$$

with the kinetic energy functional

$$T_{\text{s}}[n] = \sum_i \int \phi_i^*(\mathbf{r}) \left(-\frac{1}{2}\nabla^2 \right) \phi_i(\mathbf{r}) d^3r \, . \tag{2.24}$$

In order to guarantee that the KS system has the same ground-state density as the interacting one, Kohn and Sham rewrite the universal functional $F[n]$ of the interacting, many electron system as a sum of the kinetic energy $T_{\text{s}}[n]$ of the non-interacting system, the Hartree energy

$U_{\mathrm{H}}[n]$, and an exchange-correlation (xc) energy

$$F[n] = T_{\mathrm{s}}[n] + U_{\mathrm{H}}[n] + E_{\mathrm{xc}}[n]\,, \tag{2.25}$$

where E_{xc} subsumes all many-electron exchange and correlation effects and the difference between the kinetic energy of the interacting and the non-interacting system.

Then, the stationary equation (2.15) becomes

$$\frac{\delta T_{\mathrm{s}}}{\delta n(\mathbf{r})} + V_{\mathrm{H}}(\mathbf{r}) + \frac{\delta E_{\mathrm{xc}}}{\delta n(\mathbf{r})} + V(\mathbf{r}) - \mu = 0\,. \tag{2.26}$$

This Euler-Lagrange equation is formally equivalent to that obtained for the non-interacting KS system, if the effective potential fulfills

$$V_{\mathrm{eff}}(\mathbf{r}) = V(\mathbf{r}) + V_{\mathrm{H}}(\mathbf{r}) + V_{\mathrm{xc}}(\mathbf{r}) \tag{2.27}$$

with the xc potential given by

$$V_{\mathrm{xc}}(\mathbf{r}) = \frac{\delta E_{\mathrm{xc}}[n]}{\delta n(\mathbf{r})}\,. \tag{2.28}$$

Consequently, Kohn and Sham recast the problem such that the ground-state density $n_0(\mathbf{r})$ of the interacting system can be found by solving the one-particle KS equations (2.22) with the potential (2.27) and subsequently occupying the electron states according to the Pauli principle. The density is then given by a sum over the occupied KS orbitals

$$n_0(\mathbf{r}) = \sum_{i}^{\mathrm{occ.}} |\phi_i(\mathbf{r})|^2\,. \tag{2.29}$$

As $V_{\mathrm{eff}}(\mathbf{r})$ itself depends on the density, the set of equations (2.22) must be solved self-consistently. The ground-state energy E_0 is finally obtained from

$$E_0 = E[n_0] = T_{\mathrm{s}}[n_0] + U_{\mathrm{H}}[n_0] + E_{\mathrm{xc}}[n_0] + \int V(\mathbf{r}) n_0(\mathbf{r}) d^3r\,. \tag{2.30}$$

Formally, the mapping of the interacting system onto the KS system is exact. However, except for the formal definition of the xc energy functional

$$E_{\mathrm{xc}}[n] = F[n] - T_{\mathrm{s}}[n] - U_{\mathrm{H}}[n] \tag{2.31}$$

its exact form is unknown. $E_{\mathrm{xc}}[n]$ is usually split into an exchange and a correlation part

$$E_{\mathrm{xc}}[n] = E_{\mathrm{x}}[n] + E_{\mathrm{c}}[n] \tag{2.32}$$

which are defined by

$$E_{\mathrm{x}}[n] = \langle \Phi[n] | V_{ee} | \Phi[n] \rangle - U_{\mathrm{H}}[n] \tag{2.33}$$

$$E_{\mathrm{c}}[n] = \langle \Psi[n] | T + V_{ee} | \Psi[n] \rangle - \langle \Phi[n] | T + V_{ee} | \Phi[n] \rangle \,. \tag{2.34}$$

Here, $\Phi[n]$ denotes the KS single Slater determinant that yields the density $n(\mathbf{r})$ and $\Psi[n]$ is the many-electron ground-state wave function of density n.

In practice, the xc energy functional must be approximated. Chapter 3 gives some physical insight into the xc functional, discusses the nowadays routinely used local-density approximation (LDA) and generalized gradient approximation (GGA), and finally introduces orbital-dependent functionals.

In contrast to the Thomas-Fermi approach, the KS method approximates the kinetic energy by the exact orbital-dependent, non-interacting kinetic energy term instead of an explicit density functional. In this way, the dominant contribution to the total energy is described well and only the smaller difference to the exact kinetic energy must be approximated by E_{xc}. This explains, at least partially, the success of KS DFT, as already relatively simple approximations for E_{xc} lead to reliable results for a wide range of materials.

2.4. Spin DFT

The DFT formalism, developed so far, does not incorporate the spin of the electron as a degree of freedom. However, the spin is essential to describe, for example, the magnetism in the $3d$ metals Fe, Co, Ni, and Cr. Here, we sketch the extension of the Hohenberg and Kohn theorem as well as the KS formalism to spin DFT.

Instead of the spin-independent interacting Hamiltonian (2.4), the interacting Pauli-type Hamiltonian

$$H = \sum_i \left[-\frac{1}{2}\nabla_i^2 + V(\mathbf{r}_i) + \mu_{\mathrm{B}} \boldsymbol{\sigma} \cdot \mathbf{B}(\mathbf{r}_i) \right] + \frac{1}{2} \sum_i \sum_{j \neq i} \frac{1}{|\mathbf{r}_i - \mathbf{r}_j|} \tag{2.35}$$

forms the starting point of spin DFT, where μ_{B} is the Bohr magneton, $\boldsymbol{\sigma}$ is the vector of the Pauli spin matrices, and $\mathbf{B}(\mathbf{r})$ denotes a magnetic field. Von Barth and Hedin [50] showed that the ground-state wave function $|\Psi\rangle$ of the Hamiltonian (2.35) and hence all ground-state properties are functionals of the density matrix, which is defined by

$$n^{\sigma\sigma'}(\mathbf{r}) = \langle \Psi | \psi_\sigma^+(\mathbf{r}) \psi_{\sigma'}(\mathbf{r}) | \Psi \rangle \,. \tag{2.36}$$

Here, $\psi_\sigma(\mathbf{r})$ denotes the field operator for an electron of spin σ ($\sigma = \uparrow, \downarrow$). This statement

corresponds to the first part of the Hohenberg and Kohn theorem for non-spin-polarized systems. Accordingly, the second part – the variational principle – can be generalized: the ground-state energy E is stationary with respect to variations of the density matrix $n^{\sigma\sigma'}(\mathbf{r})$.

The concept of the KS system as an auxiliary system of non-interacting electrons, which yield the same ground-state density (matrix) can be carried over, too. The KS equations for the KS orbitals, which are then two-component Pauli spinors $\begin{pmatrix} \phi_i^{\uparrow}(\mathbf{r}) \\ \phi_i^{\downarrow}(\mathbf{r}) \end{pmatrix}$, thus become

$$\left\{\left[-\frac{1}{2}\nabla^2 + \int \frac{n(\mathbf{r}')}{|\mathbf{r}-\mathbf{r}'|} d^3r' + V_{\text{ext}}(\mathbf{r})\right]\delta^{\sigma\sigma'} + \mu_{\text{B}}(\boldsymbol{\sigma}\cdot\mathbf{B})^{\sigma\sigma'} + \frac{\delta E_{\text{xc}}}{\delta n^{\sigma\sigma'}(\mathbf{r})}\right\}\phi_i^{\sigma'}(\mathbf{r}) = \epsilon_i^{\sigma'}\phi_i^{\sigma'}(\mathbf{r})\,. \tag{2.37}$$

The density matrix in terms of the occupied KS spinors is given by

$$n^{\sigma\sigma'}(\mathbf{r}) = \sum_i^{\text{occ.}} \phi_i^{\sigma *}(\mathbf{r})\phi_i^{\sigma'}(\mathbf{r})\,. \tag{2.38}$$

For collinear structures, on which we will focus in this thesis, i.e., ferromagnetic or antiferromagnetic materials, the KS Hamiltonian becomes diagonal and Eq. (2.37) decouples into two equations

$$\left\{\left[-\frac{1}{2}\nabla^2 + \int \frac{n(\mathbf{r}')}{|\mathbf{r}-\mathbf{r}'|} d^3r' + V_{\text{ext}}(\mathbf{r})\right] + \mu_{\text{B}}B(\mathbf{r}) + V_{\text{xc}}^{\uparrow}(\mathbf{r})\right\}\phi_i^{\uparrow}(\mathbf{r}) = \epsilon_i^{\uparrow}\phi_i^{\uparrow}(\mathbf{r}) \tag{2.39}$$

$$\left\{\left[-\frac{1}{2}\nabla^2 + \int \frac{n(\mathbf{r}')}{|\mathbf{r}-\mathbf{r}'|} d^3r' + V_{\text{ext}}(\mathbf{r})\right] - \mu_{\text{B}}B(\mathbf{r}) + V_{\text{xc}}^{\downarrow}(\mathbf{r})\right\}\phi_i^{\downarrow}(\mathbf{r}) = \epsilon_i^{\downarrow}\phi_i^{\downarrow}(\mathbf{r})\,, \tag{2.40}$$

where $V_{\text{xc}}^{\sigma}(\mathbf{r})$ is the spin-dependent generalization of the xc potential defined as

$$V_{\text{xc}}^{\sigma}(\mathbf{r}) = \frac{\delta E_{\text{xc}}}{\delta n^{\sigma}(\mathbf{r})} \tag{2.41}$$

and the N lowest states are occupied without regard to the spin such that the particle number is conserved

$$N = \sum_{\sigma}\int n^{\sigma}(\mathbf{r})\,d^3r = \sum_{\sigma}\sum_{\substack{i \\ \epsilon_i^{\sigma}\le E_{\text{F}}}}\int \phi_i^{\sigma *}(\mathbf{r})\phi_i^{\sigma}(\mathbf{r})\,d^3r\,. \tag{2.42}$$

The energy of the highest occupied state corresponds to the Fermi energy E_{F} of the system.

3. The exchange-correlation energy functional of KS DFT

Kohn-Sham (KS) density-functional theory (DFT) relies on an exact mapping of the interacting, many-electron system onto an auxiliary one of non-interacting electrons such that the ground-state densities of the auxiliary and true systems coincide. All complicated many-body effects are taken into account in the KS formalism, in principle, via the exchange-correlation (xc) energy functional. The exact form of the latter, however, is unknown, so that approximations for E_{xc} are mandatory in practice. Fortunately, already simple approximations give reliable results for a wide range of materials.

In this chapter we give some physical insight into the xc functional of DFT. We begin with the adiabatic-connection method, which connects the KS with the true, fully interacting system by gradually switching on the electron-electron interaction. It provides a definition of the xc energy in terms of the xc hole and constitutes the basis for the rest of this chapter. Then, we introduce the nowadays standard functionals the local-density approximation (LDA) and the generalized gradient approximation (GGA) and shortly discuss their success and failures. For the construction of approximate functionals, exact constraints for the xc functional are of utmost importance. Such constraints can, for example, be developed by the technique of uniform coordinate scaling. The latter will be explained and a link between uniform coordinate scaling and the adiabatic-connection method will be established. Afterwards, based on the adiabatic-connection method, we introduce the hybrid functionals that combine orbital-dependent exact exchange with (semi-)local xc functionals. While the hybrids exactly describe the coupling constant integrand in the non-interacting limit ($\lambda = 0$), a systematic expansion of the xc functional in the electron-electron interaction around $\lambda = 0$ is provided by Görling-Levy perturbation theory. The perturbation theory yields, in principle, an exact expansion of the xc functional. Finally, we point out a different route for the construction of approximate functionals by combining many-body perturbation theory (MBPT) and KS DFT. The Sham-Schlüter equation connects the self-energy of MBPT with the xc potential. In principle, a diagrammatic expansion of the dynamical and non-local self-energy in higher and higher orders of the electron-electron interaction leads to xc potentials of ever increasing

accuracy. We close this chapter by a short summary.

For the sake of simplicity, we have suppressed the spin index throughout this chapter.

3.1. Adiabatic-connection method

In the adiabatic connection [18–20], which is sometimes also called coupling-constant integration method, the KS system is connected with the fully interacting many-electron system by adiabatically switching on the electron-electron interaction V_{ee}

$$H^\lambda = T + \lambda V_{ee} + V^\lambda \tag{3.1}$$

and adjusting the external potential V^λ such that the ground-state density equals the real physical density of the interacting system for any $\lambda \in [0,1]$. For $\lambda = 0$ the external potential V^λ then corresponds to the effective KS potential, whereas for $\lambda = 1$ it is the true external potential.

According to the coupling-constant Hamiltonian H^λ, the universal functional $F[n]$ of Eq. (2.13) may be generalized to

$$F^\lambda[n] = \min_{\Psi\to n}\langle\Psi|T + \lambda V_{ee}|\Psi\rangle\,. \tag{3.2}$$

In analogy to Eq. (2.31), the xc energy functional that corresponds to H^λ is defined by

$$E_{\mathrm{xc}}^\lambda[n] = F^\lambda[n] - T_{\mathrm{s}}[n] - \lambda U_{\mathrm{H}}[n]\,. \tag{3.3}$$

In the limit $\lambda = 0$, E_{xc}^λ is zero, as $F^{\lambda=0}[n] = T_{\mathrm{s}}[n]$ holds, which reflects that the KS system of a non-interacting system is the system itself. Consequently, the xc energy functional can be written as

$$E_{\mathrm{xc}}[n] = \int_0^1 \frac{dE_{\mathrm{xc}}^\lambda}{d\lambda}d\lambda = \int_0^1 \left[\langle\Psi^\lambda|V_{ee}|\Psi^\lambda\rangle - U_{\mathrm{H}}[n]\right]d\lambda\,, \tag{3.4}$$

where Ψ^λ denotes the many-electron ground-state wave function of H^λ.

At first glance, this exact equation for E_{xc} seems to be of little practical use, as the many-electron wave function Ψ^λ enters for each λ. But we will see in the following that it is a central equation for developing and understanding functionals.

We define the λ dependent pair-density

$$n_2^\lambda(\mathbf{r},\mathbf{r}') = \langle\Psi^\lambda|\sum_{\substack{i,j\\(i\neq j)}}\delta(\mathbf{r}-\mathbf{r}_i)\delta(\mathbf{r}'-\mathbf{r}_j)|\Psi^\lambda\rangle \tag{3.5}$$

and the λ dependent xc hole

$$n_{\mathrm{xc}}^{\lambda}(\mathbf{r},\mathbf{r}') = \frac{n_2^{\lambda}(\mathbf{r},\mathbf{r}') - n(\mathbf{r})n(\mathbf{r}')}{n(\mathbf{r})}\,. \tag{3.6}$$

The latter describes the reduced probability of finding an electron at $\mathbf{r}'$ if a given electron sits at $\mathbf{r}$. This hole is, on the one hand, created by the Coulomb repulsion and, on the other hand, by the Pauli principle separating two electrons of equal spin in space. Combining Eq. (3.4) with Eqs. (3.5) and (3.6) we obtain for the xc energy

$$E_{\mathrm{xc}}[n] = \frac{1}{2}\iint \frac{1}{|\mathbf{r}-\mathbf{r}'|}\left[\int n_2^{\lambda}(\mathbf{r},\mathbf{r}') - n(\mathbf{r})n(\mathbf{r}')d\lambda\right] d^3r\, d^3r' \tag{3.7}$$

$$= \frac{1}{2}\iint \frac{n(\mathbf{r})n_{\mathrm{xc}}(\mathbf{r},\mathbf{r}')}{|\mathbf{r}-\mathbf{r}'|} d^3r\, d^3r'\,, \tag{3.8}$$

where we additionally introduced the λ-averaged xc hole

$$n_{\mathrm{xc}}(\mathbf{r},\mathbf{r}') = \int_0^1 n_{\mathrm{xc}}^{\lambda}(\mathbf{r},\mathbf{r}')\, d\lambda\,. \tag{3.9}$$

Thus, the xc energy is the Coulomb energy of the electron density with the surrounding xc hole. The xc hole around an electron at $\mathbf{r}$ does not depend on the absolute position $\mathbf{r}'$. Thus, we can represent the xc hole $n_{\mathrm{xc}}(\mathbf{r},\mathbf{r}')$ by

$$n_{\mathrm{xc}}(\mathbf{r},\mathbf{r}') = \sum_{l=0}^{\infty}\sum_{m=-l}^{l} n_{\mathrm{xc},lm}(\mathbf{r},|\mathbf{r}-\mathbf{r}'|)\, Y_{lm}(\widehat{\mathbf{r}-\mathbf{r}'})\,. \tag{3.10}$$

Using this expansion in Eq. (3.8) it becomes evident that only the spherical average of the xc hole $n_{\mathrm{xc},00}(\mathbf{r},r')$ determines the xc energy

$$E_{\mathrm{xc}}[n] = \frac{1}{2}\sqrt{4\pi}\int n(\mathbf{r}) \int n_{\mathrm{xc},00}(\mathbf{r},r')r'\, dr'\, d^3r\,. \tag{3.11}$$

Approximate xc functionals therefore must not mimic the exact xc hole, it is sufficient if they are able to reproduce its spherical average. Moreover, the exact xc hole obeys the sum rule

$$\int n_{\mathrm{xc}}(\mathbf{r},\mathbf{r}')d^3r' = -1\,. \tag{3.12}$$

In the next section the nowadays routinely used approximations for the xc functional, the LDA and the GGA, are discussed.

3.2. LDA and GGA

The LDA assumes that the interacting electron system locally acts as a homogeneous electron gas. Correspondingly, the xc energy is written as an integral over space, where at each point in space the xc energy is approximated by the xc energy density $\epsilon_{\mathrm{xc}}^{\mathrm{LDA}}$ of the homogeneous electron gas

$$E_{\mathrm{xc}}^{\mathrm{LDA}}[n] = \int n(\mathbf{r})\epsilon_{\mathrm{xc}}^{\mathrm{LDA}}(n(\mathbf{r}))\, d^3r\,. \tag{3.13}$$

The exchange part of $\epsilon_{\mathrm{xc}}^{\mathrm{LDA}}$ can be derived exactly within the Hartree-Fock (HF) method

$$\epsilon_{\mathrm{x}}^{\mathrm{LDA}}(n) = -\frac{3}{4\pi}(3\pi^2 n)^{\frac{1}{3}}\,, \tag{3.14}$$

while the remaining correlation energy is parametrized by a fit to quantum Monte-Carlo calculations [4]. The different available LDA xc functionals, e.g. Vosko-Wilk-Nusair (VWN) [5], Perdew-Zunger (PZ) [9], and Perdew-Wang (PW) [6] differ in details of the parametrization for $\epsilon_{\mathrm{c}}^{\mathrm{LDA}}$.

Despite its simplicity, the LDA gives reliable results for a wide range of materials and properties. Its success goes back to the fact that $E_{\mathrm{xc}}^{\mathrm{LDA}}$ provides (nearly) an exact description of the xc energy for the model system of the homogeneous electron gas. Therefore, the LDA xc hole fulfills the sum rule (3.12) and its spherical average is usually a reasonable approximation to the exact average, whereas the full non-spherical hole is usually in poor agreement with the exact one [51].

A simple expansion around the uniform limit by taking into account the inhomogeneity of the system via its density gradient leads in practice to less accurate results as the LDA [52, 53]. Explicit incorporation of the sum rule (3.12) and additional exact constraints finally lead to the generalized-gradient approximation (GGA) with an improved accuracy in general. The GGA is often called a semi-local approximation and formally given by

$$E_{\mathrm{xc}}^{\mathrm{GGA}}[n] = \int n(\mathbf{r})\epsilon_{\mathrm{xc}}^{\mathrm{GGA}}(n(\mathbf{r}), \nabla n(\mathbf{r}))\, d^3r. \tag{3.15}$$

A large variety of GGA functionals exists nowadays: Perdew-Wang-91 (PW91) [8], Perdew-Burke-Ernzerhof (PBE) [7], Becke-Lee-Yang-Parr (BLYP) [54, 55] and many others.

For a comparison of the performance of LDA and GGA we cite some well known trends [56–58]:

- LDA as well as GGA give ground-state structural properties with a deviation of a few percent to the experimental value. The LDA usually underestimates the lattice parameter. It over-binds. On the contrary, GGA has a tendency to under-bind, where the

magnitude of the error is typically not as large as the LDA one.

- With respect to the experimental values cohesive energies are in general significantly overestimated in LDA. The GGA gives usually better energies.

- KS band gaps of LDA and GGA are far too small in comparison with experimental results. This is often called the band gap problem of LDA and GGA.

- Due to the self-interaction error inherent in LDA and GGA, localized d- and f-electron states are often bound to loosely and their binding energies appear too high in energy. In the worst case, this can lead to a metallic instead of an insulating ground state.

The self-interaction error arises from the separation of the Hartree energy in Eq. (2.25) and the only approximate treatment of exchange in LDA and GGA. Hence the total energy $E[n]$ contains an unphysical self-interaction, i.e., the electrons move in an effective potential which is partially created by its own charge. The error is more severe for localized states, like d- and f-electrons of transition metal oxides, and tends to delocalize these electrons.

3.3. Uniform coordinate scaling and the adiabatic connection

As already pointed out, exact constraints for the xc functional are essential for the construction of approximate xc functionals E_{xc}. Each constraint limits the 'phase space' of possible forms for E_{xc}. In particular, the technique of uniform coordinate scaling has been proven as a useful tool to find such constraints [59, 60].

The uniformly scaled density $n_\gamma(\mathbf{r})$ arises from $n(\mathbf{r})$ by scaling all length scales by γ and ensuring that $n_\gamma(\mathbf{r})$ is still normalized to N electrons

$$n_\gamma(\mathbf{r}) = \gamma^3 n(\gamma\mathbf{r}) \quad \gamma \in [0, \infty[\,. \tag{3.16}$$

For $\gamma \in [0, 1[$ the scaled density $n_\gamma(\mathbf{r})$ is stretched in comparison with $n(\mathbf{r})$, whereas $\gamma \in]1, \infty[$ corresponds to a compression of the density. Accordingly, the uniformly scaled KS single Slater determinant Φ_γ and the many-electron wave function Ψ_γ are defined by

$$\Phi_\gamma(\mathbf{r}_1, \ldots, \mathbf{r}_N) = \gamma^{3N/2}\Phi(\gamma\mathbf{r}_1, \ldots, \gamma\mathbf{r}_N) \tag{3.17}$$

$$\Psi_\gamma(\mathbf{r}_1, \ldots, \mathbf{r}_N) = \gamma^{3N/2}\Psi(\gamma\mathbf{r}_1, \ldots, \gamma\mathbf{r}_N)\,. \tag{3.18}$$

The kinetic energy of the scaled wave function depends quadratically on the scaling factor γ

$$T[\Psi_\gamma] = \langle \Psi_\gamma | T | \Psi_\gamma \rangle = \gamma^2 \langle \Psi | T | \Psi \rangle = \gamma^2 T[\Psi] \,. \tag{3.19}$$

On the contrary, the expectation value of the electron-electron interaction is linear in γ

$$V_{ee}[\Psi_\gamma] = \langle \Psi_\gamma | V_{ee} | \Psi_\gamma \rangle = \gamma \langle \Psi | V_{ee} | \Psi \rangle = \gamma V_{ee}[\Psi] \,. \tag{3.20}$$

The scaling relations of T and V_{ee} are here given for the physical many-electron wave function, but they hold as well for the KS wave function.

The question arises which is the KS or physical ground-state wave function belonging to the scaled density? We first answer the question for the KS wave function. The KS wave function of density n is the wave function that minimizes $\langle \Phi[n] | T | \Phi[n] \rangle$. As the scaled KS wave function Φ_γ also minimizes the kinetic energy

$$\langle \Phi_\gamma[n] | T | \Phi_\gamma[n] \rangle = \gamma^2 \langle \Phi[n] | T | \Phi[n] \rangle \,, \tag{3.21}$$

the KS ground-state wave function for the scaled density is the scaled KS wave function of density n

$$\Phi[n_\gamma] = \Phi_\gamma[n] \,. \tag{3.22}$$

For the physical interacting problem this is not the case anymore, i.e., the scaled wave function Ψ_γ is not the ground-state wave function that gives the scaled density n_γ. The many-electron wave function Ψ of density n minimizes $\langle \Psi[n] | T + V_{ee} | \Psi[n] \rangle$. Due to the electron-electron interaction Ψ_γ does not minimize $\langle \Psi_\gamma[n] | T + V_{ee} | \Psi_\gamma[n] \rangle$.

However, the scaled ground-state wave function Ψ^λ_γ of the coupling-constant Hamiltonian (3.1) fulfills

$$\langle \Psi^\lambda_\gamma[n] | T + V_{ee} | \Psi^\lambda_\gamma[n] \rangle = \langle \Psi^\lambda[n] | \gamma^2 T + \gamma V_{ee} | \Psi^\lambda[n] \rangle = \gamma^2 \langle \Psi^\lambda[n] | T + \frac{1}{\gamma} V_{ee} | \Psi^\lambda[n] \rangle. \tag{3.23}$$

Here, we used the scaling relations Eqs. (3.19) and (3.20). We note that the ground-state wave function Ψ^λ of the coupling constant Hamiltonian minimizes $\langle \Psi^\lambda | T + \lambda V_{ee} | \Psi^\lambda \rangle$. So, if we choose the coupling constant λ as the reciprocal value of the scaling factor

$$\lambda = \frac{1}{\gamma} \,, \tag{3.24}$$

the wave function $\Psi^{1/\gamma}_\gamma$ minimizes $T + V_{ee}$, since $\Psi^{1/\gamma}$ minimizes $T + \frac{1}{\gamma} V_{\mathrm{ee}}$. Consequently, the many-electron ground-state wave function of density n_γ is the scaled ground-state wave

function of the coupling constant Hamiltonian with $\lambda = 1/\gamma$

$$\Psi[n_\gamma] = \Psi_\gamma^{1/\gamma}[n]\,. \tag{3.25}$$

Conversely, the many-electron ground-state wave function Ψ^λ of the coupling-constant Hamiltonian (3.1) is the uniformly scaled ground-state wave function of density $n_{1/\lambda}$ of the fully interacting system

$$\Psi^\lambda[n] = \Psi_\lambda[n_{1/\lambda}]\,. \tag{3.26}$$

This manifests an important relation between coordinate scaling and the adiabatic connection approach.

From Eq. (3.22) the scaling relations for the non-interacting kinetic energy (2.24) and the exchange energy (2.33) follow immediately

$$T_\mathrm{s}[n_\gamma] = T_\mathrm{s}[\Phi[n_\gamma]] = T_\mathrm{s}[\Phi_\gamma[n]] = \gamma^2 T_\mathrm{s}[n] \tag{3.27}$$

$$E_\mathrm{x}[n_\gamma] = E_\mathrm{x}[\Phi[n_\gamma]] = E_\mathrm{x}[\Phi_\gamma[n]] = \gamma E_\mathrm{x}[n]\,. \tag{3.28}$$

Combination of Eq. (3.26) with Eqs. (3.19) and (3.20) yields the relation for the universal functional (3.2) of the coupling-constant Hamiltonian

$$F^\lambda[n] = \langle \Psi^\lambda[n] | T + \lambda V_{ee} | \Psi^\lambda[n] \rangle = \lambda^2 F[n_{1/\lambda}]\,. \tag{3.29}$$

The coupling-constant dependent xc energy functional (3.3) fulfills an equivalent relation

$$E_\mathrm{xc}^\lambda[n] = \lambda^2 F[n_{1/\lambda}] - \lambda^2 T_\mathrm{s}[n_{1/\lambda}] - \lambda^2 U_\mathrm{H}[n_{1/\lambda}] = \lambda^2 E_\mathrm{xc}[n_{1/\lambda}]\,. \tag{3.30}$$

The xc energy of the Hamiltonian H^λ with coupling constant λ is identical to λ^2 times the xc energy at $\lambda = 1$ but evaluated at the scaled density $n_{1/\lambda}$. This last relation can be used to calculate the coupling constant integrand $dE_\mathrm{xc}^\lambda/d\lambda$ (3.4)

$$\frac{dE_\mathrm{xc}^\lambda}{d\lambda} = \frac{d}{d\lambda}\left[\lambda^2 E_\mathrm{xc}[n_{1/\lambda}]\right] \tag{3.31}$$

for any approximate xc functional.

For small systems it is possible to calculate the coupling constant integrand

$$\frac{dE_\mathrm{xc}^\lambda}{d\lambda} = \langle \Psi^\lambda | V_{ee} | \Psi^\lambda \rangle - U_\mathrm{H}[n] \tag{3.32}$$

exactly. A comparison of the exact integrand with its approximate counterpart gives insight

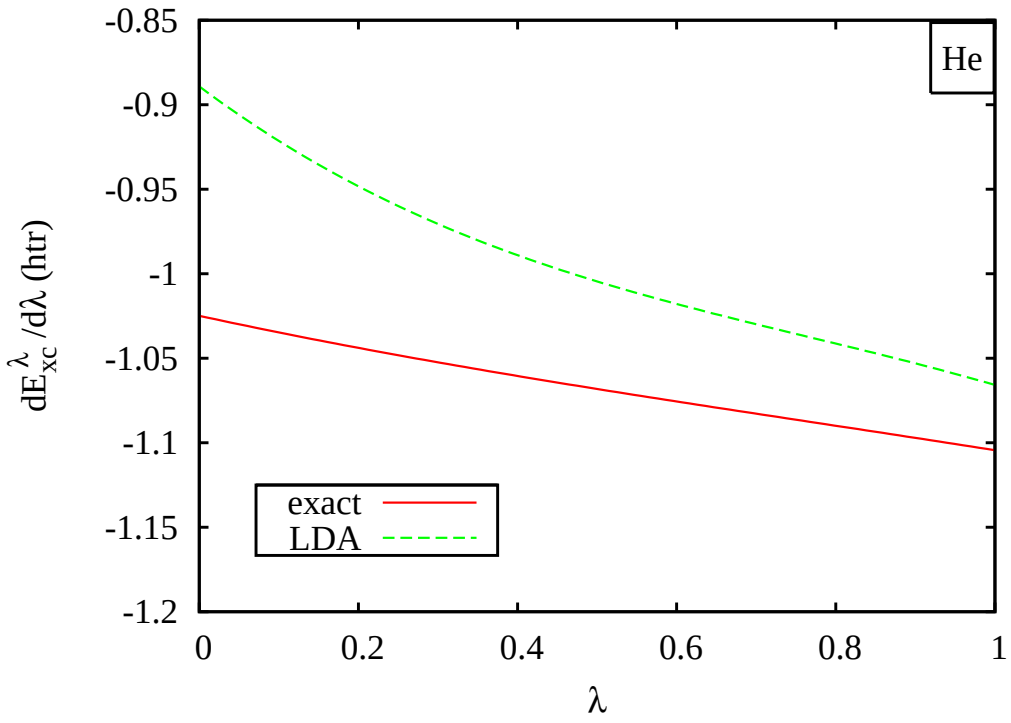

Figure 3.1.: Exact and LDA coupling-constant integrand $E_{\mathrm{xc}}^{\lambda}$ of the He atom. (Data of graph taken from Ref. 60.)

into the power and shortcomings of the approximate xc functional. The calculation of the exact integrand requires to solve the interacting electron system H^{λ} many times. In a first step for each coupling constant λ the external potential, that keeps the density fixed at the ground-state density of the fully interacting system, must be found. Then the many electron ground-state wave function Ψ^{λ} can be determined. As an example Fig. 3.1 shows the exact and LDA integrand $dE_{\mathrm{xc}}^{\lambda}/d\lambda$ for the He atom. The LDA integrand has been evaluated by means of Eq. (3.31). For $\lambda = 0$ the LDA overestimates the exact value quite notable. Here, the curve is solely determined by exchange, as $dE_{\mathrm{xc}}^{\lambda}/d\lambda$ at $\lambda = 0$ is identical to the exact exchange energy (2.33). With increasing λ the distance between the LDA and the exact integrand decreases. The LDA can, thus, be considered as more accurate in the limit $\lambda \to 1$.

Moreover, Fig. 3.1 demonstrates the often cited error cancellation between the exchange and correlation part of the LDA. According to Eqs. (3.28) and (3.31) the exchange contribution

$dE_x^\lambda/d\lambda$ to the coupling-constant integrand is a constant and given by the integrand at $\lambda = 0$

$$\frac{dE_x^\lambda}{d\lambda} = \left.\frac{dE_{xc}^\lambda}{d\lambda}\right|_{\lambda=0} . \tag{3.33}$$

Hence, the area between the constant $dE_x^\lambda/d\lambda$ and the curve $y = 0$ corresponds to the exchange energy, whereas the correlation energy can be identified with the area between the coupling-constant integrand $dE_{xc}^\lambda/d\lambda$ and the constant $dE_x^\lambda/d\lambda$. A simple comparison of both areas for the LDA and the exact integrand shows that the LDA overestimates the exchange energy for He, but underestimates the correlation energy. Their sum, however, is a reasonable approximation for the exact xc energy, since the correlation energy counterbalances the overestimation of the exchange energy. This error cancellation between exchange and correlation energy, here observed for He, is a quite general statement. It holds for larger systems as well as for the GGA.

As there is a quite substantial deviation between the exact integrand and the LDA in the limit $\lambda \to 0$, one might think of using the exact orbital-dependent expression for the exchange energy (2.33) instead of an explicit density-dependent approximation as in LDA or GGA. In this way, the $\lambda = 0$ limit would be described exactly. As in the opposite limit $\lambda \to 1$ the LDA performs quite well, a suitable combination of exact exchange with LDA or GGA might be a good approximation for E_{xc}. This is the underlying idea of hybrid functionals and will be discussed in more detail in the next section.

3.4. Hybrid functionals

Hybrid functionals combine local or semi-local functionals with the exact orbital-dependent exchange term E_x (2.33). This class of functionals relies on the observation that LDA as well as GGA perform better in the $\lambda \to 1$ limit of the coupling-constant integration method than in the limit $\lambda \to 0$, where the exact integrand is known and is given by the exact exchange energy (2.33). Nowadays, a whole zoo of hybrid functionals is available. We concentrate our discussion here on three prototype hybrid functionals.

The simplest way to approximate the coupling constant integrand $dE_{xc}^\lambda/d\lambda$ is a linear interpolation between its limits $\lambda = 0$ and $\lambda = 1$

$$\frac{dE_{xc}^\lambda}{d\lambda} = \left.\frac{dE_{xc}^\lambda}{d\lambda}\right|_{\lambda=0} + \lambda\left(\left.\frac{dE_{xc}^\lambda}{d\lambda}\right|_{\lambda=1} - \left.\frac{dE_{xc}^\lambda}{d\lambda}\right|_{\lambda=0}\right) . \tag{3.34}$$

After integration we obtain for the xc energy functional

$$E_{\mathrm{xc}} = \int \frac{dE_{\mathrm{xc}}^{\lambda}}{d\lambda} d\lambda = \frac{1}{2}\left(\left.\frac{dE_{\mathrm{xc}}^{\lambda}}{d\lambda}\right|_{\lambda=0} + \left.\frac{dE_{\mathrm{xc}}^{\lambda}}{d\lambda}\right|_{\lambda=1} \right). \tag{3.35}$$

For the $\lambda = 0$ end the orbital dependent exact exchange energy is used $dE_{\mathrm{xc}}^{\lambda}/d\lambda\big|_{\lambda=0} = E_{\mathrm{x}}$, whereas in the opposite limit $dE_{\mathrm{xc}}^{\lambda}/d\lambda\big|_{\lambda=1}$ is usually approximated by a local or semi-local density functional (DF) $dE_{\mathrm{xc}}^{\lambda}/d\lambda\big|_{\lambda=1} = E_{\mathrm{xc}}^{\mathrm{DF}}$. We note, however, that the latter is an additional approximation beyond the linearization of the integrand Eq. (3.34). Consequently, one finally obtains the functional

$$E_{\mathrm{xc}} = \frac{1}{2}\left(E_{\mathrm{x}} + E_{\mathrm{xc}}^{\mathrm{DF}}\right), \tag{3.36}$$

which is known as half and half (HaH) mixing and which has been proposed by Becke [21].

Perdew *et al.* [22] proposed to interpolate the λ dependence of the integrand by

$$\frac{dE_{\mathrm{xc}}^{\lambda}}{d\lambda} = \frac{dE_{\mathrm{xc}}^{\mathrm{DF},\lambda}}{d\lambda} + (E_{\mathrm{x}} - E_{\mathrm{x}}^{\mathrm{DF}})(1-\lambda)^{n-1} \tag{3.37}$$

where $dE_{\mathrm{xc}}^{\mathrm{DF},\lambda}/d\lambda$ denotes the λ-dependent integrand of any local or semi-local functional, which is given by (3.31), and $E_{\mathrm{x}}^{\mathrm{DF}}$ is the exchange part of the DF functional. The integer n determines how rapid the integrand tends to $dE_{\mathrm{xc}}^{\mathrm{DF},\lambda}/d\lambda$ for $\lambda \to 1$. It is argued [22], that the integer n should be the lowest order of Møller-Plesset (MP) perturbation theory, which provides a realistic description of the many-electron system. As for a large class of materials MP perturbation theory of fourth order (MP4) gives accurate results, it follows

$$E_{\mathrm{xc}} = E_{\mathrm{xc}}^{\mathrm{DF}} + \frac{1}{4}(E_{\mathrm{x}} - E_{\mathrm{x}}^{\mathrm{DF}}). \tag{3.38}$$

With the density functional of Perdew, Burke, and Ernzerhof $E_{\mathrm{xc}}^{\mathrm{DF}} = E_{\mathrm{xc}}^{\mathrm{PBE}}$ [7] Eq. (3.38) defines the PBE0 functional.

In Fig. 3.2 the exact coupling-constant integrand for the He atom is compared with the integrand of the LDA and the integrand of the hybrids introduced so far. The HaH-I curve corresponds to the half and half mixing of Eq. (3.35), where $dE_{\mathrm{xc}}^{\lambda}/d\lambda\big|_{\lambda=1} = dE_{\mathrm{xc}}^{\mathrm{LDA},\lambda}/d\lambda\big|_{\lambda=1}$ has been used. The curve denoted with HaH-II is the hybrid of Eq. (3.36) with $E_{\mathrm{xc}}^{\mathrm{DF}} = E_{\mathrm{xc}}^{\mathrm{LDA}}$, and the one labelled with Perdew corresponds to Eq. (3.37). In the last case we have employed the LDA for $E_{\mathrm{x}}^{\mathrm{DF}}$ and $dE_{\mathrm{xc}}^{\mathrm{DF},\lambda}/d\lambda$. By construction the hybrids match the exact curve at $\lambda = 0$. This graphical analysis reveals that the HaH-I hybrid should be the most accurate approximation for the xc functional for the He atom. It is closely followed by the functional labelled with Perdew. Furthermore, Fig. 3.2 clearly demonstrates that the additional approximation

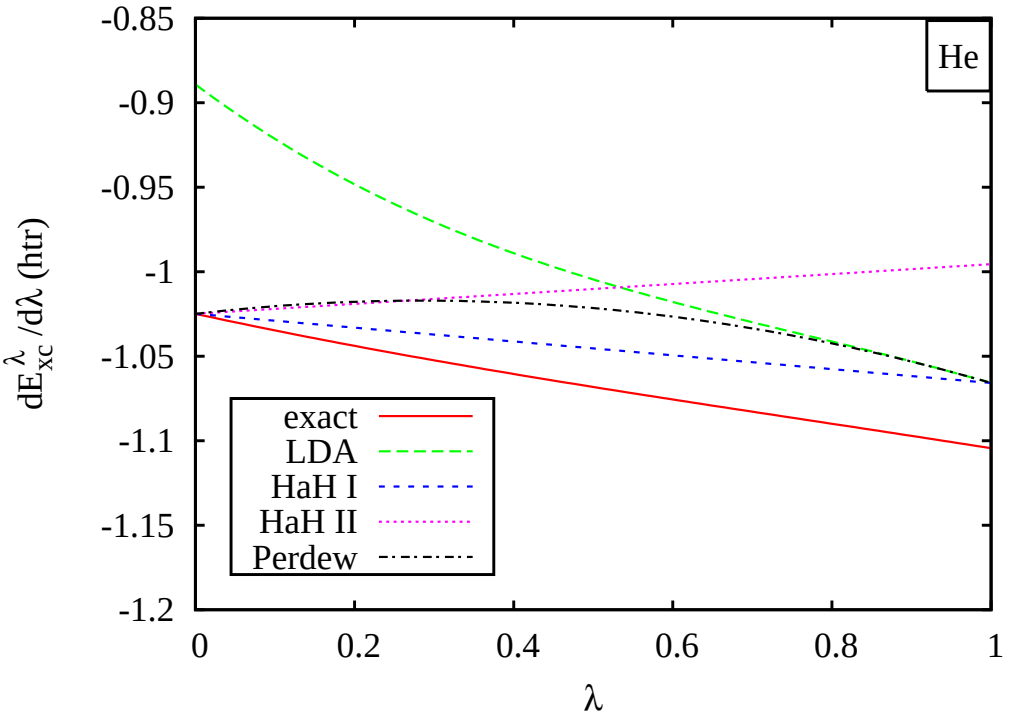

Figure 3.2.: The exact coupling-constant integrand $E_{\mathrm{xc}}^{\lambda}$ for the He atom is compared with the integrand in the LDA, the half-and-half hybrid according to Eq. (3.35) denoted by HaH-I, the half-and-half hybrid of Eq. (3.36) denoted by HaH-II, and finally with the hybrid proposed by Perdew *et al.* with $n = 4$ [Eq. (3.37)]. For all three hybrids $E_{\mathrm{xc}}^{\mathrm{DF}} = E_{\mathrm{xc}}^{\mathrm{LDA}}$ is used.

made in the HaH-II of replacing the integrand at $dE_{\mathrm{xc}}^{\lambda}/d\lambda\big|_{\lambda=1}$ by the full functional worsens the description of the integrand.

The hybrid functionals introduced so far are derived from theoretical considerations. Thus, they are often considered as *ab-initio* functionals. However, there exist a few hybrid functionals, whose parameters are fitted to experimental data sets. The most famous one is the B3LYP hybrid [61, 62], which has the generic form

$$E_{\mathrm{xc}} = E_{\mathrm{xc}}^{\mathrm{LDA}} + a_0(E_{\mathrm{x}} - E_{\mathrm{x}}^{\mathrm{LDA}}) + a_{\mathrm{x}}(E_{\mathrm{x}}^{\mathrm{B88}} - E_{\mathrm{x}}^{\mathrm{LDA}}) + a_{\mathrm{c}}(E_{\mathrm{c}}^{\mathrm{LYP}} - E_{\mathrm{c}}^{\mathrm{LDA}})\,. \tag{3.39}$$

The B stands for its inventor Becke, 3 denotes the three parameters a_0, a_{x}, and a_{c}, which are determined by a fit to 56 atomization energies, 42 ionization energies, 8 proton affinities and the 10 first-row total atomic energies of the molecules of the G1 database [63, 64], and LYP specifies the correlation functional of Lee, Yang, and Parr [55].

In conclusion, hybrid functionals interpolate the coupling constant integrand between its exact exchange limit for $\lambda = 0$ and the fully interacting limit $\lambda = 1$, where local or semi-local functionals are supposed to work well. For the hybrid functionals introduced so far correlation is treated on the level of LDA and GGA. Alternatively, one can search for orbital-dependent expressions for the correlation energy. Görling-Levy perturbation theory for example offers a systematic expansion of the xc energy functional in terms of orbital-dependent functionals and thus provides an orbital definition of correlation.

3.5. Görling-Levy perturbation theory

Görling-Levy perturbation theory [16] expresses the ground-state energy of the coupling-constant Hamiltonian H^λ [Eq. (3.1)] by a perturbation expansion in the scaling parameter λ of the electron-electron interaction around $\lambda = 0$. The coupling constant λ appears in the interaction term and in the external potential $V^\lambda(\mathbf{r})$, which keeps the density independent from λ. With the help of uniform coordinate scaling Görling and Levy have been able to specify the λ-dependent external potential $V^\lambda(\mathbf{r})$ in the coupling-constant integration Hamiltonian (3.1) and carry out the perturbation theory, which finally provides a systematic expansion of the xc energy functional in terms of KS wave functions and eigenvalues.

In section 3.3 all necessary equations are already developed in order to derive Görling-Levy perturbation theory. Combination of Eqs. (3.30) and (3.28) links the xc energy of the scaled system E_{xc}^λ with those at $\lambda = 1$

$$E_{\mathrm{xc}}^\lambda[n] = \lambda^2(E_{\mathrm{x}}[n_{1/\lambda}] + E_{\mathrm{c}}[n_{1/\lambda}]) = \lambda E_{\mathrm{x}}[n] + \lambda^2 E_{\mathrm{c}}[n_{1/\lambda}]\,, \tag{3.40}$$

where we split up the xc energy into exchange and correlation contributions. The effective potential V_{eff}^λ of the KS system, that corresponds to the scaled interacting system H^λ, is therefore given by

$$V_{\mathrm{eff}}^\lambda(\mathbf{r}) = V^\lambda(\mathbf{r}) + \lambda V_{\mathrm{H}}(\mathbf{r}) + \lambda V_{\mathrm{x}}(\mathbf{r}) + \lambda^2 \frac{\delta E_{\mathrm{c}}[n_{1/\lambda}]}{\delta n(\mathbf{r})}\,. \tag{3.41}$$

This effective potential V_{eff}^λ ensures that the ground-state density of the KS system is identical to the ground-state density of the interacting scaled system H^λ. Per construction of the adiabatic connection, however, the density of the latter is identical to the true ground-state density for $\lambda = 1$ and hence independent of λ. According to the Hohenberg and Kohn theorem V_{eff}^λ must, thus, be the same for each λ up to a constant. Consequently, the λ-dependent external potential can be written as

$$V^{\lambda}(\mathbf{r}) = V^{\lambda=0}(\mathbf{r}) - \lambda\left(V_{\mathrm{H}}(\mathbf{r}) + V_{\mathrm{x}}(\mathbf{r}) + \lambda\frac{\delta E_{\mathrm{c}}[n_{\frac{1}{\lambda}}]}{\delta n(\mathbf{r})}\right). \tag{3.42}$$

The potential $V^{\lambda=0}(\mathbf{r})$ is identical to the effective potential of the KS system, which mimics the fully interacting many-electron system. According to Eq. (2.27) it is partitioned into external, Hartree, and xc part

$$V^{\lambda=0}(\mathbf{r}) = V^{\lambda=1}(\mathbf{r}) + V_{\mathrm{H}}(\mathbf{r}) + \mathrm{V}_{\mathrm{xc}}(\mathbf{r}) = V(\mathbf{r}) + V_{\mathrm{H}}(\mathbf{r}) + \mathrm{V}_{\mathrm{xc}}(\mathbf{r}). \tag{3.43}$$

Thus, the coupling constant Hamiltonian H^{λ} can be written as

$$H^{\lambda} = H_0 - \lambda\sum_i\left(V_{\mathrm{H}}(\mathbf{r}_i) + V_{\mathrm{x}}(\mathbf{r}_i) + \lambda\frac{\delta E_{\mathrm{c}}[n_{\frac{1}{\lambda}}]}{\delta n(\mathbf{r}_i)}\right) + \lambda V_{ee}\,, \tag{3.44}$$

where H_0 is independent of λ

$$H_0 = \sum_i\left(-\frac{1}{2}\nabla^2 + V(\mathbf{r}_i) + V_{\mathrm{H}}(\mathbf{r}_i) + \mathrm{V}_{\mathrm{xc}}(\mathbf{r}_i)\right). \tag{3.45}$$

By means of standard perturbation theory the ground-state energy of H^{λ} can be expressed in terms of the scaling parameter λ of the electron-electron interaction. At full coupling strength ($\lambda = 1$) it finally becomes

$$E[n] \quad = \quad \sum_{i=0}^{\infty} E^i[n] = T_{\mathrm{s}}[n] + \int n(\mathbf{r})V(\mathbf{r})d^3r + U_{\mathrm{H}}[n] + E_{\mathrm{x}}[n] + E_{\mathrm{c}}[n]\,.$$

While the zero-order ($i = 0$) terms of the expansion are given by the kinetic energy $T_{\mathrm{s}}[n]$ and the energy contribution arising from the external potential $V(\mathbf{r})$, the first-order terms ($i = 1$) are the Hartree energy $U_{\mathrm{H}}[n]$ and the exact exchange energy

$$E_{\mathrm{x}}[n] = -\frac{1}{2}\sum_{i,j}^{\mathrm{occ.}}\iint\frac{\phi_i^*(\mathbf{r})\phi_j(\mathbf{r})\phi_j^*(\mathbf{r}')\phi_i(\mathbf{r}')}{|\mathbf{r}-\mathbf{r}'|}d^3r\,d^3r'\,. \tag{3.46}$$

All higher-order terms ($i = 2, \ldots, \infty$) define the correlation energy in terms of the KS wave functions and eigenvalues

$$E_{\mathrm{c}} = \sum_{j=2}^{\infty} E_{\mathrm{c}}^j[n]\,. \tag{3.47}$$

The leading term of the correlation energy E_{c}^2 is given by

$$E_c^2 = -\sum_{i=1}^{\infty} \frac{|\langle \Phi | V_{ee} - V_H - V_x | \Phi^i \rangle|^2}{E_{KS}^i - E_{KS}}, \tag{3.48}$$

where Φ is the ground-state KS single Slater determinant and Φ^i denotes the i-th excited KS Slater determinant. E_{KS} and E_{KS}^i are the corresponding total energies. The correlation energy E_c^2 is very similar to the energy expression of second-order MP perturbation theory. In fact, Eq. (3.48) can be decomposed into a contribution, which is formally identical to the energy in second-order MP perturbation theory, but evaluated with the KS orbitals and KS eigenvalues, and a second term, which arises from the difference between non-local and local treatment of exchange in MP perturbation theory and KS DFT, respectively [65]. In contrast to Eq. (3.46), E_c^2 and all higher-order correlation terms depend on the unoccupied states. The complexity of the mathematical expressions increases with the order of the expansion. However, the consideration of E_c^2 already enables a description of dispersion forces [17, 66]. Unfortunately, there is no guarantee that the higher-order terms are negligible. In fact, a partial re-summation of the perturbation series is required for a variationally stable functional [67].

Taking everything into consideration, Görling-Levy perturbation theory provides a systematic and exact expansion of the xc energy in terms of orbital-dependent functionals. One order after the other can be used to define xc functionals of increasing accuracy, in principle. The leading term in this expansion is the exact exchange energy. Furthermore, Görling-Levy perturbation theory can be combined with the idea of hybrid functionals, as the Görling-Levy expansion of the xc energy simultaneously defines a series for the coupling constant integrand

$$\frac{dE_{xc}^{\lambda}}{d\lambda} = E_x + 2E_c^2\lambda + O(\lambda^2). \tag{3.49}$$

While E_x is the exact value of the coupling constant integrand at $\lambda = 0$, the slope of the integrand at $\lambda = 0$ is given by twice the correlation energy E_c^2. In elaborate hybrid functionals [68] both informations, the exact value together with the exact slope at $\lambda = 0$, are incorporated.

3.6. Sham-Schlüter equation

An alternative approach for a systematic improvement of the xc potential of DFT is provided by the Sham-Schlüter equation [69, 70], which connects the xc potential of DFT with MBPT.

By construction of the KS system its ground-state density equals the true ground-state density of the many-electron system. The KS density as well as the density of the many-

electron system can be expressed by the respective Green function

$$0 = n(\mathbf{r}) - n_{\mathrm{KS}}(\mathbf{r}) = \frac{1}{\pi}\Im \int d\omega G(\mathbf{r},\mathbf{r},\omega) - \frac{1}{\pi}\Im \int d\omega G_{\mathrm{KS}}(\mathbf{r},\mathbf{r},\omega). \tag{3.50}$$

With the Dyson equation that connects many-electron and KS Green function

$$\begin{aligned} G(\mathbf{r},\mathbf{r}',\omega) &= G_{\mathrm{KS}}(\mathbf{r},\mathbf{r}',\omega) \\ &- \iint G_{\mathrm{KS}}(\mathbf{r},\mathbf{r}'',\omega)\left[\Sigma_{\mathrm{xc}}(\mathbf{r}'',\mathbf{r}''',\omega) - V_{\mathrm{xc}}(\mathbf{r}'')\delta(\mathbf{r}''-\mathbf{r}''')\right] G(\mathbf{r}''',\mathbf{r}',\omega) d^3r'' d^3r''' \end{aligned} \tag{3.51}$$

the density condition (3.50) becomes

$$\iiint G_{\mathrm{KS}}(\mathbf{r},\mathbf{r}',\omega)\left[\Sigma_{\mathrm{xc}}(\mathbf{r}',\mathbf{r}'',\omega) - V_{\mathrm{xc}}(\mathbf{r}')\delta(\mathbf{r}'-\mathbf{r}'')\right] G(\mathbf{r}'',\mathbf{r},\omega) d^3r'\, d^3r''\, d\omega = 0. \tag{3.52}$$

This is the so-called Sham-Schlüter equation. It establishes a direct link between the self-energy Σ_{xc} of MBPT and the xc potential of DFT. The xc potential corresponding to a given self-energy Σ_{xc} can be understood as the best local approximation to the non-local dynamic self-energy. As the self-energy can be improved diagrammatically, Eq. (3.52) offers a way for a systematic improvement of the xc potential. However, the solution of Eq. (3.52) is by far not trivial. The linear-response Sham-Schlüter equation, which is obtained by combining Eqs. (3.51) and (3.52) and neglecting all non-linear terms in $\left[\Sigma_{\mathrm{xc}}(\mathbf{r},\mathbf{r}',\omega) - V_{\mathrm{xc}}(\mathbf{r})\delta(\mathbf{r}-\mathbf{r}')\right]$, has been solved to our knowledge so far only for bulk silicon [11, 71] and for a jellium surface [72].

3.7. Summary

Orbital-dependent xc functionals of DFT have been introduced and motivated in this chapter. It has been shown that the orbital-dependent exact exchange energy E_{x}, which is formally identical to the HF exchange energy, but evaluated with the KS orbitals, improves the description of the coupling-constant integrand in the $\lambda \to 0$ limit. So, it is reasonable to combine E_{x} with pure density functionals like LDA or GGA, which usually perform well in the opposite limit $\lambda \to 1$, into one functional, a hybrid functional. We have demonstrated that E_{x} is, furthermore, the leading term in a systematic expansion of the xc functional in powers of the electron-electron interaction. The higher order terms in this expansion define an orbital and eigenvalue dependent correlation functional.

The introduction of orbital dependent xc functionals is conceptionally comparable with the transition from the Thomas-Fermi method to the KS approach, where the density functional for the kinetic energy has been replaced by the orbital dependent kinetic energy of

non-interacting electrons. Any orbital dependent xc functional in analogy to the KS kinetic energy is still an implicit functional of the density, because the KS orbitals are functionals of the effective potential through the KS single-particle Schrödinger equation and the effective potential is a functional of the density through the Hohenberg and Kohn theorem. The same argumentation holds for functionals, which are additionally eigenvalue-dependent.

The construction of the xc potential from an orbital-dependent functional has not been discussed so far. Two substantially different approaches are available: on the one hand, a strict treatment of orbital-dependent functionals within the KS framework, which requires a local multiplicative xc potential, per definition, for the KS system as a non-interacting electron system. However, a straight-forward analytical functional derivative of the xc energy with respect to the density is not feasible in contrast to LDA and GGA. This problem is resolved in the optimized effective potential (OEP) method, which yields the local xc potential as the solution of an integral equation. The OEP approach as well as its numerical implementation within the full-potential linearized augmented-plane-wave (FLAPW) method is discussed in detail in chapter 6.

On the other hand, instead of constructing a local xc potential in agreement with the KS formalism one can define a different reference system, the so-called generalized Kohn-Sham (gKS) system. Hybrid functionals are typically treated within the latter. The orbital-dependent exchange energy, which is characteristic for hybrid functionals, leads to a non-local HF like exchange term in the one-particle equations of the gKS system. The gKS scheme, its implementation as well as its application are discussed in chapter 5. Before, we will introduce the FLAPW method in the next chapter.

4. Electronic structure methods: the FLAPW approach

A wide spectrum of electronic structure methods exists for the numerical solution of the Kohn-Sham (KS) equation. These methods can be divided into all-electron and pseudopotential approaches. In the latter only the valence electrons are described explicitly, while the core electrons are frozen in their atomic configuration, and the Coulomb potential of the nuclei is replaced by a smooth effective one, the pseudopotential. The smoothness of the potential, which in turn leads to smooth pseudo wave functions, enables to use plane waves for the representation of the wave functions. Plane waves have several advantages: each power of the momentum operator is diagonal, in particular the kinetic energy, the charge density can be calculated efficiently via a fast Fourier transform (FFT), and the Hartree potential can be obtained by a simple algebraic expression in reciprocal space. The plane-wave pseudopotential approach, however, faces its limits in the precise treatment of localized electron-states, e.g. $3d$ or $4f$ electron-states.

The all-electron approaches, on the contrary, treat core and valence electrons on an equal footing without any pseudization of the potential. The presence of the $1/r$-like behavior of the true potential in the vicinity of the atomic nuclei leads to rapidly varying wave functions there. Thus, an enormous number of plane waves would be required for the accurate description of the all-electron wave function. This shows that plane waves do not constitute the optimal basis set in an all-electron method. Typically, in all-electron methods space is partitioned into atom-centered spheres, the so-called muffin-tin (MT) spheres, and the remaining interstitial region (IR). In order to cope with the $1/r$-like potential in the MT spheres, one usually uses numerical functions, which explicitly incorporate the rapid oscillations caused by the $1/r$ singularity of the potential. These numerical functions are then matched to an envelope function in the IR. The muffin-tin orbital (MTO) and augmented plane-wave (APW) method and its linearized variants LMTO and LAPW belong to this kind of approach.

In the following, we will introduce the LAPW method step by step. We will begin with the APW approach, the precursor of the LAPW method. Then, we discuss the LAPW method, where we concentrate in particular on the formulation for bulk solids, and its local-orbital

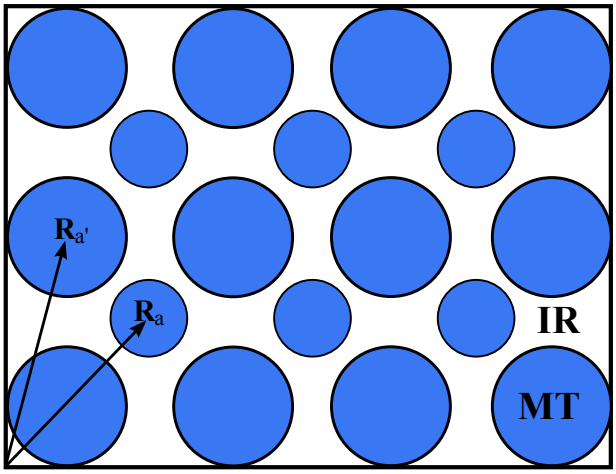

Figure 4.1.: Division of space into muffin-tin (MT) spheres and the interstitial region (IR). Each atomic nucleus lies in a center $\mathbf{R}_a$ of a MT sphere of radius S_a. The radii of the spheres are chosen such that the spheres do not overlap.

extension. Finally, we introduce the mixed product basis (MPB), which is an auxiliary basis for the representation of LAPW wave-function products. The MPB fully preserves the all-electron character of the product and can be converged in a systematic manner.

4.1. APW method

As already pointed out in the introduction of the chapter, the APW approach [73] partitions space into atom-centered MT spheres and the IR (s. Fig. 4.1). The potential in the IR is relatively smooth, which allows to use plane waves as basis functions there. In the MT spheres, solutions of the scalar-relativistic, spin-dependent, spherical Schrödinger equation are employed and matched to the interstitial plane wave. Thus, for a given unit cell the APW basis function of Bloch vector $\mathbf{k}$, reciprocal lattice vector $\mathbf{G}$ and spin index σ is given by

$$\varphi^{\sigma}_{\mathbf{kG}}(\mathbf{r},E) = \begin{cases} \frac{1}{\sqrt{\Omega}} \exp\left[i\left(\mathbf{k}+\mathbf{G}\right)\cdot\mathbf{r}\right] & \mathbf{r}\in \mathrm{IR} \\ \sum_{lm} \alpha^{a\sigma}_{lm}(\mathbf{k},\mathbf{G},E) u^{a\sigma}_{l}(|\mathbf{r}_a|,E) Y_{lm}(\widehat{\mathbf{r}_a}) & \mathbf{r}\in \mathrm{MT}(a) \end{cases}, \tag{4.1}$$

where the vector $\mathbf{r}_a$ has its origin at the center of the sphere $\mathbf{R}_a$, Ω is the unit-cell volume, and $u^{a\sigma}_l(r,E)$ is the radial solution of the Schrödinger equation

$$\left[-\frac{1}{2}\frac{\partial^2}{\partial r^2} + \frac{l(l+1)}{2r^2} + V^{a\sigma}_{\mathrm{eff},0}(r) - E\right] r u^{a\sigma}_l(r,E) = 0 \tag{4.2}$$

with the spin-dependent, spherical effective potential $V^{a\sigma}_{\text{eff},0}(r)$ at atom a and the energy parameter E.[1] The coefficient $\alpha^{a\sigma}_{lm}(\mathbf{k},\mathbf{G},E)$ is solely determined from the requirement of continuity at the sphere boundary

$$\alpha^{a\sigma}_{lm}(\mathbf{k},\mathbf{G},E) = \frac{4\pi}{\sqrt{\Omega}} \exp\left[i(\mathbf{k}+\mathbf{G})\cdot\mathbf{R}_a\right] i^l Y^*_{lm}(\widehat{\mathbf{k}+\mathbf{G}}) \frac{j_l(|\mathbf{k}+\mathbf{G}|S_a)}{u^{a\sigma}_l(S_a,E)}\,, \tag{4.3}$$

where S_a denotes the radius of the MT sphere of atom a and $j_l(r)$ are the spherical Bessel functions. The latter arise from the Rayleigh expansion of the plane wave $\exp\left[i\,(\mathbf{k}+\mathbf{G})\cdot\mathbf{r}\right]$. The KS wave function of Bloch vector $\mathbf{k}$ and band index n is then expressed in the APW basis

$$\phi^\sigma_{n\mathbf{k}}(\mathbf{r}) = \sum_{\mathbf{G}} z^\sigma_{\mathbf{G}}(n,\mathbf{k})\varphi^\sigma_{\mathbf{kG}}(\mathbf{r},E)\,. \tag{4.4}$$

In this way, the differential KS equation [Eq. (2.22)] is cast into an algebraic form

$$\sum_{\mathbf{G}'}\left[H^\sigma_{\mathbf{GG}'}(\mathbf{k},E) - \epsilon^\sigma_{n\mathbf{k}} S^\sigma_{\mathbf{GG}'}(\mathbf{k},E)\right] z^\sigma_{\mathbf{G}'}(n,\mathbf{k}) = 0 \tag{4.5}$$

with the Hamiltonian

$$H^\sigma_{\mathbf{GG}'}(\mathbf{k},E) = \int \varphi^{\sigma*}_{\mathbf{kG}}(\mathbf{r},E)\left[-\frac{1}{2}\nabla^2 + V^\sigma_{\text{eff}}(\mathbf{r})\right]\varphi^\sigma_{\mathbf{kG}'}(\mathbf{r},E)\,d^3r \tag{4.6}$$

and the overlap matrix

$$S^\sigma_{\mathbf{GG}'}(\mathbf{k},E) = \int \varphi^{\sigma*}_{\mathbf{kG}}(\mathbf{r},E)\varphi^\sigma_{\mathbf{kG}'}(\mathbf{r},E)\,d^3r\,, \tag{4.7}$$

respectively. It turns out, that the APW basis only leads to an accurate description of the wave function $\phi^\sigma_{n\mathbf{k}}$ if the energy parameter E is set to the eigenvalue $\epsilon^\sigma_{n\mathbf{k}}$. As the eigenvalue is not known a priori, Eq. (4.5) constitutes a non-linear problem. Starting with a initial guess for the eigenvalue $\epsilon^\sigma_{n\mathbf{k}}$ the APW basis (4.1), the Hamiltonian (4.6), and the overlap matrix (4.7) are constructed with $E = \epsilon^\sigma_{n\mathbf{k}}$. The root of the determinant

$$\det\left|H^\sigma_{\mathbf{GG}'}(\mathbf{k},E) - \epsilon^\sigma_{n\mathbf{k}} S^\sigma_{\mathbf{GG}'}(\mathbf{k},E)\right| = 0 \tag{4.8}$$

then yields a refined guess for the eigenvalue $\epsilon^\sigma_{n\mathbf{k}}$. This scheme is iterated until input and output guess coincide. In this way, the true eigenvalue $\epsilon^\sigma_{n\mathbf{k}}$ is found. Afterwards the eigenvector $z^\sigma_{\mathbf{G}}(n,\mathbf{k})$ can be calculated by solving Eq. (4.5). This procedure must be repeated for

[1] For simplicity, we give the non-relativistic equations here. A discussion of the scalar-relativistic equations is deferred to Appendix B.

each band n, Bloch vector $\mathbf{k}$, and spin σ, which makes the APW method computationally demanding.

Additionally, the APW approach suffers from the so-called asymptote problem, i.e., the decoupling of the radial function and the plane wave at the MT sphere boundary, if $u_l^{a\sigma}(r, E)$ vanishes for $r = S_a$. A more detailed discussion of the APW method can be found in Ref. 74.

The non-linearity and the asymptote problem of the APW approach are overcome in the LAPW method by using an additional radial function in the MT spheres as described in the next section.

4.2. LAPW method

The LAPW method [24–27] is the linearized version of the APW approach. It uses, similar to the APW method, piecewise defined functions to deal simultaneously with the atomic-like potential close to the nuclei and the smooth potential in the IR. However, the flexibility in the MT spheres in contrast to the APW basis is enhanced by adding for each angular momentum l and each MT sphere a second radial function $\dot{u}_l^{a\sigma}(r)$, which is the energy derivative of $u_l^{a\sigma}(r)$. Additionally, a separate energy parameter $E_l^{a\sigma}$ is introduced for each atom a, angular momentum l, and spin σ. In this way, for a given unit cell the LAPW basis function of Bloch vector $\mathbf{k}$ and reciprocal lattice vector $\mathbf{G}$ is given by

$$\varphi_{\mathbf{kG}}^{\sigma}(\mathbf{r}) = \begin{cases} \frac{1}{\sqrt{\Omega}} \exp\left[i\left(\mathbf{k}+\mathbf{G}\right)\cdot\mathbf{r}\right] & \mathbf{r} \in \mathrm{IR} \\ \sum_{lm}\left[\alpha_{lm}^{a\sigma}(\mathbf{k},\mathbf{G})u_l^{a\sigma}(|\mathbf{r}_a|) + \beta_{lm}^{a\sigma}(\mathbf{k},\mathbf{G})\dot{u}_l^{a\sigma}(|\mathbf{r}_a|)\right] Y_{lm}(\widehat{\mathbf{r}_a}) & \mathbf{r} \in \mathrm{MT}(a) \end{cases} . \quad (4.9)$$

For the sake of clarity, we suppressed the dependence of the radial functions $u_l^{a\sigma}(r)$, $\dot{u}_l^{a\sigma}(r)$ as well as of the coefficients $\alpha_{lm}^{a\sigma}(\mathbf{k},\mathbf{G})$, $\beta_{lm}^{a\sigma}(\mathbf{k},\mathbf{G})$ on the energy parameter $E_l^{a\sigma}$.

While the radial function $u_l^{a\sigma}(r)$ is the solution of Eq. (4.2) for $E = E_l^{a\sigma}$, the energy derivative $\dot{u}_l^{a\sigma}(r)$ obeys the inhomogeneous Schrödinger equation

$$\left[-\frac{1}{2}\frac{\partial^2}{\partial r^2} + \frac{l(l+1)}{2r^2} + V_{\mathrm{eff},0}^{a\sigma}(r) - E_l^{a\sigma}\right] r\dot{u}_l^{a\sigma}(r) = r u_l^{a\sigma}(r) . \quad (4.10)$$

Its solution becomes unique by the additional requirement that $\dot{u}_l^{a\sigma}(r)$ is orthogonal to $u_l^{a\sigma}(r)$. The coefficients $\alpha_{lm}^{a\sigma}(\mathbf{k},\mathbf{G})$ and $\beta_{lm}^{a\sigma}(\mathbf{k},\mathbf{G})$ ensure continuity in value and first radial

derivative at the MT sphere boundary

$$\alpha_{lm}^{a\sigma}(\mathbf{k},\mathbf{G}) \tag{4.11}$$
$$= \frac{4\pi}{\sqrt{\Omega}} \exp\left[i\left(\mathbf{k}+\mathbf{G}\right)\cdot\mathbf{R}_a\right] i^l Y_{lm}^*(\widehat{\mathbf{k}+\mathbf{G}}) \frac{1}{\left[\dot{u}_l^{a\sigma}(S_a), u_l^{a\sigma}(S_a)\right]} \left[\dot{u}_l^{a\sigma}(S_a), j_l(|\mathbf{k}+\mathbf{G}|S_a)\right]$$
$$\beta_{lm}^{a\sigma}(\mathbf{k},\mathbf{G}) \tag{4.12}$$
$$= \frac{4\pi}{\sqrt{\Omega}} \exp\left[i\left(\mathbf{k}+\mathbf{G}\right)\cdot\mathbf{R}_a\right] i^l Y_{lm}^*(\widehat{\mathbf{k}+\mathbf{G}}) \frac{-1}{\left[\dot{u}_l^{a\sigma}(S_a), u_l^{a\sigma}(S_a)\right]} \left[u_l^{a\sigma}(S_a), j_l(|\mathbf{k}+\mathbf{G}|S_a)\right].$$

The square brackets denote the Wronskian

$$\left[f(r), g(r)\right] = f(r)\frac{dg(r)}{dr} - \frac{df(r)}{dr}g(r). \tag{4.13}$$

The addition of the energy derivative in the MT spheres enables to represent a solution $u_l^{a\sigma}(r,E)$ of the radial Schrödinger equation (4.2) of energy E by the radial functions $u_l^{a\sigma}(r)$ and $\dot{u}_l^{a\sigma}(r)$

$$u_l^{a\sigma}(r,E) = u_l^{a\sigma}(r,E_l^{a\sigma}) + \dot{u}_l^{a\sigma}(r,E_l^{a\sigma})\left(E-E_l^{a\sigma}\right) + \mathcal{O}\left((E-E_l^{a\sigma})^2\right) \tag{4.14}$$

up to an error which is quadratic in the energy difference $E - E_l^{a\sigma}$. With this increased flexibility the energy parameters $E_l^{a\sigma}$ need not equal the band energies as in the APW method, so that the algebraic equation (4.5) becomes linear in the LAPW basis. All eigenvalues and eigenvectors for a given Bloch vector and spin are then obtained by a single diagonalization.

Furthermore, there is no asymptote problem in the LAPW approach. By using Eqs. (4.2) and (4.10) it can be shown that the denominator in Eqs. (4.11) and (4.12) does not vanish. Instead it fulfills the relation

$$\left[\dot{u}_l^{a\sigma}(S_a), u_l^{a\sigma}(S_a)\right] = \frac{2}{S_a^2}. \tag{4.15}$$

The LAPW basis functions $\varphi_{\mathbf{kG}}^{\sigma}(\mathbf{r})$ are usually employed to represent the valence-electron states accurately. Therefore, the energy parameters $E_l^{a\sigma}$ are placed in the valence band region. One possible choice is to set $E_l^{a\sigma}$ in the center of gravity of the l-like band.

However, the LAPW method is an all-electron approach comprising valence and core states. The orthogonality of the tightly bound core states with respect to the LAPW basis [27, 75] allows to separate the core from the valence states. Due to the spatial confinement of the core electrons it is an excellent approximation to describe them as atomic states by solving a fully relativistic Dirac equation with the spherically symmetric part of the effective potential.

Although the LAPW basis functions are constructed with respect to the spherical average of the effective potential, the full potential enters in Eq. (4.6) without shape approximations. It is commonly accepted that the LAPW basis possesses sufficient flexibility to represent the full-potential KS wave function within the MT spheres. A comparison between the full-potential LAPW (FLAPW) method and the full-potential Korringa-Kohn-Rostocker (KKR) method, where the basis functions are constructed with respect to the full non-spherical potential, yields a perfect agreement [76] and is thus a practical justification of this procedure.

For the representation of the all-electron potential and density, similar to the LAPW basis, a dual representation is employed, i.e., plane waves in the IR and radial functions times spherical harmonics in the MT spheres. Density and potential are invariant under symmetry operations of the system, which enables to decrease the basis set size considerably. This is achieved by constructing symmetry-adapted linear combinations of plane waves, so-called stars, in the IR and symmetry-adapted spherical harmonics, so-called lattice harmonics, in the MT spheres for the representation of the density and potential [27]. The number of stars and lattice harmonics is usually much smaller than the number of plane waves and spherical harmonics, respectively.

Furthermore, for a practical calculation cutoff values for the reciprocal lattice vectors $|\mathbf{k} + \mathbf{G}| \leq G_{\max}$ and the angular momentum $l \leq l_{\max}$ are introduced.

4.2.1. Local-orbital extension

States that lie in the vicinity of the energy parameters $E_l^{a\sigma}$ are accurately described by the LAPW basis. However, the basis becomes less adequate for states that are energetically far away from $E_l^{a\sigma}$. These are for example semi-core states, i.e., high-lying core states, whose wave functions extend considerably over the MT sphere. Due to their spatial extent a treatment as core states is not justified. Nevertheless, the linearization error of the standard LAPW basis prohibits an accurate description of such states, as well. High-lying unoccupied states are another example, where the linearization error matters.

In order to improve the representation of such states, the basis may be extended with local orbitals (LOs) [77–79]. Let us assume that we want to improve the LAPW basis for states with an angular momentum l in the MT sphere of atom a around an energy $E_{\mathrm{LO}}^{a\sigma}$. Then, an additional radial function $u_l^{a\sigma}(r, E_{\mathrm{LO}}^{a\sigma})$ is constructed from Eq. (4.2) for the energy parameter $E_{\mathrm{LO}}^{a\sigma}$. This radial function is combined with $u_l^{a\sigma}(r)$ and $\dot{u}_l^{a\sigma}(r)$ to

$$u_{l,\mathrm{LO}}^{a\sigma}(r) = \alpha_{l,\mathrm{LO}}^{a\sigma} u_l^{a\sigma}(r) + \beta_{l,\mathrm{LO}}^{a\sigma} \dot{u}_l^{a\sigma}(r) + \gamma_{l,\mathrm{LO}}^{a\sigma} u_l^{a\sigma}(r, E_{\mathrm{LO}}^{a\sigma}), \tag{4.16}$$

such that $u_{l,\mathrm{LO}}^{a\sigma}(r)$ is normalized and its value and radial derivative vanish at the MT sphere

boundary. In this way, the local orbital is completely confined to the MT sphere and does not need to be matched to a plane wave. Multiplication of the radial function $u^{a\sigma}_{l,\mathrm{LO}}(r)$ with the spherical harmonic $Y_{lm}(\hat{\mathbf{r}})$ then leads to $(2l+1)$ additional LAPW basis functions in the unit cell

$$\varphi^{a\sigma,\mathrm{LO}}_{\mathbf{k},lm}(\mathbf{r}, E^{a\sigma}_{\mathrm{LO}}) = \begin{cases} 0 & \mathbf{r} \in \mathrm{IR} \\ u^{a\sigma}_{l,\mathrm{LO}}(|\mathbf{r}_a|) Y_{lm}(\widehat{\mathbf{r}_a}) & \mathbf{r} \in \mathrm{MT}(a) \end{cases} . \tag{4.17}$$

For the improved description of a semi-core state of atom a, which is nearly dispersion-less, the energy parameter $E^{a\sigma}_{\mathrm{LO}}$ is fixed at the semi-core energy level.

In order to improve the linearization error for the unoccupied states, two different schemes are possible. On the one hand, local orbitals can be added, where $u^{a\sigma}_l(r, E^{a\sigma}_{\mathrm{LO}})$ is replaced by a higher energy derivative evaluated at $E^{a\sigma}_{\mathrm{LO}} = E^{a\sigma}_l$ [75]. Therewith the order of the Taylor series expansion (4.14) is increased and the LAPW basis becomes more and more flexible in a window around $E^{a\sigma}_l$. This ansatz does not require the choice of an additional energy parameter, but it has the disadvantage that due to the improved variational freedom around $E^{a\sigma}_l$ with respect to higher as well as lower energies, core states can appear in the valence energy window. Alternatively, the LAPW basis can be extended by local orbitals, where the energy parameter $E^{a\sigma}_{\mathrm{LO}}$ is determined such that the logarithmic derivative of the solution $u^{a\sigma}_l(r, E^{a\sigma}_{\mathrm{LO}})$ of Eq. (4.2) fulfills

$$\frac{d}{dr}\left[\ln\left(u^{a\sigma}_l(r, E^{a\sigma}_{\mathrm{LO}})\right)\right]\Big|_{r=S_a} = -(l+1) \tag{4.18}$$

at the MT sphere boundary $r = S_a$ [80]. This condition yields for each l quantum number [cf. Fig. 4.2] a series of orthogonal solutions of increasing energies and number of nodes. Consecutively, local orbitals constructed from these series of radial functions can be added for a systematic convergence of the LAPW basis with respect to the unoccupied states. The advantage of the latter approach is that the LAPW basis is only improved for the unoccupied states. Core states do not occur in the valence window.

In order to demonstrate that the addition of local orbitals to the LAPW basis makes the MT LAPW basis more and more complete, we calculate the radial function $u^{a\sigma}_l(r, E)$ that solves Eq. (4.2) at energy mesh points E over an energy range from −2 to 40 htr. At each energy the exact solution $u^{a\sigma}_l(r, E)$ is represented by the radial MT functions of the LAPW basis set. We define the error Δ_l in the representation of the exact radial function $u^{a\sigma}_l(r, E)$ at the energy E by the integral

$$\Delta_l(E) = \int_0^{S_a} |u^{a\sigma}_l(r, E) - \sum_p c_p u^{a\sigma}_{lp}(r)|^2 r^2 \, dr \,, \tag{4.19}$$

where c_p are the expansion coefficients of the exact solution $u^{a\sigma}_l(r, E)$ in the radial LAPW functions $u^{a\sigma}_{lp}(r)$. For a unified notation, we have subsumed the different radial functions

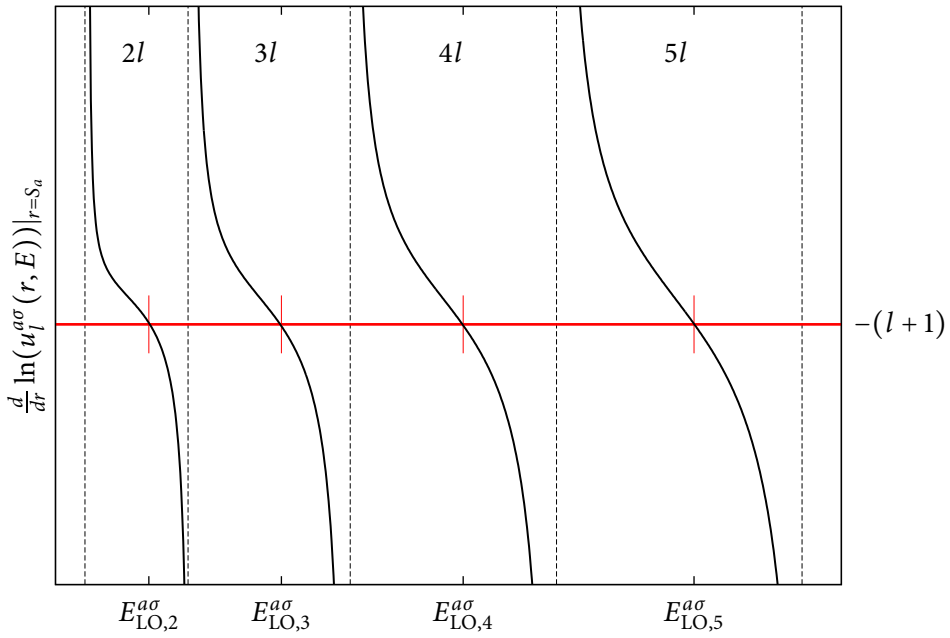

Figure 4.2.: Logarithmic derivative of the radial function $u_l^{a\sigma}(r)$ as a function of the energy parameter E at the MT sphere boundary S_a. The logarithmic derivative splits up into branches, in which the radial functions $u_l^{a\sigma}(r)$ have a constant number of nodes for $r < S_a$. A branch of type nl has $n - (l+1)$ nodes. The intersection points of the red line, which corresponds to $-(l+1)$, with the curve representing the logarithmic derivative define a series of energies, which are used to converge the LAPW basis with respect to the unoccupied states.

into the composite index p

$$u_{lp}^{a\sigma}(r) = \begin{cases} u_l^{a\sigma}(r) & p = 1 \\ \dot{u}_l^{a\sigma}(r) & p = 2 \\ u_l^{a\sigma}(r, E_{\mathrm{LO}}^{a\sigma}) & p \geq 3\,. \end{cases} \tag{4.20}$$

Figure 4.3 shows the representation error $\Delta_l(E)$ for the case of diamond for different LAPW basis-set configurations. As an example, we have chosen the angular momentum $l = 0$. A similar behavior is observed for the higher angular momenta, as well. The red curve corresponds to the conventional LAPW basis without any local orbitals. For the green, blue, and magenta curves one, two, and three local orbitals have been added according to the prescription (4.18), respectively. The energy parameters of the conventional LAPW basis and local orbitals correspond to the spikes in the curves. The conventional LAPW basis set provides an accurate description around the energy parameter of the conventional radial LAPW functions ($E_{l=0}^{a\sigma} = -0.23\,\mathrm{htr}$). However, with increasing energy the representation error increases and approaches 1 at about 10 htr, which means that the radial functions $u_{lp}^{a\sigma}(r)$ ($p = 1, 2$) are (nearly) orthogonal to the exact solution $u_l(r, E)$. By adding one local orbital (green curve) the representation error can be reduced to 1‰ in an energy range of about 10 htr. Yet, above an energy of 20 htr the exact radial function cannot be represented. The addition of more and more local orbitals reduces the linearization error $\Delta_l(E)$ over an increasing energy range. Three local orbitals are necessary to restrict the error $\Delta_l(E)$ below 5‰ over an energy range of 40 htr. In conclusion, Fig. 4.3 demonstrates that the LAPW basis becomes more and more complete over a wide energy range by adding local orbitals constructed according to Eq. (4.18).

4.2.2. Mixed product basis

The mixed product basis (MPB) is specifically designed for the representation of products of LAPW wave functions. Such products naturally occur in orbital-dependent functionals. The MPB retains the all-electron description of the product and can be converged in a systematic manner. We will describe the construction of the MPB in the following.

In order to accurately describe the products of two LAPW wave functions in the MT spheres the MPB must be capable of describing the products

$$u_{lp}^{a\sigma}(r) Y_{lm}^*(\mathbf{r}) u_{l'p'}^{a\sigma}(r) Y_{l'm'}(\mathbf{r}) = u_{lp}^{a\sigma}(r) u_{l'p'}^{a\sigma}(r) \sum_{\substack{L \in \{|l-l'|,\ldots,l+l'\} \\ M=-L,\ldots,L}} G_{LM,l'm',lm} Y_{LM}(\mathbf{r})\,, \tag{4.21}$$

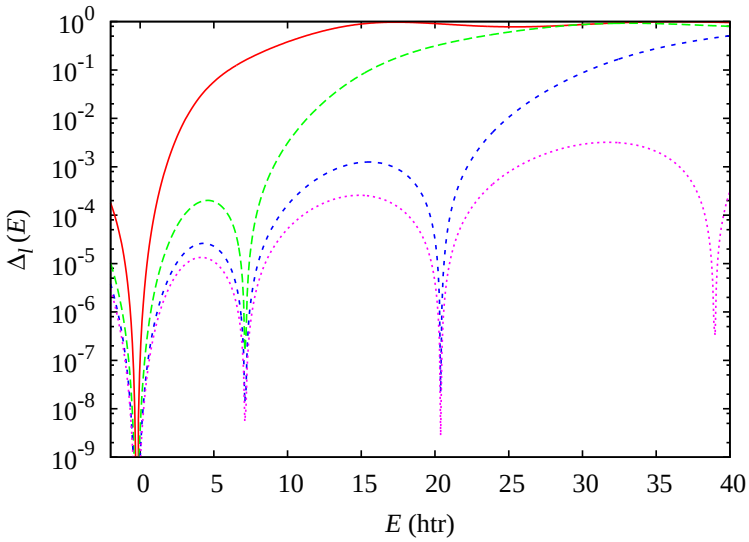

Figure 4.3.: Representation error $\Delta_l(E)$ for the case of diamond and for $l = 0$ as a function of the energy and the number of local orbitals added to the LAPW basis set. The red curve corresponds to an LAPW basis without any local orbitals, whereas for the green, blue, and magenta curves we consecutively add one local orbital more with energy parameters according to Eq. (4.18).

where we exploit the addition theorem of spherical harmonics and $G_{LM,l'm',lm}$ are the Gaunt coefficients

$$G_{LM,l'm',lm} = \int Y^*_{LM}(\hat{\mathbf{r}})\, Y_{l'm'}(\hat{\mathbf{r}})\, Y^*_{lm}(\hat{\mathbf{r}})\, d\Omega\,. \tag{4.22}$$

For a given angular momentum L we define the set of radial functions by

$$U^{a\sigma}_{LP}(r) = u^{a\sigma}_{lp}(r) u^{a\sigma}_{l'p'}(r)\,, \tag{4.23}$$

where P counts all combination of p, p', l, and l' that contribute to L. This set of radial functions exhibits usually a high degree of linear dependence. In order to remove the linear dependence, we diagonalize the overlap matrix

$$O^{a\sigma\sigma'}_{L,PP'} = \int U^{a\sigma}_{LP}(r) U^{a\sigma'}_{LP'}(r)\, r^2\, dr \tag{4.24}$$

for each a and L, and retain only those eigenfunctions whose eigenvalues exceed a given threshold value (typically 0.0001). Thus, the (nearly) linearly dependent combinations are removed and a smaller, but still flexible basis is obtained. In the case of spin-polarized calculations the resulting radial functions become spin-independent as products of spin-up and

spin-down radial functions enter in the overlap matrix. Additionally, we add a constant function to the optimized set of spherical radial product functions. From the resulting radial MT functions $M^a_{LP}(r)$ we then construct Bloch functions

$$M^a_{\mathbf{k},LMP}(\mathbf{r}) = \frac{1}{\sqrt{N}} \sum_{\mathbf{T}} M^a_{LP}(|\mathbf{r} - \mathbf{R}_a - \mathbf{T}|)\, Y_{LM}(\widehat{\mathbf{r} - \mathbf{R}_a - \mathbf{T}}) \exp\left[i\mathbf{k}(\mathbf{T} + \mathbf{R}_a)\right] , \tag{4.25}$$

where the sum runs over the lattice vectors $\mathbf{T}$ and N denotes the number of unit cells. In the IR, the product of two LAPW wave functions gives rise to products of interstitial plane waves (IPWs), which yield another IPW. Therefore, the MPB in the IR consists of IPWs

$$M_{\mathbf{k},\mathbf{G}}(\mathbf{r}) = \frac{1}{\sqrt{N\Omega}} \exp\left[i\,(\mathbf{k} + \mathbf{G})\,\mathbf{r}\right] \Theta(\mathbf{r}) \tag{4.26}$$

with the step function

$$\Theta(\mathbf{r}) = \begin{cases} 1 & \mathbf{r} \in \text{IR} \\ 0 & \mathbf{r} \in \text{MT} \end{cases} . \tag{4.27}$$

From here we can proceed in two ways: we can either combine the MT and IR functions to a full MPB, that consists of two spatially separate basis sets, which are not matched at the MT sphere boundary, or we can alternatively construct continuous functions with a continuous radial derivative over all space.

The former concept is used for the implementation of hybrid functionals (cf. Chap. 5), where the MPB is employed to represent products of wave functions. The partition of the MPB in MT and IR functions, which are either zero in the IR or in the MT spheres, enables to accelerate the most time consuming part of a hybrid functional calculation, the computation of the non-local exchange potential (s. Sec. 5.2.1). On the contrary, in the optimized effective potential (OEP) approach (cf. Chap. 6), a continuous MPB is essential in order to avoid discontinuities in the resulting local potential. Therefore, we form linear combinations of the MT functions and IPWs that are continuous in value and first radial derivative at the MT sphere boundary. We can use the same construction as for the LAPW basis, i.e., two radial functions per lm channel are used to augment the IPWs in the MT spheres. As there are usually far more than two radial functions per lm channel in the MPB, local orbitals are constructed from the remaining MT functions. A more general approach, which allows to elegantly incorporate further constraints, is deferred to Appendix A.

In both cases, the final MPB functions are not orthogonal and hence give rise to a non-diagonal overlap matrix

$$O_{IJ}(\mathbf{k}) = \int M^*_{\mathbf{k},I}(\mathbf{r}) M_{\mathbf{k},J}(\mathbf{r})\, d^3r\,, \tag{4.28}$$

where I and J are used to index the MPB functions. Due to the non-orthogonality the completeness relation of the MPB, which is only valid in the subspace spanned by the MPB, becomes

$$1 = \sum_{I,J} |M_{\mathbf{k},I}\rangle O^{-1}_{IJ}(\mathbf{k}) \langle M_{\mathbf{k},J}| \,. \tag{4.29}$$

With the definition of the biorthogonal set

$$\tilde{M}_{\mathbf{k},I}(\mathbf{r}) = \sum_{J} O^{-1}_{JI}(\mathbf{k}) M_{\mathbf{k},J}(\mathbf{r}) \,, \tag{4.30}$$

the completeness relation can be written in a more compact form

$$1 = \sum_{J} |\tilde{M}_{\mathbf{k},J}\rangle \langle M_{\mathbf{k},J}| = \sum_{J} |M_{\mathbf{k},J}\rangle \langle \tilde{M}_{\mathbf{k},J}| \,. \tag{4.31}$$

Biorthogonal and normal MPB are pairwise orthogonal

$$\langle M_{\mathbf{k},I} | \tilde{M}_{\mathbf{k},J}\rangle = \delta_{IJ} \,. \tag{4.32}$$

In chapter 5 and 6, the MPB with its completeness relation (4.31) is employed to implement hybrid functionals as well as the OEP method in the FLAPW method.

5. Hybrid functionals within the generalized Kohn-Sham scheme

In chapter 3, we already introduced the hybrid functionals, which approximate the coupling-constant integrand by combining exact exchange with (semi-)local approximations for the exchange-correlation (xc) functional of density-functional theory (DFT). Typically, hybrid functionals are treated within the generalized Kohn-Sham (gKS) system instead of the Kohn-Sham (KS) system. While the latter requires a local, multiplicative potential by construction (cf. Chap. 2), the gKS system allows a non-local Hartree-Fock(HF)-like exchange potential to be used in the one-particle Schrödinger equations. After a short introduction to the gKS system the focus of this chapter is on the implementation of the non-local exchange potential within the full-potential linearized augmented-plane-wave (FLAPW) method. It employs the mixed product basis (MPB) (s. Sec. 4.2.2) with which the matrix elements of the non-local potential, which correspond to state-dependent six-dimensional integrals, decompose into two three-dimensional and one state-independent six-dimensional integral. While the three-dimensional integrals must be calculated for each self-consistent field (SCF) cycle, the state-independent six-dimensional integral is evaluated only once at the beginning of the calculation. By subsuming the three- and six-dimensional integrals into state-dependent vectors and a matrix, the Coulomb matrix, the matrix elements of the non-local exchange potential can be formulated as a Brillouin-zone (BZ) sum over vector-matrix-vector products.

The calculation of the non-local potential constitutes the most-time consuming step in a practical hybrid functional calculation. We present several techniques to accelerate the computation. For example, the Coulomb matrix is made sparse by a unitary transformation of the muffin-tin (MT) MPB functions. Its sparsity is then exploited to reduce the computational demand of the vector-matrix-vector product considerably. Furthermore, spatial and time-reversal symmetries are used to decide in advance which matrix elements are non-zero, and only these are calculated. Symmetry arguments also allow to restrict the BZ sum in the non-local exchange potential to a smaller, irreducible set of $\mathbf{k}$ points. The convergence of the BZ sum with respect to the $\mathbf{k}$-point sampling, however, is hampered by a divergence of the Coulomb matrix at the Γ point. For a favorable convergence of the BZ sum with respect to the

k-point sampling, the divergence of the Coulomb matrix at the Γ point must be properly taken into account. For this purpose, the BZ sum is separated into a divergent and a non-divergent contribution. The divergent part, whose leading term is proportional to $1/q^2$, is integrated analytically, while the non-divergent contribution is treated numerically by a weighted sum.

Furthermore, we report the convergence behavior of the gKS transition energies employing the PBE0 hybrid functional for Si and $SrTiO_3$ as well as of the total energy for Si. Then, we apply the PBE0 hybrid functional to a set of prototype semiconductors and insulators and find a reasonable agreement with recent results from the literature. Moreover, we show band structure and density-of-states calculations with the PBE0 hybrid functional exploiting the Wannier interpolation technique [81, 82]. Finally, we apply the PBE0 hybrid functional to EuO and discuss its structural, electronic, and magnetic properties.

5.1. Generalized KS system

The central idea of the KS formalism is the introduction of an auxiliary system of non-interacting electrons, whose single Slater determinant yields the ground-state density of the real interacting system. So instead of the complicated many-electron system, a set of one-particle equations must be solved. The complexity of the interacting electron system, however, is hidden in the xc energy functional of the KS system (s. Chap. 3). Yet, the KS system is only one specific, arbitrary reference system. Different choices of reference systems are possible [23]. For example, we can define a reference system, whose many-body wave function is still a single Slater determinant of one-particle orbitals, but a fraction of exchange is treated by a orbital-dependent, non-local HF-like exchange potential. This corresponds to an approximation of the universal spin-dependent functional[1] $F[n^\uparrow, n^\downarrow]$ as the minimum of the sum of kinetic and scaled electron-electron interaction over all Slater determinants Φ yielding the spin densities $n^\uparrow(\mathbf{r})$ and $n^\downarrow(\mathbf{r})$

$$F^{\mathrm{gKS}}[n^\uparrow, n^\downarrow] = \min_{\Phi \to n^\uparrow, n^\downarrow} \langle \Phi | T + aV_{ee} | \Phi \rangle + (1-a) U_{\mathrm{H}}[n^\uparrow + n^\downarrow] \,. \tag{5.1}$$

The parameter a ($a \in [0,1]$) scales the electron-electron interaction V_{ee} and will be fixed later. By adding $(1-a)$ times the Hartree energy $U_{\mathrm{H}}[n^\uparrow + n^\downarrow]$ in Eq. (5.1), we pick up in combination with the Hartree term contained in the expectation value of aV_{ee} the Hartree energy completely. The difference between the exact universal functional $F[n^\uparrow, n^\downarrow]$ and $F^{\mathrm{gKS}}[n^\uparrow, n^\downarrow]$

[1] For the spin-independent case the definition of the universal functional is given in Eq. (2.13).

defines in analogy to the KS system the xc energy functional of the gKS system

$$E_{\mathrm{xc}}^{\mathrm{gKS}}[n^{\uparrow}, n^{\downarrow}] = F[n^{\uparrow}, n^{\downarrow}] - F^{\mathrm{gKS}}[n^{\uparrow}, n^{\downarrow}]\,. \tag{5.2}$$

If $\Psi[n^{\uparrow}, n^{\downarrow}]$ denotes the true many-electron ground-state wave function of spin-densities $n^{\uparrow}(\mathbf{r})$ and $n^{\downarrow}(\mathbf{r})$ and if $\Phi^{\mathrm{gKS}}[n^{\uparrow}, n^{\downarrow}]$ is accordingly the ground-state single Slater determinant of the gKS system, the xc energy (5.2) can be written as

$$\begin{aligned} E_{\mathrm{xc}}^{\mathrm{gKS}}[n^{\uparrow}, n^{\downarrow}] &= \langle \Psi[n^{\uparrow}, n^{\downarrow}] | T + V_{ee} | \Psi[n^{\uparrow}, n^{\downarrow}] \rangle - \langle \Phi^{\mathrm{gKS}}[n^{\uparrow}, n^{\downarrow}] | T | \Phi^{\mathrm{gKS}}[n^{\uparrow}, n^{\downarrow}] \rangle \\ &\quad - a E_{\mathrm{x}}^{\mathrm{gKS}}[n^{\uparrow}, n^{\downarrow}] - U_{\mathrm{H}}[n^{\uparrow}, n^{\downarrow}]\,. \end{aligned} \tag{5.3}$$

Here, $E_{\mathrm{x}}^{\mathrm{gKS}}[n^{\uparrow}, n^{\downarrow}]$ is the exact exchange energy (2.33) evaluated with the gKS Slater determinant $\Phi^{\mathrm{gKS}}[n^{\uparrow}, n^{\downarrow}]$. Using the definition of the xc functional of the KS system [cf. Eq. (2.25)] the xc energy of the gKS system turns into a sum of the xc energy of the KS system, the exact exchange energy $E_{\mathrm{x}}^{\mathrm{gKS}}$, and a correction for the kinetic energy, which arises from the difference between KS and gKS single Slater determinant

$$\begin{aligned} E_{\mathrm{xc}}^{\mathrm{gKS}}[n^{\uparrow}, n^{\downarrow}] &= E_{\mathrm{xc}}^{\mathrm{KS}}[n^{\uparrow}, n^{\downarrow}] - a E_{\mathrm{x}}^{\mathrm{gKS}}[n^{\uparrow}, n^{\downarrow}] \\ &\quad + \langle \Phi^{\mathrm{KS}}[n^{\uparrow}, n^{\downarrow}] | T | \Phi^{\mathrm{KS}}[n^{\uparrow}, n^{\downarrow}] \rangle - \langle \Phi^{\mathrm{gKS}}[n^{\uparrow}, n^{\downarrow}] | T | \Phi^{\mathrm{gKS}}[n^{\uparrow}, n^{\downarrow}] \rangle\,. \end{aligned} \tag{5.4}$$

Usually, this difference between the KS and the gKS single Slater determinant is neglected and Eq. (5.4), thus, becomes

$$E_{\mathrm{xc}}^{\mathrm{gKS}}[n^{\uparrow}, n^{\downarrow}] = (1 - a) E_{\mathrm{x}}^{\mathrm{KS}}[n^{\uparrow}, n^{\downarrow}] + E_{\mathrm{c}}^{\mathrm{KS}}[n^{\uparrow}, n^{\downarrow}]\,. \tag{5.5}$$

The one-particle orbitals of band index n, Bloch vector $\mathbf{k}$, and spin index σ that correspond to the minimizing Slater determinant Φ^{gKS} of Eq. (5.1) are solutions of

$$\left[-\frac{1}{2}\nabla^2 + V_{\mathrm{eff}}^{\sigma}(\mathbf{r}) \right] \phi_{n\mathbf{k}}^{\sigma}(\mathbf{r}) + a \int V_{\mathrm{x}}^{\mathrm{NL},\sigma}(\mathbf{r}, \mathbf{r}') \phi_{n\mathbf{k}}^{\sigma}(\mathbf{r}') d^3 r' = \epsilon_{n\mathbf{k}}^{\sigma} \phi_{n\mathbf{k}}^{\sigma}(\mathbf{r}) \tag{5.6}$$

with the non-local exchange potential

$$V_{\mathrm{x}}^{\mathrm{NL},\sigma}(\mathbf{r}, \mathbf{r}') = -\sum_{n}^{\mathrm{occ.}} \sum_{\mathbf{k}}^{\mathrm{BZ}} \frac{\phi_{n\mathbf{k}}^{\sigma}(\mathbf{r}) \phi_{n\mathbf{k}}^{\sigma *}(\mathbf{r}')}{|\mathbf{r} - \mathbf{r}'|} \tag{5.7}$$

and the local effective potential

$$V_{\mathrm{eff}}^{\sigma}(\mathbf{r}) = V(\mathbf{r}) + V_{\mathrm{H}}(\mathbf{r}) + V_{\mathrm{xc}}^{\mathrm{gKS},\sigma}(\mathbf{r})\,. \tag{5.8}$$

The xc potential of the gKS system $V_{\mathrm{xc}}^{\mathrm{gKS},\sigma}(\mathbf{r})$ is defined in analogy to the KS system by

$$V_{\mathrm{xc}}^{\mathrm{gKS},\sigma}(\mathbf{r}) = \frac{\delta E_{\mathrm{xc}}^{\mathrm{gKS}}}{\delta n^{\sigma}(\mathbf{r})}\,. \tag{5.9}$$

We note that Eq. (5.1) together with (5.2) defines a whole series of reference systems. Each choice of a corresponds to a different reference system with a different xc energy functional $E_{\mathrm{xc}}^{\mathrm{gKS}}$. In the case $a = 0$, the gKS system is identical to the KS system. The opposite limit $a = 1$ corresponds to a HF scheme with a DFT correlation functional. In principle, however, the gKS formalism is exact for each a.

The gKS system is usually employed for the hybrid functionals (cf. Sec. 3.4). For example, for the PBE0 hybrid functional [22] the amount of orbital-dependent non-local HF-type exchange is set to $a = 0.25$ and the xc energy functional $E_{\mathrm{xc}}^{\mathrm{gKS}}$ is approximated by $E_{\mathrm{xc}}^{\mathrm{gKS}} = 0.75\,E_{\mathrm{x}}^{\mathrm{PBE}} + E_{\mathrm{c}}^{\mathrm{PBE}}$.

5.2. Implementation of hybrid functionals

In the LAPW basis [Eq. (4.9)] the differential equation (5.6) becomes a generalized eigenvalue problem

$$\sum_{\mathbf{G}'}\left[H_{\mathbf{G}\mathbf{G}'}^{\sigma}(\mathbf{k}) + aV_{\mathrm{x},\mathbf{G}\mathbf{G}'}^{\mathrm{NL},\sigma}(\mathbf{k})\right] z_{\mathbf{G}'}^{\sigma}(n,\mathbf{k}) = \epsilon_{n\mathbf{k}}^{\sigma}\sum_{\mathbf{G}'} S_{\mathbf{G}\mathbf{G}'}^{\sigma}(\mathbf{k}) z_{\mathbf{G}'}^{\sigma}(n,\mathbf{k})\,, \tag{5.10}$$

where $H_{\mathbf{G}\mathbf{G}'}^{\sigma}(\mathbf{k})$ is the representation of the local part $-\frac{1}{2}\nabla^2 + V_{\mathrm{eff}}^{\sigma}(\mathbf{r})$ of (5.6), $V_{\mathrm{x},\mathbf{G}\mathbf{G}'}^{\mathrm{NL},\sigma}(\mathbf{k})$ denotes the matrix of the non-local exchange potential Eq. (5.7), and $S_{\mathbf{G}\mathbf{G}'}^{\sigma}(\mathbf{k})$ is the overlap matrix of the LAPW basis functions. $H_{\mathbf{G}\mathbf{G}'}^{\sigma}(\mathbf{k})$ and $S_{\mathbf{G}\mathbf{G}'}^{\sigma}(\mathbf{k})$ are nowadays calculated routinely in FLAPW DFT codes. Therefore, we will concentrate in the following on the computation of the non-local exchange matrix elements, whose evaluation is by far the most time-consuming step in DFT calculations employing hybrid xc functionals. The reason is the non-locality of the operator in Eq. (5.7), which gives rise to six-dimensional integrals

$$V_{\mathrm{x},\mathbf{G}\mathbf{G}'}^{\mathrm{NL},\sigma}(\mathbf{k}) = -\sum_{n''}^{\mathrm{occ.}}\sum_{\mathbf{q}}^{\mathrm{BZ}}\iint \frac{\varphi_{\mathbf{k}\mathbf{G}}^{\sigma *}(\mathbf{r})\phi_{n''\mathbf{q}}^{\sigma}(\mathbf{r})\phi_{n''\mathbf{q}}^{\sigma *}(\mathbf{r}')\varphi_{\mathbf{k}\mathbf{G}'}^{\sigma}(\mathbf{r}')}{|\mathbf{r}-\mathbf{r}'|} d^3r\, d^3r'\,. \tag{5.11}$$

In contrast, for the local operators in standard DFT calculations only three-dimensional integrals must be evaluated.

A representation of the exchange operator in terms of the wave functions instead of the

LAPW basis

$$V_{\mathrm{x},nn'}^{\mathrm{NL},\sigma}(\mathbf{k}) = -\sum_{n''}^{\mathrm{occ.}}\sum_{\mathbf{q}}^{\mathrm{BZ}}\iint \frac{\phi_{n\mathbf{k}}^{\sigma *}(\mathbf{r})\phi_{n''\mathbf{q}}^{\sigma}(\mathbf{r})\phi_{n''\mathbf{q}}^{\sigma *}(\mathbf{r}')\phi_{n'\mathbf{k}}^{\sigma}(\mathbf{r}')}{|\mathbf{r}-\mathbf{r}'|} d^3r\, d^3r' \tag{5.12}$$

is advantageous for two reasons: (a) If the states n and n' fall into different irreducible symmetry representations, the corresponding matrix element is zero and need not be calculated at all. (b) Although very important, the exchange energy is a relatively small energy contribution compared to kinetic and potential energies. Therefore, we can afford to describe the non-local exchange potential in a subspace of wave functions up to a band cutoff $n_{\max}$. The matrix (5.12) is then only constructed for the elements with $n, n' \leq n_{\max}$ and the rest is set to zero. $n_{\max}$ is a convergence parameter and we will show in section 5.4 that the results converge reasonably fast with respect to this parameter. The matrix $V_{\mathrm{x},\mathbf{GG}'}^{\mathrm{NL},\sigma}(\mathbf{k})$ is obtained from $V_{\mathrm{x},nn'}^{\mathrm{NL},\sigma}(\mathbf{k})$ by multiplying with the inverse matrix of eigenvectors and its adjoint from the right and left, respectively

$$V_{\mathrm{x},\mathbf{GG}'}^{\mathrm{NL},\sigma}(\mathbf{k}) = \sum_{n,n'}\left[\sum_{\mathbf{G}''} S_{\mathbf{GG}''}^{\sigma *}(\mathbf{k}) z_{\mathbf{G}''}^{\sigma}(n,\mathbf{k})\right] V_{\mathrm{x},nn'}^{\mathrm{NL},\sigma}(\mathbf{k}) \left[\sum_{\mathbf{G}''} z_{\mathbf{G}''}^{\sigma *}(n',\mathbf{k}) S_{\mathbf{G}''\mathbf{G}'}^{\sigma}(\mathbf{k})\right]. \tag{5.13}$$

The inverse matrix of eigenvectors results from the normalization condition

$$\sum_{\mathbf{G},\mathbf{G}'} z_{\mathbf{G}}^{\sigma *}(n,\mathbf{k}) S_{\mathbf{GG}'}^{\sigma}(\mathbf{k}) z_{\mathbf{G}'}^{\sigma}(n,\mathbf{k}) = 1\,. \tag{5.14}$$

The sum over the occupied states in Eq. (5.12) involves core and valence states. The core states in the FLAPW method are the solutions of the fully relativistic Dirac equation with the spherically averaged effective potential. They are, thus, classified by the principal quantum number n, the angular momentum quantum number l, the total angular momentum quantum number $j = l \pm 1/2$, and the magnetic quantum number m_j ($m_j = -j, \ldots, j$). Due to the sphericity of the potential the core states are degenerate with respect to the magnetic quantum number. For each n and l we average over the two different values of j weighted by its degeneracy of $2j + 1$. With this, we go over to a non-relativistic description of the core states and can apply the formula by Dagens and Perot [83] to compute the core contribution to the matrix elements of Eq. (5.12). Its evaluation is simple and computationally cheap, in contrast to the valence electron contribution.

For the latter, we employ the MPB (s. Sec. 4.2.2). The products of valence-electron wave functions are represented by the MPB such that the six-dimensional integral, Eq. (5.12), de-

composes into a vector-matrix-vector product

$$V_{\mathrm{x},nn'}^{\mathrm{NL},\sigma}(\mathbf{k}) = -\sum_{n''}^{\text{occ.}} \sum_{\mathbf{q}}^{\text{BZ}} \sum_{IJ} \langle \phi_{n\mathbf{k}}^{\sigma} | \phi_{n''\mathbf{k}-\mathbf{q}}^{\sigma} M_{\mathbf{q},I} \rangle v_{IJ}(\mathbf{q}) \langle M_{\mathbf{q},J} \phi_{n''\mathbf{k}-\mathbf{q}}^{\sigma} | \phi_{n'\mathbf{k}}^{\sigma} \rangle \,. \tag{5.15}$$

The vectors $\langle M_{\mathbf{q},J} \phi_{n''\mathbf{k}-\mathbf{q}}^{\sigma} | \phi_{n'\mathbf{k}}^{\sigma} \rangle$ are defined by $\langle f|g\rangle = \int f^*(\mathbf{r}) g(\mathbf{r})\, d^3r$ and represent the wave function product $\phi_{n''\mathbf{k}-\mathbf{q}}^{\sigma *}(\mathbf{r}) \phi_{n'\mathbf{k}}^{\sigma}(\mathbf{r})$ in the MPB. In order to ensure that $\mathbf{k}-\mathbf{q}$ is again a member of the $\mathbf{k}$-point set, we choose an equidistant $\mathbf{k}$-point mesh. Additionally, we require that the $\mathbf{k}$-point set contains the Γ point. This is necessary for an accurate treatment of the divergence of the Coulomb matrix

$$v_{IJ}(\mathbf{q}) = \iint \frac{\tilde{M}_{\mathbf{q},I}^{*}(\mathbf{r}) \tilde{M}_{\mathbf{q},J}(\mathbf{r}')}{|\mathbf{r}-\mathbf{r}'|} d^3r\, d^3r' \tag{5.16}$$

around $\mathbf{q} = \mathbf{0}$ (s. Sec. 5.2.3). The Coulomb matrix does not dependent on the wave functions. As the MPB does not change during the SCF, the Coulomb matrix is constructed once at the beginning of the SCF cycle, while the vectors are calculated in each iteration. Due to the partition of the MPB in MT functions and interstitial plane waves (IPWs) the Coulomb matrix consists of four distinct blocks: the diagonal parts MT-MT and IPW-IPW as well as the two off-diagonal part MT-IPW and IPW-MT, which are the complex conjungates of each other. The evaluation of the different blocks is discussed in detail in Ref. 84.

5.2.1. Sparsity of the Coulomb matrix

The vector-matrix-vector products of Eq. (5.15) must be evaluated in every iteration of the self-consistent field cycle for each combination of band indices n, n', and n'' as well as Bloch vectors $\mathbf{k}$ and $\mathbf{q}$. This easily amounts to billion matrix-vector operations or more. We will show that the matrix-vector product becomes considerably faster, if the Coulomb matrix is made sparse. This is achieved by a unitary transformation of the MT functions that acts in the subspace of each atom and LM channel.

Let us consider the two radial MT functions $M_{L1}^{a}(r)$ and $M_{L2}^{a}(r)$, whose electrostatic multipole moments are given by

$$\mu_{LP}^{a} = \int_0^{S_a} M_{LP}^{a}(r) r^{L+2} dr \tag{5.17}$$

for $P = 1, 2$. If we apply the unitary transformation

$$M^{a'}_{L1}(r) = \frac{1}{\sqrt{(\mu^a_{L1})^2 + (\mu^a_{L2})^2}} \left[\mu^a_{L1} M^a_{L1}(r) + \mu^a_{2L} M^a_{L2}(r)\right] \tag{5.18}$$

$$M^{a'}_{L2}(r) = \frac{1}{\sqrt{(\mu^a_{L1})^2 + (\mu^a_{L2})^2}} \left[\mu^a_{L2} M^a_{L1}(r) - \mu^a_{L1} M^a_{L2}(r)\right] \tag{5.19}$$

the multipole moment of the second function $M^{a'}_{L2}(r)$ will vanish. With this procedure we can generally transform a set of MT functions so that the resulting functions are multipole-free for all except one function. For example, out of ten functions we obtain nine multipole-free functions and one with a non-vanishing multipole moment. We denote the sets of these transformed functions by $\mathrm{MT}(\mu = 0)$ and $\mathrm{MT}(\mu \neq 0)$, respectively. By construction, the former does not generate a potential outside the MT spheres. So, the Coulomb matrix elements involving such a function can only be non-zero, if the other function is a MT function residing in the same MT sphere. Matrix elements with a MT function in a different MT sphere or an interstitial plane wave vanish. This leads to a very sparse, nearly block-diagonal form of the Coulomb matrix as illustrated in Fig. 5.1. We have ordered the MPB according to: $\mathrm{MT}(\mu = 0)$, $\mathrm{MT}(\mu \neq 0)$, and IPWs. There are on-site blocks (one for each LM channel) for the $\mathrm{MT}(\mu = 0)$ part and one big block for the combined set of the $\mathrm{MT}(\mu \neq 0)$ and the IPWs. Only a few off-diagonal elements exists between $\mathrm{MT}(\mu = 0)$ and $\mathrm{MT}(\mu \neq 0)$ functions at the same atom. Exploiting this sparsity in the matrix-vector products of Eq. (5.15) drastically reduces the number of floating point operations and, thus, the computational demand.

In order to demonstrate the reduction in the computational demand and, thus, the speed-up we report timings for 100 000 matrix-vector products with and without the sparse matrix technique. The conventional matrix-vector product scales quadratically with the size N of the MPB ($N = N_{\mathrm{MT}} + N_{\mathrm{IPW}}$), whereas the timing of the sparse-matrix vector product is usually dominated by the large block of IPWs and $\mathrm{MT}(\mu \neq 0)$ functions. The size of this block is given by $N_{\mathrm{IPW+MT}(\mu\neq 0)} = N_{\mathrm{IPW}} + N_{\mathrm{atom}} \cdot (L_{\max} + 1)^2$. Hence, we can ideally obtain a speed-up of $(N/N_{\mathrm{IPW+MT}(\mu\neq 0)})^2$. For the simple case of diamond with 2 atoms in the unit cell and a MPB that consists of 59 interstitial plane waves ($G'_{\max} = 3.2\,\mathrm{a}_0^{-1}$) and 210 MT function ($L_{\max} = 4$), the sparse matrix approach is a factor 2.8 faster than the conventional matrix-vector product.[2] This factor is much smaller than the ideal speed-up of 6.1, which, however, does not consider the time for the multiplication of the block-diagonal matrix $[\mathrm{MT}(\mu = 0)]$ with the vector. Due to the relatively small number of interstitial plane waves in this example the timing for the block-diagonal part $[\mathrm{MT}(\mu = 0)]$ is not negligible. For the perovskite $SrTiO_3$ with 389 interstitial plane waves ($G'_{\max} = 3.8\,\mathrm{a}_0^{-1}$) and 683 MT functions ($L_{\max} = 4$) the conventional

[2] The calculations have been performed on a single core of a Intel Core I5 processor with 2.67 GHz.

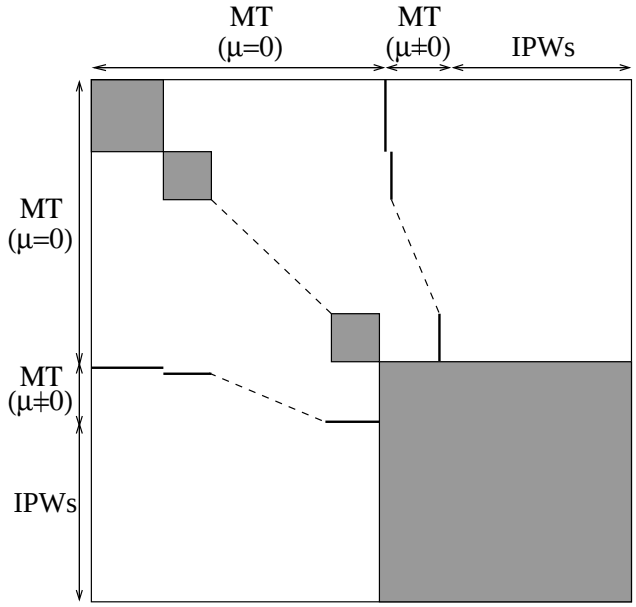

Figure 5.1.: Illustration of the Coulomb matrix after transforming the MPB according to Eqs. (5.18) and (5.19). The elements that are in general non-zero are marked. The matrix is predominantly block-diagonal.

approach requires about 40.7 s to execute the matrix product 100 000 times, while the sparse matrix approach needs only 11.4 s. Consequently, the sparse-matrix approach is a factor of 3.6 faster, which is quite close to the ideal factor of 4.4. We note that the number of matrix vector products easily amounts to 100 000: a combination of merely 10 **k** points, 10 **q** points, 20 occupied bands, and 50 unoccupied bands already yields in total 100 000 products.

5.2.2. Symmetry

In addition to the sparse-matrix technique, we accelerate the calculation of $V_{\mathrm{x},nn'}^{\mathrm{NL},\sigma}(\mathbf{k})$ by exploiting spatial and time reversal symmetries. These symmetries can be used to facilitate the computation in three ways: (a) Inversion symmetry leads to real-valued quantities. (b) If the wave functions $\phi_{n\mathbf{k}}^{\sigma}$ and $\phi_{n'\mathbf{k}}^{\sigma}$ in Eq. (5.15) fall into different irreducible representations, the corresponding exchange matrix element vanishes. This can be used as a criterion whether an element must be calculated explicitly or not. And (c), for each **k** chosen from the irreducible wedge of the BZ the **q** summation in Eq. (5.15) is restricted to a smaller set of Bloch vectors giving rise to an extended irreducible BZ. We will discuss each item in the following in detail.

(a) Inversion symmetry

In general, the Coulomb matrix (5.16) is Hermitian. However, if the system under consideration exhibits inversion symmetry and the MPB functions fulfill the condition

$$f(-\mathbf{r}) = f^*(\mathbf{r})\,, \tag{5.20}$$

it becomes real-symmetric. Similarly, the vectors in (5.15) are then real instead of complex. This reduces the computational demand in terms of both CPU time and memory considerably. However, presently the condition only holds for the IPWs, but not for the MT functions. We, therefore, combine the MT functions of each pair of atoms a and $-a$, which are related via inversion symmetry,

$$M^{a\prime}_{\mathbf{k},LMP}(\mathbf{r}) = \frac{1}{\sqrt{2}}\left[M^{a}_{\mathbf{k},LMP}(\mathbf{r}) + (-1)^{L+M} M^{-a}_{\mathbf{k},L(-M)P}(\mathbf{r})\right] \tag{5.21a}$$

$$M^{a\prime}_{\mathbf{k},L(-M)P}(\mathbf{r}) = \frac{i}{\sqrt{2}}\left[M^{a}_{\mathbf{k},LMP}(\mathbf{r}) - (-1)^{L+M} M^{-a}_{\mathbf{k},L(-M)P}(\mathbf{r})\right]. \tag{5.21b}$$

If the atom is placed in the origin, i.e., the atom indices a and $-a$ correspond to the same atom, the transformations (5.21a) and (5.21b) only hold for the integer index $M < 0$, and we define

$$M^{a\prime}_{\mathbf{k},L0P}(\mathbf{r}) = \begin{cases} M^{a}_{\mathbf{k}L0P}(\mathbf{r})\,, & \text{if } L \text{ even} \\ i \cdot M^{a}_{\mathbf{k}L0P}(\mathbf{r})\,, & \text{if } L \text{ odd} \end{cases} \tag{5.22}$$

for $M = 0$. It is then easy to show that the transformed functions will fulfill the condition (5.20). We note that this symmetrization does not destroy the form of the Coulomb matrix shown in Fig. 5.1.

(b) Irreducible representations

The great orthogonality theorem of group theory [85] demands that the matrix elements $\langle \phi^{\sigma}_{n\mathbf{k}} | A | \phi^{\sigma}_{n'\mathbf{k}} \rangle$ of any operator A, which commutes with the symmetry operations of the system, are zero, if the wave functions fall into different irreducible representations. In particular, this holds for the exchange operator (5.7). Instead of evaluating the irreducible representations explicitly, we exploit the fact that the great orthogonality theorem applies to *any* operator that has the full symmetry of the system. A suitable operator is given by the MT step function

$$\Theta^{\mathrm{MT}}(\mathbf{r}) = 1 - \Theta(\mathbf{r})\,, \tag{5.23}$$

where $\Theta(\mathbf{r})$ is defined according to Eq. (4.27). The calculation of its matrix elements $\langle\phi^{\sigma}_{n\mathbf{k}}|\Theta^{\mathrm{MT}}|\phi^{\sigma}_{n'\mathbf{k}}\rangle$ is elementary and takes negligible CPU time. If the matrix elements between two groups of degenerate wave functions are numerically zero, we conclude that these two groups belong to different irreducible representations. Then the corresponding matrix elements of the non-local exchange potential (5.15) must be zero, too. The question remains whether, conversely, the matrix elements of (5.23) are always non-zero, if the two irreducible representations are identical. This is not fulfilled in only two cases. First, either of the two wave functions is completely confined to the MT sphere. This can be ruled out, since we deal with valence or conduction states. Second, the matrix elements are zero by accident: the overlaps in the interstitial and the MT spheres exactly cancel. This is extremely unlikely, verging on the impossible. We find that the procedure provides a fast and reliable criterion to decide in advance, which exchange matrix elements are non-zero and must be calculated explicitly.

(c) Extended irreducible BZ

In general, if a symmetry operation, which leaves the Hamiltonian invariant, acts on a wave function, it generates another wave function with the same energy. In other words, the solutions of the one-particle equations at two different $\mathbf{k}$ points are equivalent, if the $\mathbf{k}$ vectors are related by a symmetry operation. This can be used to restrict the set of $\mathbf{k}$ points, at which the Hamiltonian must be diagonalized, to a smaller set, whose members are not pair-wise related. This defines the so-called irreducible Brillouin zone (IBZ), which is routinely employed in calculations with periodic boundary conditions. In a similar way, the summation over $\mathbf{q}$ points in the non-local exchange term can be confined, too. However, due to the additional dependence on $\mathbf{k}$ and $\mathbf{k}-\mathbf{q}$, we can only employ those symmetry operations $P_i^{\mathbf{k}}$ that leave the given $\mathbf{k}$ vector invariant, i.e., $P_i^{\mathbf{k}}\mathbf{k} = \mathbf{k} + \mathbf{G}_i^{\mathbf{k}}$, where $\mathbf{G}_i^{\mathbf{k}}$ is a reciprocal lattice vector. This subset of operations $\{P_i^{\mathbf{k}}\}$ is commonly called *little group* $\mathrm{LG}(\mathbf{k})$. In the same way as for the IBZ the little group gives rise to a minimal set of inequivalent $\mathbf{q}$ points, which we denote by the extended IBZ [$\mathrm{EIBZ}(\mathbf{k})$]. The exchange potential in the LAPW basis can then be written as

$$
\begin{aligned}
&V_{\mathrm{x},\mathbf{G}\mathbf{G}'}^{\mathrm{NL},\sigma}(\mathbf{k}) \qquad (5.24)\\
&= -\sum_{i}^{\mathrm{LG}(\mathbf{k})}\sum_{\mathbf{q}}^{\mathrm{EIBZ}(\mathbf{k})}\frac{1}{N_{\mathbf{k},\mathbf{q}}}\sum_{n}^{\mathrm{occ.}}\iint\frac{\varphi^{\sigma *}_{\mathbf{k}\mathbf{G}}(\mathbf{r})[P_i^{\mathbf{k}^{-1}}\phi^{\sigma}_{n\mathbf{k}-\mathbf{q}}(\mathbf{r})][P_i^{\mathbf{k}^{-1}}\phi^{\sigma *}_{n\mathbf{k}-\mathbf{q}}(\mathbf{r}')]\varphi^{\sigma}_{\mathbf{k}\mathbf{G}'}(\mathbf{r}')}{|\mathbf{r}-\mathbf{r}'|}d^3r\,d^3r'\\
&= -\sum_{i}^{\mathrm{LG}(\mathbf{k})}\sum_{\mathbf{q}}^{\mathrm{EIBZ}(\mathbf{k})}\frac{1}{N_{\mathbf{k},\mathbf{q}}}\sum_{n}^{\mathrm{occ.}}\iint\frac{\varphi^{\sigma *}_{\mathbf{k}(P_i^{\mathbf{k}}\mathbf{G}+\mathbf{G}_i^{\mathbf{k}})}(\mathbf{r})\phi^{\sigma}_{n\mathbf{k}-\mathbf{q}}(\mathbf{r})\phi^{\sigma *}_{n\mathbf{k}-\mathbf{q}}(\mathbf{r}')\varphi^{\sigma}_{\mathbf{k}(P_i^{\mathbf{k}}\mathbf{G}'+\mathbf{G}_i^{\mathbf{k}})}(\mathbf{r}')}{|\mathbf{r}-\mathbf{r}'|}d^3r\,d^3r'\,,
\end{aligned}
$$

where $N_{\mathbf{k},\mathbf{q}}$ is the number of symmetry operations that are members of both LG($\mathbf{k}$) and LG($\mathbf{q}$). As a result, we can restrict the $\mathbf{q}$ summation to the EIBZ($\mathbf{k}$) and add the contribution of all other $\mathbf{q}$ points by transforming the final matrix with the operations LG($\mathbf{k}$) and summing up the transformed matrices. This takes very little computation time, because a symmetry operation acts as a one-to-one mapping in the space of the augmented plane waves as indicated in Eq. (5.24). Local orbitals transform in a similar way. This is why we apply the symmetrization to $V^{\mathrm{NL},\sigma}_{\mathrm{x},\mathbf{G}\mathbf{G}'}(\mathbf{k})$ instead of $V^{\mathrm{NL},\sigma}_{\mathrm{x},nn'}(\mathbf{k})$. In the latter case we would need the irreducible representations again. We note that the whole formalism can be easily extended to the case of non-symmorphic and time-reversal symmetry operations.

In conclusion, we compute the non-local exchange potential $V^{\mathrm{NL},\sigma}_{\mathrm{x},nn'}(\mathbf{k})$ in the space of the wave functions, where we restrict the $\mathbf{q}$ summation to the EIBZ($\mathbf{k}$) and evaluate only those band combinations n and n', which can be expected to be non-zero. We then apply the transformation (5.13) and sum up the different matrix elements according to (5.24).

5.2.3. Singularity of the Coulomb matrix

Due to the long-range nature of the Coulomb interaction the matrix $v_{IJ}(\mathbf{q})$, Eq. (5.16), is singular at $\mathbf{q} = 0$, which leads to a divergent integrand in (5.15). As the divergence is proportional to $1/q^2$, a three-dimensional integration over the BZ yields a finite value. However, in a practical calculation the $\mathbf{q}$ summation in (5.15) is not an integral, but a weighted sum over the discrete BZ mesh. A simple way to avoid the divergence is to exclude the point $\mathbf{q} = \mathbf{0}$ from the $\mathbf{k}$-point set. Then all terms in (5.15) are finite, and the $\mathbf{q}$ sum can be evaluated easily. This, however, leads to very poor convergence with respect to the BZ sampling, because the quantitatively important region around $\mathbf{q} = \mathbf{0}$ is not properly taken into account. Hence, it is advantageous to explicitly treat the Γ point and the singularity of the Coulomb matrix at Γ. This is possible by a decomposition of $v_{IJ}(\mathbf{q})$ into a divergent and a non-divergent part [84]

$$v_{IJ}(\mathbf{q}) = \frac{4\pi}{V}\frac{1}{q^2}\langle \tilde{M}_{\mathbf{q},I}|e^{i\mathbf{q}\cdot\mathbf{r}}\rangle\langle e^{i\mathbf{q}\cdot\mathbf{r}}|\tilde{M}_{\mathbf{q},J}\rangle + v'_{IJ}(\mathbf{q})\,, \tag{5.25}$$

where the second term $v'_{IJ}(\mathbf{q})$ is finite for all $\mathbf{q}$ and is identical to $v_{IJ}(\mathbf{q})$ for $\mathbf{q} \neq 0$. The divergent first term is exact in the limit $\mathbf{q} \to \mathbf{0}$, as the MPB contains the constant basis function explicitly (s. Sec. 4.2.2). Correspondingly, the combination of Eq. (5.25) and (5.15) yields two contributions, a divergent and a non-divergent one, to the matrix element $V^{\mathrm{NL},\sigma}_{\mathrm{x},nn'}(\mathbf{k})$

$$V^{\mathrm{NL},\sigma}_{\mathrm{x},nn'}(\mathbf{k}) = V^{\mathrm{NL},\sigma}_{\mathrm{x},nn'}(\mathbf{k})\big|_{\mathrm{non-div}} + V^{\mathrm{NL},\sigma}_{\mathrm{x},nn'}(\mathbf{k})\big|_{\mathrm{div}}\,, \tag{5.26}$$

where the non-divergent part is given by

$$V_{\mathrm{x},nn'}^{\mathrm{NL},\sigma}(\mathbf{k})\big|_{\mathrm{non-div}} = -\sum_{n''}^{\mathrm{occ.}}\sum_{\mathbf{q}}^{\mathrm{BZ}}\sum_{IJ}\langle\phi_{n\mathbf{k}}^{\sigma}|\phi_{n''\mathbf{k}-\mathbf{q}}^{\sigma}M_{\mathbf{q},I}\rangle v_{IJ}'(\mathbf{q})\langle M_{\mathbf{q},J}\phi_{n''\mathbf{k}-\mathbf{q}}^{\sigma}|\phi_{n'\mathbf{k}}^{\sigma}\rangle\,. \tag{5.27}$$

Its $\mathbf{q}$ summation can be performed numerically. For the divergent part $V_{\mathrm{x},nn'}^{\mathrm{NL},\sigma}(\mathbf{k})\big|_{\mathrm{div}}$ we switch from a representation with the MPB to a representation with plane waves $e^{i\mathbf{q}\cdot\mathbf{r}}$. For the important region close to $\mathbf{q}=0$ this is exact. Thus, $V_{\mathrm{x},nn'}^{\mathrm{NL},\sigma}(\mathbf{k})\big|_{\mathrm{div}}$ is given by

$$V_{\mathrm{x},nn'}^{\mathrm{NL},\sigma}(\mathbf{k})\big|_{\mathrm{div}} = -\frac{1}{2\pi^2}\left(\sum_{n''}^{\mathrm{occ.}}\int_{\mathrm{BZ}}\langle\phi_{n\mathbf{k}}^{\sigma}|\phi_{n''\mathbf{k}-\mathbf{q}}^{\sigma}e^{i\mathbf{q}\cdot\mathbf{r}}\rangle\frac{1}{q^2}\langle e^{i\mathbf{q}\cdot\mathbf{r}}\phi_{n''\mathbf{k}-\mathbf{q}}^{\sigma}|\phi_{n'\mathbf{k}}^{\sigma}\rangle d^3q - \mathrm{d.c.}\right), \tag{5.28}$$

where d.c. denotes a double-counting correction for the finite $\mathbf{q}$ points (see below). In the limit $\mathbf{q}\to\mathbf{0}$ we can replace $\langle\cdot|\cdot\rangle$ in (5.28) by $\delta_{nn''}$ and $\delta_{n'n''}$, respectively. For an expansion of $\langle\cdot|\cdot\rangle$ beyond the leading term in $\mathbf{q}$ we refer to Refs. 42 and 86. The integration in Eq. (5.28) is restricted to the first part of the BZ. An extension over the whole reciprocal space requires to take the periodicity of the integrand into account explicitly. Therefore, we replace $1/q^2$ by the function

$$F(\mathbf{q}) \quad = \quad \sum_{\mathbf{G}}\frac{e^{-\beta|\mathbf{q}+\mathbf{G}|^2}}{|\mathbf{q}+\mathbf{G}|^2}\,, \tag{5.29}$$

which was proposed by Massidda *et al.* in Ref. 87. In contrast to Ref. 87 we choose the parameter β as small as possible such that (5.29) is sufficiently close to $1/q^2$. After inserting (5.29) in (5.28) we obtain

$$V_{\mathrm{x},nn'}^{\mathrm{NL},\sigma}(\mathbf{k})\big|_{\mathrm{div}} = -\delta_{nn'}f_{n\mathbf{k}}^{\sigma}\left(\frac{1}{2\pi^2}\int\frac{e^{-\beta|\mathbf{q}|^2}}{q^2}d^3q - \frac{1}{N_{\mathbf{k}}\Omega}\sum_{q\neq 0}\frac{e^{-\beta|\mathbf{q}|^2}}{q^2}\right), \tag{5.30}$$

where the summation over $q\neq 0$ avoids double counting, $N_{\mathbf{k}}$ denotes the number of $\mathbf{k}$ points and $f_{n\mathbf{k}}^{\sigma}$ is the occupation number. Eq. (5.30) shows that the divergent contribution is only non-zero for diagonal, occupied matrix elements. In order to evaluate the integral and the sum in Eq. (5.30) we introduce a reciprocal cutoff radius q_0 and finally obtain

$$V_{\mathrm{x},nn'}^{\mathrm{NL},\sigma}(\mathbf{k})\big|_{\mathrm{div}} \quad = \quad -\delta_{nn'}f_{n\mathbf{k}}^{\sigma}\left(\frac{1}{\sqrt{\pi\beta}}\,\mathrm{erf}\left(\sqrt{\beta}q_0\right) - \frac{1}{N_{\mathbf{k}}\Omega}\sum_{0<q\leq q_0}\frac{e^{-\beta|\mathbf{q}|^2}}{q^2}\right). \tag{5.31}$$

We get rid off the convergence parameter q_0 by relating β and q_0 by $e^{-\beta q_0^2}=\beta$. This relation ensures that a small parameter β, which corresponds to a slow exponential decay, entails a

large q_0. We find that $\beta = 0.005$ is a good choice in practice.

In Fig. 5.2 the convergence of the exchange energy $E_x^{NL} = 2\sum_{n\mathbf{k}}^{occ.} V_{x,nn}^{NL}(\mathbf{k})$ with respect to the $\mathbf{k}$-point sampling for NaCl is demonstrated. While the separate contributions from the divergent term, Eq. (5.31), and the remainder converge poorly, their sum nearly looks constant on the energy scale of Fig. 5.2(a). As shown in Fig. 5.2(b), the $\mathbf{k}$-point convergence can be improved further by taking corrections at $\mathbf{q} = \mathbf{0}$ into account that arise from multiplying $1/q^2$ with second-order terms of $\langle\cdot|\cdot\rangle\langle\cdot|\cdot\rangle$ derived by $\mathbf{k}\cdot\mathbf{p}$ perturbation theory [42, 86].

5.3. Self-consistent field cycle

The one-particle equation (5.6) must be solved self-consistently, as the effective potential $V_{eff}^{\sigma}(\mathbf{r})$, which enters in $H_{\mathbf{GG'}}^{\sigma}(\mathbf{k})$, and the non-local HF potential $V_{x,\mathbf{GG'}}^{NL,\sigma}(\mathbf{k})$ depend on the density and density matrix, respectively. In standard DFT calculations employing a local or semi-local xc functional, the one-particle KS equation solely depends on the density. In order to achieve self-consistency in this case an elaborate mixing scheme, for example Broyden mixing [88, 89], is applied, where a new density out of the densities of the previous iterations is constructed as the input density for the next iteration. Hybrid functionals, in principle, require a mixing of the density matrix, as well. Indeed, we find that a standard Broyden mixing of the density and simply using the output density matrix as the input for the next iteration leads to a poor convergence. 27 iterations for Si and more than 200 iterations for $SrTiO_3$ are required to obtain converged PBE0 results (s. Fig. 5.3), where we consider a calculation as converged if the root-mean square of the density difference Δn between input and output densities fall below $10^{-5}\,\mathrm{me}/\mathrm{a}_0^3$ (e denotes the elementary charge and a_0 is the Bohr radius). The definition of a mixing scheme for the density matrix in the FLAPW method, however, is difficult, maybe impossible, as the LAPW basis for the wave functions changes in each iteration. We propose here an alternative approach, which leads to a fast density convergence. It consists of an outer self-consistency cycle for the density-matrix and an inner one for the density (cf. Fig. 5.4). After the construction of the non-local exchange potential we keep its matrix representation $V_{x,\mathbf{GG'}}^{NL,\sigma}$ fixed and iterate Eq. (5.6), until self-consistency in the density is reached; only then the exchange potential $V_{x,\mathbf{GG'}}^{NL,\sigma}$ is updated from the current wave functions, which starts a new set of inner self-consistency iterations. With this nested iterative procedure the *outer* loop converges after eight steps for a PBE0 calculation of Si (s. Fig. 5.3) and after only twelve steps for $SrTiO_3$. One iteration of the *inner* loop lasts only 1.0 s for Si and 8.3 s for $SrTiO_3$ on a single Intel Xeon X5355 at 2.66 GHz using a 4×4×4 $\mathbf{k}$-point set. This is negligible compared with the cost for the construction of the non-local potential in the *outer* loop, which amounts to 11.9 s for Si and 573.1 s for $SrTiO_3$. In summary, the nested iteration

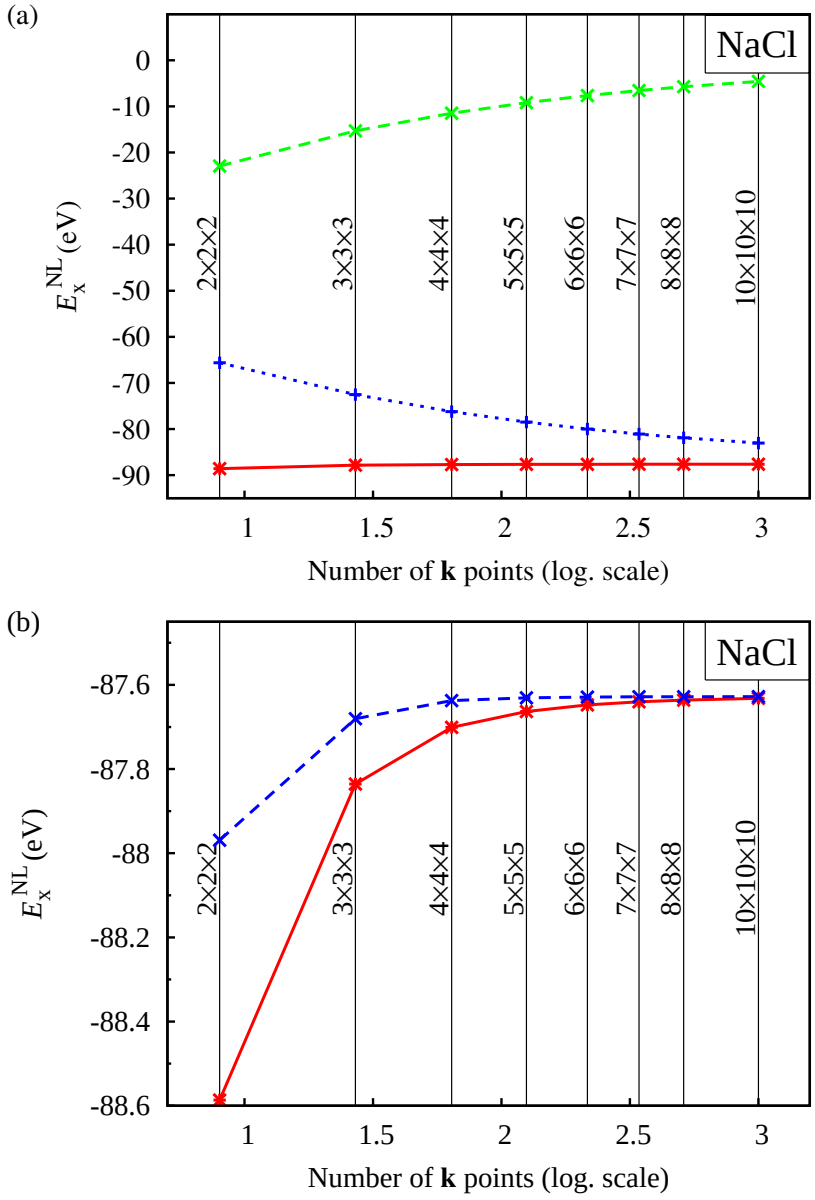

Figure 5.2.: (a) Exchange energy as a function of the **k**-point mesh for NaCl. The green dashed and blue dotted curves correspond to the divergent contribution Eq. (5.31) and the remaining numerical sum, respectively. The sum of both is shown by the red solid curve. (b) Convergence of the exchange energy with (blue dashed curve) and without (red solid curve) higher-order corrections at $\mathbf{q} = \mathbf{0}$. Please note the different scale of the exchange energy in figures (a) and (b).

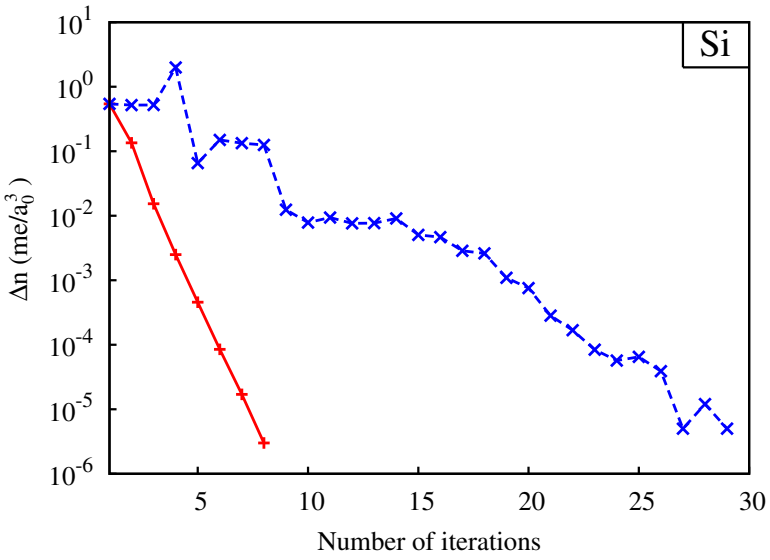

Figure 5.3.: Convergence behavior of the electron density for Si: the change in the density Δn is shown as a function of the self-consistent-field cycles. The red solid and blue dashed curves correspond to calculations with and without the nested density convergence scheme (see text).

scheme constitutes a practical SCF scheme which leads to a considerably faster convergence.

5.4. Convergence tests

In order to assess the efficiency of our numerical scheme, we analyze the convergence of the gKS transition energies and of the total energy with respect to the numerical cutoff parameters $L_{\max}$ and $G'_{\max}$ of the MPB as well as the number of bands $n_{\max}$, which are used to represent the non-local exchange potential. In particular, we show the convergence of the $\Gamma_{25'v} \rightarrow \Gamma_{15c}$ and $\Gamma_{25'v} \rightarrow X_{1c}$ transitions for Si and the $\Gamma_{15c} \rightarrow \Gamma_{25'c}$ and $R_{15'v} \rightarrow \Gamma_{25'c}$ transition energies for $SrTiO_3$ as functions of the convergence parameters for the PBE0 functional. Figure 5.5(a) and (b) demonstrate that the convergence of these transition energies, obtained from a self-consistent solution of Eq. (5.6), is achieved to within 0.01 eV for $G'_{\max} = 2.0\,a_0^{-1}$ and $G'_{\max} = 2.7\,a_0^{-1}$ for Si and $SrTiO_3$, respectively. It is remarkable that these cutoff values are far below the exact limit of $G'_{\max} = 2G_{\max}$ for the wave function products ($G_{\max} = 3.6\,a_0^{-1}$ for Si and $G_{\max} = 4.3\,a_0^{-1}$ for $SrTiO_3$) and even below the reciprocal cutoff radius $G_{\max}$ for the wave functions themselves. A similar observation can be made for the cutoff parameter for the angular momentum $L_{\max}$. For both materials $L_{\max} = 4$ [s. Fig. (5.5)] is sufficient, while an

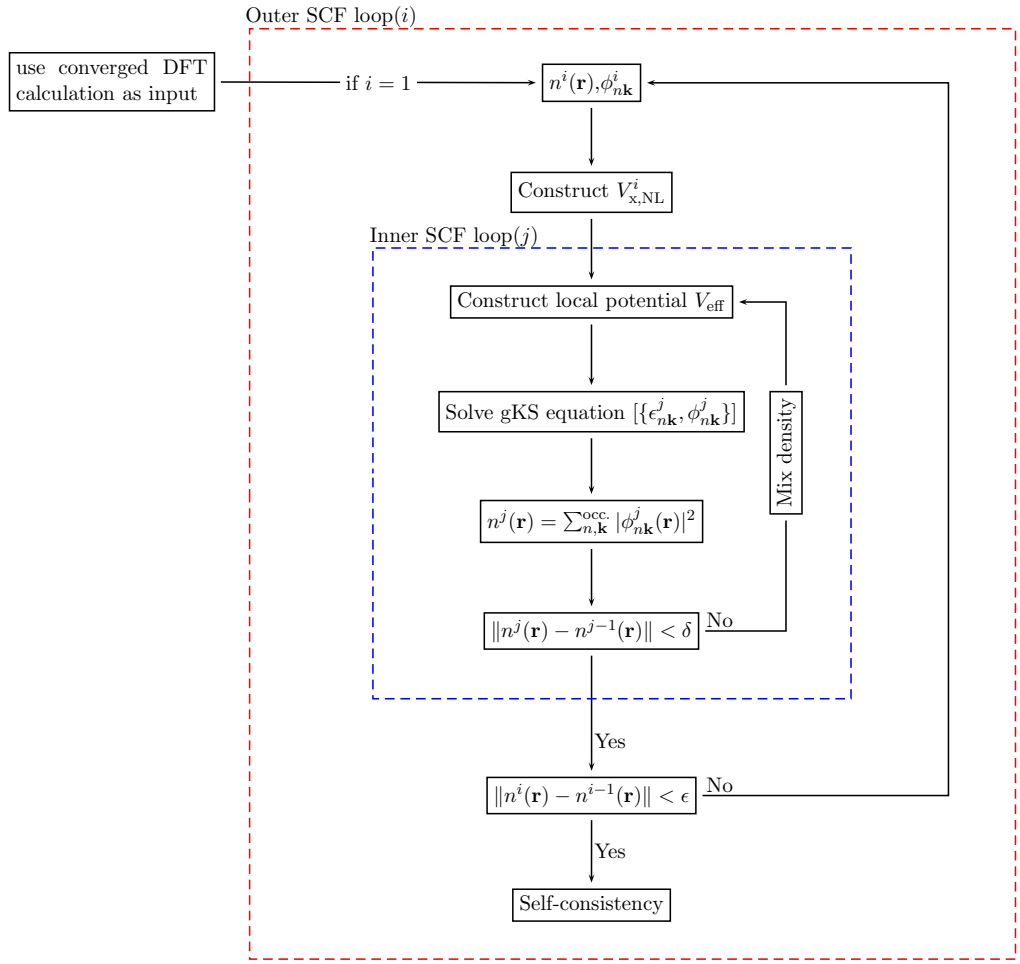

Figure 5.4.: Schematic illustration of the nested SCF cycle for hybrid functional calculations.

exact representation of the wave function products would require $L_{\max} = 2l_{\max}$ ($l_{\max} = 8$ for Si and $l_{\max} = 11$ for $SrTiO_3$). The number of bands $n_{\max}$ that defines the Hilbert space, in which the exchange potential is represented, can be restricted to only ~ 50 bands per atom. This amounts to 100 and 250 bands for Si and $SrTiO_3$, respectively.

Furthermore, we examine the convergence of the total energy difference between the diamond and wurtzite crystal structure of Si. The total energy difference is converged to an accuracy of 1 meV with a reciprocal cutoff radius $G'_{\max} = 2.25\,a_0^{-1}$, an angular-momentum cutoff $L_{\max} = 4$, and $n_{\max} = 20$. We note that the accuracy of 1 meV is one order of magnitude smaller than the tolerance for the transition energies and well below the error resulting from the BZ discretization of the 4×4×4 **k**-point sampling. With an 8×8×8 **k**-point mesh the calculations are converged to within 2 meV. The diamond structure is 112 meV lower in energy than the wurtzite structure. For the PBE functional the energy difference amounts to 92 meV.

In conclusion, as demonstrated for the example of Si and $SrTiO_3$ we found that $G'_{\max}$ can be chosen universally smaller than $G_{\max}$. Typically $G'_{\max} = 0.75 G_{\max}$ is a reasonable choice. The angular-momentum cutoff $L_{\max}$ and the number of bands $n_{\max}$ is more material specific. Thorough convergence tests are necessary for these parameters.

5.5. Results for prototype semiconductors and insulators

For the semiconductors and insulators Si, C, GaAs, MgO, NaCl, and crystalline Ar we report in Table 5.1 gKS transition energies obtained with the PBE0 hybrid functional.[3] All calculations are performed at the experimental lattice constant. The transition energies are converged to within 0.01 eV with respect to the MPB parameters $G'_{\max}$, $L_{\max}$ and the band cutoff $n_{\max}$. A 12×12×12 **k**-point mesh ensures converged results with respect to the sampling of the BZ.

While the PBE functional (s. Table 5.1) underestimates the $\Gamma \rightarrow \Gamma$, $\Gamma \rightarrow$ L, and $\Gamma \rightarrow$ X transitions for this set of materials substantially, the admixture of 25% HF exchange in the PBE0 functional leads to a consistent increase of the energies. Consequently, the PBE0 values come closer to the experimental results. A slight overestimation of the energies is observed for the semiconductors Si and GaAs. In contrast, the transition energies for the insulators are still underestimated by PBE0. The mean absolute error of the PBE transition energies with respect to the available experimental values of 197% is reduced to 86% by the PBE0 functional.

We, furthermore, compare our results with recent projector augmented-wave (PAW) calculations [30]. For Si and GaAs the FLAPW PBE and PBE0 transition energies deviate by

[3] For crystalline Ar we augmented the LAPW basis set in the MT spheres by 4 local orbitals. Two of them are added to the angular momentum $l = 0$ and the other two to $l = 1$. The energy parameters of these local orbitals have been determined according to Eq. (4.18).

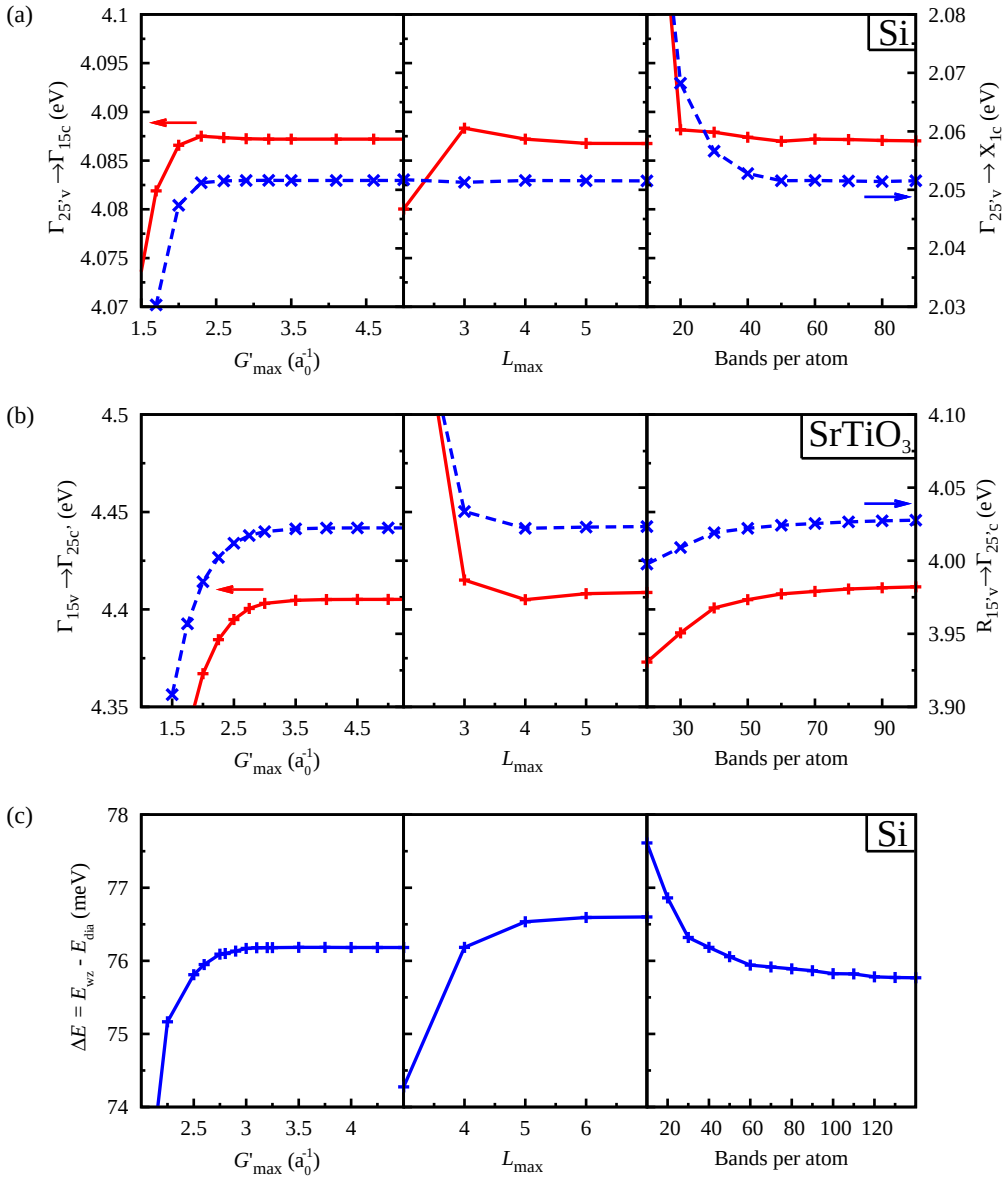

Figure 5.5.: Convergence of (a) the $\Gamma_{25'v} \rightarrow \Gamma_{15c}$ (red solid line, left scale) and $\Gamma_{25'v} \rightarrow X_{1c}$ (blue dashed line, right scale) transitions for Si, (b) the direct (red solid line, left scale) and indirect band gaps (blue dashed line, right scale) of $SrTiO_3$, and (c) the total energy difference ΔE between the wurtzite (wz) and diamond (dia) phases of Si with respect to the reciprocal cutoff values G'_{max} and the angular momentum cutoff L_{max} for the MPB, as well as the number of bands per atom used to construct the exchange potential in the space of the wave functions. For these convergence tests we have employed a 4×4×4 **k**-point set.

maximally 0.02 eV from the corresponding PAW values. Larger discrepancies are observed for the residual systems with larger band gaps. However, these differences are already present on the PBE level. So, we assume that they result from the different basis sets used in the FLAPW and PAW approach. Overall, we find a good agreement between the PBE0 results in both methods.

5.6. Calculation of band structures and density of states

In a DFT calculation with a purely local effective potential the strategy for constructing a band structure is a follows: in a first step the calculation is converged with a moderate **k**-point mesh. Then, the converged density and thus the converged effective potential is used to setup and diagonalize the Hamiltonian along a **k**-point path through the BZ, which finally results in the band structure. In contrast, for hybrid functionals the diagonalization of the Hamiltonian at an arbitrary **k**-point in the BZ would require the knowledge of all occupied states at the points $\mathbf{k}-\mathbf{q}$. These wave functions are, however, unknown in general. Therefore, we employ the Wannier interpolation technique as realized in the Wannier90 code [95] to interpolate the band energies between the **k**-points of the finite mesh.

We give a short introduction to the construction of Wannier functions and then discuss the Wannier interpolation technique. As examples, we finally show the PBE and PBE0 interpolated band structure of Si and the Wannier interpolated PBE0 density of states (DOS) for ZnO.

The Wannier function $w^{\sigma}_{n\mathbf{R}}(\mathbf{r})$ is defined as the Fourier transform of the KS wave function $\phi^{\sigma}_{n\mathbf{k}}$

$$w^{\sigma}_{n\mathbf{R}}(\mathbf{r}) = \sqrt{\frac{\Omega}{8\pi^3}} \int \exp\left(-i\mathbf{k}\mathbf{R}\right) \phi^{\sigma}_{n\mathbf{k}}(\mathbf{r})\, d^3k\,, \tag{5.32}$$

where **R** denotes a lattice vector and Ω is the unit cell volume. While the wave functions $\phi^{\sigma}_{n\mathbf{k}}$ are Bloch functions and represented in reciprocal space, the Wannier functions $w^{\sigma}_{n\mathbf{R}}(\mathbf{r})$ are characterized by the real space lattice vector **R**. Similar to the KS wave functions the Wannier functions form an orthonormal, complete basis

$$\langle w^{\sigma}_{n\mathbf{R}} | w^{\sigma}_{n'\mathbf{R}'} \rangle = \delta_{n,n'}\,\delta_{\mathbf{R},\mathbf{R}'} \tag{5.33}$$

$$\sum_{n\mathbf{R}} w^{\sigma}_{n\mathbf{R}}(\mathbf{r}) w^{\sigma *}_{n\mathbf{R}}(\mathbf{r}') = \delta(\mathbf{r}-\mathbf{r}')\,. \tag{5.34}$$

However, the Wannier functions as defined in Eq. (5.32) are not unique, because the wave functions $\phi^{\sigma}_{n\mathbf{k}}(\mathbf{r})$ are only defined up to an arbitrary phase factor. If $\phi^{\sigma}_{n\mathbf{k}}(\mathbf{r})$ is an eigenfunction of the Hamiltonian, $\exp[i\theta]\phi^{\sigma}_{n\mathbf{k}}(\mathbf{r})$ is also a solution of the Hamiltonian corresponding to the

		This work		PAW[a]		
		PBE	PBE0	PBE	PBE0	Expt.
Si	$\Gamma \to \Gamma$	2.56	3.96	2.57	3.97	3.4[b]
	$\Gamma \to X$	0.71	1.93	0.71	1.93	—
	$\Gamma \to L$	1.54	2.87	1.54	2.88	2.4[b]
C	$\Gamma \to \Gamma$	5.64	7.74	5.59	7.69	7.3[b]
	$\Gamma \to X$	4.79	6.69	4.76	6.66	—
	$\Gamma \to L$	8.58	10.88	8.46	10.77	—
GaAs	$\Gamma \to \Gamma$	0.55	2.02	0.56	2.01	1.63[b]
	$\Gamma \to X$	1.47	2.69	1.46	2.67	2.18[b], 2.01[b]
	$\Gamma \to L$	1.02	2.38	1.02	2.37	1.84[b],1.85[b]
MgO	$\Gamma \to \Gamma$	4.84	7.31	4.75	7.24	7.7[c]
	$\Gamma \to X$	9.15	11.63	9.15	11.67	—
	$\Gamma \to L$	8.01	10.51	7.91	10.38	—
NaCl	$\Gamma \to \Gamma$	5.08	7.13	5.20	7.26	8.5[d]
	$\Gamma \to X$	7.39	9.59	7.60	9.66	—
	$\Gamma \to L$	7.29	9.33	7.32	9.41	—
Ar	$\Gamma \to \Gamma$	8.71	11.15	8.68	11.09	14.15[e]

[a]Reference 90 [b]Reference 91 [c]Reference 92
[d]Reference 93 [e]Reference 94

Table 5.1.: PBE and PBE0 transition energies in eV for Si, C, GaAs, MgO, NaCl, and Ar compared with theoretical and experimental values from the literature. All results are obtained with a 12×12×12 **k**-point set.

same eigenvalue. Furthermore, for degenerate wave functions any unitary transformation within the degenerate subspace leads to another valid set of wave functions. While physical observables do not depend on the choice of the phase, the spatial localization of the Wannier functions substantially varies with the phase. The freedom in the phase of the wave function can be used to localize the Wannier functions $w^{\sigma}_{n\mathbf{R}}(\mathbf{r})$ around the lattice vector $\mathbf{R}$. Therefore, definition (5.32) may be generalized to

$$w^{\sigma}_{n\mathbf{R}}(\mathbf{r}) = \sqrt{\frac{\Omega}{8\pi^3}} \int \exp\left(-i\mathbf{k}\mathbf{R}\right) \left[\sum_m U^{\sigma}_{mn}(\mathbf{k}) \phi^{\sigma}_{m\mathbf{k}}(\mathbf{r}) \right] d^3k \,, \tag{5.35}$$

which explicitly considers the freedom in the phase by the unitary matrix $U^{\sigma}(\mathbf{k})$. The latter has the dimension of the eigenspace of $\phi^{\sigma}_{n\mathbf{k}}$. Following an approach proposed by N. Marzari and D. Vanderbilt [81], the unitary transformations $U^{\sigma}(\mathbf{k})$ are determined such that the spread

$$S = \sum_n \left[\langle w^{\sigma}_{n\mathbf{0}} | r^2 | w^{\sigma}_{n\mathbf{0}} \rangle - \langle w^{\sigma}_{n\mathbf{0}} | r | w^{\sigma}_{n\mathbf{0}} \rangle^2 \right] \tag{5.36}$$

of the Wannier functions is minimized. The sum in Eq. (5.36) runs over all Wannier functions n. In this way, maximally localized Wannier functions (MLWFs) are obtained. The algorithm for minimizing the spread S by Marzari and Vanderbilt [81] is only applicable to isolated groups of bands, but it has been extended to entangled energy bands by Souza *et al.* [82].

Due to their spatial localization, the MLWFs are an efficient basis for an interpolation of the band structure. In a first step, the Hamiltonian H is expressed in the MLWFs

$$H^{\sigma}_{nm}(\mathbf{R}) = \langle w^{\sigma}_{n\mathbf{0}} | H | w^{\sigma}_{m\mathbf{R}} \rangle \,. \tag{5.37}$$

We note that one Wannier function can be chosen to reside at $\mathbf{0}$ without loss of generality. In order to interpolate onto an arbitrary $\mathbf{k}$-point, we perform the inverse Fourier transform

$$H^{\sigma}_{nm}(\mathbf{k}) = \sum_{\mathbf{R}} \exp\left(i\mathbf{k}\mathbf{R}\right) H^{\sigma}_{nm}(\mathbf{R}) \,. \tag{5.38}$$

Diagonalization of $H^{\sigma}_{nm}(\mathbf{k})$ then leads to the band energies at $\mathbf{k}$. Due to the exponential decay of the MLWFs, which has been confirmed numerically for several materials [96], the matrix elements $H^{\sigma}_{nm}(\mathbf{R})$ exhibit this exponential decay with $|\mathbf{R}|$, as well. This permits to truncate the sum over $\mathbf{R}$ in Eq. (5.38) without loosing (much) accuracy.

As an example, we show in Fig. 5.6 the PBE and PBE0 interpolated band structure for Si. We have generated 8 sp^3-like MLWFs, four for the valence and four for the lowest conduction bands. To demonstrate the accuracy of the Wannier interpolation, we compare in Fig. 5.6(a) the PBE band structure of Si obtained either by explicitly diagonalizing the PBE Hamilto-

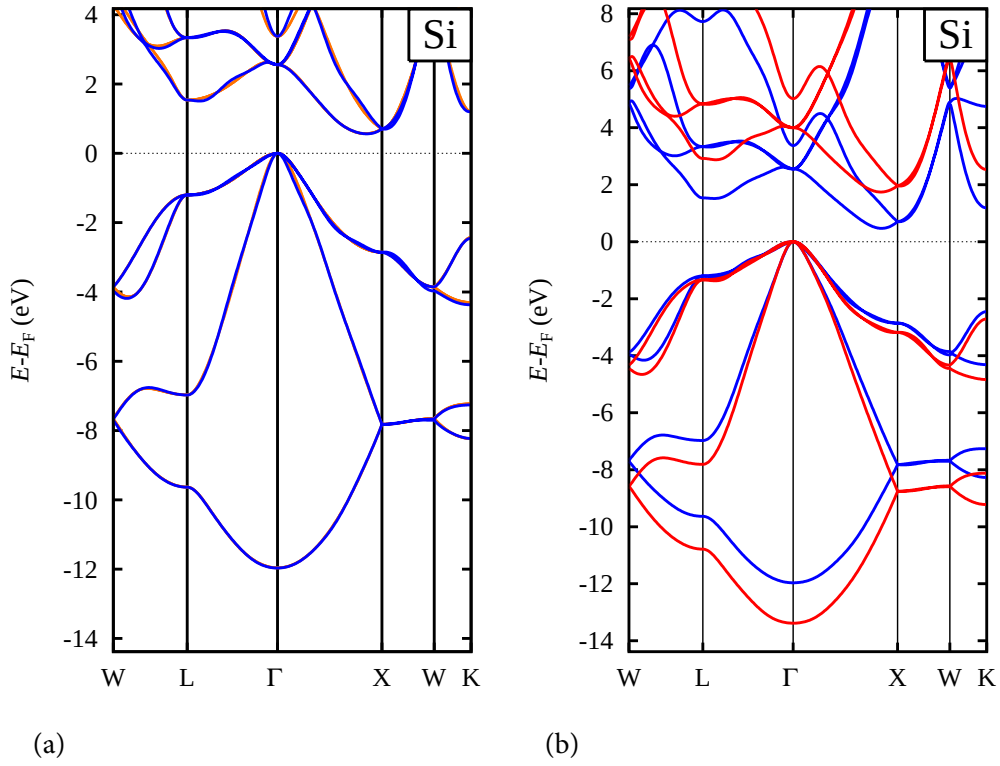

Figure 5.6.: (a) Comparison of routinely generated PBE (orange) and Wannier interpolated (blue) band structure for Si. (b) Comparison of PBE (blue) and the Wannier-interpolated PBE0 band structure (red) for Si.

nian along the **k**-point path in the BZ or by employing the Wannier interpolation technique. Only minor differences between both approaches are observable. Hence, we expect a similar accuracy for the interpolated PBE0 band structure. A comparison of PBE and PBE0 band structure [s. Fig. 5.6(b)] reveals that the PBE0 hybrid functional opens the gap from 0.47 eV in PBE to 1.74 eV in PBE0. In comparison, the experimental value amounts to 1.17 eV [91]. The conduction band minimum is for both functionals close to the X point. Moreover, the PBE0 hybrid increases the band width of the occupied states from 11.98 eV for the PBE functional to 13.39 eV. The experimentally measured band width of Si is 12.4 ± 0.6 eV [97]. Apart from the upward shift, the dispersion of the lowest conduction bands in PBE and PBE0 are very similar (nearly indistinguishable).

The Wannier interpolation technique can be used to calculate the DOS, as well. The DOS at energy E measures the number of states per energy

$$D(E) = \sum_{\sigma} \sum_{n} \frac{1}{V_{\mathrm{BZ}}} \int_{\mathrm{BZ}} \delta(E - \epsilon^{\sigma}_{n\mathbf{k}})\, d^3k\,. \tag{5.39}$$

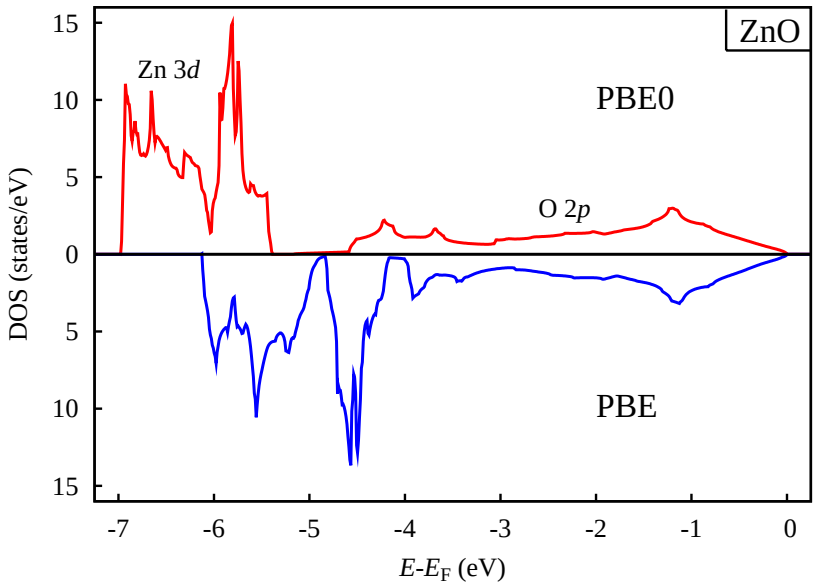

Figure 5.7.: Comparison of PBE (blue) and PBE0 (red) density of states (DOS) for ZnO.

The δ-function is usually smeared out by a Gaussian distribution function, and the BZ integral becomes a sum over a finite number of **k** points. For a highly resolved DOS a large number of **k**-points is necessary, which in turn leads to a large computational cost in the case of the hybrid functionals. However, the MLWFs permit to interpolate the eigenvalues $\epsilon^{\sigma}_{n\mathbf{k}}$ accurately from a coarse to a fine **k**-point mesh. Hence, we can calculate a highly resolved DOS for hybrid functionals at a moderate computational expense.

We use this approach to calculate the DOS of the II-VI semiconductor ZnO in its wurtzite structure. Using five MLWFs for the Zn 3*d* and three MLWFs for O 2*p* states the eigenvalues $\epsilon^{\sigma}_{n\mathbf{k}}$ are interpolated from a 4×4×4 to a dense 125×125×125 **k**-point mesh. The eigenvalues on the dense mesh are then used to evaluate Eq. (5.39). The corresponding DOS is shown in Fig. 5.7. In the case of the PBE functional the Zn 3*d* states hybridize strongly with the O 2*p* states. The PBE0 functional, on the contrary, binds the Zn 3*d* more strongly. The center of gravity of the *d* bands changes from 5.1 eV in PBE to 6.3 eV in PBE0, whereas the experimental value is 7.8 eV [98]. Due to the stronger binding of the Zn 3*d* states, the *d*-*p* hybridization becomes less pronounced and the O *p* valence band width is increased from 4.2 eV in PBE to 5.2 eV in PBE0, which is in excellent agreement with the experimental value [98]. Concomitantly, the band gap opens from 0.94 eV to 3.32 eV. The wrong *d* band position relative to the *p* states is commonly attributed to the unphysical self-interaction error inherent in

the local-density approximation (LDA) and the generalized gradient approximation (GGA) (cf. Sec. 3.2), which is larger for localized than delocalized electrons. The admixture of HF exchange into the hybrid functionals partly cancels this error and leads for ZnO to a lowering of the relative d band position. We note that we also observe a stronger binding of the d electrons in Ge and GaAs.

5.7. EuO: a case study

EuO is a ferromagnetic semiconductor with a band gap of 0.95 eV in the limit of 0 K [99], which crystallizes in the rock-salt structure. It is of major interest in the field of spintronics due to its ability to generate a highly spin-polarized current by combining non-magnetic electrodes with EuO in-between as a magnetic tunnel barrier. The spin-dependent tunnel barrier of EuO acts as a spin-filter, since the tunnel current depends exponentially on the respective barrier height [100, 101]. EuO exhibits a remarkable spectrum of magnetic properties which are induced by carrier doping, including colossal magnetoresistance ($\Delta\rho/\rho \approx 10^6$) [102], a metal-insulator transition ($\Delta\rho/\rho \approx 10^{13}$) [103, 104], spin polarized carriers ($> 90\%$) [105, 106], and an enhancement of the Curie temperature (T_c) [107].

From a theoretical point of view, however, the description of EuO from first-principles calculations constitutes a challenge. LDA and GGA functionals predict ferromagnetic EuO to be metallic. This is commonly attributed to the self-interaction error of LDA and GGA, which becomes severe for the strongly localized f electrons of Eu. The LDA+U approach represents a practical solution by adding on-site Coulomb repulsion through the parameter U. If the parameter U is chosen properly, the correct electronic ground state of EuO is obtained [108, 109]. Actually, Ingle *et al.* [109] applied two different U, one on the O $2p$ and one on the Eu $4f$ state to describe EuO reasonably well. However, the LDA+U approach is unsatisfactory, because the parameter U is not universal. It strongly depends on the material and the material property under consideration [110].[4] In the following, we will demonstrate that the PBE0 hybrid functional, which does not contain an adjustable parameter, leads to a consistent description of EuO with respect to its structural, electronic, and magnetic properties.

We have determined the numerical parameters of the LAPW basis for EuO such that the difference in the total energy calculated for the experimental and a 1% larger lattice constant is converged up to 1 meV. This requires a reciprocal cutoff of $G_{\max} = 4.3\,a_0^{-1}$, an angular momentum of $l_{\max} = 8$, and the addition of one local orbital for each atom and each angular momentum l from $l = 0, \ldots, 3$. The energy parameters of these local orbitals have been

[4] We note that methods have been developed to calculate U from first principles [111, 112].

atom	$l_{\max}$	$L_{\max}$	S_a
Eu	8	6	2.60
O	8	6	2.16
	$G_{\max}$	$4.3\,\mathrm{a}_0^{-1}$	
	$G'_{\max}$	$3.5\,\mathrm{a}_0^{-1}$	

Table 5.2.: Numerical parameters of the LAPW and mixed product basis for EuO.

determined according to Eq. (4.18). While the Eu $4f$ states are treated explicitly by the LAPW basis, the semi-core $5s$ and $5p$ states of Eu are described by local orbitals. In this case, the energy parameters of the local orbital lie at the corresponding energy of the semi-core states. The MPB has been converged in a similar manner. The resulting parameters are summarized in Table 5.2.

In order to find the optimal lattice constant of ferromagnetic rock-salt EuO, we calculate the total energy for 9 different lattice constants in the vicinity of the experimental lattice constant. The parabolic shape of the total energy as function of the lattice parameter a is shown in Fig. 5.8. By a fit to a Murnaghan equation of state [113]

$$E(V) = \frac{B_0 V}{B_0'(B_0'-1)}\left[B_0'\left(1-\frac{V_0}{V}\right)+\left(\frac{V_0}{V}\right)^{B_0'}-1\right]+E(V_0) \tag{5.40}$$

we determine the equilibrium unit-cell volume V_0, which is related to the equilibrium lattice constant a_0 by $a_0 = \sqrt[3]{4V_0}$, the equilibrium bulk modulus B_0 ($B_0 = V_0\partial^2 E/\partial V^2|_{V=V_0}$) and its derivative B_0'. While the PBE functional predicts an equilibrium lattice constant of $9.571\,\mathrm{a}_0$, the PBE0 hybrid gives a larger lattice constant of $9.678\,\mathrm{a}_0$. In comparison with the experimental lattice constant at room temperature of $9.721\,\mathrm{a}_0$ [114], PBE and PBE0 functional tend to over-bind. However, the thermal expansion, which leads to an increase of the experimental lattice constant at room temperature, is not taken into account in the calculations. A lattice constant of $9.689\,\mathrm{a}_0$ is observed at $T = 4.2\,\mathrm{K}$ [114]. In comparison with this value, the PBE still underestimates the experimental value by 1.2%. The optimized PBE0 lattice constant deviates from the experimental value at $T = 4.2\,\mathrm{K}$ by only 1.1‰. It is an order of magnitude more accurate than the PBE result. The bulk modulus B_0, which corresponds to the curvature of the energy-versus-volume curve at the relaxed volume V_0, amounts to 94.89 GPa for the PBE and 96.46 GPa for the PBE0 functional. Both values lie within the error bar of the experimentally determined value of $91 \pm 8\,\mathrm{GPa}$ [115]. We note that the experiment was performed at 77K.

In Fig. 5.9 the spin-resolved DOS for ferromagnetic EuO is shown for the PBE and PBE0 functionals. While EuO is metallic in the PBE, the PBE0 functional opens a gap between the

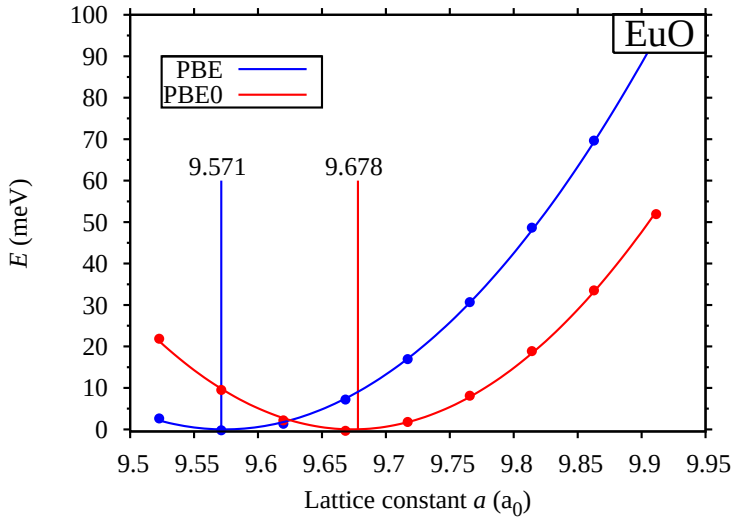

Figure 5.8.: PBE and PBE0 total energy E as a function of the lattice constant a for ferromagnetic EuO. For both curves the energy zero has been chosen to lie at the minimum of the curve.

spin-up Eu $4f$ states at the Fermi energy and the spin-up states of Eu $5d$ and $6s$ character. The gap amounts to 0.85 eV. Experimentally, a band gap of 1.12 eV at room temperature [99] and of 0.95 eV in the limit $T = 0$K [116] is observed. In analogy to the lattice constant, the theoretical gap is in much better agreement with the experimental result in the zero Kelvin limit. Apart from the opening of the band gap, the different energetic position of the unoccupied spin-down Eu $4f$ states becomes evident. While spin-up and spin-down Eu $4f$ states are split by about 4 eV in the PBE, they are separated by 11 eV in the PBE0 approach. Moreover, the bottom of the conduction bands is split by 1.10 eV. It is this quantity which determines the efficiency of EuO as a spin filter. Experimentally, values of 0.54 eV [100] and 0.60 eV [106] are reported, respectively. The opening of the band gap and, thus, the total filling of the spin-up Eu $4f$ states gives rise to an increase of the magnetic moment from 6.77 μ_B for the PBE to 6.90 μ_B for the PBE0 functional.

In order to describe the magnetic order of EuO, we apply a classical Heisenberg Hamiltonian

$$H = -\frac{1}{2}\sum_{i\neq j} J_{ij}\mathbf{e}_i\mathbf{e}_j\,, \tag{5.41}$$

where J_{ij} describes the exchange coupling between two Eu atoms at the sites i and j and $\mathbf{e}_i$ is a unit vector pointing in the direction of the magnetic moment at site i. Due to the definition of the Heisenberg Hamiltonian with a minus sign in Eq. (5.41) a positive exchange constant

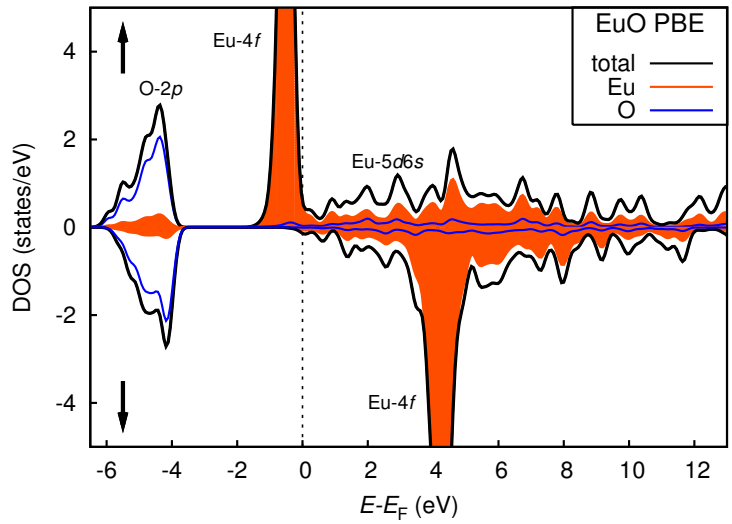

(a)

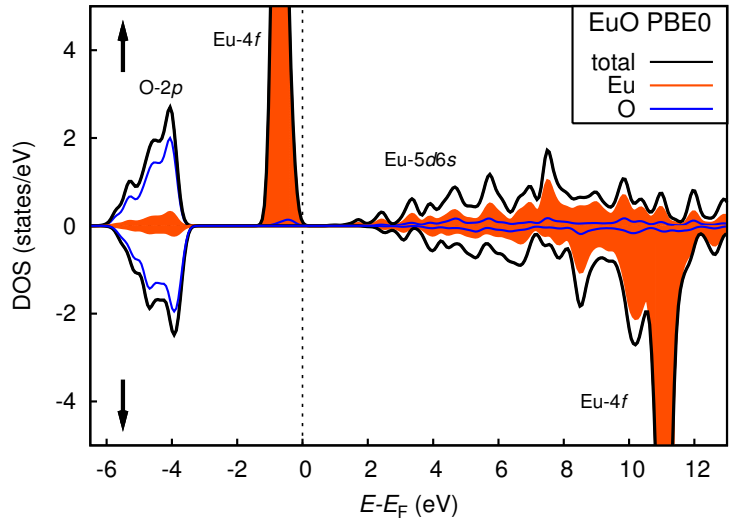

(b)

Figure 5.9.: Density of states (DOS) of ferromagnetic EuO for (a) the PBE and (b) the PBE0 functional. While the total DOS is shown in black, the partial DOS of Eu and O is drawn in red and blue, respectively.

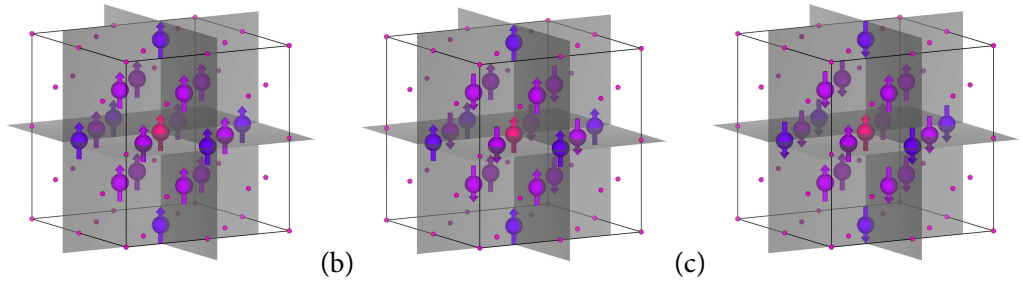

Figure 5.10.: Nearest and next-nearest neighbors of a representative Eu atom (colored in red) for (a) the FM, (b) the AFM-I, and (c) the AFM-II configuration. The nearest and next-nearest neighbors are shown in pink and blue, respectively. All remaining Eu atoms are indicated by the small circles. For simplicity, the oxygen atoms are not drawn.

corresponds to ferromagnetic coupling. We restrict the coupling to nearest neighbor (nn) and next-nearest neighbor (nnn) interactions

$$H = -\frac{1}{2}\sum_i \mathbf{e}_i \left[J_1 \sum_{j\in \mathrm{nn}} \mathbf{e}_j + J_2 \sum_{j\in \mathrm{nnn}} \mathbf{e}_j \right]. \tag{5.42}$$

In order to extract the coupling constants J_1 and J_2 from a DFT calculation we calculate EuO in its different magnetic configurations. The rock-salt structure of EuO allows the Eu atoms to couple in four different collinear magnetic configurations [117]: simple ferromagnetic (FM) ordering, antiferromagnetic (AFM) ordering of type AFM-I, AFM-II, and AFM-III. In the AFM-I configuration the Eu atoms along the [001] direction are coupled antiferromagnetically. The AFM-II type structure corresponds to an antiferromagnetic coupling in the [111] direction, and the AFM-III exhibits two layers of Eu atoms with alternating spins in the [001] direction. We restrict ourselves here to the AFM-I, AFM-II, and FM configuration, as they are sufficient for a determination of the exchange coupling constants J_1 and J_2. According to the Heisenberg model [s. Eq. (5.42)], the energy per Eu atom for the FM spin configuration amounts to

$$E_{\mathrm{FM}} = -\frac{1}{2}[12J_1 + 6J_2] = -6J_1 - 3J_2,$$

because each Eu atom is surrounded by 12 nn and 6 nnn with parallel spin configuration [cf. Fig. 5.10]. In the case of the AFM-I structure each Eu atom has 4 nn which are coupled ferromagnetically, while 8 nn exhibit a antiferromagnetic spin alignment. The 6 nnn are all

EuO	PBE	PBE0	Expt.
J_1 (meV)	4.94	2.61	
J_2 (meV)	4.54	0.64	
T_c^{MFA} (K)	335	136	69[a]
T_c^{RPA} (K)	272	105	

[a] Reference 118

Table 5.3.: Nearest and next-nearest neighbor exchange coupling constants J_1 and J_2 calculated with the PBE and PBE0 functional as well as the resulting Curie temperature in the mean-field approximation (MFA) T_c^{MFA} and the random-phase approximation (RPA) T_c^{RPA}.

coupled ferromagnetically, so that the energy per Eu atom for the AFM-I is given by

$$E_{\mathrm{AFM-I}} = -\frac{1}{2}(-4J_1 + 6J_2) = 2J_1 - 3J_2\,. \tag{5.43}$$

In the AFM-II phase the contribution of the nn mutually cancels out as each Eu atom is surrounded by 6 Eu atoms with parallel and 6 atoms with antiparallel spin. As the nnn are all aligned antiferromagnetically, we obtain

$$E_{\mathrm{AFM-II}} = -\frac{1}{2}(-6J_2) = 3J_2 \tag{5.44}$$

for the energy per Eu. The energy difference between the AFM-I and FM configuration allows to calculate the nn coupling constant

$$J_1 = (E_{\mathrm{AFM-I}} - E_{\mathrm{FM}})/8\,. \tag{5.45}$$

Combination of Eq. (5.45) with the energy difference between AFM-II and FM results in J_2

$$J_2 = (E_{\mathrm{AFM-II}} - E_{\mathrm{FM}})/6 - (E_{\mathrm{AFM-I}} - E_{\mathrm{FM}})/8\,. \tag{5.46}$$

In order to avoid numerical inaccuracies, the energy difference between AFM and FM configuration is computed in the corresponding AFM unit cell. Moreover, we apply the previously optimized PBE and PBE0 lattice constants.

The exchange coupling constants extracted in this way are shown in Table 5.3. As the FM configuration turns out to be energetically the most favorable configuration, the nn as well as nnn coupling constants are positive. This is in accordance with the ferromagnetic ordering observed in experiment below a Curie temperature of 69 K [118]. At least for the PBE0

functional the nnn exchange coupling constant J_2 is significantly smaller than J_1, which justifies to disregard contributions from neighbors further afar. The mean-field approximation (MFA) [119, 120], which neglects the fluctuation of the spins around its thermal average, allows to estimate the Curie temperature from the exchange constants J_1 and J_2 by

$$T_c^{\mathrm{MFA}} = \frac{1}{3k_{\mathrm{B}}}(12J_1 + 6J_2)\,, \tag{5.47}$$

where k_{B} denotes the Boltzmann constant. It is known that the MFA tends to overestimate the experimental Curie temperature [121]. Indeed, the PBE and PBE0 exchange constants J_1 and J_2 yield a too large T_c in comparison with experiment (s. Table 5.3). Nevertheless, the deviation between MFA and experimental T_c is drastically reduced by the PBE0 functional. A further improvement can be achieved by employing the random-phase approximation (RPA) instead of the MFA. The RPA was introduced by Tyablikov [122] for spin 1/2 and generalized by Callen [123] to Bravais lattices with general spin quantum number. The Curie temperature in the RPA is finally given by

$$T_c^{\mathrm{RPA}} = \frac{1}{3k_{\mathrm{B}}}\left(\sum_{\mathbf{q}} \frac{1}{J(\mathbf{0}) - J(\mathbf{q})}\right)^{-1}\,, \tag{5.48}$$

where $J(\mathbf{q})$ is the Fourier transform of the exchange coupling constants

$$J(\mathbf{q}) = \sum_{j \neq i} J_{0j} \exp\left[i\mathbf{q}\mathbf{R}_j\right] = J_1 \sum_{j \in \mathrm{nn}} \exp[i\mathbf{q}\mathbf{R}_j] + J_2 \sum_{j \in \mathrm{nnn}} \exp[i\mathbf{q}\mathbf{R}_j]\,. \tag{5.49}$$

For the fcc lattice of Eu atoms, Eq. (5.49) becomes

$$\begin{aligned} J(\mathbf{q}) \quad = \quad & 4J_1 \left\{ \cos(q_x \frac{a}{2}) \left[\cos(q_z \frac{a}{2}) + \cos(q_y \frac{a}{2}) \right] + \cos(q_z \frac{a}{2}) \cos(q_y \frac{a}{2}) \right\} \\ & + 2J_2 \left\{ \cos(q_x a) + \cos(q_y a) + \cos(q_z a) \right\}\,. \end{aligned} \tag{5.50}$$

As shown in Table 5.3, the RPA leads to a reduction of the Curie temperature in comparison with the MFA. For the PBE0 functional we obtain a T_c of 105 K in the RPA, which still overestimates the experimental value of 69 K.

The exchange coupling constants, moreover, allow to calculate the energy dispersion of spin waves. A spin wave is a propagating collective excitation of spins, which can be characterized by its frequency ω and wave vector $\mathbf{q}$. In a classical Heisenberg model both quantities are connected by the dispersion relation

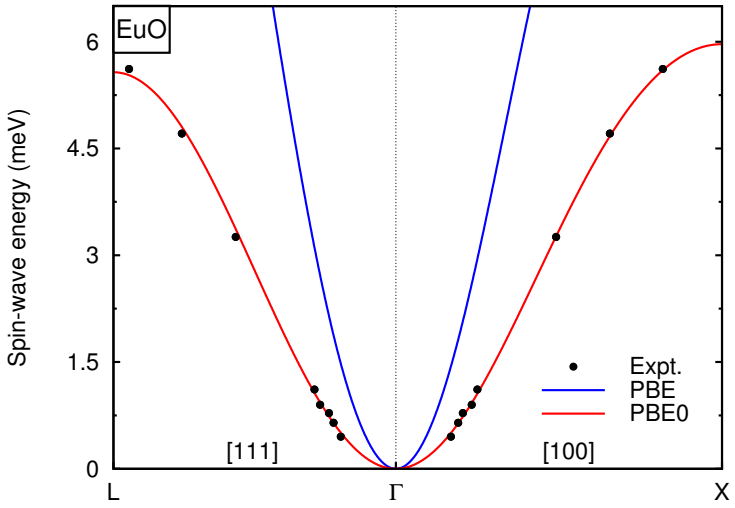

Figure 5.11.: PBE and PBE0 spin-wave energies are compared with experiment in the [111] and [100] direction. The experimental data points are taken from Ref. 118.

$$\omega(\mathbf{q}) = \frac{1}{M}[J(\mathbf{0}) - J(\mathbf{q})]\,, \tag{5.51}$$

where M corresponds to the magnetization of the Eu atoms ($M = 7$) and $J(\mathbf{q})$ is the Fourier transform of the coupling constants as defined above. Insertion of Eq. (5.50) into (5.51) enables to calculate the spin-wave dispersion for any $\mathbf{q}$. In Fig. 5.11 we compare the PBE and PBE0 spin-wave dispersions with experimental data along the directions [100] and [111]. The experimental values are measured by inelastic neutron scattering [118]. For small $\mathbf{q}$ around Γ the spin-wave dispersion is proportional to q^2. The proportionality factor is the spin-wave stiffness D, which is given by $D = (J_1 + J_2)a^2/M$. As already observable from Fig. 5.11 the PBE functional substantially overestimates the spin-wave stiffness $D^{\mathrm{PBE}} = 124.1\,\mathrm{meV\,a_0^2}$ with respect to the experiment $D^{\mathrm{exp}} = 38.6\,\mathrm{meV\,a_0^2}$ [118]. The PBE0 functional slightly overestimates the experimental stiffness $D^{\mathrm{PBE0}} = 43.5\,\mathrm{meV\,a_0^2}$, but reproduces the spin-wave dispersion in the [100] and [111] direction quite accurately. We note the small energy scale from 0 up to 6 meV.

In conclusion, the PBE0 functional constitutes a definite improvement over the PBE functional for the first-principles description of the rare-earth oxide EuO. The structural, electronic, and magnetic properties are predicted in good agreement with experiment.

5.8. Summary

A numerical scheme for the calculation of the non-local exchange potential, which is the central ingredient of hybrid functionals, within the all-electron FLAPW method has been introduced. Our algorithm relies on the auxiliary mixed product basis (MPB) for the representation of wave-function products. In this way, the six-dimensional integrals of the non-local potential transform into vector-matrix-vector products. The matrix that corresponds to the representation of the Coulomb interaction in the MPB can be made sparse by a unitary transformation of the basis leading to a reduction of the computational cost for the matrix-vector product. The algorithm is accelerated additionally (a) by a redefinition of the MPB in the case of inversion symmetry such that the Coulomb matrix and the vectors become real-valued quantities, (b) by using spatial and time-reversal symmetries. The latter allows to identify those exchange matrix elements that are non-zero and must be calculated explicitly and, furthermore, to restrict the $\mathbf{q}$-point summation arising from the sum over all occupied states to an irreducible wedge of the BZ.

The aforementioned techniques are used to accelerate the calculation of the non-local exchange potential. Self-consistency of a hybrid functional calculation, though, requires to calculate the potential in each iteration of the self-consistent field cycle until self-consistency is achieved. We have shown that, while a direct iteration scheme requires many steps to converge, a nested self-consistent field cycle consisting of an outer density-matrix and an inner density-only iteration loop accelerates the convergence of the self-consistent field cycle considerably.

For the PBE0 hybrid functional and the two materials Si and $SrTiO_3$ we have demonstrated that PBE0 transition and total energies are easily converged with respect to the numerical parameters of the MPB. Hence, the MPB provides a small but accurate all-electron basis for the construction of the exchange potential. Moreover, we have reported PBE0 transition energies for a set of prototype semiconductors and insulators. In comparison with PBE they lie much closer to the experimental values. Furthermore, they are in favorable agreement with recent PBE0 calculations within the PAW method [30].

The non-locality of the exchange potential hampers the calculation of a band structure or a density of states (DOS). In order to circumvent this, we have employed the Wannier interpolation technique. It allows to construct an accurate band structure and DOS at a reasonable numerical cost. We have demonstrated this for the PBE0 band structure of Si and the DOS of ZnO. The band structure of Si shows that the PBE0 functional opens the band gap, but leaves the dispersion of the bands nearly unchanged apart from an increase of the valence band width. For ZnO the reduced self-interaction of the PBE0 functional gives rise to a stronger

binding of the Zn d states. As a consequence, their position comes closer to the experimental value. The stronger binding, in turn, entails a reduced hybridization of the Zn $3d$ states with the O $2p$ states, such that the band width of the O p states is increased.

Moreover, we have applied the PBE0 functional to EuO. In comparison with the PBE functional, the latter provides a significant improvement with respect to the structural, electronic, and magnetic properties of EuO. The PBE0 equilibrium lattice constant deviates by only 1‰ from the experimental one at $T = 4.2\,\mathrm{K}$. Concerning the electronic properties, EuO is correctly predicted to be a ferromagnetic semiconductor with an indirect band gap of 0.85 eV, while the experimental gap amounts to 0.95 eV in the limit of 0 K. Application of a classical Heisenberg model with nearest and next-nearest-neighbors coupling gives access to the magnetic properties. In contrast to the PBE functional, the PBE0 spin-wave dispersion agrees qualitatively and even quantitatively with experiment. The Curie temperature of ferromagnetic EuO is overestimated by both functionals in the mean-field as well as the random-phase approximation. Yet, the PBE0 Curie temperature is in significant better agreement with experiment.

We note that the numerical scheme is not restricted to the PBE0 hybrid functional. It can be used to implement any other hybrid functional with an unscreened non-local exchange potential, for example the B3LYP functional [62]. Moreover, the numerical procedure can be generalized to also enable the calculation of a screened non-local exchange potential, that is, for example, employed in the HSE functional [124, 125]. The Coulomb matrix must be simply replaced by the matrix of the screened Coulomb interaction [126]. Furthermore, the matrix elements of the non-local exchange potential are an essential ingredient in the EXX-OEP formalism, in which a local potential is constructed from the non-local exact exchange energy. The EXX-OEP method will be discussed in the next chapter.

6. Exact exchange within the optimized effective potential method

In the previous chapter, hybrid functionals combining a fraction of non-local exact exchange with local approximations for the remaining exchange-correlation (xc) energy functional were discussed. They are usually applied in the generalized Kohn-Sham (gKS) scheme, where the electrons experience a local as well as a non-local potential. The Kohn-Sham (KS) system, however, requires by construction a purely local potential. Therefore, the treatment of hybrid functionals as described in the previous chapter is outside the realm of KS density-functional theory (DFT).

The construction of a local xc potential from any orbital-dependent and maybe eigenvalue-dependent approximation to the xc energy will be described in the present chapter for the example of the orbital-dependent exact exchange energy. The optimized effective potential (OEP) method, which is sometimes called optimized potential method (OPM) in the literature, forms the general theoretical framework for the construction of a local potential from an orbital- and (or) eigenvalue-dependent approximation to the xc energy.

The chapter is organized as follows. After a theoretical introduction into the OEP method we discuss the numerical implementation of the exact exchange OEP (EXX-OEP) approach within the full-potential linearized augmented-plane-wave (FLAPW) method. It employs a specifically adjusted mixed product basis (MPB) for the representation of the local exchange potential. For the case of diamond we carefully analyze the conditions and requirements on the LAPW and mixed product basis to obtain stable and physical local EXX potentials. The LAPW basis must be converged with respect to the MPB. We compare our all-electron full potential KS transition energies for C, Si, SiC, Ge, GaAs, solid Ne and Ar with pseudopotential plane-wave and experimental results from the literature and find a favorable agreement. For the III-V nitrides and rock-salt ScN we analyze the effect of the derivative discontinuity of the EXX functional on the theoretical fundamental band gap. In order to improve the convergence of the EXX potential with respect to the LAPW basis set size, we propose and explore a finite basis correction (FBC) for the response functions of density and KS wave-

function, which are substantial ingredients of the EXX-OEP equation. We then apply the EXX functional to the cubic perovskites $CaTiO_3$, $SrTiO_3$, and $BaTiO_3$ as well as the antiferromagnetic transition metal oxides MnO, FeO, and CoO. Finally, we present a generalization of the EXX-OEP approach to metals and report on calculations for Na, Al, and Cu.

6.1. Optimized effective potential method

The optimized effective potential (OEP) method is a quite general approach, which allows to construct a local, multiplicative xc potential from any orbital- and (or) eigenvalue-dependent xc functional. In order to derive the basic equations for the OEP approach, we go back to the definition of the xc potential of KS DFT as the functional derivative of the xc energy with respect to the density [cf. Eq. (2.28) for the paramagnetic and Eq. (2.41) for the spin-polarized case]

$$V_{\mathrm{xc}}^{\sigma}(\mathbf{r}) = \frac{\delta E_{\mathrm{xc}}}{\delta n^{\sigma}(\mathbf{r})} \,. \tag{6.1}$$

In the case of the local-density approximation (LDA) or the generalized gradient approximation (GGA), where the xc energy depends locally on the spin densities and for the GGA also on their gradients, the functional derivative translates to a derivative of a function and is evaluated in a straightforward way. However, an orbital- and (or) eigenvalue-dependent functional is only an indirect functional of the spin densities, as the KS orbitals $\phi_{n\mathbf{k}}^{\sigma}(\mathbf{r})$ and the KS eigenvalues $\epsilon_{n\mathbf{k}}^{\sigma}$ are functionals of the effective potential $V_{\mathrm{eff}}^{\sigma}(\mathbf{r})$ through the KS equation and the effective potential $V_{\mathrm{eff}}^{\sigma}(\mathbf{r})$ is a functional of the spin density $n^{\sigma}(\mathbf{r})$ through the Hohenberg and Kohn theorem. This interdependence of the KS orbitals and eigenvalues on the density via the effective potential is exploited to evaluate the functional derivative by means of the chain rule for functional derivatives [33, 34]

$$V_{\mathrm{xc}}^{\sigma}(\mathbf{r}) = \sum_{n\mathbf{k}} \int \left[\left(\int \frac{\delta E_{\mathrm{xc}}}{\delta \phi_{n\mathbf{k}}^{\sigma}(\mathbf{r}')} \frac{\delta \phi_{n\mathbf{k}}^{\sigma}(\mathbf{r}')}{\delta V_{\mathrm{eff}}^{\sigma}(\mathbf{r}'')} \, d^3r' + \mathrm{c.c.} \right) + \frac{\delta E_{\mathrm{xc}}}{\delta \epsilon_{n\mathbf{k}}^{\sigma}} \frac{\delta \epsilon_{n\mathbf{k}}^{\sigma}}{\delta V_{\mathrm{eff}}^{\sigma}(\mathbf{r}'')} \right] \frac{\delta V_{\mathrm{eff}}^{\sigma}(\mathbf{r}'')}{\delta n^{\sigma}(\mathbf{r})} \, d^3r'' \,. \tag{6.2}$$

As the KS orbitals $\phi_{n\mathbf{k}}^{\sigma}(\mathbf{r})$ are in general complex, we can either differentiate with respect to the real and imaginary part of $\phi_{n\mathbf{k}}^{\sigma}(\mathbf{r})$ or with respect to $\phi_{n\mathbf{k}}^{\sigma}(\mathbf{r})$ and its complex conjungate (c.c.) $\phi_{n\mathbf{k}}^{\sigma *}(\mathbf{r})$. Here, we performed the differentiation with respect to $\phi_{n\mathbf{k}}^{\sigma}(\mathbf{r})$ and its complex conjungate. The sum in Eq. (6.2) runs over all KS states present in a given approximate functional E_{xc}. Moreover, we have exploited that the wave-function response $\delta \phi_{n\mathbf{k}}^{\sigma'}(\mathbf{r}')/\delta V_{\mathrm{eff}}^{\sigma}(\mathbf{r}'')$, the eigenvalue response $\delta \epsilon_{n\mathbf{k}}^{\sigma'}/\delta V_{\mathrm{eff}}^{\sigma}(\mathbf{r}'')$, and the inverse single-particle response function $\delta V_{\mathrm{eff}}^{\sigma'}(\mathbf{r}'')/\delta n^{\sigma}(\mathbf{r})$ are diagonal in spin space for semiconductors and insulators. An extension of the formalism to metals is discussed in section 6.10.

The linear response of the wave function $\phi^\sigma_{n\mathbf{k}}(\mathbf{r}')$ due to a change in the effective potential at $\mathbf{r}''$ is exactly accessible in first-order perturbation theory and given by

$$\frac{\delta\phi^\sigma_{n\mathbf{k}}(\mathbf{r}')}{\delta V^\sigma_{\text{eff}}(\mathbf{r}'')} = \sum_{n'\neq n} \frac{\phi^{\sigma*}_{n'\mathbf{k}}(\mathbf{r}'')\phi^\sigma_{n\mathbf{k}}(\mathbf{r}'')}{\epsilon^\sigma_{n\mathbf{k}} - \epsilon^\sigma_{n'\mathbf{k}}} \phi^\sigma_{n'\mathbf{k}}(\mathbf{r}') \,. \tag{6.3}$$

With this, the single-particle spin-density response function $\chi^\sigma_{\text{s}}(\mathbf{r},\mathbf{r}') = \delta n^\sigma(\mathbf{r})/\delta V^\sigma_{\text{eff}}(\mathbf{r}')$ becomes

$$\chi^\sigma_{\text{s}}(\mathbf{r},\mathbf{r}') = \sum_{n\mathbf{k}}^{\text{occ.}} \sum_{n'\neq n} \frac{\phi^{\sigma*}_{n\mathbf{k}}(\mathbf{r})\phi^\sigma_{n'\mathbf{k}}(\mathbf{r})\phi^{\sigma*}_{n'\mathbf{k}}(\mathbf{r}')\phi^\sigma_{n\mathbf{k}}(\mathbf{r}')}{\epsilon^\sigma_{n\mathbf{k}} - \epsilon^\sigma_{n'\mathbf{k}}} + \text{c.c.} \,. \tag{6.4}$$

The combinations of occupied (occ.) states n with occupied states n' cancel mutually in Eq. (6.4), so that the sum over n' can be restricted to the unoccupied (unocc.) states. Additionally, we can exploit time-reversal symmetry $[\phi^{\sigma*}_{n(-\mathbf{k})}(\mathbf{r}) = \phi^\sigma_{n\mathbf{k}}(\mathbf{r})]$ and, thus, Eq. (6.4) turns into

$$\chi^\sigma_{\text{s}}(\mathbf{r},\mathbf{r}') = 2\sum_{n\mathbf{k}}^{\text{occ.}} \sum_{n'}^{\text{unocc.}} \frac{\phi^{\sigma*}_{n\mathbf{k}}(\mathbf{r})\phi^\sigma_{n'\mathbf{k}}(\mathbf{r})\phi^{\sigma*}_{n'\mathbf{k}}(\mathbf{r}')\phi^\sigma_{n\mathbf{k}}(\mathbf{r}')}{\epsilon^\sigma_{n\mathbf{k}} - \epsilon^\sigma_{n'\mathbf{k}}} \,. \tag{6.5}$$

Multiplication of Eq. (6.2) with the single-particle spin-density response function $\chi^\sigma_{\text{s}}(\mathbf{r},\mathbf{r}')$, integration, and use of the symmetry $\chi^\sigma_{\text{s}}(\mathbf{r},\mathbf{r}') = \chi^\sigma_{\text{s}}(\mathbf{r}',\mathbf{r})$ result in an integral equation for the xc potential

$$\int \chi^\sigma_{\text{s}}(\mathbf{r},\mathbf{r}') V^\sigma_{\text{xc}}(\mathbf{r}')\, d^3r' = \sum_{n\mathbf{k}} \left[\left(\int \frac{\delta E_{\text{xc}}}{\delta\phi^\sigma_{n\mathbf{k}}(\mathbf{r}')} \frac{\delta\phi^\sigma_{n\mathbf{k}}(\mathbf{r}')}{\delta V^\sigma_{\text{eff}}(\mathbf{r})}\, d^3r' + \text{c.c.} \right) + \frac{\delta E_{\text{xc}}}{\delta\epsilon^\sigma_{n\mathbf{k}}} \frac{\delta\epsilon^\sigma_{n\mathbf{k}}}{\delta V^\sigma_{\text{eff}}(\mathbf{r})} \right] . \tag{6.6}$$

So far, the derivation holds for any orbital- and (or) eigenvalue-dependent xc functional. In the following, we will concentrate on the orbital-dependent exact-exchange (EXX) functional

$$E_{\text{x}} = -\frac{1}{2} \sum_\sigma \sum_{n\mathbf{k}}^{\text{occ.}} \sum_{n'\mathbf{q}}^{\text{occ.}} \iint \frac{\phi^{\sigma*}_{n\mathbf{k}}(\mathbf{r})\phi^\sigma_{n'\mathbf{q}}(\mathbf{r})\phi^{\sigma*}_{n'\mathbf{q}}(\mathbf{r}')\phi^\sigma_{n\mathbf{k}}(\mathbf{r}')}{|\mathbf{r}-\mathbf{r}'|} d^3r\, d^3r' \,. \tag{6.7}$$

It has been shown in section 3.5 that E_{x} is the leading term of the exact xc functional in terms of the electron-electron interaction. As E_{x} is only orbital-dependent, the functional derivative of E_{x} with respect to the KS eigenvalues $\epsilon^\sigma_{n\mathbf{k}}$ is zero, whereas the derivative of E_{x} with respect to the KS wave function is given by

$$\frac{\delta E_{\text{x}}}{\delta\phi^\sigma_{n\mathbf{k}}(\mathbf{r}')} = \int \phi^{\sigma*}_{n\mathbf{k}}(\mathbf{r}'') V^{\text{NL},\sigma}_{\text{x}}(\mathbf{r}'',\mathbf{r}')\, d^3r'' \,. \tag{6.8}$$

$V^{\text{NL},\sigma}_{\text{x}}$ is the non-local exchange potential as defined in Eq. (5.7). Consequently, the integral

equation (6.6) for the EXX functional (6.7) becomes

$$\int \chi_{\mathrm{s}}^{\sigma}(\mathbf{r},\mathbf{r}')\, V_{\mathrm{x}}^{\sigma}(\mathbf{r}')\, d^3r' = t^{\sigma}(\mathbf{r}) \tag{6.9}$$

with the right-hand side

$$t^{\sigma}(\mathbf{r}) = 2\sum_{n\mathbf{k}}^{\text{occ.}}\sum_{n'}^{\text{unocc.}} \langle \phi_{n\mathbf{k}}^{\sigma}|V_{\mathrm{x}}^{\mathrm{NL},\sigma}|\phi_{n'\mathbf{k}}^{\sigma}\rangle \frac{\phi_{n'\mathbf{k}}^{\sigma *}(\mathbf{r})\phi_{n\mathbf{k}}^{\sigma}(\mathbf{r})}{\epsilon_{n\mathbf{k}}^{\sigma}-\epsilon_{n'\mathbf{k}}^{\sigma}} \tag{6.10}$$

and

$$\langle \phi_{n\mathbf{k}}^{\sigma}|V_{\mathrm{x}}^{\mathrm{NL},\sigma}|\phi_{n'\mathbf{k}}^{\sigma}\rangle = \iint \phi_{n\mathbf{k}}^{\sigma *}(\mathbf{r})\, V_{\mathrm{x}}^{\mathrm{NL},\sigma}(\mathbf{r},\mathbf{r}')\phi_{n'\mathbf{k}}^{\sigma}(\mathbf{r}')\, d^3r\, d^3r' \,. \tag{6.11}$$

We have exploited time-reversal symmetry for the right-hand side, as well.

The integral equation for the local EXX potential in the form of Eq. (6.9) is often called OEP equation. So far, we have derived the latter within the framework of KS DFT. However, originally this equation goes back to Sharp and Horton and the year 1953 [32]. Sharp and Horton searched for an approximation to the Hartree-Fock (HF) approach, where the orbitals forming the single Slater determinant, are the solution of a Schrödinger equation with a local instead of the non-local HF potential. Therefore, they minimized the HF total energy with respect to the orbitals under the constraint that the orbitals move in a local, effective potential. As the orbitals are functionals of the local, effective potential, the constrained minimization is equivalent to an unconstrained minimization of the total HF energy with respect to the local potential. With a partition of the local potential into external, Hartree, and exchange parts, in analogy to the KS potential, the ansatz of Sharp and Horton finally leads to Eq. (6.9), as well. The equivalence of the variational principle of Hohenberg and Kohn and the condition of Sharp and Horton can be easily demonstrated. By applying the chain rule the variational principle of Hohenberg and Kohn

$$\frac{\delta E}{\delta n(\mathbf{r})} = 0 \tag{6.12}$$

can be written as

$$0 = \frac{\delta E}{\delta n(\mathbf{r})} = \int \frac{\delta E}{\delta V_{\mathrm{eff}}(\mathbf{r}')}\frac{\delta V_{\mathrm{eff}}(\mathbf{r}')}{\delta n(\mathbf{r})}\, d^3r'. \tag{6.13}$$

As Eq. (6.13) holds for an arbitrary density variation, which does not change the particle number ($\int \delta n(\mathbf{r}) d^3r = 0$), it follows that

$$\frac{\delta E}{\delta V_{\mathrm{eff}}(\mathbf{r}')} = 0 \tag{6.14}$$

must be fulfilled. This is the condition of Sharp and Horton. Sahni *et al.* [127] realized in

1982 that the approach of Sharp and Horton is equivalent to the EXX formalism of KS DFT. According to Eq. (6.14), the local exact exchange potential can be understood as the best local potential which minimizes the HF total energy. Moreover, the construction of Sharp and Horton shows that HF total energies must always be lower than EXX total energies, because in the HF approach the total energy is minimized over all possible orbitals without an additional constraint.

Before the implementation of the EXX-OEP integral equation is discussed in the next section, we note that Eq. (6.9) can also be obtained from the linearized Sham-Schlüter equation [cf. Eq. (3.52)] if one approximates the self-energy Σ_{xc} by the HF energy.

6.2. Implementation of the EXX functional

In order to solve the integral equation for the local EXX potential numerically, we introduce an auxiliary basis set $\{M_I(\mathbf{r})\}$ for the representation of $V_{\mathrm{x}}^{\sigma}(\mathbf{r})$ [$V_{\mathrm{x}}^{\sigma}(\mathbf{r}) = \sum_J V_{\mathrm{x},J}^{\sigma} M_J(\mathbf{r})$]. The EXX-OEP equation (6.9) then becomes a linear algebraic equation for the vector $\mathbf{V}_{\mathrm{x}}^{\sigma}$ representing the local EXX potential

$$\sum_J \chi_{\mathrm{s},IJ}^{\sigma} V_{\mathrm{x},J}^{\sigma} = t_I^{\sigma} \tag{6.15}$$

with the spin-density response matrix

$$\chi_{\mathrm{s},IJ}^{\sigma} = 2 \sum_{n\mathbf{k}}^{\text{occ.}} \sum_{n'}^{\text{unocc.}} \frac{\langle M_I \phi_{n\mathbf{k}}^{\sigma} | \phi_{n'\mathbf{k}}^{\sigma} \rangle \langle \phi_{n'\mathbf{k}}^{\sigma} | \phi_{n\mathbf{k}}^{\sigma} M_J \rangle}{\epsilon_{n\mathbf{k}}^{\sigma} - \epsilon_{n'\mathbf{k}}^{\sigma}} \tag{6.16}$$

and the vector of the right-hand side

$$t_I^{\sigma} = 2 \sum_{n\mathbf{k}}^{\text{occ.}} \sum_{n'}^{\text{unocc.}} \langle \phi_{n\mathbf{k}}^{\sigma} | V_{\mathrm{x}}^{\mathrm{NL},\sigma} | \phi_{n'\mathbf{k}}^{\sigma} \rangle \frac{\langle M_I \phi_{n'\mathbf{k}}^{\sigma} | \phi_{n\mathbf{k}}^{\sigma} \rangle}{\epsilon_{n\mathbf{k}}^{\sigma} - \epsilon_{n'\mathbf{k}}^{\sigma}} \,. \tag{6.17}$$

Eq. (6.15) can be solved for the exchange potential by a matrix inversion of $\chi_{\mathrm{s}}^{\sigma}$.

So far, the auxiliary basis set $\{M_I(\mathbf{r})\}$ has not been specified. The form of the response matrix (6.16) and the vector (6.17) shows that the auxiliary basis should be primarily constructed from products of KS wave functions. In section 4.2.2 we have already introduced such a basis, the mixed product basis (MPB), which was constructed from products of LAPW basis functions. The MPB has been employed in chapter 5 to calculate the matrix elements of the non-local exchange potential. For the solution of the EXX-OEP equation we will slightly modify the MPB. First, the MPB can be restricted to $\mathbf{k} = \mathbf{0}$, as the EXX potential is strictly periodic. Second, atomic EXX calculations show that the local exchange potential has pronounced humps, which reflect the atomic shell structure. Due to the spatial contraction of

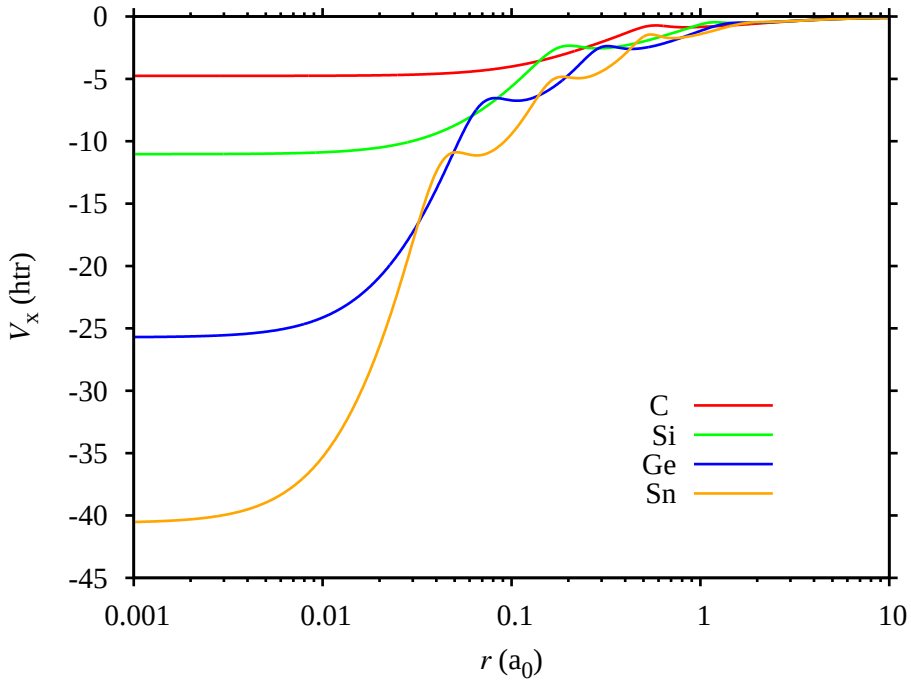

Figure 6.1.: Atomic EXX potentials obtained with the RELKS code for the C, Si, Ge, and Sn atom. With increasing atomic number from C (Z=6) to Sn (Z=50) the intershell humps move closer and closer to the atomic nuclei (at $r = 0$). Simultaneously, more and more intershell humps in the EXX potential appear, one for each atomic shell.

the electron orbitals these humps move closer to the atomic nucleus with increasing atomic number [s. Fig. (6.1)]. An accurate description of these humps would require a very flexible basis. However, the crystal EXX potential should resemble the atomic one in the vicinity of the nuclei. Therefore, we add the atomic EXX potential to the spherical muffin-tin (MT) MPB functions. The other MT basis functions then only have to describe the difference between the spherical atomic and the crystal EXX potential. The atomic EXX potential is obtained from the relativistic atomic-structure program RELKS [66, 128, 129]. Moreover, we form linear combinations of the MT and IR MPB functions that are continuous in value and derivative over the whole space to avoid discontinuities in the resulting EXX potential at the MT sphere boundaries. This can be achieved by a construction similar to that of the LAPW basis, i.e., two radial functions of the MT MPB in each lm channel are used to augment an interstitial plane wave in the MT spheres. As the MT MPB usually consists of more than two radial functions per lm channel, the remaining radial functions are used to form local orbitals. In a last step, the matched MPB functions are orthogonalized with respect to a constant function in order

to guarantee that the response matrix $\chi^{\sigma}_{\mathrm{s},IJ}$ [Eq. (6.16)] is invertible. This is necessary, because a change of the effective potential by a constant does not change the electron density. So any constant function is an eigenfunction of the response matrix with eigenvalue zero. Therefore, we must go over to a restricted function space that excludes constant potential variations. As a consequence, the solution of the integral equation (6.15) is not unique. If we have found one solution $V^{\sigma}_{\mathrm{x}}(\mathbf{r})$, also $V^{\sigma}_{\mathrm{x}}(\mathbf{r}) + c$ solves Eq. (6.15), where c denotes a real number.

In Appendix A we present a different approach to construct the subspace of the MPB, which fulfills the constraints of continuity in value and first radial derivative at the MT sphere boundaries and is orthogonal with respect to a constant function. This approach has the benefit that it is more general in the sense that further constraints to the MPB can easily be incorporated as long as the constraint can be formulated as an orthogonality condition to the MPB. We note that the construction of the modified MPB in analogy to the LAPW basis – as discussed above – and that described in Appendix A lead to a MPB spanning the same Hilbert space.

The response matrix elements (6.16) and the right-hand side (6.17) of the EXX-OEP equation contain a sum over all occupied states. Here, both core and valence states are taken into account.[1] Consequently, matrix elements of the non-local exchange potential between occupied (core and valence) and unoccupied valence states enter on the right-hand side. In the previous chapter, we already introduced a numerical scheme to compute the matrix elements of the non-local exchange potential between valence states. This scheme is extended to also calculate the matrix elements between core and valence states as well as core and core states. The matrix elements of the latter are, in fact, not needed for the calculation of the local exchange potential but required to compute the all-electron EXX energy. As the non-local exchange potential $V^{\mathrm{NL},\sigma}_{\mathrm{x}}(\mathbf{r},\mathbf{r}')$ [Eq. 5.7] contains a sum over all occupied states, which comprise core and valence electron states, we distinguish between two cases: the two wave functions arising from the sum in $V^{\mathrm{NL},\sigma}_{\mathrm{x}}$ correspond to (a) valence or (b) core states. In case (a) we employ a MPB to represent wave function products at the same spatial coordinate. We note that we employ two different MPB sets. One for the representation of the local exchange potential $V^{\sigma}_{\mathrm{x}}(\mathbf{r})$, as explained above, and the other to calculate the matrix elements of the non-local exchange operator $V^{\mathrm{NL},\sigma}_{\mathrm{x}}(\mathbf{r},\mathbf{r}')$ as accurately as possible. The latter is typically much larger than the former. With the MPB the six-dimensional integral that corresponds to the matrix element of $V^{\mathrm{NL},\sigma}_{\mathrm{x}}(\mathbf{r},\mathbf{r}')$ turns into a vector-matrix-vector product, where the matrix represents the Coulomb kernel $1/|\mathbf{r}-\mathbf{r}'|$ in the MPB. The vectors correspond to the representation of the product of two valence states or the product of valence times core state.

[1] For the core states we switch to a non-relativistic description by averaging for each principal quantum number n and angular momentum l the radial solutions of the Dirac equation with $j = l + 1/2$ and $j = l - 1/2$.

For an accurate representation of valence times core state we generalize the MT MPB for the calculation of $V_{\mathrm{x}}^{\mathrm{NL},\sigma}$ such that its radial functions are constructed from products of LAPW radial functions as well as products of LAPW and core radial functions. The techniques developed in chapter 5 to accelerate the calculation of the matrix elements of $V_{\mathrm{x}}^{\mathrm{NL},\sigma}$ can be applied in this more general case, as well. The computation of the contribution type (b) to the matrix elements does not require the MPB. Instead, these matrix elements can be calculated analytically, as the core states are dispersionless and confined to the MT spheres [83, 86].

Furthermore, we exploit spatial and time-reversal symmetries to restrict the $\mathbf{k}$-point sums in Eq. (6.16) and (6.17) to the irreducible wedge of the Brillouin zone (BZ) in a similar manner as for the matrix elements of the non-local exchange potential (s. Sec. 5.2.2). For the response matrix we will discuss the usage of symmetry in detail. A restriction of the BZ sum in Eq. (6.16) to the irreducible BZ (IBZ) is possible without changing the value of the matrix element $\chi_{\mathrm{s},IJ}^{\sigma}$, if we simultaneously run over all symmetry operations $\{P_i, i = 1, \ldots, N\}$ of the crystal

$$\chi_{\mathrm{s},IJ}^{\sigma} = \sum_{i=1}^{N}\left[2\sum_{\mathbf{k}}^{\mathrm{IBZ}}\frac{1}{N_P(\mathbf{k})}\sum_{n}^{\mathrm{occ.}}\sum_{n'}^{\mathrm{unocc.}}\frac{\langle M_I[P_i\phi_{n\mathbf{k}}^{\sigma}]|[P_i\phi_{n'\mathbf{k}}^{\sigma}]\rangle\langle[P_i\phi_{n'\mathbf{k}}^{\sigma}]|[P_i\phi_{n\mathbf{k}}^{\sigma}]M_J\rangle}{\epsilon_{n\mathbf{k}}^{\sigma}-\epsilon_{n'\mathbf{k}}^{\sigma}}\right]. \tag{6.18}$$

The factor $1/N_P(\mathbf{k})$ avoids a multi-counting of certain Bloch vectors $\mathbf{k}$. For example, without this factor the Γ point is contained in Eq. (6.18) N-times. Consequently, $N_P(\mathbf{k})$ is the number of symmetry operations, which leave $\mathbf{k}$ invariant, or, to be more precise, $N_P(\mathbf{k})$ is the number of members in the little group of $\mathbf{k}$. Instead of operating with the symmetry operation P_i on $\phi_{n\mathbf{k}}^{\sigma}$ and $\phi_{n'\mathbf{k}}^{\sigma}$, the inverse symmetry operation P_i^{-1} can be applied to M_I and M_J

$$\chi_{\mathrm{s},IJ}^{\sigma} = \sum_{i=1}^{N}\left[2\sum_{\mathbf{k}}^{\mathrm{IBZ}}\frac{1}{N_P(\mathbf{k})}\sum_{n}^{\mathrm{occ.}}\sum_{n'}^{\mathrm{unocc.}}\frac{\langle[P_i^{-1}M_I]\phi_{n\mathbf{k}}^{\sigma}|\phi_{n'\mathbf{k}}^{\sigma}\rangle\langle\phi_{n'\mathbf{k}}^{\sigma}|\phi_{n\mathbf{k}}^{\sigma}[P_i^{-1}M_J]\rangle}{\epsilon_{n\mathbf{k}}^{\sigma}-\epsilon_{n'\mathbf{k}}^{\sigma}}\right]. \tag{6.19}$$

Hence, we can restrict the BZ sum in the response matrix to the IBZ, but have to rotate the MPB functions afterwards to add the contribution of all $\mathbf{k}$ points. The rotation of the MPB functions is computationally very cheap, as it simply translates to a summation over different matrix elements.

Since an analogous argumentation holds for the vector $\mathbf{t}^{\sigma}$ of the right-hand side we only give the final result

$$t_I^{\sigma} = \sum_{i=1}^{N}\left[2\sum_{\mathbf{k}}^{\mathrm{IBZ}}\frac{1}{N_P(\mathbf{k})}\sum_{n}^{\mathrm{occ.}}\sum_{n'}^{\mathrm{unocc.}}\langle\phi_{n\mathbf{k}}^{\sigma}|V_{\mathrm{x}}^{\mathrm{NL},\sigma}|\phi_{n'\mathbf{k}}^{\sigma}\rangle\frac{\langle[P_i^{-1}M_I]\phi_{n'\mathbf{k}}^{\sigma}|\phi_{n\mathbf{k}}^{\sigma}\rangle}{\epsilon_{n\mathbf{k}}^{\sigma}-\epsilon_{n'\mathbf{k}}^{\sigma}}\right]. \tag{6.20}$$

The local exact exchange potential is then obtained by a multiplication of the inverse re-

sponse matrix with the vector $\mathbf{t}^\sigma$. Finally, the local, multiplicative exchange potential is transformed from a representation in the MPB to a representation in terms of lattice harmonics and stars (cf. Sec. 4.2) and added to the external and Hartree potential.

Numerical tests of the implementation

The spin-density response function χ_s^σ, the right-hand side t^σ, and the resulting exchange potential V_x^σ are functional derivatives of the form $\delta A(\mathbf{r})/\delta B(\mathbf{r}')$ or $\delta A/\delta B(\mathbf{r}')$. They describe the linear change of the quantity A due to a change in B. To test our implementation, we calculate the change of A due to a perturbation in B explicitly and compare the full response of A with its linear counterpart arising from $\delta A/\delta B$. The difference between exact and linear response should then vanish quadratically with the perturbation strength.

For the test of the spin-density response function and the right-hand side we perturb the Hamiltonian with the potential $V_{\text{per}}^\sigma(\mathbf{r}) = \alpha \sum_I V_{\text{per},I}^\sigma M_I(\mathbf{r})$, where $V_{\text{per},I}^\sigma$ are random numbers and α controls the strength of the perturbation. The perturbed Hamiltonian is exactly diagonalized. From the perturbed wave functions the change in the density $\Delta n^\sigma(\mathbf{r})$ and the exact exchange energy ΔE_x^σ is calculated. On the other hand, we compute the linear change $\Delta^{\text{lin}} n^\sigma$ and $\Delta^{\text{lin}} E_x^\sigma$ arising from the perturbation V_{per}^σ by

$$\Delta^{\text{lin}} n^\sigma(\mathbf{r}) = \int \chi_s^\sigma(\mathbf{r},\mathbf{r}')\, V_{\text{per}}^\sigma(\mathbf{r}')\, d^3r' \tag{6.21}$$

and

$$\Delta^{\text{lin}} E_x^\sigma = \int t^\sigma(\mathbf{r}')\, V_{\text{per}}^\sigma(\mathbf{r}')\, d^3r' \,. \tag{6.22}$$

Table 6.1(a) and (b) demonstrate for the case of diamond that the differences $\Delta n^\sigma - \Delta^{\text{lin}} n^\sigma$ and $\Delta E_x^\sigma - \Delta^{\text{lin}} E_x^\sigma$ indeed depend quadratically on the perturbation strength α, if the perturbation is small enough, so that we are in the linear regime.

For the check of the exchange potential V_x^σ itself we compare the exact change in the exchange energy ΔE_x^σ with its linear counterpart $\Delta^{\text{lin}} E_x^\sigma$, which is calculated from

$$\Delta^{\text{lin}} E_x^\sigma = \int V_x^\sigma(\mathbf{r}')\Delta n^\sigma(\mathbf{r}')\, d^3r' = \sum_I V_{x,I}^\sigma \int M_I(\mathbf{r}')\Delta n^\sigma(\mathbf{r}')\, d^3r' \,. \tag{6.23}$$

We note that Δn^σ in Eq. (6.23) is the exact change in the density due to the perturbing potential V_{per}^σ. The difference $\Delta E_x^\sigma - \Delta^{\text{lin}} E_x^\sigma$ [cf. Table 6.1(c)] shows a quadratic dependence on the perturbation strength α, as well.

These three tests confirm the validity and correctness of our implementation.

(a)

α	0.01	0.001	0.0001
$\lvert\Delta^{\mathrm{lin}}n\text{-}\Delta n\rvert$	2.16710×10^{-4}	2.17018×10^{-6}	2.17035×10^{-8}

(b)

α	0.01	0.001	0.0001
ΔE_{x}	1.69455	1.74639×10^{-1}	1.75171×10^{-2}
$\Delta^{\mathrm{lin}}E_{\mathrm{x}}$	1.75230	1.75230×10^{-1}	1.75230×10^{-2}
$\lvert\Delta^{\mathrm{lin}}E_{\mathrm{x}}\text{-}\Delta E_{\mathrm{x}}\rvert$	5.77479×10^{-2}	5.90882×10^{-4}	5.92211×10^{-6}

(c)

α	0.01	0.001	0.0001
ΔE_{x}	1.69455	1.74639×10^{-1}	1.75171×10^{-2}
$\Delta^{\mathrm{lin}}E_{\mathrm{x}}$	1.67924	1.74479×10^{-1}	1.75155×10^{-2}
$\lvert\Delta^{\mathrm{lin}}E_{\mathrm{x}}\text{-}\Delta E_{\mathrm{x}}\rvert$	1.53093×10^{-2}	1.59919×10^{-4}	1.60625×10^{-6}

Table 6.1.: Numerical test of (a) the response function $\chi_{\mathrm{s}}(\mathbf{r},\mathbf{r}') = \delta n(\mathbf{r})/\delta V_{\mathrm{s}}(\mathbf{r}')$, (b) the right-hand side $t(\mathbf{r}) = \delta E_{\mathrm{x}}/\delta V_{\mathrm{s}}(\mathbf{r})$, and (c) the potential $V_{\mathrm{x}}(\mathbf{r}) = \delta E_{\mathrm{x}}/\delta n(\mathbf{r})$ for the case of diamond. In (a) the exact response of the density $\Delta n(\mathbf{r})$ is compared with its linear approximation $\Delta^{\mathrm{lin}}n(\mathbf{r}) = \sum_I n_I^{\mathrm{lin}} M_I(\mathbf{r})$ and $n_I^{\mathrm{lin}} = \alpha \sum_J \chi_{\mathrm{s},IJ} V_{\mathrm{per},J}$ by the L2 norm $[\int |\Delta n^{\mathrm{lin}}(\mathbf{r}) - \Delta n(\mathbf{r})|^2 d^3r]^{1/2}$. In cases (b) and (c) the exact response of the exchange energy ΔE_{x} is opposed to its linear approximation, which is calculated by $\Delta^{\mathrm{lin}}E_{\mathrm{x}} = \alpha \sum_I t_I^* V_{\mathrm{per},I}$ in (b) or by $\Delta^{\mathrm{lin}}E_{\mathrm{x}} = \sum_I V_{\mathrm{x},I} \int M_I(\mathbf{r}) \Delta n(\mathbf{r}) d^3r$ in (c). The difference between exact and linear response shows in all three cases a quadratic dependence on the perturbation strength α.

6.3. Balance of MPB and FLAPW basis

After the discussion of the implementation of the EXX-OEP approach within the FLAPW method, we demonstrate in this section that LAPW and mixed product basis are not independent from each other. In fact, both basis sets are intertwined through the response functions Eqs. (6.3) and (6.4). We show in particular that a smooth and physical local EXX potential requires a balance of LAPW and mixed product basis, i.e., the LAPW basis for the KS wave functions must be converged with respect to a given MPB until the EXX potential does not change anymore. A similar behavior has been observed in EXX-OEP implementations employing plane-wave and Gaussian basis sets [130, 131].

In Fig. 6.2 the local EXX potential for diamond is shown between two neighboring carbon atoms along (a) the [111] and (b) the [100] direction. The position of the corresponding atoms and directions in the cubic unit cell of diamond are indicated in Fig. 6.3. For these calculations we have employed a MPB for the EXX potential with a reciprocal cutoff radius of $G'_{\max} = 3.4\,\mathrm{a}_0^{-1}$ and $L_{\max} = 4$, which amounts to five $s-$, four $p-$, four $d-$, three $f-$, and two $g-$type radial functions per carbon atom. Moreover, the LAPW basis-set parameters are $G_{\max} = 4.2\,\mathrm{a}_0^{-1}$ and $l_{\max} = 6$, and a 4×4×4 $\mathbf{k}$-point sampling has been employed. If we use the conventional LAPW basis set (green dashed curve), the local EXX potential tends to a positive value at the atomic nuclei. This behavior is unphysical, as the exchange interaction is attractive. We say that both basis sets are *unbalanced* in this case. However, if we add local orbitals to the LAPW basis set, the potential becomes smooth and physical (red solid curve). The EXX potential then starts at the atomic nuclei with a value of about −4 htr. At roughly $0.6\,\mathrm{a}_0$ it shows the typical intershell hump and goes smoothly over to the interstitial region. At the MT sphere boundary ($S_a = 1.42\,\mathrm{a}_0$) a tiny discontinuity in the potential is observable, which results from the finite angular momentum cutoff in the MT spheres. We find that for a converged EXX potential six local orbitals per lm channel from $l = 0, \ldots, 5$ and $|m| \leq l$, placed at higher energies according to the criterion (4.18), are needed. The requirement of local orbitals from $l = 0, \ldots, 5$ is reasonable, as in the projections $\langle M_I \phi^\sigma_{n'\mathbf{k}} | \phi^\sigma_{n\mathbf{k}} \rangle$ the occupied $2s$ and $2p$ states of diamond and the MT MPB functions with $L_{\max} = 4$ can maximally couple to unoccupied states with angular character of $l = 5$. The need of so many local orbitals increases the number of basis functions by approximately a factor of 5. We note that we take all resulting KS bands, about 530, in the sums over the unoccupied states in Eqs. (6.16) and (6.17) into account.

For comparison, we also show the atomic EXX potential (blue dotted curve) in Fig. 6.2. As expected, in the direct vicinity of the carbon nucleus the atomic and the (balanced) crystal EXX potentials are indistinguishable. However, towards the MT sphere boundary atomic

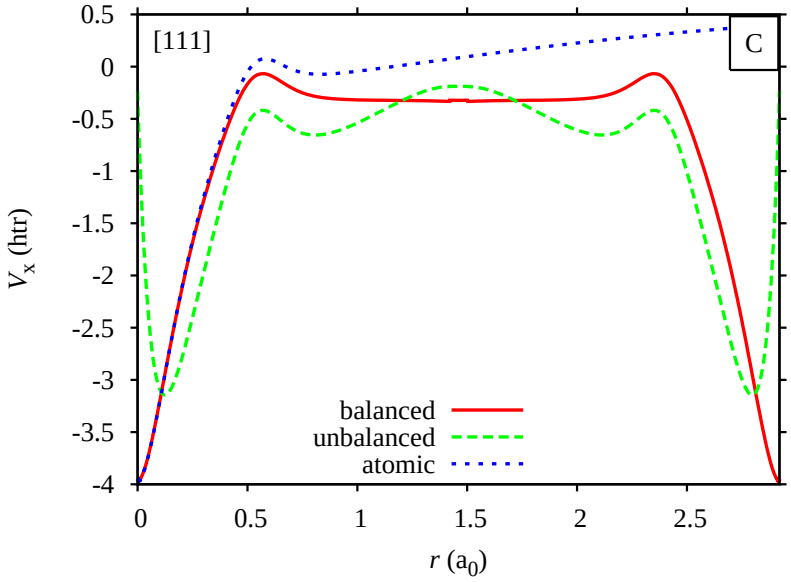

(a)

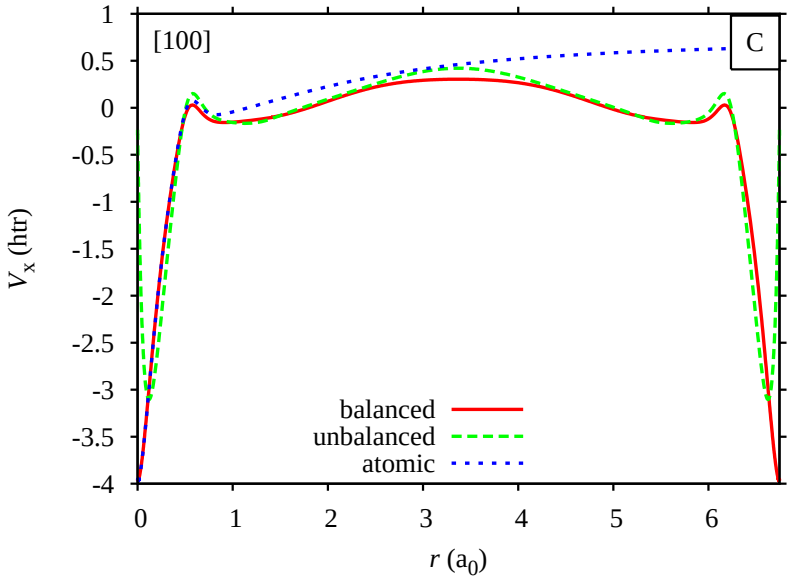

(b)

Figure 6.2.: Local EXX potential of diamond between two C atoms (a) along the [111] and (b) along the [100] directions for the cases where the MPB and LAPW basis set are unbalanced (green dashed line) and balanced (red solid line). Moreover, the atomic EXX potential of C is shown as blue dotted lines. It is shifted to align with the crystal potential at the atomic nucleus at $r = 0$.

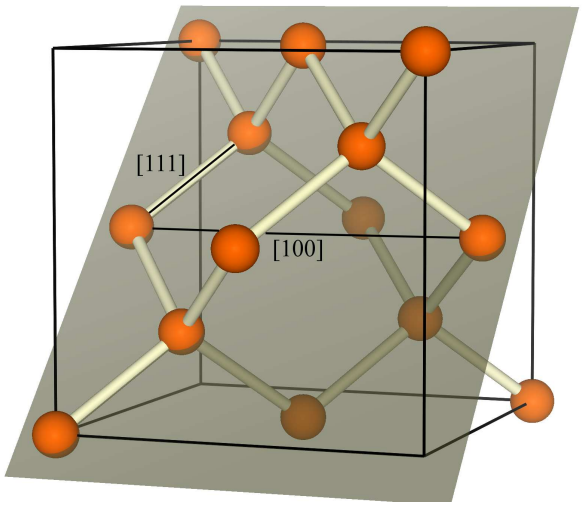

Figure 6.3.: Cubic unit cell of diamond with the $(01\bar{1})$ plane. The lines along the [111] and [100] directions corresponding to Fig. 6.2 are indicated.

and crystal EXX potential start to deviate. There, the atomic EXX potential already shows the typical $1/r$ behavior, from which the crystal potential deviates due to the demand of periodicity. Hence, it is not surprising, that the MPB function which corresponds to the atomic EXX potential, gets the largest weight in the MT spheres and, thus, contributes most to the MT part of the potential. The constant function in the MT spheres, which enables an alignment of the MT to the interstitial potential, gets the second largest weight.

So far, we pointed out that a physical and stable EXX potential in the MT spheres requires a balance of LAPW and mixed product basis, which is achieved by adding local orbitals to the LAPW basis set. In analogy, in the interstitial region the reciprocal cutoff radius $G_{\max}$ of the LAPW basis must be converged with respect to the reciprocal cutoff of the MPB $G'_{\max}$. In order to demonstrate this behavior more clearly, we have chosen a rather large reciprocal cutoff value for the MPB $G'_{\max} = 5.8\,a_0^{-1}$ (s. Fig. 6.4). If $G_{\max}$ is smaller than $G'_{\max}$, the EXX potential shows spurious oscillations in the interstitial region. In fact, the potential oscillates around the converged curve obtained here with $G_{\max} = 6.00\,a_0^{-1}$. Fortunately, the converged EXX potential is a smooth function, and moderate reciprocal cutoff radii $G'_{\max}$ for the MPB are sufficient. We found that $G'_{\max} = 0.75 G_{\max}$ is a reasonable choice. For diamond for example the combination of $G'_{\max} = 3.4\,a_0^{-1}$ and $G_{\max} = 4.2\,a_0^{-1}$ leads to stable results.

We go back to the EXX-OEP equation (6.9) to understand the requirement of the basis set balance in more detail. This equation contains two response functions: on the left-hand

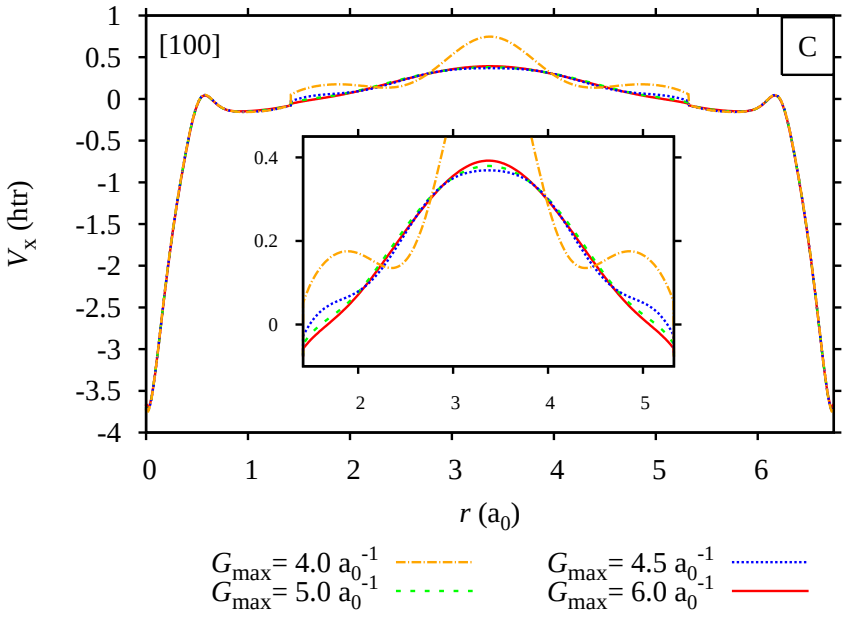

Figure 6.4.: The convergence of the interstitial EXX potential is demonstrated for different reciprocal cutoff radii G_{max} of the LAPW basis on a line connecting two carbon atoms along the [100] direction. The reciprocal MPB cutoff is chosen as $5.8\,a_0^{-1}$.

side the density response function χ_s, which must be inverted to obtain V_x, and on the right-hand side the KS wave-function response. They describe the change of the density and KS wave function, respectively, due to a change in the effective potential. As we represent the EXX-OEP equation in terms of the MPB, the changes in the effective potential are given by the MPB. On the contrary, the change in the density and KS wave function are described by first-order perturbation theory giving rise to a sum over all unoccupied states. In practice, of course, only a finite number N of unoccupied states is available and the sum over the unoccupied states is truncated. Thus, the response is determined by the quality of the LAPW basis. The latter must provide enough flexibility to enable the density or KS wave function to respond adequately to changes in the effective potential. This explains the behavior observed above, and it is confirmed by the convergence behavior of the density response function with respect to the LAPW basis as demonstrated in Fig. 6.5. The relative change in the eigenvalues of the density response function as a function of the number of local orbitals n_{LO} added to the LAPW basis is shown. In each step, $2l+1$ local orbitals per l channel from $l = 0, \ldots, 5$ are added to the LAPW basis resulting in 36 additional functions per atom. While we observe a change in the eigenvalues in the range of 100% between zero and one set of local orbitals, the relative changes are of the order of 0.1% to 1.0% between $n_{LO} = 5$ and $n_{LO} = 6$. Fortunately,

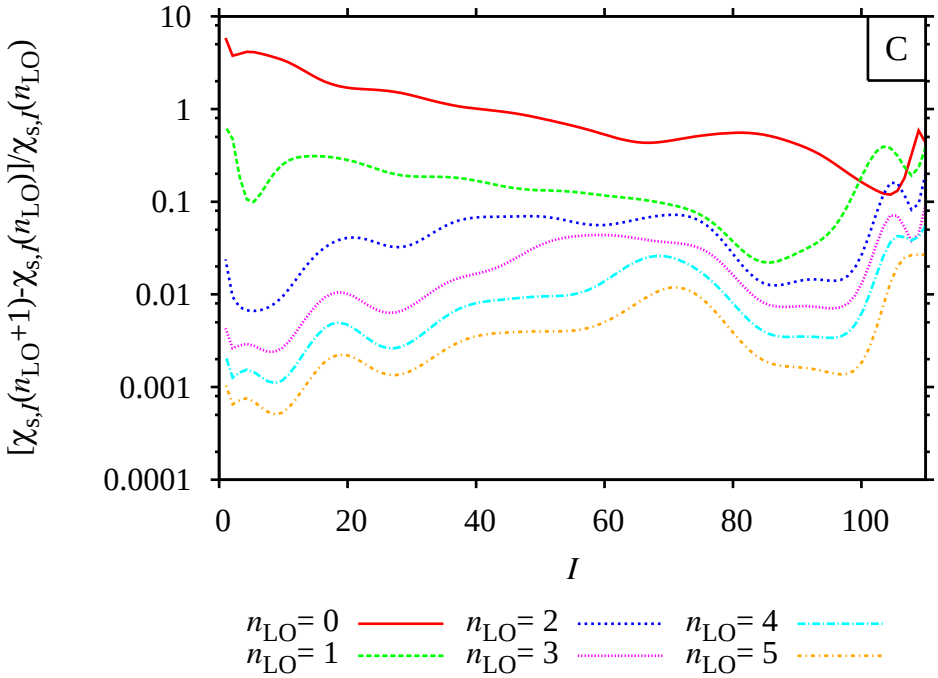

Figure 6.5.: Convergence of the eigenvalues of the density response function χ_s for diamond with respect to the number of local orbitals added to the LAPW basis. n_{LO} denotes the number of local orbitals added in each lm channel from $l = 0, \ldots, 5$ to the conventional LAPW basis. The eigenvalues $\chi_{s,I}$ are ordered according to their absolute values along the x axis. The y axis shows the relative change of the eigenvalue.

in particular the small eigenvalues of the response function, which become important in the inverse response function, converge well.

The observation that the orbital LAPW basis and auxiliary MPB are not independent and must be balanced for a physical density-response function and consequently physical EXX potential, can be understood by analyzing a model system of independent electrons in a constant potential [130]. For this system the eigenfunctions are known analytically and given by simple plane waves. But let us assume that we perform an electronic-structure calculation for such a system, where the orbital basis is given by plane waves, too. Then, each basis function is also an eigenfunction of the Hamiltonian. In order to be able to describe all occupied states, the reciprocal cutoff value G_{max}^{orb} for the orbital basis set is chosen to be larger than the vector G_F corresponding to the Fermi energy. Moreover, let us assume that we represent the density response function χ_s by an auxiliary basis of plane waves with the cutoff G_{max}^{aux}. The density

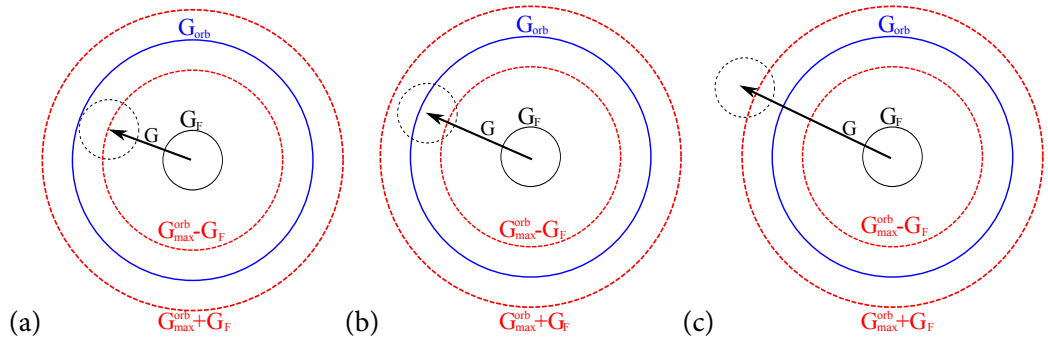

Figure 6.6.: Visualization of the three limiting cases for the representation of the density response function χ_s for the model system of independent electrons in a constant potential. In case (a) with $G^{\text{aux}}_{\text{max}} \leq G^{\text{orb}}_{\text{max}} - G_{\text{F}}$ all matrix elements of χ_s are obtained with their correct value as for any $\mathbf{G}$ of the auxiliary basis the vector $\mathbf{G} + \mathbf{G}''$ lies within the orbital cutoff radius $G^{\text{orb}}_{\text{max}}$. In the case (b) with $G^{\text{orb}}_{\text{max}} - G_{\text{F}} < G^{\text{aux}}_{\text{max}} \leq G^{\text{orb}}_{\text{max}} + G_{\text{F}}$ the matrix elements with $G^{\text{orb}}_{\text{max}} - G_{\text{F}} < |\mathbf{G}| \leq G^{\text{orb}}_{\text{max}} + G_{\text{F}}$ are incorrect, while for (c) with $|\mathbf{G}| > G^{\text{orb}}_{\text{max}} + G_{\text{F}}$ all matrix elements are zero.

response matrix then becomes a diagonal matrix with the entries

$$\chi_{\text{s},\mathbf{G}\mathbf{G}'} = 4\delta_{\mathbf{G},\mathbf{G}'} \sum_{|\mathbf{G}''| \leq G_{\text{F}}} \frac{1}{|\mathbf{G}''|^2 - |\mathbf{G}'' + \mathbf{G}|^2} \,. \tag{6.24}$$

We now distinguish three cases: in the first case, $G^{\text{aux}}_{\text{max}} \leq G^{\text{orb}}_{\text{max}} - G_{\text{F}}$, all matrix elements of the density response matrix are obtained with their correct analytical value, because all states corresponding to $\mathbf{G}'' + \mathbf{G}$ are accessible in the orbital basis set (cf. Fig. 6.6). In the second case, $G^{\text{orb}}_{\text{max}} - G_{\text{F}} < G^{\text{aux}}_{\text{max}} \leq G^{\text{orb}}_{\text{max}} + G_{\text{F}}$, however all matrix elements with $G^{\text{orb}}_{\text{max}} - G_{\text{F}} < |\mathbf{G}| \leq G^{\text{orb}}_{\text{max}} + G_{\text{F}}$ are incorrect, i.e., their entry deviates from their analytical value, as some of the unoccupied states required for these matrix elements are not contained in the orbital basis set. The third case, $G^{\text{aux}}_{\text{max}} > G^{\text{orb}}_{\text{max}} + G_{\text{F}}$, is the extreme case, where all diagonal elements with $|\mathbf{G}| > G^{\text{orb}}_{\text{max}} + G_{\text{F}}$ are zero, as none of the required unoccupied states is accessible by the orbital basis set. In conclusion, this simple model shows that auxiliary and orbital basis cannot be chosen arbitrarily for a correct representation of the density response function. It confirms our observation that for a stable and physical EXX potential the orbital LAPW basis set must be converged with respect to the auxiliary basis MPB.

6.4. Comparison of EXX and LDA exchange potential

So far, the local EXX potential has only been shown on a line between two neighboring carbon atoms. An overall view of the potential on the $(01\bar{1})$ plane of diamond is provided in Fig. 6.7. The $(01\bar{1})$ plane contains the [111] and [100] directions that correspond to Fig. 6.2. The position of the plane in the cubic unit cell is displayed in Fig. 6.3.

Figure 6.7(a) shows that the EXX potential around the atomic nuclei is predominantly spherical. Towards the MT sphere boundary, however, the potential becomes strongly anisotropic. In particular, the C-C bond axes stand out. Furthermore, Fig. 6.7(a) demonstrates that the MT potential goes smoothly over to the corrugated interstitial potential at the MT sphere boundary.

In comparison with the LDA exchange potential [s. Fig. 6.7(b)], the EXX potential exhibits much more structure and is considerably more anisotropic in the MT spheres. The LDA exchange potential is exact for the homogeneous electron gas and scales with the electron density $V_{\mathrm{x}}^{\mathrm{LDA}}(\mathbf{r}) \propto n(\mathbf{r})^{1/3}$, which explains its similarity to the electron density distribution (cf. Fig. 6.8). However, diamond is a covalently bonded material and, hence, substantially deviates from the homogeneous electron gas. The difference between LDA and EXX potential, thus, arises from the fact that in the latter the full non-locality of the EXX functional and the full inhomogeneity of the system is taken into account by means of the KS wave functions. In particular in the MT spheres, where the KS wave functions are strongly oscillating, the EXX potential features, in contrast to the LDA exchange potential, strong non-sphericity. In the interstitial region, on the other hand, both potentials are similar. This reveals that a full-potential treatment, incorporating the non-spherical contributions of the potential, is considerably more important in the case of the EXX-OEP formalism than in the LDA.

Of course, the different shapes of LDA and EXX potentials influence the electron density. In Fig. 6.8(a) the electron density distribution corresponding to the EXX potential is shown as a color-coded contour plot on the $(01\bar{1})$ plane. As naturally expected, the electrons aggregate at the atomic nuclei and along the bond axes. Despite the obvious changes between the LDA and EXX potential the differences between the densities become only clearly visible in a logarithmic plot of the density difference $|n_{\mathrm{EXX}}(\mathbf{r}) - n_{\mathrm{LDA}}(\mathbf{r})|$ [s. Fig. 6.8(b)]. The black regions are areas on the plane, where EXX and LDA density coincide (at least up to $10^{-4}\,\mathrm{a}_0^{-3}$). The regions, where charge has been accumulated in comparison to the LDA density, are marked with a plus sign. The EXX functional tends to accumulate charge at the atomic nuclei and along the bond axes. The LDA, on the contrary, tends to distribute the density more homogeneously, which we attribute to the self-interaction error, which is inherent in the LDA but completely eliminated in the EXX approach.

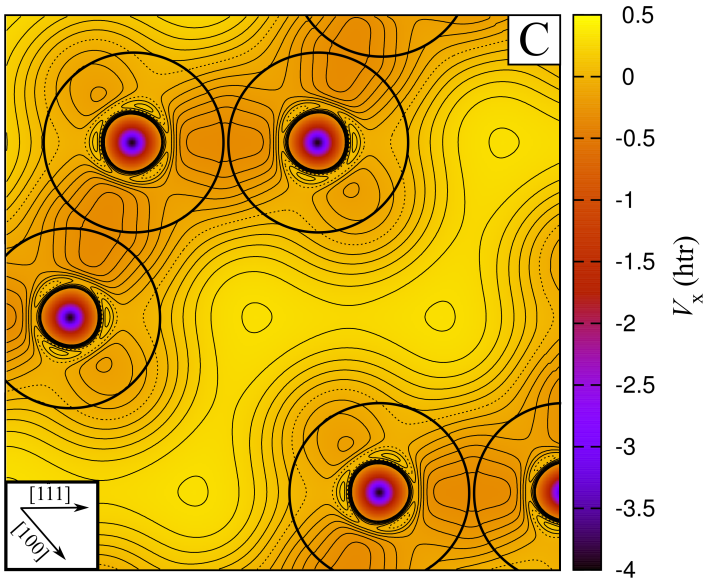

(a)

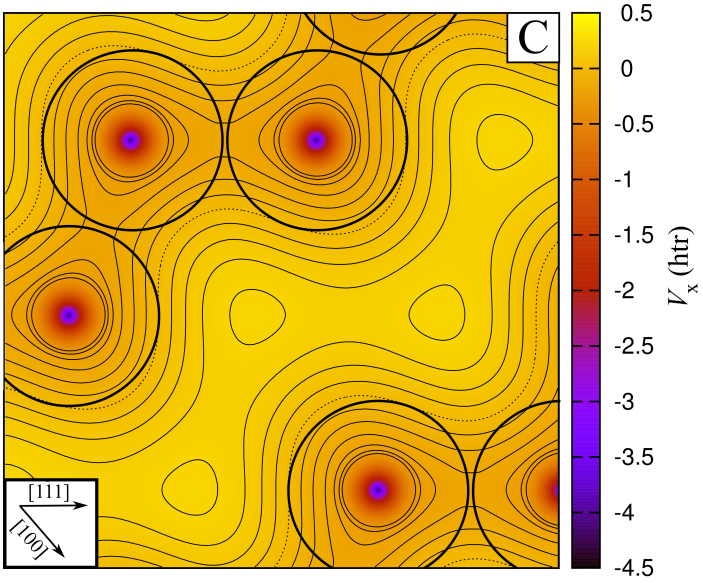

(b)

Figure 6.7.: Visualization of (a) the EXX potential and (b) the LDA exchange potential on the $(01\bar{1})$ plane of diamond. Both potentials are gauged such that $\int V_x(\mathbf{r})\, d^3r = 0$ holds. The contour lines which lie in the interval between −0.30 and 0.30 htr with a spacing of 0.05 htr are shown. The dotted line corresponds to $V_x = 0$ htr. Moreover, the MT sphere boundaries are shown.

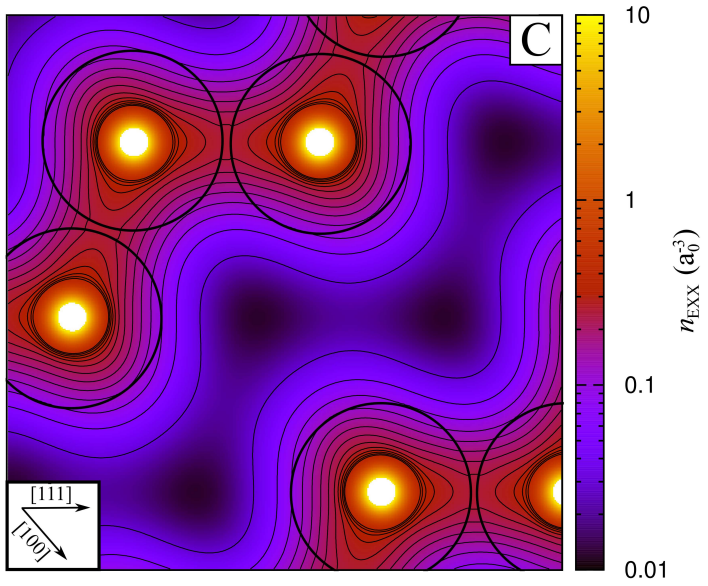

(a)

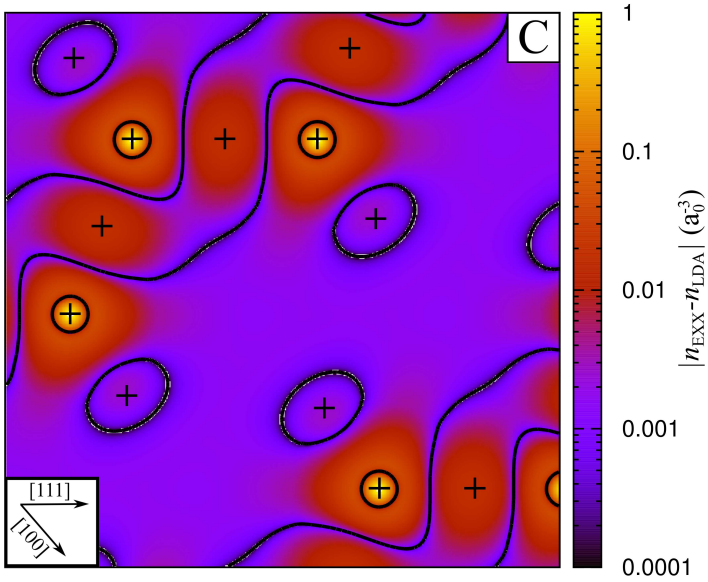

(b)

Figure 6.8.: (a) EXX total electron density on the $(01\bar{1})$ plane of diamond with equidistant contour lines between 0.03, 0.06, ..., 0.39 a_0^{-3}. (b) Logarithmic plot of the density difference $|n_{EXX}(\mathbf{r}) - n_{LDA}(\mathbf{r})|$. The area, where charge is accumulated compared with the LDA $[n_{EXX}(\mathbf{r}) - n_{LDA}(\mathbf{r}) > 0]$, is marked with a plus sign.

6.5. EXX KS transition energies of prototype semiconductors and insulators

Before we will discuss the KS band gap of the prototype semiconductors and insulators C, Si, SiC, Ge, GaAs, crystalline Ne and Ar within the EXX approach and compare our all-electron results with pseudopotential plane-wave results from the literature, we demonstrate the effect of an unbalanced LAPW and mixed product basis on the KS transition energies for the case of diamond.

In Table 6.2 the self-consistent KS transition energies from the highest occupied KS state at the Γ point to the lowest conduction band state at the Γ, L, and X points are shown for different LAPW basis sets. The basis sets have in common the cutoff values $l_{\max} = 6$ and $G_{\max} = 4.2\,\mathrm{a}_0^{-1}$, but differ in the number of local orbitals n_{LO}. The MPB parameters are $L_{\max} = 4$ and $G'_{\max} = 3.4\,\mathrm{a}_0^{-1}$. While in the interstitial region balance between both basis sets is given due to the choice of the reciprocal cutoff radii, balance in the MT spheres is gradually achieved by consecutively increasing the number of local orbitals added for each l from $l = 0, \ldots, 5$ and $|m| \leq l$. The addition of more and more local orbitals leads to a decrease in the KS transition energies. Between an unbalanced and a balanced setup the values change by about 0.2 eV. For an accuracy of 0.01 eV in the transition energies three local orbitals per lm channel, resulting in 216 additional basis functions, are required. We note that the transition energies depend similarly on the balance of the IR basis sets.

In the following, we show KS transition energies for the above defined set of prototype semiconductors and insulators employing the EXX and the EXXc functional. For the latter, correlation on the level of the LDA is added to the EXX functional. We here use the parametrization of the LDA correlation functional by Vosko, Wilk, and Nusair [5]. All calculations are performed at the experimental lattice constants and with an 8×8×8 **k**-point sampling. In particular, we make sure that the LAPW and mixed product basis sets are balanced. The LDA transition energies (first column in Table 6.3) systematically underestimate the experimental results. The EXX as well as the EXXc approach lead to KS transition energies that are much closer to experiment. The consideration of correlation on the LDA level changes the transition energies only slightly, typically by 0.1 – 0.2 eV. For the semiconductors Si, SiC, Ge, and GaAs the results are even quantitatively in reasonable agreement with experiment. For the insulators we observe larger deviations.

A comparison of the all-electron FLAPW values with pseudopotential plane-wave results from the literature shows a very good agreement for all materials except Ne. For example, for diamond we obtain a direct band gap (Γ → Γ) of 6.21 eV with the EXX functional. Engel *et al.* recently reported a direct band gap of 6.18 eV using a pseudopotential plane-wave

n_{LO}	$\Gamma \to \Gamma$	$\Gamma \to \mathrm{L}$	$\Gamma \to \mathrm{X}$
0	6.351	9.243	5.307
1	6.196	9.086	5.125
2	6.186	9.069	5.144
3	6.180	9.063	5.138
4	6.178	9.059	5.139
5	6.177	9.057	5.136
6	6.176	9.055	5.136

Table 6.2.: Convergence of KS EXX transition energies (in eV) for diamond employing LAPW basis sets including zero to six local orbitals per lm channel ($l = 0, \ldots, 5$, $|m| \leq l$).

approach but pushing the pseudopotential to its all-electron limit [40]. Our result is identical to a standard pseudopotential plane-wave approach, which employs a Troullier-Martins pseudopotential, that has been constructed from atomic EXX calculations [132]. However, the first all-electron, full-potential implementation of the EXX functional by Sharma *et al.* [39] – realized within the FLAPW approach, as well – gives a much larger value of 6.67 eV for the direct band gap for diamond. In general, their reported EXX KS transition energies deviate substantially from the published pseudopotential values and are further in considerably worse agreement with experiment. From this Sharma *et al.* draw the conclusion that (a) the success of pseudopotential EXX calculations in predicting accurate transition energies and band gaps is only an artifact of the pseudopotential approximation, which neglects by construction the core-valence exchange interaction; (b) a treatment of core and valence electrons on an equal footing is mandatory for a proper EXX calculation. We, however, obtain EXX KS transition energies, which are in excellent agreement with the pseudopotential and experimental results provided that LAPW and mixed product basis are balanced. As Sharma *et al.* [39] reported that their calculations are converged up to 0.01 eV with only 25 empty states, we speculate that they are far away from a balance between LAPW and auxiliary basis.

In conclusion, we find a very good agreement between our all-electron FLAPW and pseudopotential plane-wave EXX results provided that the basis sets are properly balanced. This confirms that the pseudopotential approximation is adequate for the EXX-OEP approach, at least for the systems examined here.

		This work			Plane-wave PP		
		LDA	EXX	EXXc	EXX	EXXc	Expt.
C	$\Gamma \to \Gamma$	5.56	6.21	6.26	6.19[a], 6.21[b]	6.28[c]	7.3[e]
	$\Gamma \to$ L	8.43	9.09	9.16	9.15[b]	9.18[c]	–
	$\Gamma \to$ X	4.71	5.20	5.33	5.34[b]	5.43[c]	–
Si	$\Gamma \to \Gamma$	2.53	3.13	3.21	3.12[b]	3.26[c]	3.4[e]
	$\Gamma \to$ L	1.42	2.21	2.28	2.21[b]	2.35[c]	2.4[e]
	$\Gamma \to$ X	0.61	1.30	1.44	1.25[b]	1.50[c]	–
SiC	$\Gamma \to \Gamma$	6.27	7.18	7.24	–	7.37[c]	–
	$\Gamma \to$ L	5.38	6.14	6.21	–	6.30[c]	–
	$\Gamma \to$ X	1.32	2.29	2.44	–	2.52[c]	2.42[e]
Ge	$\Gamma \to \Gamma$	−0.14	1.24	1.21	–	1.28[c]	1.0[e]
	$\Gamma \to$ L	0.06	0.89	0.94	–	1.01[c]	0.7[e]
	$\Gamma \to$ X	0.66	1.15	1.28	–	1.34[c]	1.3[e]
GaAs	$\Gamma \to \Gamma$	0.29	1.72	1.74	–	1.82[c]	1.63[e]
	$\Gamma \to$ L	0.85	1.79	1.86	–	1.93[c]	–
	$\Gamma \to$ X	1.35	1.95	2.12	–	2.15[c]	2.18[e]
Ne	$\Gamma \to \Gamma$	11.43	14.79	15.46	14.15[d]	14.76[d]	21.51[f]
	$\Gamma \to$ L	16.97	20.49	21.16	–	–	–
	$\Gamma \to$ X	18.27	21.85	22.56	–	–	–
Ar	$\Gamma \to \Gamma$	8.19	9.65	10.09	9.61[d]	9.95[d]	14.15[f]
	$\Gamma \to$ L	11.06	12.22	12.60	–	–	–
	$\Gamma \to$ X	10.86	12.08	12.49	–	–	–

[a] Reference 40 [b] Reference 132 [c] Reference 37
[d] Reference 133 [e] Reference 91 [f] Reference 94

Table 6.3.: KS transition energies (in eV) obtained with the local EXX and EXXc potentials and an 8×8×8 **k**-point sampling. For comparison, plane-wave PP results and experimental values from the literature are given.

6.6. EXX approach and the band gap problem of DFT: the III-V nitrides

In the previous section, we already compared KS eigenvalue differences with experimental transition energies. We will focus in the following on a particular transition of the KS system, namely the KS band gap, and its relation to the fundamental band gap of the true interacting system. The fundamental band gap is defined in terms of the total energy of the $N+1$, N, and $N-1$ electron systems

$$E_{\text{gap}} = E(N+1) + E(N-1) - 2E(N)\,, \tag{6.25}$$

whereas the KS gap is given by the eigenvalue difference of the lowest unoccupied and highest occupied KS state. The definition of the fundamental band gap (6.25) in terms of total energy differences reveals that it is in principle exactly accessible in ground-state DFT. For an infinite periodic system, however, the addition of a single electron to the system – instead of one electron per unit cell – is not practicable. However, Perdew *et al.* [134] showed by a generalization of DFT to non-integer particle numbers, that the exact total energy exhibits a linear behavior as a function of the particle number between two integer particle numbers and a derivative discontinuity at N [s. Fig. (6.9)]. The slope of the line connecting the total energy of the $N-1$ and N electron system equals the ionization energy $-I$

$$-I = E(N) - E(N-1)\,, \tag{6.26}$$

whereas the slope between the N and $N+1$ electron system corresponds to the electron affinity $-A$

$$-A = E(N+1) - E(N)\,. \tag{6.27}$$

The fundamental gap in Eq. (6.25) can thus be written as the difference of total-energy derivatives from the right and left evaluated at N and at the ground-state density n_0

$$E_{\text{gap}} = -A + I = \left(\left.\frac{\delta E}{\delta N}\right|_{N\to N+1,n_0} - \left.\frac{\delta E}{\delta N}\right|_{N\to N-1,n_0} \right). \tag{6.28}$$

The additional constraint that the derivatives have to be taken at the ground-state density n_0 is equivalent to the formulation that the addition or removal of the electron takes place at fixed effective KS potential and thus fixed KS orbitals because the density n_0 determines the KS potential (up to a constant). Hence, the change in the particle number at fixed density n_0 is only associated with the occupation of a previously unoccupied KS level or with the

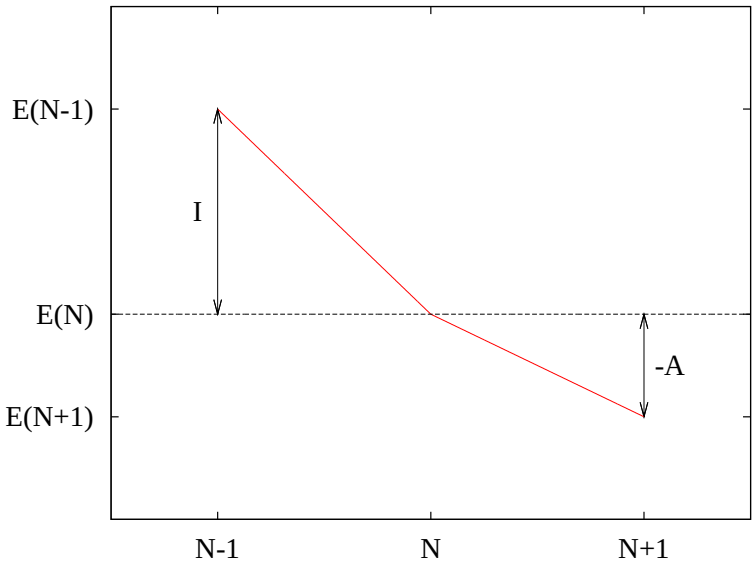

Figure 6.9.: The linear behavior of the total energy for fractional particle numbers between two subsequent integers is shown and the derivative discontinuity (kink) at N becomes visible.

emptying of a previously occupied state. With this in mind, the fundamental gap can be finally written as the KS band gap $E_{\text{gap}}^{\text{KS}}$ plus a derivative discontinuity Δ_{xc} of the xc energy functional [69, 135, 136]

$$E_{\text{gap}} = E_{\text{gap}}^{\text{KS}} + \Delta_{\text{xc}} , \tag{6.29}$$

where the latter is given by

$$\Delta_{\text{xc}} = \left(\frac{\delta E_{\text{xc}}}{\delta N}\bigg|_{N\to N+1,n_0} - \langle \phi_{N+1}|V_{\text{xc}}|\phi_{N+1}\rangle \right) - \left(\frac{\delta E_{\text{xc}}}{\delta N}\bigg|_{N\to N-1,n_0} - \langle \phi_{N-1}|V_{\text{xc}}|\phi_{N-1}\rangle \right) . \tag{6.30}$$

Here, ϕ_N and ϕ_{N+1} denote the highest occupied and lowest unoccupied KS orbitals and V_{xc} is the local xc potential. In the case of the LDA or GGA, this discontinuity Δ_{xc} is exactly zero. According to Eq. (6.29), the LDA and GGA KS band gap should then coincide with the true fundamental band gap. Yet, it is well known that both approximations underestimate the experimental gap by about 40% or even more, which is often called the band-gap problem of LDA and GGA [10].

For the EXX-OEP functional the discontinuity Δ_{xc} does not vanish. Instead it is given

by [23, 136]

$$\Delta_{\mathrm{x}}^{\mathrm{EXX}} = \left(\langle\phi_{N+1}|V_{\mathrm{x}}^{\mathrm{NL}}|\phi_{N+1}\rangle - \langle\phi_{N+1}|V_{\mathrm{x}}|\phi_{N+1}\rangle\right) - \left(\langle\phi_{N-1}|V_{\mathrm{x}}^{\mathrm{NL}}|\phi_{N-1}\rangle - \langle\phi_{N-1}|V_{\mathrm{x}}|\phi_{N-1}\rangle\right) . \tag{6.31}$$

In the following, we demonstrate for the III-V nitrides in their zincblende structure and rock-salt ScN that the discontinuity $\Delta_{\mathrm{x}}^{\mathrm{EXX}}$ results in a substantial, positive contribution to the fundamental band gap, with the consequence that the sum of the KS band gap and the discontinuity [Eq. (6.29)] strongly overestimates the experimental gap.

Table 6.4 shows that the LDA seriously underestimates the experimental gap. For InN and ScN it even predicts a metal. The EXX functional, instead, gives KS band gaps, which are closer to the experimental value. In particular, InN and ScN are correctly predicted to be semiconductors. But the discontinuity $\Delta_{\mathrm{x}}^{\mathrm{EXX}}$ amounts to several eV for these materials so that the fundamental gap [Eq. (6.29)] overshoots the experimental value quite drastically. The fundamental gap in the HF and the EXX approach, on the contrary, are very similar. As the discontinuity in Eq. (6.31) is formally equivalent to the linear change of the KS band gap if one replaces the local EXX potential by the non-local HF-like potential, the difference between EXX and HF gap merely arises from the additional self-consistency in the HF gap. The similarity of EXX and HF band gap can be explained alternatively by the observation that HF and EXX total energies are nearly identical. For example, we found for diamond that the HF total energy is merely 0.24 eV smaller than the total energy in the EXX approach. Due to the definition of the fundamental gap in terms of total-energy differences [Eq. (6.25)] and the similarity of the HF and EXX total energies, it is obvious that the EXX and HF gaps must be similar, too. Yet, the question arises why does the EXX KS band gap alone give a quantitatively good estimate for the experimental band gap? The EXX method completely ignores correlation. The usage of LDA correlation in combination with EXX leads to a slight increase of the KS band gap but does not contribute to the derivative discontinuity except indirectly through a change in the KS wave function. Consequently, the EXXc approach leads to an overestimation of the experimental fundamental gap, as well. Instead, a correlation functional, that is compatible with the orbital-dependent EXX functional, is required. Grüning *et al.* [12] combined the EXX-OEP approach with a correlation functional in the random-phase approximation (RPA) and showed that the effect of an orbital-dependent correlation functional is twofold: on the one hand, the KS band gap is decreased in comparison to that in the EXX approach. It becomes comparable with the LDA KS band gap again. On the other hand, the discontinuity arising from the EXX and the RPA correlation functional shrinks. As a consequence, the combination of both, KS band gap and derivative discontinuity, leads to a fundamental gap that is in excellent agreement with experiment (at least for the systems examined in Ref. 12).

		E_{gap}^{LDA}	$E_{gap}^{KS,EXX(c)}$	$\Delta_x^{EXX(c)}$	$E_{gap}^{EXX(c)}$	E_g^{HF}	Expt.
BN	indirect	4.34	5.42 (5.58)	8.02 (8.09)	13.44 (13.67)	14.03	6.4[a]
AlN	indirect	3.22	4.77 (4.96)	7.08 (7.17)	11.85 (12.13)	12.23	5.3[b]
GaN	direct	1.76	3.11 (3.24)	6.98 (7.06)	10.09 (10.30)	10.87	3.27[c]
InN	direct	−0.41	0.98 (1.12)	5.44 (5.55)	6.42 (6.67)	7.46	0.60[d]
ScN	indirect	−0.14	1.58 (1.67)	5.99 (6.06)	7.57 (7.73)	8.27	1.3[e]

[a]Reference 137 [b]Reference 138 [c]Reference 139
[d]Reference 140 [e]Reference 141

Table 6.4.: Fundamental band gap for the III-V nitrides in their zincblende structure and rock-salt ScN with the LDA, the EXX, and the EXXc functionals of DFT. Consideration of the derivative discontinuity of the EXX(c) functional leads to fundamental band gaps, which are very close to the corresponding HF values.

So, we conclude that in the EXX approach a fortuitous error cancellation between the neglect of orbital correlation and the neglect of the discontinuity Δ_x^{EXX} results in an EXX KS band gap that is quantitatively close to the experimental one.

6.7. Finite basis correction (FBC)

So far, EXX-OEP calculations are computationally demanding because of two reasons: (a) the calculation of the matrix elements of the non-local exchange potential $V_x^{NL,\sigma}$, which enter on the right-hand side of Eq. (6.9), is, despite our techniques developed in chapter 5, an enormous computational task for a periodic solid; (b) the demand of a very flexible LAPW basis in order to obtain a physical and stable EXX calculation makes the scheme even more expensive, as a flexible LAPW basis is equivalent to a large number of unoccupied states, which in turn means that the matrix elements of $V_x^{NL,\sigma}$ have to be evaluated for a large number of unoccupied KS states. The high quality of the LAPW basis is required as demonstrated in section 6.3 to lend the KS wave functions and thus the density sufficient flexibility to react to changes in the effective potential. In the following, we derive and examine a numerical correction, the finite basis correction (FBC), for the wave-function and density response function that arises from the observation that the LAPW basis functions themselves depend on the effective potential.

6.7.1. Derivation of the FBC

The LAPW basis functions $\varphi^{\sigma}_{\mathbf{kG}}(\mathbf{r})$ [Eq. (4.9)] do not depend on the potential in the interstitial region. However, the radial functions $u^{a\sigma}_{lp}(r)$ in the MT spheres are the solutions of the spherical Schrödinger equations (4.2) and (4.10) and thus adjusted to the spherical part of the effective potential. Hence, the response of the KS wave function $\phi^{\sigma}_{n\mathbf{k}}(\mathbf{r}) = \sum_{\mathbf{G}} z^{\sigma}_{\mathbf{G}}(n,\mathbf{k})\varphi^{\sigma}_{\mathbf{kG}}(\mathbf{r})$ to a variation in the effective potential $V^{\sigma}_{\text{eff}}(\mathbf{r}')$ consists, in principle, of two contributions

$$\frac{\delta\phi^{\sigma}_{n\mathbf{k}}(\mathbf{r})}{\delta V^{\sigma}_{\text{eff}}(\mathbf{r}')} = \sum_{\mathbf{G}} \frac{\delta z^{\sigma}_{\mathbf{G}}(n,\mathbf{k})}{\delta V^{\sigma}_{\text{eff}}(\mathbf{r}')}\varphi^{\sigma}_{\mathbf{kG}}(\mathbf{r}) + z^{\sigma}_{\mathbf{G}}(n,\mathbf{k})\frac{\delta\varphi^{\sigma}_{\mathbf{kG}}(\mathbf{r})}{\delta V^{\sigma}_{\text{eff}}(\mathbf{r}')}\,, \tag{6.32}$$

where the first describes the response of the eigenvector $z^{\sigma}_{\mathbf{G}}(n,\mathbf{k})$ and the second arises from the change in the LAPW basis function. In order to derive a formula for the wave function response $\delta\phi^{\sigma}_{n\mathbf{k}}(\mathbf{r})/\delta V^{\sigma}_{\text{eff}}(\mathbf{r}')$ that considers the dependence of the LAPW basis as well as of the eigenvector on the effective potential, we employ first-order perturbation theory in the following.

Let $\phi^{\sigma}_{n\mathbf{k}}(\mathbf{r},\lambda)$ be the solution of the perturbed Hamiltonian $H(\lambda)$

$$H(\lambda)\phi^{\sigma}_{n\mathbf{k}}(\mathbf{r},\lambda) = \left[H_0 + \lambda V^{\sigma\prime}_{\text{eff}}(\mathbf{r})\right]\phi^{\sigma}_{n\mathbf{k}}(\mathbf{r},\lambda) = \epsilon^{\sigma}_{n\mathbf{k}}(\lambda)\phi^{\sigma}_{n\mathbf{k}}(\mathbf{r},\lambda) \tag{6.33}$$

with the perturbation $\lambda V^{\sigma\prime}_{\text{eff}}(\mathbf{r})$ and eigenvalue $\epsilon^{\sigma}_{n\mathbf{k}}(\lambda)$. Expansion of $\phi^{\sigma}_{n\mathbf{k}}(\mathbf{r},\lambda)$ and $\epsilon_{n\mathbf{k}}(\lambda)$ in the perturbation strength λ under the consideration that the basis set $\{\varphi^{\sigma}_{\mathbf{kG}}\}$ for the wave functions itself depends on the perturbation yields

$$\begin{aligned}
\phi^{\sigma}_{n\mathbf{k}}(\mathbf{r},\lambda) &= \sum_{\mathbf{G}}\left[z^{\sigma 0}_{\mathbf{G}}(n,\mathbf{k}) + \lambda z^{\sigma 1}_{\mathbf{G}}(n,\mathbf{k}) + \dots\right]\left[\varphi^{\sigma 0}_{\mathbf{kG}}(\mathbf{r}) + \lambda\varphi^{\sigma 1}_{\mathbf{kG}}(\mathbf{r}) + \dots\right] && \text{(6.34a)}\\
&= \phi^{\sigma 0}_{n\mathbf{k}}(\mathbf{r}) + \lambda\sum_{\mathbf{G}}\left[z^{\sigma 1}_{\mathbf{G}}(n,\mathbf{k})\varphi^{\sigma 0}_{\mathbf{kG}}(\mathbf{r}) + z^{\sigma 0}_{\mathbf{G}}(n,\mathbf{k})\varphi^{\sigma 1}_{\mathbf{kG}}(\mathbf{r})\right] + \mathcal{O}(\lambda^2) && \text{(6.34b)}\\
\epsilon^{\sigma}_{n\mathbf{k}}(\lambda) &= \epsilon^{\sigma 0}_{n\mathbf{k}} + \lambda\epsilon^{\sigma 1}_{n\mathbf{k}} + \mathcal{O}(\lambda^2)\,. && \text{(6.34c)}
\end{aligned}$$

We label the unperturbed quantities with an index 0. The higher order terms obtain an index according to their order.

The linear change of the wave function consists of two contributions: (a) the part that results from a change in the eigenvector which we abbreviate with $\phi^{\sigma 1}_{n\mathbf{k}}(\mathbf{r}) = \sum_{\mathbf{G}} z^{\sigma 1}_{\mathbf{G}}(n,\mathbf{k})\varphi^{\sigma 0}_{\mathbf{kG}}(\mathbf{r})$, and (b) the change that arises from the linear change of the basis function. The latter is denoted with $\tilde{\phi}^{\sigma 1}_{n\mathbf{k}}(\mathbf{r}) = \sum_{\mathbf{G}} z^{\sigma 0}_{\mathbf{G}}(n,\mathbf{k})\phi^{\sigma 1}_{\mathbf{kG}}(\mathbf{r})$. Let us assume for a while that $\tilde{\phi}^{\sigma 1}_{n\mathbf{k}}(\mathbf{r})$ is known. Its calculation will be discussed later.

Insertion of Eqs. (6.34b) and (6.34c) into (6.33) gives in zeroth order the unperturbed prob-

lem. The first order terms in λ yield a equation for $\phi^{\sigma 1}_{n\mathbf{k}}(\mathbf{r})$

$$H_0[\phi^{\sigma 1}_{n\mathbf{k}}(\mathbf{r}) + \tilde{\phi}^{\sigma 1}_{n\mathbf{k}}(\mathbf{r})] + V^{\sigma\prime}_{\text{eff}}(\mathbf{r})\phi^{\sigma 0}_{n\mathbf{k}}(\mathbf{r}) = \epsilon^{\sigma 0}_{n\mathbf{k}}[\phi^{\sigma 1}_{n\mathbf{k}}(\mathbf{r}) + \tilde{\phi}^{\sigma 1}_{n\mathbf{k}}(\mathbf{r})] + \epsilon^{\sigma 1}_{n\mathbf{k}}\phi^{\sigma 0}_{n\mathbf{k}}(\mathbf{r})\,. \quad (6.35)$$

By its definition $\phi^{\sigma 1}_{n\mathbf{k}}(\mathbf{r})$ lies in the Hilbert space spanned by the original LAPW functions $\varphi^{\sigma 0}_{\mathbf{kG}}(\mathbf{r})$. Hence, a representation of $\phi^{\sigma 1}_{n\mathbf{k}}(\mathbf{r})$ in terms of the unperturbed wave functions $\phi^{\sigma 0}_{n\mathbf{k}}(\mathbf{r})$, which span the same Hilbert space as $\varphi^{\sigma 0}_{\mathbf{kG}}(\mathbf{r})$, is possible without a loss of information

$$\phi^{\sigma 1}_{n\mathbf{k}}(\mathbf{r}) = \sum_{n'} \langle \phi^{\sigma 0}_{n'\mathbf{k}} | \phi^{\sigma 1}_{n\mathbf{k}} \rangle \phi^{\sigma 0}_{n'\mathbf{k}}(\mathbf{r})\,. \quad (6.36)$$

By projecting Eq. (6.35) onto $\phi^{\sigma 0}_{n'\mathbf{k}}$ $(n' \neq n)$ the expansion coefficients are obtained

$$\langle \phi^{\sigma 0}_{n'\mathbf{k}} | \phi^{\sigma 1}_{n\mathbf{k}} \rangle = \frac{\langle \phi^{\sigma 0}_{n'\mathbf{k}} | V^{\sigma\prime}_{\text{eff}} | \phi^{\sigma 0}_{n\mathbf{k}} \rangle}{\epsilon^{\sigma 0}_{n\mathbf{k}} - \epsilon^{\sigma 0}_{n'\mathbf{k}}} - \langle \phi^{\sigma 0}_{n'\mathbf{k}} | \tilde{\phi}^{\sigma 1}_{n\mathbf{k}} \rangle\,. \quad (6.37)$$

For the case of $n' = n$ the normalization of $\phi^{\sigma}_{n\mathbf{k}}(\mathbf{r}, \lambda)$ requires that

$$\langle \phi^{\sigma 0}_{n\mathbf{k}} | \phi^{\sigma 1}_{n\mathbf{k}} \rangle = -\langle \phi^{\sigma 0}_{n\mathbf{k}} | \tilde{\phi}^{\sigma 1}_{n\mathbf{k}} \rangle \quad (6.38)$$

holds. In conclusion, the first-order change of the KS wave function becomes

$$\begin{aligned} \phi^{\sigma 1}_{n\mathbf{k}}(\mathbf{r}) + \tilde{\phi}^{\sigma 1}_{n\mathbf{k}}(\mathbf{r}) &= \sum_{n' \neq n} \frac{\langle \phi^{\sigma 0}_{n'\mathbf{k}} | V^{\sigma\prime}_{\text{eff}} | \phi^{\sigma 0}_{n\mathbf{k}} \rangle}{\epsilon^{\sigma 0}_{n\mathbf{k}} - \epsilon^{\sigma 0}_{n'\mathbf{k}}} \phi^{\sigma 0}_{n'\mathbf{k}}(\mathbf{r}) \\ &\quad + \int d^3 r' \left(\delta(\mathbf{r} - \mathbf{r}') - \sum_{n'} \phi^{\sigma 0}_{n'\mathbf{k}}(\mathbf{r}) \phi^{\sigma 0 *}_{n'\mathbf{k}}(\mathbf{r}') \right) \tilde{\phi}^{\sigma 1}_{n\mathbf{k}}(\mathbf{r}'). \end{aligned} \quad (6.39)$$

The first term is the usual expression from first-order perturbation theory, that runs over a finite number N of available states in a practical calculation. The second term, the FBC, arises from the dependence of the LAPW basis on the effective potential. It corrects the incompleteness of the basis. In the limit of a complete basis corresponding to an infinite number of states $(N \to \infty)$, the expression in the brackets would vanish and the first term would give the exact result.[2]

We now turn to the calculation of the linear change of the LAPW basis $\varphi^{\sigma 1}_{\mathbf{kG}}(\mathbf{r})$ due to the perturbing potential $V^{\sigma\prime}_{\text{eff}}$, which is required for the calculation of $\tilde{\phi}^{\sigma 1}_{n\mathbf{k}}(\mathbf{r}) = \sum_{\mathbf{G}} z^{\sigma 0}_{\mathbf{G}}(n, \mathbf{k}) \varphi^{\sigma 1}_{\mathbf{kG}}(\mathbf{r})$. According to the definition of the LAPW basis functions, their linear

[2] By starting the derivation from the differential form of the Schrödinger equation (6.33) we implicitly assume that the zero order wave functions $\phi^{\sigma 0}_{n\mathbf{k}}(\mathbf{r})$ are exact pointwise solutions of the Hamiltonian H_0. In practice, this is not the case, as only a finite LAPW basis is employed for representing the wave functions. It will lead to an additional correction, which is however much smaller than the derived FBC.

response is only non-zero in the MT spheres. While the radial LAPW functions $u_{lp}^{a\sigma}(r)$ can in principle respond to spherical and non-spherical variations of the potential, we restrict ourselves to spherical potential variations. The linear change of the LAPW basis function $\varphi_{\mathbf{kG}}^{\sigma}(\mathbf{r})$ due to the spherical perturbation $V_{\mathrm{eff},0}^{\sigma\prime}(r)$ is given by

$$\varphi_{\mathbf{kG}}^{\sigma 1}(\mathbf{r}) = \begin{cases} 0 & \text{if } \mathbf{r} \in \mathrm{IR} \\ \sum_{lmp} \Big[A_{lmp}^{a\sigma}(\mathbf{k},\mathbf{G}) u_{lp}^{a\sigma 1}(|\mathbf{r}-\mathbf{R}_a|) \\ \qquad + A_{lmp}^{a\sigma 1}(\mathbf{k},\mathbf{G}) u_{lp}^{a\sigma}(|\mathbf{r}-\mathbf{R}_a|) \Big] Y_{lm}(\widehat{\mathbf{r}-\mathbf{R}_a}) & \text{if } \mathbf{r} \in \mathrm{MT}(a) \end{cases} . \tag{6.40}$$

The index p subsumes the different radial LAPW functions [cf. Eq. (4.20)] and accordingly $A_{lmp}^{a\sigma}(\mathbf{k},\mathbf{G})$ comprises the matching coefficients Eqs. (4.11) and (4.12). The quantities $u_{lp}^{a\sigma 1}(r)$ and $A_{lmp}^{a\sigma 1}(\mathbf{k},\mathbf{G})$ denote the linear change of the radial function and the matching coefficient, respectively, due to the perturbation $V_{\mathrm{eff},0}^{\sigma\prime}(r)$. The radial functions $u_{lp}^{a\sigma 1}(r)$ are obtained from linearizing Eqs. (4.2) and (4.10). This finally results in the following differential equations

$$\left[-\frac{1}{2}\frac{\partial^2}{\partial r^2} + \frac{l(l+1)}{2r^2} + V_{0,\mathrm{eff}}^{a\sigma}(r) - \epsilon_l^{a\sigma} \right] r u_{l0}^{a\sigma 1}(r) = \left[\epsilon_l^{a\sigma 1} - V_{\mathrm{eff},0}^{a\sigma\prime}(r) \right] r u_{l0}^{a\sigma}(r) \tag{6.41}$$

$$\left[-\frac{1}{2}\frac{\partial^2}{\partial r^2} + \frac{l(l+1)}{2r^2} + V_{0,\mathrm{eff}}^{a\sigma}(r) - \epsilon_l^{a\sigma} \right] r u_{l1}^{a\sigma 1}(r) = \left[\epsilon_l^{a\sigma 1} - V_{\mathrm{eff},0}^{a\sigma\prime}(r) \right] r u_{l1}^{a\sigma}(r) + r u_{l0}^{a\sigma 1}(r) . \tag{6.42}$$

The variation of the energy parameter $\epsilon_l^{a\sigma 1}$ due to the perturbing potential $V_{\mathrm{eff},0}^{a\sigma\prime}(r)$ is given by the expectation value

$$\epsilon_l^{a\sigma 1} = \langle u_{l0}^{a\sigma} | V_{\mathrm{eff},0}^{a\sigma\prime} | u_{l0}^{a\sigma} \rangle . \tag{6.43}$$

The scalar-relativistic analogs to Eqs. (6.41) and (6.42) are deferred to Appendix B. The radial inhomogeneous differential equations can be solved in a similar way as the differential equations for $u_{lp}^{a\sigma}(r)$ by integrating from the origin $r = 0$ to the MT boundary $r = S^a$. However, the resulting solutions are not defined uniquely, as we can always add the homogeneous solution or a multiple of it. But, the normalization of $u_{l0}^{a\sigma}(r)$ imposes the additional conditions

$$\int r^2 u_{l0}^{a\sigma}(r) u_{l0}^{a\sigma 1}(r)\, dr = 0 \tag{6.44}$$

and

$$\int r^2 u_{l0}^{a\sigma}(r) u_{l1}^{a\sigma 1}(r)\, dr = -\int r^2 u_{l1}^{a\sigma}(r) u_{l0}^{a\sigma 1}(r)\, dr . \tag{6.45}$$

These equations finally fix the freedom and lead to a well defined solution. Eq. (6.43) together with (6.44) and (6.45) ensure that for a constant potential variation $V_{\mathrm{eff},0}^{a\sigma\prime}(r)$ the linear change

$u_{lp}^{a\sigma 1}(r)$ vanishes.

The calculation of the linear change in the matching coefficients $A_{lmp}^{a\sigma 1}(\mathbf{k},\mathbf{G})$ is straightforward after the radial functions $u_{lp}^{a\sigma 1}(r)$ are calculated. Differentiation of Eqs. (4.11) and (4.12) results in

$$\begin{aligned} A_{lmp}^{a\sigma 1}(\mathbf{k},\mathbf{G}) \;=\; & \frac{4\pi}{\sqrt{\Omega}} i^l Y_{lm}^*(\mathbf{k}+\mathbf{G}) \exp[i(\mathbf{k}+\mathbf{G})\mathbf{R}_a] \Bigg\{ \frac{(-1)^{p+1}}{[u_{l1}^{a\sigma}(S^a), u_{l0}^{a\sigma}(S^a)]} \\ & \times [u_{l\overline{p}}^{a\sigma 1}(S^a), j_l(|\mathbf{k}+\mathbf{G}|S^a)] - \frac{(-1)^{p+1}}{[u_{l1}^{a\sigma}(S^a), u_{l0}^{a\sigma}(S^a)]^2} \\ & \times [u_{l\overline{p}}^{a\sigma}(S^a), j_l(|\mathbf{k}+\mathbf{G}|S^a)] \left([u_{l1}^{a\sigma 1}(S^a), u_{l0}^{a\sigma}(S^a)] + [u_{l1}^{a\sigma}(S^a), u_{l0}^{a\sigma 1}(S^a)] \right) \Bigg\}, \end{aligned} \tag{6.46}$$

where $j_l(r)$ is the spherical Bessel function, $\overline{p} = 1 - p$, and the square brackets denote the Wronskian as defined in Eq. (4.13).

Finally, all constituents for the construction of $\varphi_{\mathbf{kG}}^{\sigma 1}(\mathbf{r})$ [Eq. (6.40)] are at hand. The resulting functions $\varphi_{\mathbf{kG}}^{\sigma 1}(\mathbf{r})$ and their radial derivatives go continuously to zero at the MT sphere boundary. A convolution of $\varphi_{\mathbf{kG}}^{\sigma 1}(\mathbf{r})$ with the wave function coefficients $z_{\mathbf{G}}^{\sigma 0}(n,\mathbf{k})$ finally yields the linear change in the wave function $\tilde{\phi}_{n\mathbf{k}}^{\sigma 1}(\mathbf{r})$ that results from the change in the LAPW basis functions. So, all quantities occurring in Eq. (6.39) are known and the full response, comprising the change in the eigenvector and in the LAPW basis function, can be calculated.

Our derivation, so far, only concerns the augmented plane waves Eq. (4.9). But the considerations can easily be generalized to include the local orbitals.

In contrast to that, the core-state response requires a different treatment. The core states are bound so tightly that they are confined to the MT spheres. This enables to describe them atomic-like, i.e., they are obtained by solving a fully-relativistic Dirac equation with the spherical average of the effective potential under the boundary condition that the radial eigenfunctions vanish in the limit $r \to \infty$. Under this condition, the radial Dirac equation only features solutions at certain discrete energies, the core energies. Instead of solving an inhomogeneous Dirac equation for the response of the radial core wave function, in analogy to Eqs. (6.41) and (6.42), we simply use a finite difference approach. For the potentials $V_{\mathrm{eff},0}^{a\sigma}(r) + \frac{\lambda}{2} V_{\mathrm{eff},0}^{a\sigma\prime}(r)$ and $V_{\mathrm{eff},0}^{a\sigma}(r) - \frac{\lambda}{2} V_{\mathrm{eff},0}^{a\sigma\prime}(r)$ we solve the Dirac equation with the conventional core solver, then take the difference between the two core wave functions and divide by λ. The finite difference approximates the response of the core wave function due to the perturbing potential $V_{\mathrm{eff},0}^{a\sigma\prime}(r)$. The accuracy of the finite-difference approach can be controlled by the parameter λ. Typically $\lambda = 0.0001$ is a good choice. In a similar way, we can construct the linear response of the core eigenenergies.

A comparison of the change in the core eigenvalue either calculated with the finite dif-

a	n	l	ϵ^{a1}_{nl}	$\langle\phi^a_{nl}\|V^{a\prime}_{\mathrm{eff},0}\|\phi^a_{nl}\rangle$
Sc	1	s	-1.857556	-1.857558
	2	s	-0.652439	-0.652438
	2	p	-0.670492	-0.670285
N	1	s	-0.614899	-0.614899

Table 6.5.: Comparison of the core-energy response due to a perturbation $V^{a\prime}_{\mathrm{eff},0}$ for the case of ScN obtained, on the one hand, with the finite difference approach ϵ^{a1}_{nl} (as described in the text) and, on the other hand, by the analytical formula $\langle\phi^a_{nl}|V^{a\prime}_{\mathrm{eff},0}|\phi^a_{nl}\rangle$.

ference approach or by the analytical formula $\langle\phi^{a\sigma}_{nl}|V^{a\sigma\prime}_{\mathrm{eff},0}|\phi^{a\sigma}_{nl}\rangle$ reveals the accuracy of this approach [s. Table (6.5)]. Here, $\phi^{a\sigma}_{nl}$ denotes a core state of atom a, principal quantum number n, angular momentum l, and spin σ. It is obtained by averaging over the solutions of the Dirac equation with total angular momentum $j = l + 1/2$ and $j = l - 1/2$, which corresponds to a non-relativistic description of the core states.

The consideration of the FBC for the KS wave-function response leads to additional terms in the density response matrix (6.16)

$$\begin{aligned}\chi^{\sigma}_{\mathrm{s},IJ} &= 2\sum_{n\mathbf{k}}^{\text{occ.}}\sum_{n'\le N}^{\text{unocc.}}\frac{\langle M_I\phi^{\sigma}_{n\mathbf{k}}|\phi^{\sigma}_{n'\mathbf{k}}\rangle\langle\phi^{\sigma}_{n'\mathbf{k}}|\phi^{\sigma}_{n\mathbf{k}}M_J\rangle}{\epsilon^{\sigma}_{n\mathbf{k}}-\epsilon^{\sigma}_{n'\mathbf{k}}}\\ &\quad+2\sum_{n\mathbf{k}}^{\text{occ.}}\left[\langle M_I\phi^{\sigma}_{n\mathbf{k}}|\tilde{\phi}^{\sigma}_{n\mathbf{k}J}\rangle-\sum_{n'\le N}\langle M_I\phi^{\sigma}_{n\mathbf{k}}|\phi^{\sigma}_{n'\mathbf{k}}\rangle\langle\phi^{\sigma}_{n'\mathbf{k}}|\tilde{\phi}^{\sigma}_{n\mathbf{k}J}\rangle\right]\end{aligned} \tag{6.47}$$

and the vector of the right-hand side (6.17)

$$\begin{aligned}t^{\sigma}_{I} &= 2\sum_{n\mathbf{k}}^{\text{occ.}}\sum_{n'\le N}^{\text{unocc.}}\langle\phi^{\sigma}_{n\mathbf{k}}|V^{\mathrm{NL},\sigma}_{\mathrm{x}}|\phi^{\sigma}_{n'\mathbf{k}}\rangle\frac{\langle M_I\phi^{\sigma}_{n'\mathbf{k}}|\phi^{\sigma}_{n\mathbf{k}}\rangle}{\epsilon^{\sigma}_{n\mathbf{k}}-\epsilon^{\sigma}_{n'\mathbf{k}}}\\ &\quad+2\sum_{n\mathbf{k}}^{\text{occ.}}\left[\langle\phi^{\sigma}_{n\mathbf{k}}|V^{\mathrm{NL},\sigma}_{\mathrm{x}}|\tilde{\phi}^{\sigma}_{n\mathbf{k}I}\rangle-\sum_{n'\le N}\langle\phi^{\sigma}_{n\mathbf{k}}|V^{\mathrm{NL},\sigma}_{\mathrm{x}}|\phi^{\sigma}_{n'\mathbf{k}}\rangle\langle\phi^{\sigma}_{n'\mathbf{k}}|\tilde{\phi}^{\sigma}_{n\mathbf{k}I}\rangle\right].\end{aligned} \tag{6.48}$$

Since in our formalism the linear change of the effective potential $V^{\sigma\prime}_{\mathrm{eff}}(\mathbf{r})$ is represented by the MPB, the additional index J in $\tilde{\phi}^{\sigma}_{n\mathbf{k}J}(\mathbf{r})$ stands for the MPB function $M_J(\mathbf{r})$. We note that the functions $\tilde{\phi}^{\sigma}_{n\mathbf{k}J}(\mathbf{r})$ are non-zero only for spherical MT functions $M_J(\mathbf{r})$.

In its present form, the expression in Eq. (6.47) breaks the Hermiticity of $\chi^{\sigma}_{\mathrm{s},IJ}$ because the additional term is slightly asymmetric in the indices I and J. We make $\chi^{\sigma}_{\mathrm{s},IJ}$ explicitly

Hermitian by averaging over $\chi^{\sigma}_{s,IJ}$ and $\chi^{\sigma *}_{\mathrm{s},JI}$.

6.7.2. Effect of the FBC for the example of ScN

In the following, the effect of the FBC on the convergence and stability of the EXX potential is demonstrated for the case of ScN. Before, however, we analyze the improved convergence of the single-particle response function $\chi^{\sigma}_{\mathrm{s}}$ due to the FBC.

We will refer to the first term of Eq. (6.47) as the sum-over-states (SOS) expression and to the second one as the FBC. For our analysis we split up Eq. (6.47) into a core and valence electron response part

$$\chi^{\sigma}_{\mathrm{s},IJ} = \chi^{\sigma v}_{\mathrm{s},IJ} + \chi^{\sigma c}_{\mathrm{s},IJ}\,, \tag{6.49}$$

where the sum over the occupied states in Eq. (6.47) is either restricted to the valence (v) or core (c) states. The contribution of the core electrons to the density response function will be discussed later on. Figure 6.10 shows the trace of the matrix $\chi^{\sigma v}_{\mathrm{s},IJ}$ as a function of the number of local orbitals added to the LAPW basis. n_{LO} denotes the number of local orbitals per lm channel and atom for $l = 0, \ldots, 4$ and $|m| \leq l$. Consequently, $n_{\mathrm{LO}} = 0$ corresponds to the conventional LAPW basis for ScN with a reciprocal cutoff of $G_{\max} = 3.8\,\mathrm{a}_0^{-1}$ and $l_{\max} = 8$. The $3s$ and $3p$ semi-core states of Sc are treated explicitly as valence electrons and a 4×4×4 **k**-point sampling has been employed. As the FBC is only non-zero for those diagonal elements $\chi^{\sigma}_{\mathrm{s},II}$, which correspond to spherical MT MPB functions, we restrict the trace $\mathrm{tr}(\chi_{\mathrm{s}}) = \sum_I \chi_{\mathrm{s},II}$ to these functions. Figure 6.10(a) demonstrates the slow convergence of the SOS expression (green dashed curve). It reflects the importance of adding local orbitals to describe the valence-density response adequately. The curve corresponding to the SOS expression is monotonically decreasing. In contrast, the trace of the FBC (dotted blue curve) is monotonically increasing. While the LAPW basis becomes more and more complete towards $n_{\mathrm{LO}} = 6$ the FBC becomes smaller and smaller. The sum of the two curves (red solid line) is nearly constant. The inset of Fig. 6.10(a) shows that the sum hardly shows any convergence at all. The convergence, that is achieved by the SOS expression alone with $n_{\mathrm{LO}} = 6$, is obtained in the sum of SOS and FBC with $n_{\mathrm{LO}} = 0$. Taking into account a single set of local orbitals $(n_{\mathrm{LO}} = 1)$ results in an accuracy, which would be difficult to achieve with the SOS expression alone.

So far, we have demonstrated that the combination of SOS expression and FBC leads to a converged spherical response function at much smaller LAPW basis sets. The question arises if the FBC allows to reduce the number of bands N that enter in the SOS and the FBC term in Eq. (6.47), as well. Indeed, the number of unoccupied bands can be chosen much smaller as shown in Fig. 6.10(b). For these calculations we have employed six local

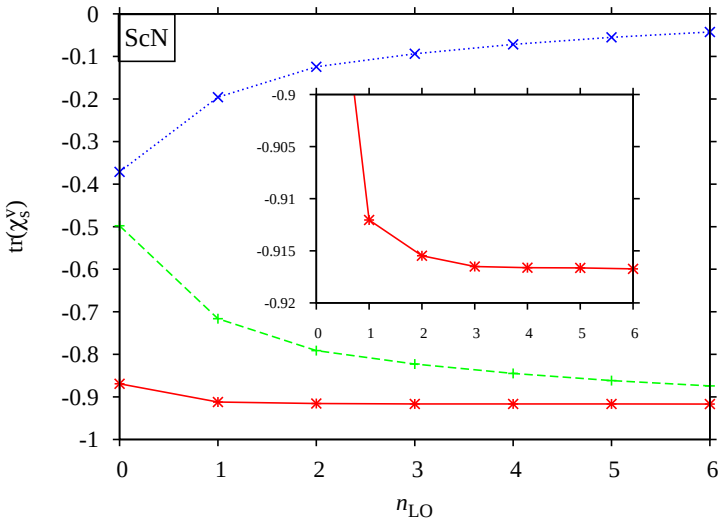

(a)

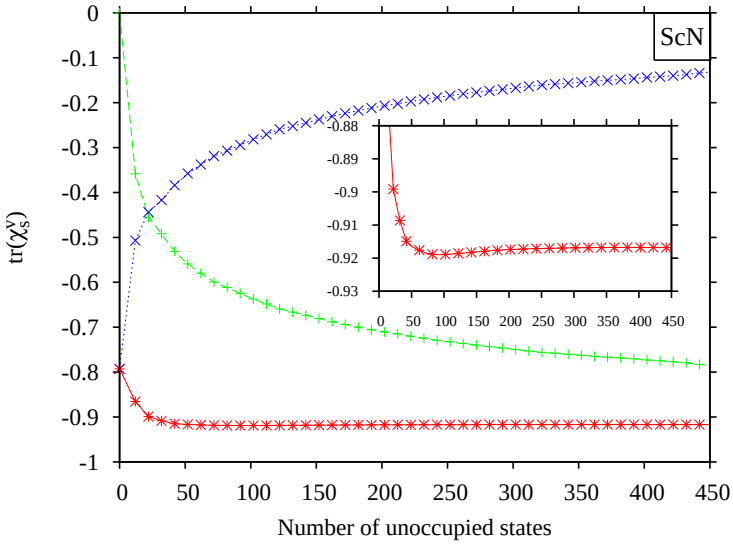

(b)

Figure 6.10.: Convergence of $\mathrm{tr}(\chi_s^\nu)$ for ScN as a function of (a) the number of local orbitals n_{LO} per l quantum number $(0 \le l \le 4)$ and atom and (b) the number of unoccupied states $(n_{\mathrm{LO}} = 6)$. We only consider spherical MPB functions, and the contribution of the core states is neglected. Dashed (green) and dotted (blue) lines correspond to the SOS and the FBC contributions, respectively. The solid (red) lines show their sum, which converges very rapidly in the two cases.

orbitals ($n_{\mathrm{LO}} = 6$) and increased the reciprocal cutoff of the LAPW basis to $G_{\max} = 5.5\,\mathrm{a}_0^{-1}$. Similar to Fig. 6.10(a) the separate contributions, SOS expression (green dashes curve) and FBC (blue dotted curve), show a slow convergence with respect to the number of unoccupied bands. Their sum, however, converges very rapidly. In fact, already 20 unoccupied states are sufficient to reproduce or even improve the accuracy that is achieved with the SOS alone using 450 unoccupied states. The inset of Fig. 6.10(b) shows that with about 50 states the trace is converged to a precision of 1‰. From this convergence behavior we can conclude that the function $\tilde{\phi}^{\sigma}_{n\mathbf{k}}(\mathbf{r})$ obtained non-perturbatively contains nearly the whole information about the infinite spectrum of unoccupied states. The second term in the FBC merely acts as a double counting correction for the SOS expression. It removes those parts of the function $\tilde{\phi}^{\sigma}_{n\mathbf{k}}(\mathbf{r})$ that are already included in the Hilbert space spanned by the KS wave functions up to band N and thus contained in the SOS expression.

Until now, we have restricted ourselves to the valence-electron contribution to the response function. We will discuss the core-electron part in the following. The FBC for the core electrons – as already discussed in the previous section – is calculated by a finite-difference approach. The function $\tilde{\phi}^{\sigma}_{n\mathbf{k}}$ exhibits in the case of a core state only a formal $\mathbf{k}$ dependence and n subsumes the principal quantum number n, the angular momentum l etc.. $\tilde{\phi}^{\sigma}_{n\mathbf{k}}$ already contains the exact response of the core state. The sum over states N in $\chi^{\sigma c}_{\mathrm{s},IJ}$ can therefore be restricted only to the occupied states so that the SOS expression does not contribute at all and the double counting term in the FBC only projects out the occupied states. This is confirmed in Fig. 6.11. With zero unoccupied states already the converged full response is obtained. Increasing the number of unoccupied states transfers a part of the core response to the SOS and accordingly less is accounted by the FBC. Yet, with 450 bands ($n_{\mathrm{LO}} = 6$) the SOS part covers only about 20% of the complete response, which manifests that the LAPW (valence) basis is incapable of describing the response of the core states. In the inset of Fig. 6.11 we observe variations of the total core response in the order of a few per mill. These variations might be caused, on the one hand, by the spherical-potential approximation for the core states and by the scalar-relativistic approximation for the valence and conduction band states, on the other hand.

In comparison with the valence-electron response, the core part accounts for about 80% of the response function for the example of ScN. However, the influence of the core electrons on the EXX potential is rather small, as the relevant quantity for the EXX potential is not the response function, but its inverse in which the large eigenvalues of $\chi^{\sigma}_{\mathrm{s}}$ become comparatively unimportant. We will discuss this point later on.

In Fig. 6.12, the local EXX potential is shown between neighboring Sc and N atoms in the [100] direction for three different calculations. None of them employs any local orbitals for

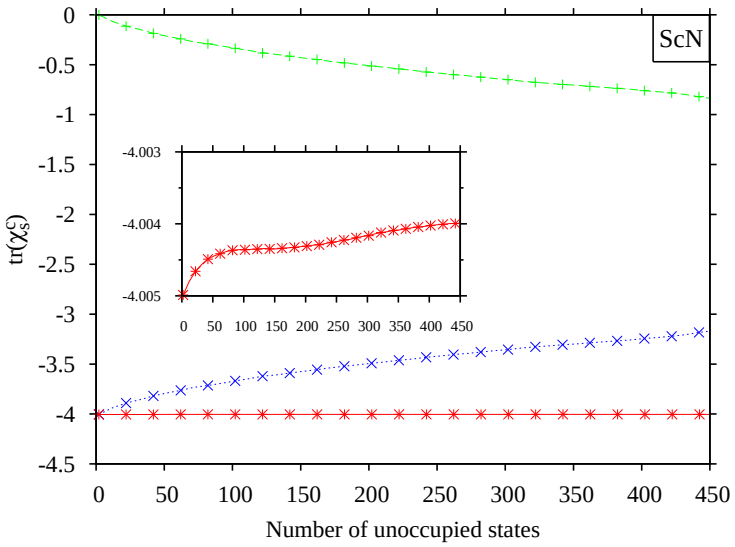

Figure 6.11.: Convergence of $\mathrm{tr}(\chi_s^c)$ as a function of the number of unoccupied bands. Dashed green and blue dotted line correspond to the SOS and FBC contribution. The red solid line is their sum.

the unoccupied states ($n_{\mathrm{LO}} = 0$). For the first calculation (green dashed line), the FBC is switched off. The EXX potential then is oscillatory and even tends to an unphysical positive value at the N atom. This is the situation, where both basis sets are out of balance. As discussed in section 6.3, this can be cured by the addition of local orbitals. But the same effect can be achieved by employing the FBC (blue dotted curve). We stress again that no local orbitals are used in this calculation.

At closer inspection, in the direct vicinity of the N nucleus, one still observes slight anomalies of the blue dotted curve. From our experience, the region close to the atomic nuclei is difficult to converge, which results from the fact that the radial MT potential always enters with an integration weight r^2 into the EXX-OEP equation. However, the total effective potential in this region is dominated by the potential of the nucleus $-Z/r$ so that slight inaccuracies in the EXX potential are of no or little consequence for the electronic-structure calculation. Yet, we can simply improve the EXX potential and its stability around the atomic nuclei by demanding that the gradient of the potential vanishes at the position of the atomic nuclei. This is not an ad-hoc postulate. It is motivated by the observation that the local EXX potential (always) shows this behavior (cf. EXX potentials in Refs. 142–144 or Fig. 6.1). The condition of vanishing gradient at the atomic position can easily be incorporated into the MPB by the approach discussed in Appendix A. As only the spherical MT MPB functions are non-zero at the atomic nuclei, it is sufficient to demand a zero gradient only for the spherical MT func-

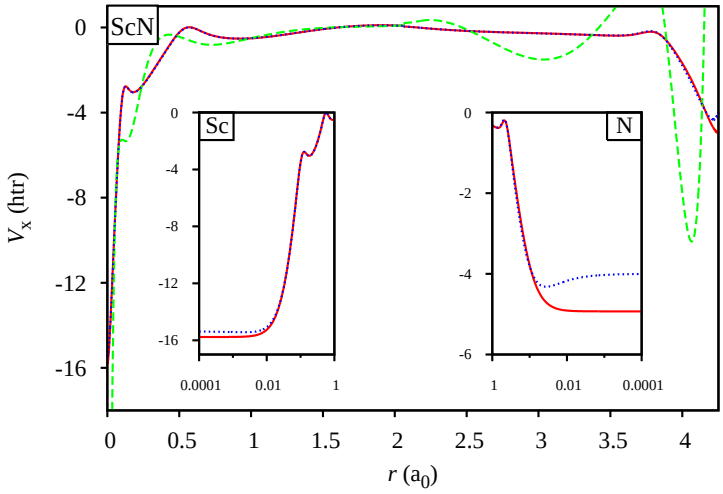

Figure 6.12.: Local EXX potential for ScN on a line along the [100] direction connecting neighboring Sc ($r = 0$) and N ($r = 4.25\,a_0$) atoms. We have used a conventional LAPW basis without local orbitals for the unoccupied states. The blue dotted and green dashed curves correspond to calculations with and without the FBC. For the red solid curve, we have employed an additional constraint for the MPB (see text). Eq. (6.6) defines the potential only up to a constant. Here, we use the convention $\int V_x(\mathbf{r})\, d^3r = 0$.

tions at the atomic nuclei. This modification of the MPB finally causes that the irregularities in the EXX potential around the N atom vanish as demonstrated by the red solid curve in Fig. 6.12.

The FBC only applies for spherical potential variations. So we still need a few local orbitals to fully converge the EXX potential, in particular the non-spherical and interstitial parts of the potential. For the example of ScN, the effect of these additional local orbitals on the potential is most pronounced around the Sc atom as shown in Fig. 6.13(a). The potential with one set of local orbitals ($n_{LO} = 1$) is opposed to the potential without any. The slight change in the potential influences the KS transition energies ($\Gamma \to \Gamma$, $\Gamma \to X$, $\Gamma \to L$) in the order of 0.10 – 0.15 eV. The changes in the potential, which emerge from a second set of local orbitals, are not visible on the scale of Fig. 6.13(a) and result in a change less than 0.03 eV in the transitions. We note that the calculations with or without the FBC converge to the same result.

Finally, we illustrate the effect of the exact core response on the local EXX potential. The FBC for the core electrons is switched off and the resulting potential is compared with the one

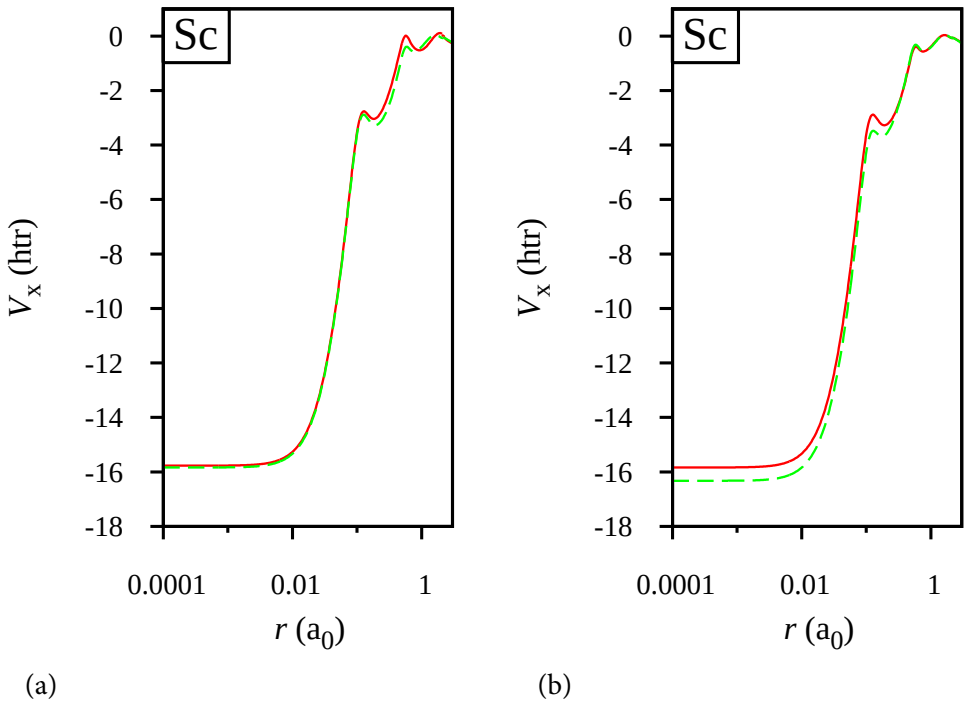

Figure 6.13.: (a) Comparison of $V_x(\mathbf{r})$ around the atomic nucleus of Sc for calculations with (green dashed line, $n_{LO} = 1$) and without (red solid line, $n_{LO} = 0$) local orbitals. (b) Local exact exchange potential $V_x(\mathbf{r})$ with (red solid line) and without (green dashed line) the explicit core response of the FBC.

obtained with the full core response [s. Fig. 6.13(b)]. Despite the large contribution of the FBC to the core response (cf. Fig. 6.11), it has a rather small influence on the shape of the potential because the inverse response function, instead of the response function, determines $V_x(\mathbf{r})$. Interestingly, the changes in the potential are spatially restricted to the region close to the Sc nuclei, which is not self-evident due to the non-locality of the EXX-OEP equation. These changes due to the different treatment of the core states affect the KS transition energies by less than 0.04 eV.

6.8. Perovskites: $CaTiO_3$, $SrTiO_3$, $BaTiO_3$

The perovskites form a large class of materials with various physical properties, for example, colossal magneto-resistance, ferroelectricity, charge ordering etc.. Their unifying property is their chemical composition ABO_3, where A and B are typically metals and O is oxygen. The metals A and B behave cationic and transfer electrons to the O atoms. In the ideal perovskite crystal, the A cations sit at the corners, while the B cation is located in the center of the cubic unit cell. The oxygen anions are placed at the centers of the cube faces (s. Fig. 6.14). Thus, the B cation is surrounded by an octahedron of 6 oxygen atoms, while the A atom has 12 oxygen neighbors. The perovskite $SrTiO_3$ exhibits this ideal cubic structure at room temperature. However, many perovskites differ from this cubic arrangement, for example by a displacement of the B cation within the oxygen octahedron or by tilting of the octahedron. The former distortion, lowering the symmetry from cubic to tetragonal, is typical for $BaTiO_3$ below 120 °C. Due to the displacement of the Ti atom towards one of the oxygen atoms, an electric dipole moment is formed that makes $BaTiO_3$ ferroelectric. A tilting of the complete oxygen octahedron is observable for $CaTiO_3$.

In the following, we investigate the electronic structure of the transition metal (TM) perovskites $ATiO_3$, where A stands for Ca, Sr, and Ba. To our knowledge, these are the first first-principles calculations of these perovskites employing the EXX functional. Deviations from the ideal cubic structure, which are observed experimentally for $CaTiO_3$ and $BaTiO_3$, are neglected in the calculations. For each material, we employ its experimental lattice constant ($CaTiO_3$: 7.35 a_0; $SrTiO_3$: 7.46 a_0; $BaTiO_3$: 7.60 a_0). The 3s and 3p semi-core states of the transition metal Ti as well as the first subshell of the A cations (Ca: 3s3p; Sr: 4s4p; Ba: 5s5p) are treated as valence states. The LAPW and MPB cutoff parameters are summarized in Table 6.6 and a 6×6×6 **k**-point mesh has been used for the calculations. LAPW and MPB are carefully balanced to obtain converged and stable EXX results.

Figures 6.15, 6.16, and 6.17 show the KS band structure and density of states (DOS) for all three perovskites obtained with the LDA and the EXX functionals. The contribution of the

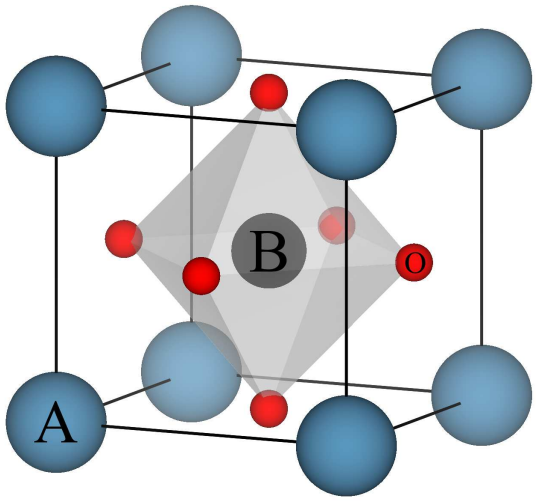

Figure 6.14.: Crystal structure of the ideal cubic perovskite ABO_3.

O 2*p* and Ti 3*d* states to the total DOS (black line) are drawn in red and green, respectively. Moreover, the partial DOS of the A cation *nd*-states (Ca: 3*d*; Sr: 4*d*; Ba: 5*d*) is shown as a blue line. The bands forming the highest valence bands are mainly of O 2*p* character and accommodate 18 electrons. The band width of these states reduces over this series of elements. The lowest conduction band states show Ti 3*d* behavior. The crystal field generated by the oxygen octahedron splits the five Ti 3*d* states into three states of t_{2g} symmetry (labelled after their irreducible representation) and two states of e_g symmetry. The three lowest conduction bands have t_{2g} character and are energetically separated from the two bands with e_g character. The bands corresponding to the A-cation *d* states lie several eV above the Fermi energy. Consequently, independently from the A cation, the highest occupied valence and lowest unoccupied conduction bands exhibit O 2*p* and Ti 3*d* character. With the consequence that the shape of the band structure around the Fermi energy is nearly identical for all three materials. In particular, all three oxides possess an indirect band gap between the highest occupied valence band at R and the lowest conduction band at Γ, and the direct gap lies at the Γ point.

The discussion of the band structure above holds for the LDA as well as the EXX functional. In comparison to the LDA, the band width of the O 2*p* bands is reduced by the EXX functional. This reduction amounts to 0.29eV for $CaTiO_3$, 0.07 eV for $SrTiO_3$, and 0.15eV for $BaTiO_3$. Moreover, the EXX functional leads to a distinct opening of the band gap by about 2 eV for each of these three oxides. The exact values of direct and indirect band gap are given

	$CaTiO_3$	$SrTiO_3$	$BaTiO_3$
G_{max}	$4.6\,a_0^{-1}$	$4.3\,a_0^{-1}$	$4.3\,a_0^{-1}$
l_{max}	8 (Ti); 12(Ca); 6 (O)	9 (Ti); 11(Sr); 7 (O)	8 (Ti); 12(Ba); 8 (O)
G'_{max}		$3.00\,a_0^{-1}$	
L_{max}		6	

Table 6.6.: Numerical input parameters of LAPW and MPB for the three perovskites $CaTiO_3$, $SrTiO_3$, and $BaTiO_3$.

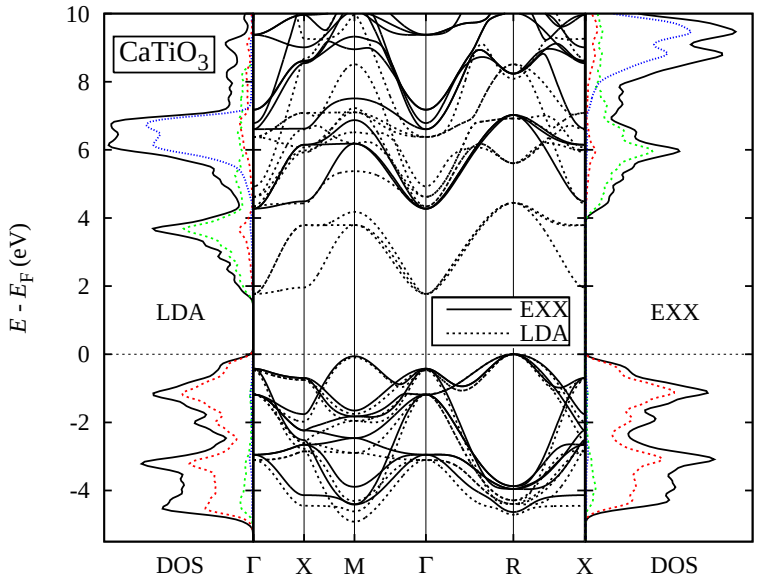

Figure 6.15.: LDA and EXX KS band structure and DOS for the perovskite $CaTiO_3$. The total DOS (in units of states/eV) is shown in black, whereas the partial DOS of O 2*p*, Ti 3*d*, and Ca 3*d* is drawn in red, green, and blue.

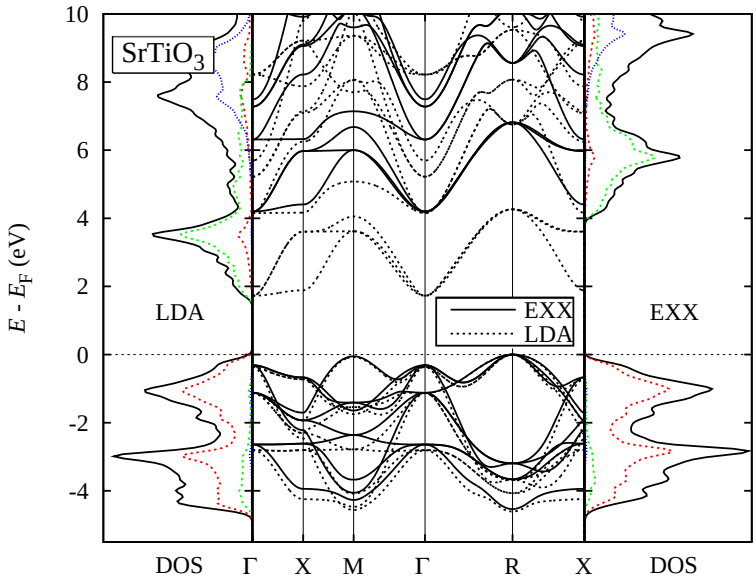

Figure 6.16.: Same as Fig. 6.15 for $SrTiO_3$.

in Table 6.7. By substituting Ca by Sr and finally by Ba both gaps, direct and indirect, shrink and become more and more similar so that for $BaTiO_3$ direct and indirect EXX gap are even identical (at least with an accuracy of 0.01 eV). The addition of LDA correlation to the EXX functional leads to a slightly different direct and indirect gap again.

If there is no hybridization of the states of the A cation (Ca, Sr, Ba) with the O $2p$ and Ti $3d$ bands, between which the gap is formed, the question arises what causes the band gap to decrease if one replaces Ca by Sr and finally by Ba. In order to analyze whether this effect goes back to the increase of the lattice constant from $CaTiO_3$ to $BaTiO_3$ or whether it is caused by a change in the potential induced through the replacement of the A cation, we calculate the band gap of $CaTiO_3$ at the lattice constant of the two other materials. Additionally, we replace the cation Ca by Sr and Ba at the lattice constant of $CaTiO_3$. The corresponding changes in the gaps employing the LDA are shown in Table 6.8. By increasing the lattice constant of $CaTiO_3$ the direct and the indirect band gap shrink. The indirect gap of $CaTiO_3$ at the lattice constant of $SrTiO_3$ or $BaTiO_3$ is slightly smaller than those obtained for the real material, while the direct gap exhibits the opposite behavior. The replacement of the A cation at the fixed lattice constant of $CaTiO_3$ yields an increase in the indirect gap and a decrease in the direct gap. If one combines both effects, the band gap of the 'true' material can be constructed (up to small inaccuracies). For example, the change of the lattice constant from $CaTiO_3$ to $SrTiO_3$ leads to a reduction of the direct gap of 0.06 eV, whereas the interchange of Ca by Sr at fixed lattice

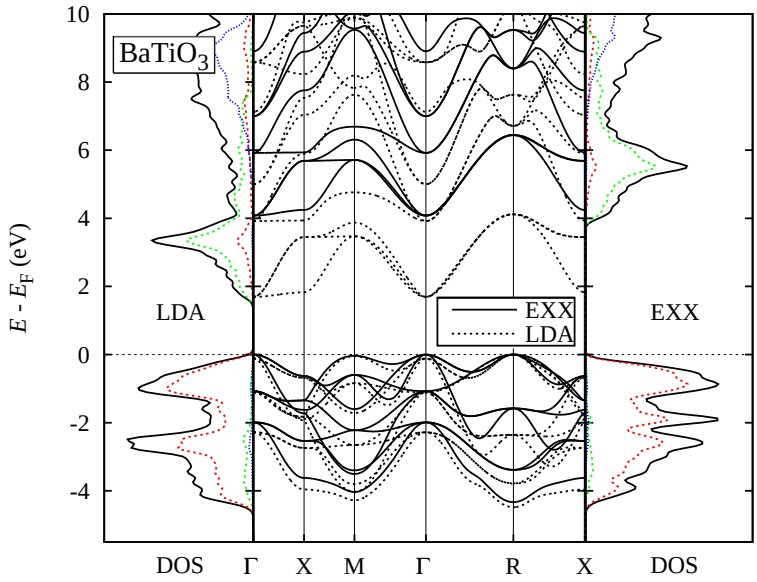

Figure 6.17.: Same as Fig. 6.15 for $BaTiO_3$.

constant decreases the direct gap by 0.10 eV. In combination the direct gap of $SrTiO_3$ should be 0.16 eV smaller than the direct gap of $CaTiO_3$, which deviates from the 'true' gap of $SrTiO_3$ by only 0.01 eV. In conclusion, the reduction of the band gap from $CaTiO_3$ to $BaTiO_3$ is not merely caused by the increase in the lattice constant. The change in the potential due to the change of the A cation is as important as the increase in the lattice constant.

In comparison with experiment (s. Table 6.8), the LDA underestimates the direct and indirect band gap by roughly 50%. The EXX as well as the EXXc functional yield KS gaps that are closer to the experimental values. However, we observe a pronounced overestimation by about 25%. This might have two reasons: (a) the error cancellation between the neglect of correlation on the one hand and of the derivative discontinuity on the other hand – as discussed in section 6.6 – may not work for these transition metal oxides, (b) deviations of the experimental crystal structure at room temperature from the ideal cubic structure employed in the calculations may influence the gap. At room temperature, $CaTiO_3$ is orthorhombic, $BaTiO_3$ is tetragonal, and $SrTiO_3$ is cubic. In Ref. 148, PBE DFT calculations are reported for the cubic as well as the room-temperature crystal structure of the three perovskites. For orthorhombic $CaTiO_3$ a band gap, which is about 0.5 eV smaller than that of cubic $CaTiO_3$, is found. If we assume that we can simply transfer this reduction observed for the PBE functional to the EXX band gap, we obtain for $CaTiO_3$ a significant improvement with the experimental result. Yet, the discrepancies for the other two materials, in particular for $SrTiO_3$, can not be explained

		LDA	EXX	EXXc	Expt.
$CaTiO_3$	$\Gamma \to \Gamma$	2.24	4.70	4.74	–
	$R \to \Gamma$	1.77	4.28	4.31	3.57[a]
$SrTiO_3$	$\Gamma \to \Gamma$	2.09	4.51	4.54	3.88[b]
	$R \to \Gamma$	1.73	4.20	4.22	3.20[b]
$BaTiO_3$	$\Gamma \to \Gamma$	1.81	4.08	4.12	3.92[c]
	$R \to \Gamma$	1.7	4.08	4.11	3.27[c]

[a] Reference 145 [b] Reference 146
[c] Reference 147

Table 6.7.: Direct and indirect KS band gaps (in eV) for the cubic perovskites $CaTiO_3$, $SrTiO_3$, and $BaTiO_3$ and comparison with experiment.

$CaTiO_3$	LDA	
	$\Gamma \to \Gamma$	$R \to \Gamma$
a_{CaTiO_3}	2.24	1.77
a_{SrTiO_3}	2.18	1.69
a_{BaTiO_3}	2.09	1.60

(a)

a_{CaTiO_3}	LDA	
	$\Gamma \to \Gamma$	$R \to \Gamma$
$CaTiO_3$	2.24	1.77
$SrTiO_3$	2.14	1.80
$BaTiO_3$	1.89	1.89

(b)

Table 6.8.: Direct and indirect LDA KS gap (in eV) for (a) $CaTiO_3$ at the lattice constant of $CaTiO_3$, $SrTiO_3$ and $BaTiO_3$, (b) the three perovskites at the lattice constant of $CaTiO_3$.

in this way.

In conclusion, we have investigated the electronic structure of the three cubic perovskites $CaTiO_3$, $SrTiO_3$, and $BaTiO_3$ using the EXX(c) functional. In comparison with the LDA the EXX(c) approach leads to an opening of the band gap for all three materials. The dispersion of the bands is nearly unaffected except for a slight reduction of the valence band width. While the LDA underestimates the band gaps by about 50%, the EXX(c) approach overcompensates this error and leads to an overestimation of 25%. Possible reasons for this overestimation have been discussed.

6.9. Transition metal oxides: MnO, FeO, and CoO

The transition-metal (TM) oxides MnO, FeO, and CoO are antiferromagnetic insulators, which crystallize in the rock-salt structure with antiferromagnetic ordering along the [111] di-

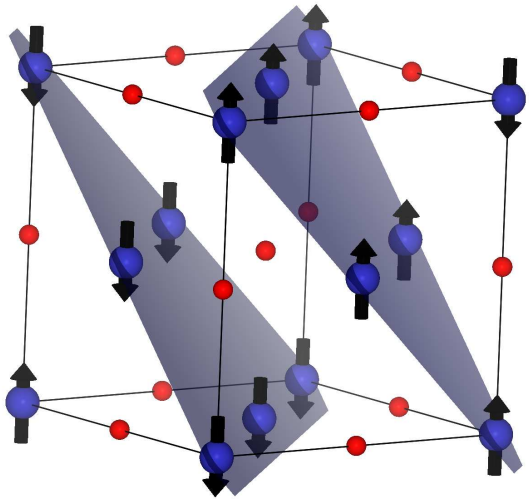

Figure 6.18.: Cubic unit-cell of the transition metal oxides MnO, FeO, and CoO in their antiferromagnetic order (AFM-II). The transition metal atoms with their actual spin orientation are depicted in blue, while the oxygen atoms are red.

rection (AFM-II). The TM ions within the (111) plane are coupled ferromagnetically, whereas TM ions in adjacent (111) planes are aligned antiferromagnetically (s. Fig. 6.18). Experimentally, all three TM oxides remain insulating even above the Néel temperature T_N [149]. In particular, the latter is in contradiction to band theory, that would predict metallic behavior for the paramagnetic state above T_N due to the partially filled d states (Mn^{2+} d^5, Fe^{2+} d^6, Co^{2+} d^7). Peierls [150] pointed out in 1937 that "it is quite possible that the electrostatic interaction between the electrons prevents them from moving at all". Based on this idea Mott developed a model how electron correlation may explain the insulating behavior. Metallic behavior of a material requires mobile electrons, that move through the crystal, hopping from site to site. In the case of the relatively localized d electrons, the hopping is determined by two competing mechanisms: on the one hand, the reduced localization of the electrons due to the hopping leads to a gain in kinetic energy ($-t$). On the other hand, one has to pay the Coulomb energy U arising from the electrostatic repulsion of the hopping electrons with those residing at the sites. If $U \gg t$, the energy loss of this process exceeds the gain so that the electrons avoid to hop and the material is insulating. This is a sketch of the physical picture developed by Mott in order to explain the insulating behavior of the TM oxides even above T_N. Therefore, this class of materials is nowadays coined Mott insulators.

In DFT, which is in principle an exact theory, electron correlation is taken into account

by the xc energy functional E_{xc}. In the following, we will demonstrate that if the latter is approximated by the EXX functional, DFT predicts an insulating behavior for this set of TM oxides in their antiferromagnetic configuration, whereas in the LDA and the GGA, FeO and CoO are metallic and the gap of MnO is seriously underestimated.

For all materials, we treat the complete M shell of the TM comprising the 3*s*, 3*p*, and 3*d* electrons as valence states. The electronic wave functions are described by an LAPW basis set with the reciprocal cutoff radius $G_{max} = 3.90\,a_0^{-1}$ (MnO), $G_{max} = 4.00\,a_0^{-1}$ (FeO), and $G_{max} = 4.50\,a_0^{-1}$ (CoO) in the interstitial region. An angular momentum cutoff (l_{max}) of 8 is employed for all materials in the MT spheres. The MPB for the representation of the local EXX potential is formed by IPWs with $G'_{max} = 3.00\,a_0^{-1}$ and numerical functions with $L_{max} = 6$ in the MT spheres. The parameters of the MPB apply to all three TM oxides and the BZ is sampled by a 4×4×4 **k**-point set. The structure of the compounds is of rock-salt type. Their experimental lattice constants are $8.40\,a_0$ for MnO, $8.19\,a_0$ for FeO, and $8.04\,a_0$ for CoO.[151] The antiferromagnetic ordering along the [111] direction reduces the symmetry to the space group $R3\overline{m}$. This fact will become important later. In experiment, small lattice distortions are observed [152]. These distortions, which are rhombohedral for MnO and FeO and tetragonal for CoO, are neglected in the calculations. For the EXXc calculations, LDA correlation is combined with the orbital-dependent EXX functional. In particular, we use the parametrization of the LDA correlation energy of Vosko, Wilk, and Nusair [5].

In Figs. 6.19, 6.20, and 6.21 PBE and EXX band structures and DOS are shown for each of the three TM oxides. The corresponding path in the rhombohedral BZ is shown in Fig. 6.22. Due to the antiferromagnetic order spin-up and spin-down eigenvalue spectra are identical. While FeO and CoO are metallic in the PBE functional, the EXX approach predicts a semiconducting behavior with a direct gap at the Γ point for all three oxides. The location of the indirect gap between the valence-band maximum and the conduction-band minimum is material specific. While the conduction-band minimum lies at the Γ point for all three materials, the valence-band maximum is located at T for MnO and at F for CoO. The highest valence band for FeO is extremely narrow and hardly shows any dispersion. For all three oxides, the highest valence band exhibits TM 3*d* character with some admixture of O 2*p* (cf. Figs. 6.19, 6.20, and 6.21). Due to the localization of the 3*d* states, these bands possess little dispersion. On the contrary, the lowest conduction band exhibits a parabolic shape in particular around its minimum at the Γ point reflecting the TM 4*s* character of this band. Above this 4*s*-type state, the bands corresponding to the unoccupied *d* states follow.

In the case of MnO, each of the two Mn atoms in the magnetic unit cell posseses five *d* electrons. At one of the Mn atoms they occupy five spin-up *d* states, whereas at the other atom five spin-down states are filled. Occupied and unoccupied *d* states of the same Mn atom are

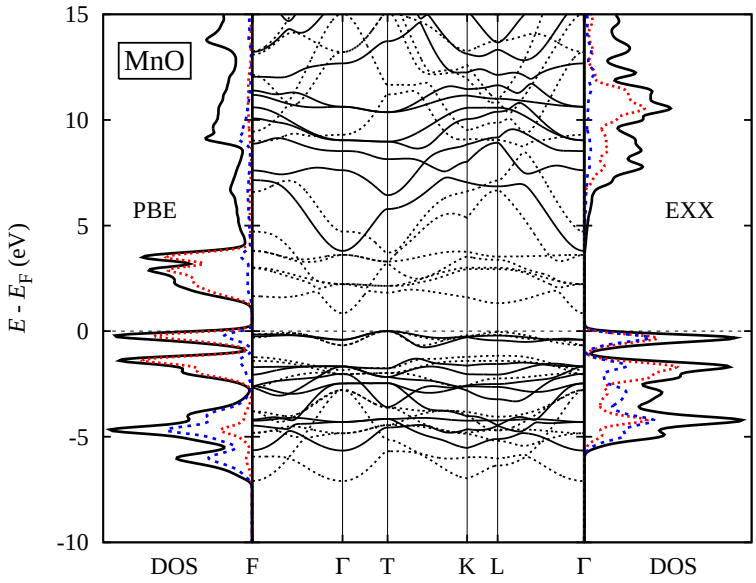

Figure 6.19.: PBE (dashed black lines) and EXX (solid black lines) KS band structure and DOS (in units of states/eV) for the transition-metal oxide MnO. The contribution of the TM *d* states to the total DOS (black line) is drawn in red. The partial DOS for the O 2*p* states is shown in blue.

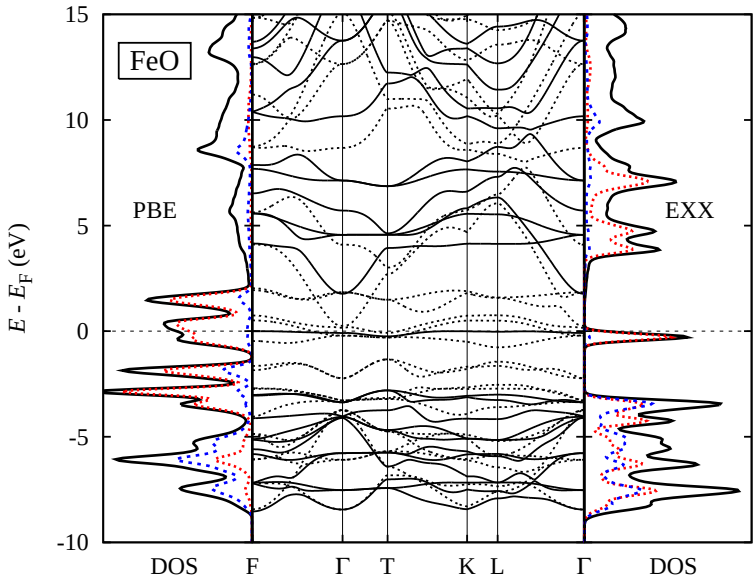

Figure 6.20.: Same as Fig. 6.19 but for FeO.

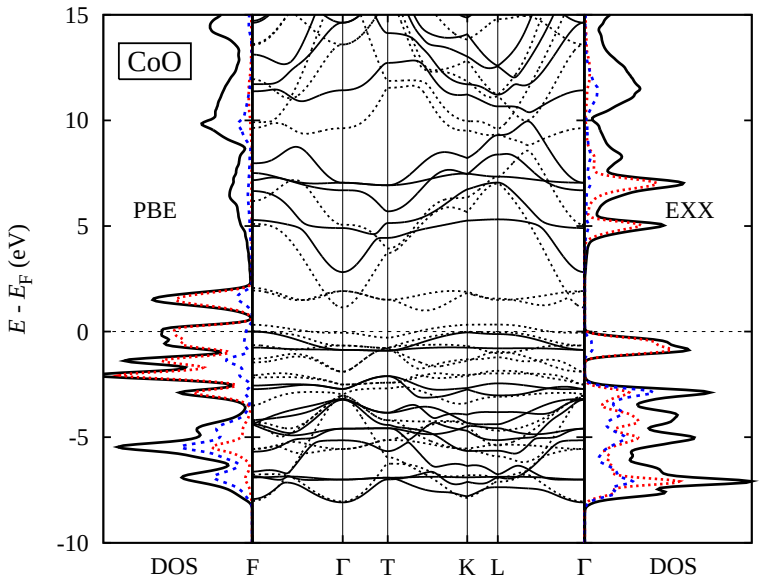

Figure 6.21.: Same as Figs. 6.19 and 6.20 but for the CoO.

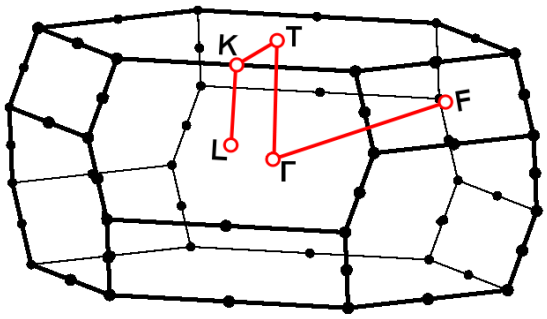

Figure 6.22.: Path in the rhombohedral BZ of the antiferromagnetic TM oxides for the band structures of Figs. 6.19, 6.20, and 6.21.

split by 4.6 eV in the PBE and by 10.8 eV in the EXX approach, where we measure from the center of the occupied to the center of the unoccupied d states. This exchange splitting of the d states makes MnO an antiferromagnetic semiconductor. As Fe provides an additional d electron in contrast to Mn, one would naively expect that FeO is metallic. However, the antiferromagnetic ordering reduces the symmetry from $Fm3\overline{m}$ in the chemical unit cell to $R3\overline{m}$ in the magnetic unit cell. While the former splits the five d bands into three t_{2g} and two e_g states at the Γ point, the latter divides the d states into a single degenerate state of symmetry a_{1g} and two doubly degenerate bands of symmetry e_g and e_u. Therefore, the additional d electron of Fe can occupy the singly degenerate d state of a_{1g} symmetry instead of occupying a multiply degenerate state fractionally. Moreover, the occupation of this d state in the EXX approach causes the corresponding single-particle energy to fall such that it is energetically separated from the remaining unoccupied d states. In this way, a gap is formed in FeO. The single, nearly dispersionless d band at the Fermi energy is separated from the unoccupied states by about 1.67 eV and from the remaining occupied bands by about 2.5 eV. We note that in the case of the LDA or GGA one usually observes that a single-particle energy rises if the level is occupied and falls if it is emptied [153]. This is exactly the opposite behavior as observed here for the EXX functional.

Each Co atom in CoO provides yet another d electron. At a given Co atom the seven d electrons occupy five spin-up and two spin-down d states. The two spin-down states have e_g symmetry at the Γ point. In analogy to FeO, the energy levels of the two occupied spin-down d states are lowered with respect to the unoccupied ones so that they are separated from the unoccupied states by 2.82 eV.

In Table 6.9, we summarize the direct and indirect gap for the three oxides and compare them with experimental values, which are either measured by optical absorption or photoemission experiments. We note again that, in contrast to the PBE functional, the EXX approach predicts a semiconducting behavior for all three oxides. The addition of LDA correlation to the EXX functional (EXXc) leads to a further opening of the gap by about $0.2 - 0.3$ eV.

According to Hund's first rule, we would expect a magnetic moment of $5\,\mu_B$ for MnO, $4\,\mu_B$ for FeO, and $3\,\mu_B$ for CoO. Within the TM muffin-tin spheres the calculated moments are smaller (s. Table 6.10). The magnetic moments in the EXX as well as the EXXc approach are consistently larger than those in the PBE and closer to Hund's first rule, while EXX and EXXc moments are (nearly) identical. The opening of the band gap, in particular in the case of FeO and CoO, and the increased localization of the KS wave functions due to removal of the self-interaction error in the EXX method are responsible for the enhancement of the magnetic moment with respect to the PBE functional. We note, however, that the moment depends

		PBE	EXX	EXXc	Expt.
MnO	direct	1.36	4.21	4.37	3.6 . . . 3.8[a]
	indirect	0.85	3.80	3.96	3.90 ± 0.4[b]
FeO	direct	–	1.86	2.17	2.4[c]
	indirect	–	1.67	1.99	–
CoO	direct	–	3.68	3.99	5.43[d]
	indirect	–	2.82	3.13	2.5 ± 0.3[e]

[a] Reference 154 [b] Reference 155 [c] Reference 156
[d] Reference 157 [e] Reference 158

Table 6.9.: Direct and indirect band gaps (in eV) for the TM oxides MnO, FeO, and CoO calculated with the PBE, EXX, and EXXc functional. For comparison, experimental values from the literature are also given. The indirect (direct) gap is measured by photoemission (optical absorption) measurements.

	PBE	EXX	EXXc	Expt.
MnO	4.18	4.60	4.60	4.58[a]
FeO	3.38	3.76	3.75	3.32[b]; 4.2[c]
CoO	2.43	2.85	2.84	3.35[d]; 3.8[b]; 3.98[e]

[a] Reference 164 [b] Reference 165 [c] Reference 159
[d] Reference 166 [e] Reference 167

Table 6.10.: Spin magnetic-moments (in μ_B) of the antiferromagnetic TM oxides for the PBE, EXX, and EXXc functionals and a comparison with experimental values.

on the choice of the MT sphere radius S_a. Moreover, we note that the experimental magnetic moments comprise spin and orbital contributions. For example for FeO and CoO, it is argued in Refs. 159–163 that the orbital moment may contribute to the total magnetic moment with a value of about 1 μ_B.

In summary, the EXX approach predicts all three transition-metal monoxides to be insulating in their anti-ferromagnetic (AFM-II) configuration. While for MnO the spin splitting of the 3d states is sufficient for the formation of the gap, in the case of FeO and CoO it is the interplay of the reduced symmetry of the magnetic unit cell with the property of the EXX functional that the energy of a single particle level falls if it is occupied, which finally makes FeO and CoO insulating as well. Moreover, we have shown that the EXX functional, in comparison with the PBE, leads to an enhancement of the spin magnetic moment.

6.10. Metals

Until now, we have restricted our discussion to semiconducting or insulating materials. In metals, in contrast to semiconductors and insulators, occupied and unoccupied states are not clearly separated by an energy gap so that an often complex Fermi energy surface is formed. This has the consequence that the convergence of BZ integrals with respect to the $\mathbf{k}$-point sampling is slow. A common approach to improve the convergence is to smear out the sharp, step-like distinction between occupied and unoccupied sates. States lying a little above or below the Fermi energy E_F are fractionally occupied. For example, the step-function is replaced by a Fermi-Dirac distribution function

$$f_{n\mathbf{k}}^{\sigma,\mathrm{FD}} = \frac{1}{\exp\left[\frac{\epsilon_{n\mathbf{k}}^{\sigma}-E_\mathrm{F}}{k_B T}\right]+1} \tag{6.50}$$

describing the occupation of a state $\phi_{n\mathbf{k}}^{\sigma}$ with energy $\epsilon_{n\mathbf{k}}^{\sigma}$. Alternatively, a Gaussian distribution function can be used

$$f_{n\mathbf{k}}^{\sigma,\mathrm{G}} = \frac{1}{2}\left[1-\mathrm{erf}\left(\frac{\epsilon_{n\mathbf{k}}^{\sigma}-E_\mathrm{F}}{k_B T}\right)\right]. \tag{6.51}$$

In both approaches, the artificial temperature T or the artificial energy $k_B T$ with the Boltzmann factor k_B controls the degree of smearing. In the literature, further broadening schemes are discussed [168], but we restrict ourselves here to those mentioned above.

In order to retain the variational property of the total energy with respect to density variations an additional term must be added to the total energy that takes into account the fractional occupations [169, 170]. In the case of the Fermi-Dirac distribution, this additional term has the following form

$$-TS = k_B T \sum_{n\mathbf{k}} \left[f_{n\mathbf{k}}^{\mathrm{FD}}\ln(f_{n\mathbf{k}}^{\mathrm{FD}}) + (1-f_{n\mathbf{k}}^{\mathrm{FD}})\ln(1-f_{n\mathbf{k}}^{\mathrm{FD}})\right]. \tag{6.52}$$

While for a Gaussian distribution it is given by

$$-TS = -k_B T \sum_{n\mathbf{k}} \frac{1}{\sqrt{\pi}} \exp\left[-\left(\frac{\epsilon_{n\mathbf{k}}-E_\mathrm{F}}{k_B T}\right)^2\right]. \tag{6.53}$$

For the Fermi-Dirac distribution, the variational total energy $E-TS$ is identical in its form to the total energy in finite-temperature density-functional theory for grand canonical ensembles [171]. In this special case and only in this case, the variational total energy corresponds to the thermodynamic free energy F and the artificial temperature T can be associated with

the real temperature of the system.

Besides an improved **k**-point convergence, the introduction of fractional occupation also stabilizes the convergence of the SCF cycle. While in the case of a sharp step-like occupation an interchange of an occupied and an unoccupied state at the Fermi energy in two subsequent SCF iterations lead to a jump in the density, which often impedes the convergence of the SCF cycle, the usage of a Fermi-Dirac or Gaussian distribution function suppresses the dependence of the density on such interchanges at the Fermi level.

6.10.1. EXX-OEP formalism for metals

In the following, a generalization of the EXX-OEP formalism for metals, which allows for fractional occupation, will be discussed. A formulation for spin-unpolarized systems can be found in Ref. 172. For its extension to spin-polarized systems, we refer to Ref. 173.
Let us first concentrate on the spin-density response function. Due to the introduction of the smearing function $f^{\sigma}_{n\mathbf{k}}$ (here and in the following $f^{\sigma}_{n\mathbf{k}}$ stands for Fermi-Dirac or Gaussian distribution) the electron spin density turns into a sum over all states and **k** points

$$n^{\sigma}(\mathbf{r}) = \sum_{\mathbf{k}}^{\mathrm{BZ}} \sum_{n} f^{\sigma}_{n\mathbf{k}} |\phi^{\sigma}_{n\mathbf{k}}(\mathbf{r})|^2 \,, \tag{6.54}$$

where $f^{\sigma}_{n\mathbf{k}}$ controls if a state is totally ($f^{\sigma}_{n\mathbf{k}} = 1$) or fractionally occupied ($f^{\sigma}_{n\mathbf{k}} \in]0,1[$) or unoccupied ($f^{\sigma}_{n\mathbf{k}} = 0$). The density has to be varied with respect to the effective potential for the calculation of the spin-density response function. In contrast to a semiconductor or insulator, an additional term appears in the spin-density response function that arises from the variation of $f^{\sigma}_{n\mathbf{k}}$ with respect to the effective potential $V^{\sigma'}_{\mathrm{eff}}$

$$\begin{aligned}
\chi_{\mathrm{s}}^{\sigma\sigma'}(\mathbf{r},\mathbf{r}') &= \frac{\delta n^{\sigma}(\mathbf{r})}{\delta V^{\sigma'}_{\mathrm{eff}}(\mathbf{r}')} && \text{(6.55a)} \\
&= \delta_{\sigma\sigma'} \sum_{\mathbf{k}}^{\mathrm{BZ}} \sum_{n} f_{n\mathbf{k}} \left[\sum_{n' \neq n} \frac{\phi^{\sigma *}_{n\mathbf{k}}(\mathbf{r}) \phi^{\sigma}_{n'\mathbf{k}}(\mathbf{r}) \phi^{\sigma *}_{n'\mathbf{k}}(\mathbf{r}') \phi^{\sigma}_{n\mathbf{k}}(\mathbf{r}')}{\epsilon^{\sigma}_{n\mathbf{k}} - \epsilon^{\sigma}_{n'\mathbf{k}}} + \mathrm{c.c.} \right] \\
&\quad + \sum_{\mathbf{k}}^{\mathrm{BZ}} \sum_{n} \frac{\delta f^{\sigma}_{n\mathbf{k}}}{\delta V^{\sigma'}_{\mathrm{eff}}(\mathbf{r}')} \phi^{\sigma *}_{n\mathbf{k}}(\mathbf{r}) \phi^{\sigma}_{n\mathbf{k}}(\mathbf{r}) \,. && \text{(6.55b)}
\end{aligned}$$

While the first term is diagonal in the spin σ, the second additional term is not, as will be illustrated later on. In the case of a spin-polarized metal with fractional occupation, the potentials $V^{\uparrow}_{\mathrm{x}}(\mathbf{r})$ and $V^{\downarrow}_{\mathrm{x}}(\mathbf{r})$ are, therefore, not obtained by solving two independent EXX-OEP equations for each spin channel. Instead, one equation that determines both $V^{\uparrow}_{\mathrm{x}}(\mathbf{r})$ and $V^{\downarrow}_{\mathrm{x}}(\mathbf{r})$

must be solved

$$\int \begin{pmatrix} \chi_s^{\uparrow\uparrow}(\mathbf{r},\mathbf{r}') & \chi_s^{\uparrow\downarrow}(\mathbf{r},\mathbf{r}') \\ \chi_s^{\downarrow\uparrow}(\mathbf{r},\mathbf{r}') & \chi_s^{\downarrow\downarrow}(\mathbf{r},\mathbf{r}') \end{pmatrix} \begin{pmatrix} V_x^{\uparrow}(\mathbf{r}') \\ V_x^{\downarrow}(\mathbf{r}') \end{pmatrix} d^3r' = \begin{pmatrix} t^{\uparrow}(\mathbf{r}) \\ t^{\downarrow}(\mathbf{r}) \end{pmatrix}. \tag{6.56}$$

In a similar way as for the single-particle response function, an additional term is present in the spinor of the right-hand side

$$\begin{aligned} t^{\sigma}(\mathbf{r}) &= \frac{\delta}{\delta V_{\mathrm{eff}}^{\sigma}(\mathbf{r}')} \left[\frac{1}{2} \sum_{\sigma'} \sum_{n\mathbf{k}} f_{n\mathbf{k}}^{\sigma'} \langle \phi_{n\mathbf{k}}^{\sigma'} | V_x^{\mathrm{NL},\sigma'} | \phi_{n\mathbf{k}}^{\sigma'} \rangle \right] && \text{(6.57a)} \\ &= \sum_{\mathbf{k}}^{\mathrm{BZ}} \sum_{n} f_{n\mathbf{k}}^{\sigma} \left[\sum_{n' \neq n} \langle \phi_{n\mathbf{k}}^{\sigma} | V_x^{\mathrm{NL},\sigma} | \phi_{n'\mathbf{k}}^{\sigma} \rangle \frac{\phi_{n'\mathbf{k}}^{\sigma *}(\mathbf{r}') \phi_{n\mathbf{k}}^{\sigma}(\mathbf{r})}{\epsilon_{n\mathbf{k}}^{\sigma} - \epsilon_{n'\mathbf{k}}^{\sigma}} + \mathrm{c.c.} \right] \\ &\quad + \sum_{\sigma'} \sum_{\mathbf{k}}^{\mathrm{BZ}} \sum_{n} \frac{\delta f_{n\mathbf{k}}^{\sigma'}}{\delta V_{\mathrm{eff}}^{\sigma}(\mathbf{r}')} \langle \phi_{n\mathbf{k}}^{\sigma'} | V_x^{\mathrm{NL},\sigma'} | \phi_{n\mathbf{k}}^{\sigma'} \rangle , && \text{(6.57b)} \end{aligned}$$

where the definition of the non-local exchange potential has been generalized to

$$V_x^{\mathrm{NL},\sigma}(\mathbf{r},\mathbf{r}') = -\sum_{\mathbf{q}}^{\mathrm{BZ}} \sum_{n'} f_{n'\mathbf{q}}^{\sigma} \frac{\phi_{n'\mathbf{q}}^{\sigma}(\mathbf{r}) \phi_{n'\mathbf{q}}^{\sigma *}(\mathbf{r}')}{|\mathbf{r} - \mathbf{r}'|}. \tag{6.58}$$

In contrast to semiconductors and insulators the sum over n' in the square brackets in Eqs. (6.55b) and (6.57b) can not be restricted solely to the unoccupied states ($f_{n'\mathbf{k}}^{\sigma} = 0$), as the occupation number $f_{n\mathbf{k}}^{\sigma}$ prohibits, in general, that combinations of occupied bands n ($f_{n\mathbf{k}}^{\sigma} \neq 0$) with occupied bands n' ($f_{n'\mathbf{k}}^{\sigma} \neq f_{n\mathbf{k}}^{\sigma} \neq 0$) cancel each other.

The calculation of the variation of $f_{n\mathbf{k}}^{\sigma}$ due to a change in the effective potential is discussed in the following for the Fermi-Dirac distribution $f_{n\mathbf{k}}^{\sigma,\mathrm{FD}}$. However, the derivation can be easily transferred to the Gaussian distribution function $f_{n\mathbf{k}}^{\sigma,\mathrm{G}}$. According to the rules of functional derivatives, the occupation number response obeys

$$\frac{\delta f_{n\mathbf{k}}^{\sigma,\mathrm{FD}}}{\delta V_{\mathrm{eff}}^{\sigma'}(\mathbf{r}')} = -\frac{1}{k_B T} f_{n\mathbf{k}}^{\sigma,\mathrm{FD}} [1 - f_{n\mathbf{k}}^{\sigma,\mathrm{FD}}] \left\{ \phi_{n\mathbf{k}}^{\sigma *}(\mathbf{r}') \phi_{n\mathbf{k}}^{\sigma}(\mathbf{r}') \delta_{\sigma\sigma'} - \frac{\delta E_{\mathrm{F}}}{\delta V_{\mathrm{eff}}^{\sigma'}(\mathbf{r}')} \right\}. \tag{6.59}$$

The first term in the curled brackets arises from the variation of the eigenvalue $\epsilon_{n\mathbf{k}}^{\sigma}$ and is, therefore, diagonal in spin space. On the contrary, the second term couples spin-up and spin-down electrons, because a variation of the effective potential of spin σ' can change the eigenvalues $\epsilon_{n\mathbf{k}}^{\sigma'}$ with respect to the eigenvalues of the opposite spin direction $\epsilon_{n\mathbf{k}}^{\sigma}$ so that a different occupation of the energy levels $\epsilon_{n\mathbf{k}}^{\sigma}$ becomes preferable. In order to explicitly calculate

the variation of the Fermi energy E_F, we exploit that the total particle number N is conserved

$$0 = \frac{\delta N}{\delta V_{\mathrm{eff}}^{\sigma'}(\mathbf{r}')} = \sum_\sigma \sum_{\mathbf{k}}^{\mathrm{BZ}} \sum_n \frac{\delta f_{n\mathbf{k}}^{\sigma,\mathrm{FD}}}{\delta V_{\mathrm{eff}}^{\sigma'}(\mathbf{r}')}\,, \tag{6.60}$$

which together with Eq. (6.59) gives

$$\frac{\delta E_\mathrm{F}}{\delta V_{\mathrm{eff}}^{\sigma'}(\mathbf{r}')} = \frac{1}{Z} \sum_{\mathbf{k}}^{\mathrm{BZ}} \sum_n f_{n\mathbf{k}}^{\sigma',\mathrm{FD}}[1 - f_{n\mathbf{k}}^{\sigma',\mathrm{FD}}]\phi_{n\mathbf{k}}^{\sigma'*}(\mathbf{r}')\phi_{n\mathbf{k}}^{\sigma'}(\mathbf{r}')\,, \tag{6.61}$$

where we have introduced Z as an abbreviation for

$$Z = \sum_\sigma \sum_{\mathbf{k}}^{\mathrm{BZ}} \sum_n f_{n\mathbf{k}}^{\sigma,\mathrm{FD}}[1 - f_{n\mathbf{k}}^{\sigma,\mathrm{FD}}]\,. \tag{6.62}$$

Inserting Eqs. (6.59) and (6.61) into Eq. (6.55b), the components of the density response matrix finally become

$$\begin{aligned}
\chi_\mathrm{s}^{\sigma\sigma'}(\mathbf{r},\mathbf{r}') \;=\;& \delta_{\sigma\sigma'} \sum_{\mathbf{k}}^{\mathrm{BZ}} \sum_n f_{n\mathbf{k}} \sum_{n'\neq n} \left[\frac{\phi_{n\mathbf{k}}^{\sigma*}(\mathbf{r})\phi_{n'\mathbf{k}}^{\sigma}(\mathbf{r})\phi_{n'\mathbf{k}}^{\sigma*}(\mathbf{r}')\phi_{n\mathbf{k}}^{\sigma}(\mathbf{r}')}{\epsilon_{n\mathbf{k}}^{\sigma} - \epsilon_{n'\mathbf{k}}^{\sigma}} + \mathrm{c.c.} \right] \\
& - \delta_{\sigma\sigma'} \frac{1}{k_B T} \sum_{\mathbf{k}}^{\mathrm{BZ}} \sum_n f_{n\mathbf{k}}^{\sigma,\mathrm{FD}}[1 - f_{n\mathbf{k}}^{\sigma,\mathrm{FD}}]\phi_{n\mathbf{k}}^{\sigma*}(\mathbf{r})\phi_{n\mathbf{k}}^{\sigma}(\mathbf{r})\phi_{n\mathbf{k}}^{\sigma*}(\mathbf{r}')\phi_{n\mathbf{k}}^{\sigma}(\mathbf{r}') \\
& + \frac{1}{k_B T} \frac{1}{Z} \left[\sum_{\mathbf{k}}^{\mathrm{BZ}} \sum_n f_{n\mathbf{k}}^{\sigma,\mathrm{FD}}[1 - f_{n\mathbf{k}}^{\sigma,\mathrm{FD}}]\phi_{n\mathbf{k}}^{\sigma*}(\mathbf{r})\phi_{n\mathbf{k}}^{\sigma}(\mathbf{r}) \right] \\
& \times \left[\sum_{\mathbf{k}'}^{\mathrm{BZ}} \sum_{n'} f_{n'\mathbf{k}'}^{\sigma',\mathrm{FD}}[1 - f_{n'\mathbf{k}'}^{\sigma',\mathrm{FD}}]\phi_{n'\mathbf{k}'}^{\sigma'*}(\mathbf{r}')\phi_{n'\mathbf{k}'}^{\sigma'}(\mathbf{r}') \right].
\end{aligned} \tag{6.63}$$

Similarly, the spinor of the right-hand side Eq. (6.57b) turns into

$$\begin{aligned}
t^\sigma(\mathbf{r}) \;=\;& \sum_{\mathbf{k}}^{\mathrm{BZ}} \sum_n f_{n\mathbf{k}}^{\sigma} \left[\sum_{n'\neq n} \langle \phi_{n\mathbf{k}}^{\sigma} | V_\mathrm{x}^{\mathrm{NL},\sigma} | \phi_{n'\mathbf{k}}^{\sigma} \rangle \frac{\phi_{n'\mathbf{k}}^{\sigma*}(\mathbf{r}')\phi_{n\mathbf{k}}^{\sigma}(\mathbf{r})}{\epsilon_{n\mathbf{k}}^{\sigma} - \epsilon_{n'\mathbf{k}}^{\sigma}} + \mathrm{c.c.} \right] \\
& - \frac{1}{k_B T} \sum_{\mathbf{k}}^{\mathrm{BZ}} \sum_n \langle \phi_{n\mathbf{k}}^{\sigma} | V_\mathrm{x}^{\mathrm{NL},\sigma'} | \phi_{n\mathbf{k}}^{\sigma} \rangle f_{n\mathbf{k}}^{\sigma,\mathrm{FD}}[1 - f_{n\mathbf{k}}^{\sigma,\mathrm{FD}}]\phi_{n\mathbf{k}}^{\sigma*}(\mathbf{r})\phi_{n\mathbf{k}}^{\sigma}(\mathbf{r}) \\
& + \frac{1}{k_B T} \frac{1}{Z} \sum_{\mathbf{k}}^{\mathrm{BZ}} \sum_n \left[\sum_{\sigma'} \sum_{\mathbf{k}'}^{\mathrm{BZ}} \sum_{n'} \langle \phi_{n'\mathbf{k}'}^{\sigma'} | V_\mathrm{x}^{\mathrm{NL},\sigma'} | \phi_{n'\mathbf{k}'}^{\sigma'} \rangle f_{n'\mathbf{k}'}^{\sigma',\mathrm{FD}}[1 - f_{n'\mathbf{k}'}^{\sigma',\mathrm{FD}}] \right] \\
& \times f_{n\mathbf{k}}^{\sigma,\mathrm{FD}}[1 - f_{n\mathbf{k}}^{\sigma,\mathrm{FD}}]\phi_{n\mathbf{k}}^{\sigma*}(\mathbf{r})\phi_{n\mathbf{k}}^{\sigma}(\mathbf{r})\,.
\end{aligned} \tag{6.64}$$

In the limit of $T \to 0$, all temperature-dependent terms in $\chi_\mathrm{s}^{\sigma\sigma'}(\mathbf{r},\mathbf{r}')$ and $t^\sigma(\mathbf{r})$ vanish, as $f_{n\mathbf{k}}^{\sigma,\mathrm{FD}}$ is either 1 or 0. In particular, the off-diagonal elements of the density response matrix

are zero, and Eq. (6.56) decouples into two separate equations for the spin-up and spin-down potential. Finally, the equations of section 6.1 are recovered.

In order to solve Eq. (6.56) numerically for finite T, we expand the spinor of the local EXX potential in the MPB, which is by construction spin-independent (cf. Sec. 4.2.2). The basis set is thus given by

$$\left\{\left[\begin{pmatrix} M_I(\mathbf{r}) \\ 0 \end{pmatrix}, i = 1, \ldots, N_{\mathrm{MPB}}\right], \left[\begin{pmatrix} 0 \\ M_I(\mathbf{r}) \end{pmatrix}, i = 1, \ldots, N_{\mathrm{MPB}}\right]\right\} . \tag{6.65}$$

Here, N_{MPB} denotes the total number of spin-independent MPB functions. In analogy to the spin-polarized case with integer occupation, the spinor corresponding to a constant function $c\begin{pmatrix} 1 \\ 1 \end{pmatrix}$ is an eigenfunction of the response matrix in Eq. (6.55b) with eigenvalue zero and must be excluded from the Hilbert space in order to make $\chi_{\mathrm{s}}^{\sigma\sigma'}$ invertible. This is already fulfilled by the MPB (6.65) as each function $M_I(\mathbf{r})$ is by construction orthogonal to a constant function (s. Sec. 6.2). But the Hilbert space spanned by the two constant functions $c\begin{pmatrix} 1 \\ 0 \end{pmatrix}$ and $c\begin{pmatrix} 0 \\ 1 \end{pmatrix}$ additionally contains the function $c\begin{pmatrix} 1 \\ -1 \end{pmatrix}$. The latter is orthogonal to the constant spinor $c\begin{pmatrix} 1 \\ 1 \end{pmatrix}$ and enables an alignment of the spin-up part of the potential with respect to the spin-down part. Therefore, we add the spinor $\begin{pmatrix} 1 \\ -1 \end{pmatrix}$ to the MPB [Eq. (6.65)]. Consequently, the integral equation that couples the spin-up and spin-down EXX potentials turns into an algebraic equation of dimension $(2N_{\mathrm{MPB}}+1) \times (2N_{\mathrm{MPB}}+1)$, that can be solved by numerical inversion of the response matrix.

6.10.2. Metals: Na, Al, and Cu

Before we show EXX-OEP results for the metals Na, Al, and Cu at the experimental lattice constants (Na 8.11 a_0; Al 7.65 a_0; Cu 6.82 a_0), we discuss the homogeneous electron gas (HEG). The HEG is a model system, in which the positive charges of the atomic nuclei are smeared out uniformly over space. Consequently, the electron density is distributed uniformly in space, too. The HEG provides a simple model for delocalized electrons in a metal. We discuss the HEG in the HF as well as the EXX-OEP approach in order to point out the differences between both approaches for metals.

It is known that the HF method, which approximates the many-electron wave function by a single Slater determinant instead of the many-electron Hamiltonian, gives for the HEG an

eigenvalue dispersion that consists of two terms. The first one corresponds to the energy of a free electron, which is corrected by the second term arising from the explicit consideration of the electron-electron interaction

$$\epsilon^{\mathrm{HF}}_{\mathrm{HEG}}(\mathbf{k}) = \frac{1}{2}k^2 - \frac{2k_{\mathrm{F}}}{\pi}F(\frac{k}{k_{\mathrm{F}}}) \tag{6.66}$$

with the function

$$F(x) = \frac{1}{2} + \frac{1-x^2}{4x}\log\left(\frac{1+x}{|1-x|}\right) \tag{6.67}$$

and the Fermi wavevector k_{F}. The correction term F is continuous, but has a derivative discontinuity at $k = k_{\mathrm{F}}$. Because of this the HF method predicts a vanishing density of states

$$D(\epsilon) = \frac{1}{V_{\mathrm{BZ}}}\int \delta(\epsilon - \epsilon(\mathbf{k}))d^3k = \frac{V}{2\pi^2}\left.\frac{k^2}{\epsilon'(k)}\right|_{\epsilon(k)=\epsilon}. \tag{6.68}$$

at the Fermi level E_{F}, which is in contradiction to the conductivity or specific heat of metals.

The EXX-OEP approach, on the contrary, employs formally the same total energy functional as the HF approach, but requires a local instead of a non-local exchange potential. As the EXX energy is, in the case of the HEG, identical to the exchange energy of the LDA, the local EXX potential is proportional to $n^{1/3}$ and therefore a constant. Moreover, the Hartree potential and the external potential arising from the positive homogeneously smeared out charge background are constant, too. So, the KS electrons move in a constant potential and behave as free electrons with the dispersion

$$\epsilon^{\mathrm{EXX}}_{\mathrm{HEG}}(\mathbf{k}) = \frac{1}{2}k^2\,. \tag{6.69}$$

Thus, the density of states for the HEG in the EXX-OEP method is proportional to $\sqrt{\epsilon}$ and does not vanish at the Fermi energy E_{F}.

According to this argumentation, we expect that the EXX-OEP approach gives a reasonable description at least for simple metals that behave nearly free-electron-like, in contrast to the HF method. This assumption is indeed confirmed by our calculations for bcc Na and fcc Al. For the calculation of Na (Al) we use an LAPW basis set with the parameters $G_{\max} = 4.0\,\mathrm{a}_0^{-1}$ ($G_{\max} = 3.7\,\mathrm{a}_0^{-1}$) and $l_{\max} = 12$ ($l_{\max} = 10$). The corresponding cutoff values of the MPB are $G'_{\max} = 3.0\,\mathrm{a}_0^{-1}$ ($G'_{\max} = 2.8\,\mathrm{a}_0^{-1}$) and $L_{\max} = 6$ ($L_{\max} = 6$). In both calculations we have employed an 8×8×8 $\mathbf{k}$-point mesh for the self-consistency cycle and occupy the states according to the Fermi-Dirac distribution with a temperature of $T = 316\,\mathrm{K}$ ($k_B T = 1\,\mathrm{mhtr}$). Figure 6.23 shows LDA and EXX band structures and densities of states for both materials. The occupied

	LDA	EXX	Expt.
d center	-3.10	-4.74	-3.65^a
d width	3.46	2.49	3.1 ± 0.2^a

[a] Reference 174

Table 6.11.: Comparison of the center (with respect to E_F) and the width of the d states (in eV) of Cu from LDA, EXX, and experimental band structures. We used the definition of the d-band width as given in Ref. 174 as the difference between the highest and lowest occupied state at the X point in the BZ. Accordingly, the center of the d bands is defined as the midpoint of the highest and lowest occupied state at X.

spectrum in the EXX approach is nearly indistinguishable from the LDA one. EXX and LDA bands cross the Fermi energy at almost the same points in the BZ. However with increasing energy, the LDA and EXX band structures start to differ, but the shape of the band dispersions still remains very similar. Due to the similarity in the band structure between the LDA and EXX approaches, the densities of states is nearly identical, too. It shows a free-electron-like square root behavior with only minor variations.

The question arises what happens for a metal that substantially deviates from the HEG as for example a transition metal with localized d electrons. For the example of Cu, we demonstrate in Fig. 6.24 that LDA and EXX band structures and densities of states differ significantly. The calculations employ an LAPW basis (MPB) with reciprocal cutoff parameter $G_{\max} = 4.5\,\mathrm{a}_0^{-1}$ ($G'_{\max} = 3.0\,\mathrm{a}_0^{-1}$) and angular momentum cutoff $l_{\max} = 8$ ($L_{\max} = 6$). The BZ zone is sampled by an 8×8×8 **k**-point mesh and a Fermi-Dirac distribution with a temperature of $T = 316\,\mathrm{K}$ ($k_B T = 1\,\mathrm{mhtr}$) is used. Figure 6.24 shows that the lowest valence state of Cu 3*s* character is bound much stronger in the LDA than with the EXX functional. In contrast to that the Cu d states are bound more tightly in the EXX approach and their band width is reduced with respect to the LDA (cf. Table 6.11). Moreover, the dispersion of the bands around the L point close to the Fermi energy is apparently different in the LDA and EXX method. While the former results in an occupied state at roughly 1.0 eV below E_F, the latter yields an unoccupied state at about 0.33 eV above E_F at the L point.

A comparison with the experimentally measured band dispersion along the BZ path L → Γ → X is shown in Fig. 6.25. While in the LDA the Cu d states are bound to shallow with respect to experiment, the trend of the EXX functional to bind them more strongly is in accordance with experiment, even though the underbinding of the LDA is overcorrected by the EXX approach. Similarly, the tendency of the EXX method to reduce the valence band width is correct. However, quantitatively the EXX functional underestimates the experimental band

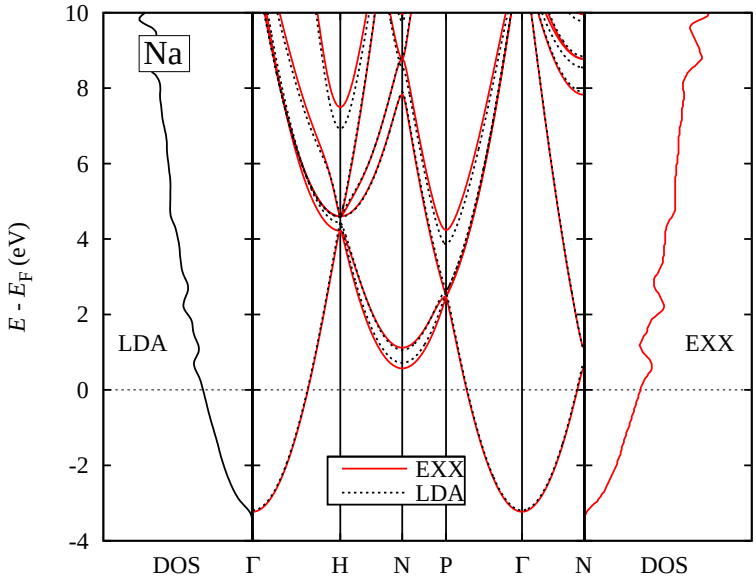

(a)

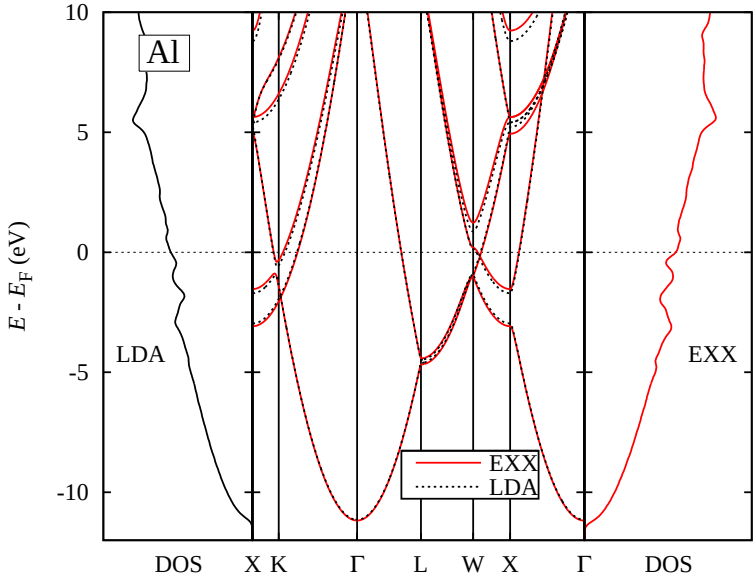

(b)

Figure 6.23.: Comparison of LDA and EXX band structures and DOS (in units of states/eV) for (a) bcc Na and (b) fcc Al.

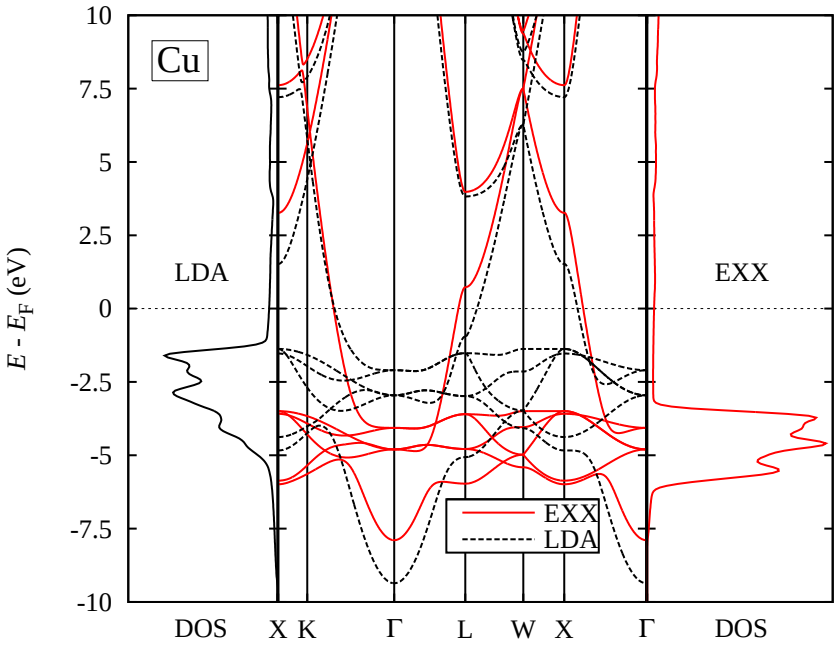

Figure 6.24.: Band structures and DOS (in units of states/eV) for copper calculated with the LDA and EXX-OEP functional.

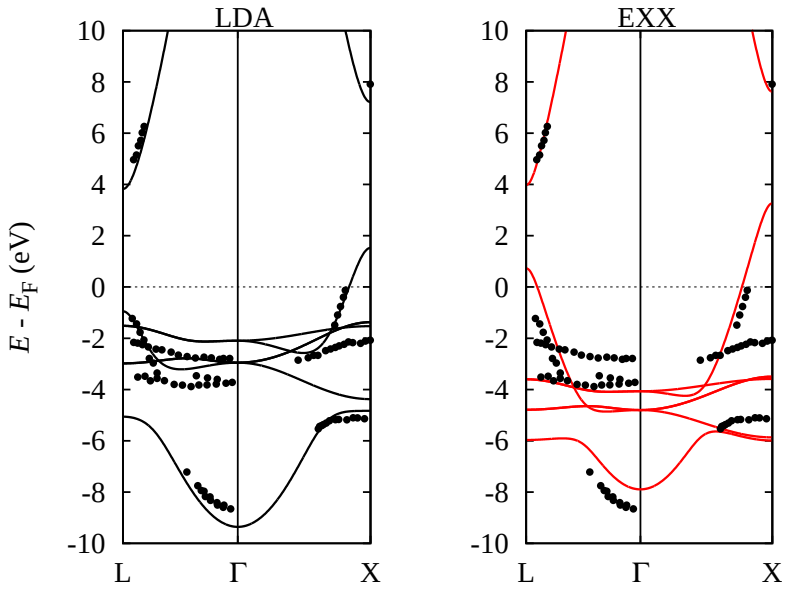

Figure 6.25.: LDA and EXX band structures for Cu and comparison with experimental data points taken from Refs. 174 and 175.

width.

The addition of LDA correlation to the orbital-dependent EXX functional does not significantly change the EXX band dispersion of Cu. Kotani [176] showed that an orbital-dependent RPA correlation functional in combination with the EXX functional leads to an eigenvalue spectrum of Cu, which is similar to the LDA spectrum again.

6.11. Summary

We have developed an all-electron full-potential implementation of the EXX-OEP method within the FLAPW approach. It is based on a representation of the local, multiplicative exchange potential by the auxiliary mixed product basis (MPB), which has been adjusted for its present purpose. In this way, the integral equation for the exchange potential becomes an algebraic equation. After exclusion of the constant function from the Hilbert space spanned by the MPB, this algebraic equation can be solved for the potential by a simple matrix inversion.

We found that a numerically stable and physical EXX potential requires a balance between LAPW and mixed product basis sets. Otherwise, the potential shows spurious oscillations. This balance can be achieved by converging the LAPW basis with respect to the MPB. In the interstitial region, the reciprocal cutoff radius of the LAPW basis must be converged with

respect to that of the MPB. Typically 1.33 times the reciprocal cutoff of the MPB leads to converged results. In the MT spheres, on the contrary, the LAPW basis must be enhanced by local orbitals. For example for diamond, we must add six local orbitals for each lm channel from $l = 0$ to $l = 5$ to obtain a smooth potential in the spheres. This increases the number of LAPW basis functions by a factor of 4. The enhanced flexibility of the LAPW basis, in contrast to LDA or GGA calculations, is necessary to enable the wave functions and, thus, the density to respond adequately to the changes of the effective potential, which are described in our formalism by the MPB. An analysis of the convergence behavior of the density response function confirms this statement.

In comparison with the LDA exchange potential, the (balanced) EXX potential exhibits a much stronger anisotropy in particular within the MT spheres. This indicates that a full-potential treatment in the case of the EXX OEP formalism is even more important than in the LDA or GGA.

The smooth or oscillatory shape of the potential naturally affects the KS eigenvalues and transition energies. For the materials C, Si, SiC, Ge, GaAs, and crystalline Ar we found a very good agreement between our all-electron full potential EXX calculations and pseudopotential plane wave results from the literature provided that both basis sets are properly balanced. This is in contradiction to a previous implementation within the FLAPW method [39], which initiated a controversy about the adequacy of the pseudopotential approximation within the EXX-OEP approach. Our results, instead, confirm the reliability of the pseudopotential approximation (at least for this set of materials) and, thus, contribute to the clarification of the contradiction.

Furthermore, we discussed the connection of the KS band gap, which corresponds to the transition of the highest occupied to the lowest unoccupied KS state, with the fundamental gap of the true interacting system. In exact DFT, the sum of KS gap and the derivative discontinuity of the xc energy functional equals the exact fundamental gap. While the discontinuity vanishes for the LDA and GGA, we demonstrated for the III-V nitrides that the discontinuity of the EXX functional amounts to a significant contribution of several eV. This has the consequence that the sum of EXX KS band gap and derivative discontinuity overestimates the experimental gap. We argued that a fortuitous error cancellation between the neglect of the discontinuity and the neglect of orbital correlation is responsible for the quantitative agreement of the EXX KS gap alone with experiment. A further improved description of the band gap can be obtained by combining exact exchange with the random-phase approximation (RPA) for the correlation energy of DFT [12].

In order to reduce the computational demand of EXX-OEP calculations, we have developed a numerical finite-basis correction (FBC) for response quantities within the LAPW ap-

proach. It considers the change of the LAPW MT functions due to a change in the effective potential explicitly. The final formula for the KS wave-function and density response consists of two terms: the usual sum-over-states expression and a correction term, the FBC, which vanishes in the limit of a complete basis. Moreover, it provides, in principle, an exact treatment of the core-state response. For the example of ScN, we demonstrated that the FBC improves the convergence of the EXX-OEP potential. Considerably fewer local orbitals are required to obtain a stable and smooth potential. We note that the FBC is not restricted to the EXX-OEP method. For example, a slightly different construction of the FBC might improve the slow convergence of *GW* calculations [177] with respect to the basis set and the number of unoccupied states.

We applied the EXX-OEP approach to the transition metal perovskites $CaTiO_3$, $SrTiO_3$, and $BaTiO_3$ as well as the antiferromagnetic oxides MnO, FeO, and CoO. For all materials, the EXX functional opens the band gap. Most notably, FeO and CoO are predicted to be semiconducting, while they are metallic in the LDA and GGA. The band gap of the three perovskites is quantitatively overestimated by about 25%, which we attribute, on the one hand, to an incomplete error cancellation between the neglect of correlation and the neglect of the xc derivative discontinuity and, on the other hand, to differences in the crystalline structure between theoretical and experimental setup.

Finally, we have presented a generalization of the EXX-OEP formalism for the calculation of metals. In contrast to semiconductors and insulators, the variation of the occupation number due to a change in the effective potential has to be taken into account. As a proof of principle, we showed results for Na, Al, and Cu. While for the simple metals bcc Na and fcc Al LDA and EXX band structures (nearly) coincide, at least for the occupied part of the spectrum, both approaches give rise to substantially different eigenvalue spectra for Cu.

7. Summary & Conclusion

In this thesis, we have implemented and explored two approaches, the Kohn-Sham (KS) [3] and the generalized Kohn-Sham (gKS) [23] formalism, for dealing with orbital-dependent exchange-correlation (xc) functionals of density-functional theory (DFT). We developed an implementation of hybrid functionals, which combine orbital-dependent exact exchange (EXX) with local or semi-local approximations for the xc energy of DFT, in the gKS formalism. In this formalism, the EXX energy leads to a non-local exchange potential in the one-particle equations. We worked, in particular, with the PBE0 hybrid functional of Perdew, Burke, and Ernzerhof [22]. Furthermore, we presented an implementation of the orbital-dependent EXX functional within the KS formalism of DFT. The KS, in contrast to the gKS formalism, requires a local instead of a non-local potential in the one-particle equations. The local, multiplicative exchange potential is constructed from the non-local exact exchange energy by the optimized effective potential (OEP) method [32–34].

Both approaches and functionals, PBE0 and EXX-OEP, have been realized within the all-electron full-potential linearized augmented-plane-wave (FLAPW) method [24–27]. They rely on an additional auxiliary basis, the mixed product basis (MPB). The latter has been built from products of LAPW basis functions and constitutes an efficient all-electron basis for the representation of wave-function products.

For the implementation of the hybrid functionals, the MPB is employed to calculate the matrix elements of the non-local exchange potential. Each element corresponds to a Brillouin zone (BZ) sum over six-dimensional integrals. Exploiting the MPB to represent the products of LAPW wave functions, the integral becomes a vector-matrix-vector product, where the matrix is the representation of the Coulomb interaction in the MPB. As the calculation of the non-local exchange potential is the most time-consuming step in a practical calculation, we have developed several techniques to accelerate our numerical scheme: the Coulomb matrix is made sparse by a unitary transformation of the MPB, which is constructed such that nearly all muffin-tin (MT) MPB functions are multipole-free. The sparsity is then used to reduce the computational demand for the matrix-vector multiplications. Moreover, we exploit spatial and time-reversal symmetries to (a) restrict the BZ sum to an irreducible part of the BZ and (b) to identify those matrix elements in advance that are zero and need not

be calculated. The **k**-point convergence of the BZ sum occurring in the non-local exchange potential is improved by separating the divergent part, resulting from the long-range nature of the Coulomb interaction, from the non-divergent one. While the latter is integrated numerically, the divergent part is treated analytically. So far, the techniques contribute to the acceleration of a single iteration. However, the one-particle equations of the gKS system must be solved self-consistently, as the local and non-local potential are functionals of the density and density matrix, respectively. We found that a nested self-consistent field (SCF) cycle consisting of an outer density-matrix and an inner density-only iteration scheme leads to a much faster convergence of the PBE0 calculations than a direct iteration scheme.

The developed implementation of the PBE0 hybrid functional is applied to Si, C, GaAs, MgO, NaCl, and crystalline Ar. For this set of materials, the PBE0 functional gives transition energies and band gaps that lie much closer to the experimental value than the respective PBE [7] value. Though, we observe an overestimation of the transitions for the semiconductors Si and GaAs and an underestimation for the large gap insulators. Our results compare well with recent PBE0 calculations within the projector augmented-wave (PAW) method [30]. Moreover, the PBE0 functional improves the description of localized states as illustrated for ZnO.

We have applied the PBE0 functional to EuO, a ferromagnetic semiconductor with localized $4f$-states that could not be described properly by the conventional local and semi-local xc functionals commonly used in DFT calculations. We examined the structural, electronic, and magnetic properties of EuO in the rock-salt structure. In contrast to the semi-local PBE functional, the PBE0 hybrid correctly predicts EuO to be a ferromagnetic semiconductor. The PBE0 and experimental lattice constant measured at $T = 4.2\,\mathrm{K}$ deviate by only 1‰, which is one order of magnitude closer to the experimental value than the PBE result. While an experimental gap of 0.95 eV is observed in the limit of $T \to 0\,\mathrm{K}$, the theoretical gap amounts to 0.85 eV, whereas the PBE functional predicts a metal. In order to measure the quality of PBE0 total-energy differences between different magnetic states, we map the total-energy differences between ferromagnetic and antiferromagnetic configurations of EuO onto a Heisenberg model with nearest and next-nearest neighbor interactions. This mapping enables to calculate the Curie temperature and magnon dispersion of EuO. The resulting Curie temperature of 105 K evaluated in the random-phase approximation overestimates the experimental value of 69 K but is in much better agreement than the corresponding PBE value of 272 K. Particularly impressive is the magnon dispersion calculated with the PBE0 functional, where the PBE0 spin stiffness of 43.5 meV a_0^2 compares extremely well with the experimental data of 38.6 meV a_0^2. This gives confidence in the energetics obtained by the PBE0 functional for different magnetic phases. From this we conclude that the PBE0 functional has the potential

to describe the properties of rare-earth chalcogenides without the need for an adjustable parameter as the Hubbard U in the LDA+U approach. The reduced self-interaction error of the PBE0 hybrid in contrast to the PBE functional seems to be pivotal for the improved description of EuO. It rectifies, in particular, the description of the strongly localized $4f$ electrons of Eu. Summarizing, an efficient implementation of the PBE0 hybrid functional within the FLAPW method has been developed. The PBE0 functional leads to an improved description of band-gap materials and materials with localized d- and f-electron states in comparison to the PBE.

For the implementation of the EXX-OEP approach within the FLAPW method, we have employed a slightly modified MPB. The basis has been specifically adjusted for the representation of the local exact exchange potential. So, the OEP integral equation becomes an algebraic equation, which can be solved for the local exact exchange potential, after the constant function has been eliminated from the MPB. We found that the LAPW basis for the representation of the KS wave functions and the MPB for the representation of the local potential are not independent. Instead, the LAPW basis must be converged with respect to the MPB to obtain a smooth and stable EXX potential. This interdependence of the basis sets arises from the density response function on the left-hand side and the KS wave function response on the right-hand side of the OEP equation. They describe the response of the density or KS wave function due to a change in the effective potential, which is given in our formalism by the MPB. If the LAPW basis, which parametrizes the KS wave function and thus also the density, is not flexible enough, the KS wave function cannot follow the changes of the effective potential, and a corrupted response function is obtained. This is the reason why the LAPW basis must be converged to an accuracy which is beyond that for conventional DFT calculations employing the local-density approximation (LDA) or generalized gradient approximation (GGA). In particular, the flexibility of the MT LAPW basis must be enlarged, which is achieved by adding an exceedingly large number of local orbitals to the LAPW basis.

The requirement of a flexible LAPW basis to obtain a stable and physical local EXX potential makes the EXX-OEP approach computationally demanding. In this thesis, we explored a novel route circumventing this problem by developing a finite basis correction (FBC), an expression that corrects the conventional formulation of first-order perturbation theory for the KS wave-function and density response functions and vanishes in the limit of a infinite, complete LAPW basis. It arises from the fact that the LAPW basis in the MT spheres itself depends on the effective potential as the radial MT functions are the solutions of radial Schrödinger equations taking into account the spherical part of the effective potential. The change in the radial LAPW functions due to a change in the effective potential is explicitly calculated by solving radial Sternheimer equations. Finally, the response consists of two con-

tributions: a term which is identical to the conventional perturbation-theory result and the FBC term. The FBC acts only within the MT spheres. As demonstrated for ScN, the FBC leads to numerical stable EXX potentials at much smaller LAPW basis sets.

Similarly to the PBE0 hybrid functional, the EXX-OEP functional leads to KS transition energies and KS band gaps which are in much better agreement with experiment. Moreover, we observe – provided that both basis sets are properly balanced – a very good agreement between our all-electron FLAPW and pseudopotential plane-wave transition energies for the semiconductors and insulators C, Si, SiC, Ge, GaAs, and crystalline Ar. This finding is in contradiction to a previous implementation of the EXX functional within the FLAPW method [39], which incited a controversy about the adequacy of the pseudopotential approximation in the context of the EXX-OEP method [40, 41]. Our results, however, confirm the pseudopotential approximation and thus contribute to the clarification of this controversy.

In contrast to LDA and GGA, the EXX functional exhibits a derivative discontinuity at integral particle numbers, which contributes to the theoretical fundamental band gap. The latter is given by the sum of the KS band gap and the derivative discontinuity. For the III-V nitrides and ScN, we showed that the discontinuity amounts to several eV so that the sum of EXX KS band gap and EXX discontinuity overestimates the experimental band gap. The theoretical fundamental band gap becomes as large as the Hartree-Fock (HF) gap. This suggests that the quantitative agreement of the EXX KS band gap with experiment (at least for the simple semiconductors) is caused by a fortuitous error cancellation between the neglect of the discontinuity and the neglect of orbital correlation.

Furthermore, we have applied the EXX approach to the cubic perovskites $CaTiO_3$, $SrTiO_3$, and $BaTiO_3$. In comparison with the LDA, we observe an opening of the KS band gap and a slight reduction of the valence band width. Apart from this, the dispersion of the bands is nearly unaffected. Quantitatively, the LDA KS gap underestimates the experimental gap for the three perovskites by about 50%. The EXX approach leads to an overestimation of 25%. This pronounced overestimation may result either from an incomplete error cancellation between the neglect of orbital correlation and the neglect of the xc derivative discontinuity or from the difference in the crystalline structure assumed in the experimental realization and the theoretical idealization by a cubic lattice.

Moreover, we have reported calculations of the antiferromagnetic transition-metal oxides MnO, FeO, and CoO in the rock-salt structure, which are insulating in experiment. LDA as well as GGA erroneously predict CoO and FeO to be metallic. With the EXX functional all three oxides become insulators with an indirect band gap. While for MnO the spin splitting of the Mn 3*d* states is responsible for the formation of the gap, we attribute the gap in FeO and CoO to the fact that in the EXX calculations the occupation of a previously unoccupied single

particle level causes its energy to fall, whereas LDA and GGA exhibit exactly the opposite behavior.

Finally, we have generalized the EXX formalism to metals and performed EXX calculations for the metals Na, Al, and Cu. The calculations for the simple metals Na and Al show that the band structure for these simple metals is equally well described within the EXX and the LDA functional. Small deviations between the EXX and the LDA band structures are seen for the unoccupied spectrum. However, we demonstrate for Cu with its localized *d* electrons that the LDA and EXX functionals give rise to significantly different KS band structures.

For future work, we propose to combine the orbital-dependent exact exchange energy with an orbital-dependent correlation functional. The latter can be either determined by Görling-Levy perturbation theory [16], by many-body perturbation theory (MBPT) [69, 70], or by the adiabatic-connection-fluctuation-dissipation (ACFD) theorem [178–180]. From such a functional we might expect (a) a better description of the band gap in the sense that the sum of KS band gap and derivative discontinuity yield a reasonable estimate for the experimental gap, (b) an improved description of complex metals, and (c) a seamless description of the van-der-Waals interaction.

Last but not least, the FBC introduced in this thesis is a general concept to evaluate response functions within electronic structure methods employing potential dependent basis functions. It opens the vista to electric field response or the calculation of phonon dispersion using incommensurate phonons within the framework of the density functional perturbation theory. Furthermore, the FBC might be generalized to the *GW* approximation of many body perturbation theory, which involves the calculation of a dynamical density response function and the single-particle Green function. In this way, the slow convergence of *GW* calculations with respect to the basis set and the number of unoccupied states [177] might be improved.

A. Incorporation of constraints in the mixed product basis

The mixed product basis (MPB) as introduced in section 4.2.2 consists of two sets of functions, plane waves in the interstitial region and products of numerical, radial functions times spherical harmonics in the muffin-tin (MT) spheres, that are simply grouped together. So, the interstitial plane waves abruptly go to zero at the MT sphere boundary and vice versa. In order to guarantee that any quantity represented by the MPB is continuous and continuous differentiable at the MT sphere boundary, it is desirable to form linear combinations of the originally discontinuous MPB functions. Moreover, the EXX-OEP approach demands that the MPB is orthogonal with respect to a constant function (s. Sec. 6.2). In the following, we will discuss a quite general numerical approach [181], which allows to construct the subspace of the MPB fulfilling the above mentioned constraints. The approach easily permits to incorporate further constraints in the construction of the MPB.

Our aim is to form linear combinations of the original MPB functions $M_{\mathbf{k},J}(\mathbf{r})$

$$M'_{\mathbf{k},I}(\mathbf{r}) = \sum_J a_{JI} M_{\mathbf{k},J}(\mathbf{r})\,, \tag{A.1}$$

that are continuous and continuous differentiable at the MT sphere boundary and orthogonal to a constant function. Each constraint can be understood as an orthogonality demand to the matrix of coefficient vectors $a_{JI.}$ For example, the demand of orthogonality of the final MPB $M'_{\mathbf{k},I}(\mathbf{r})$ with respect to a constant function requires that the integral

$$\int M'_{\mathbf{k},I}(\mathbf{r}) d^3r = 0 \tag{A.2}$$

vanishes for all indices I. Combination of Eq. (A.1) with (A.2) results in the following condition for the coefficient matrix

$$\sum_J c_J a_{JI} = 0 \tag{A.3}$$

with $c_J = \int M_{\mathbf{k},J}(\mathbf{r})\, d^3r$. Consequently, each column of the matrix $\mathbf{a}$ must be orthogonal to the constrain vector $\mathbf{c}$ to guarantee that Eq. (A.2) holds. In analogy to that the requirement of

continuity in value and first radial derivative at the MT sphere boundary leads to additional orthogonality demands on the coefficient matrix **a**. To be more precise, for each lm channel and each atom a in the unit cell we obtain two additional orthogonality constraints, one for the requirement of continuity and another for the requirement of continuous differentiability at the MT sphere boundary. The coefficient vector **c**, which enforces that the interstitial plane wave is continuously matched at the MT sphere boundary of atom a to the MT function with angular momentum l and magnetic quantum number m, is given by

$$c_J = \begin{cases} -M^a_{lmP}(S_a) & \text{if } J = almP \\ \frac{4\pi}{\sqrt{\Omega}} i^l \exp(i\mathbf{G}\mathbf{R}_a) j_l(|\mathbf{G}|S_a) Y^*_{lm}(\mathbf{k}+\mathbf{G}) & \text{if } J = \mathbf{G} \\ 0 & \text{otherwise} , \end{cases} \tag{A.4}$$

where $\mathbf{R}_a$ denotes the center of the MT sphere around atom a with radius S_a, Ω is the unit cell volume, and $j_l(x)$ is the spherical Bessel function arising from the Rayleigh decomposition of the interstitial plane wave. A similar constraint vector **c** arises from the demand of continuity in the first radial derivative at the MT boundary of atom a

$$c_J = \begin{cases} -\frac{d}{dr} M^a_{lmP}(S_a) & \text{if } J = almP \\ \frac{4\pi}{\sqrt{\Omega}} i^l \exp(i\mathbf{G}\mathbf{R}_a) \frac{d}{dr} j_l(|\mathbf{G}|S_a) Y^*_{lm}(\mathbf{k}+\mathbf{G}) & \text{if } J = \mathbf{G} \\ 0 & \text{otherwise} \end{cases} . \tag{A.5}$$

Thus, we obtain $2(L_{\max}+1)^2$ constraints for each atom a in the unit cell plus the constraint arising from the removal of a constant function, which amounts in total to $N_c = 2(L_{\max}+1)^2 N_{\text{atom}} + 1$ constraints. For example, in the case of Si with an angular momentum cutoff of $L_{\max} = 4$ for the MPB and 2 atoms in the unit-cell we finally end up with 101 constraint vectors $\mathbf{c}_i$ $(i = 1, \ldots, N_c = 101)$. The original MPB functions, represented in terms of a unit matrix **a**, are then orthogonalized with respect to the constraints $\mathbf{c}_i$. In order to simplify the orthogonalization process, we orthogonalize the constraints in a first step. Then, the original MPB functions are orthogonalized with respect to the orthogonalized constraints. Afterwards, the linear dependent functions in the set $\{M'_{\mathbf{k},I}\}$ are removed. As there are always as many linear dependent functions as constraints, the final mixed product basis is of the size $N - N_c$, if N is the size of the original basis $\{M_{\mathbf{k},I}\}$. Consequently, we end up with a rectangular coefficient matrix **a**, which is of the dimension $N \times (N - N_c)$ and mediates between the sets $\{M_{\mathbf{k},I}\}$ and $\{M'_{\mathbf{k},I}\}$. It can be understood as a projector to the subspace of continuous and continuous differentiable functions, which are additional orthogonal to a constant function.

The algorithm easily allows to incorporate any further condition in the MPB at least if it can be formulated as an orthogonality demand on the coefficient vectors. For example, the

requirement that the slope of the MPB has to vanish at the position of the atomic nuclei $\mathbf{R}_a$.

B. Scalar-relativistic approximation

Despite the relatively small (band) energy of the electrons in a solid, relativistic effects yet can become significant within the MT spheres close to the atomic nuclei, where the potential is deep and the electrons exhibit a large kinetic energy. Koelling and Harmon [182] developed an approximation, the scalar relativistic approximation (SRA), for the fully-relativistic Dirac equation with a spherical external potential which allows to incorporate relativistic effects in the full-potential linearized augmented-plane-wave (FLAPW) method. In the SRA kinematic relativistic effects are fully taken into account, whereas the spin-orbit interaction is neglected. Due to the neglect of the spin-orbit term $\mathbf{S}^2$, S_z, $\mathbf{L}^2$, and L_z commute with the scalar relativistic equation and form, in turn, a set of good quantum numbers.

The scalar relativistic wave function can be written as

$$\phi^{\sigma}_{lm}(\mathbf{r}) = \frac{1}{r}\begin{pmatrix} p^{\sigma}_{l}(r)Y_{lm}(\hat{\mathbf{r}})\chi^{\sigma} \\ q^{\sigma}_{l}(r)Y_{lm}(\hat{\mathbf{r}})\chi^{\sigma} \end{pmatrix}, \tag{B.1}$$

where χ^{σ} is a 2-component spin-up or spin-down spinor. The radial functions $p^{\sigma}_{l}(r)$ and $q^{\sigma}_{l}(r)$ are the solution of the coupled radial differential equations

$$\frac{dp^{\sigma}_{l}(r)}{dr} = 2M(r,E)cq^{\sigma}_{l}(r) + \frac{p^{\sigma}_{l}(r)}{r} \tag{B.2}$$

$$\frac{dq^{\sigma}_{l}(r)}{dr} = \frac{1}{c}\left[\frac{l(l+1)}{2M(r,E)r^2} + V^{\sigma}(r) - E\right]p^{\sigma}_{l}(r) - \frac{q^{\sigma}_{l}(r)}{r}. \tag{B.3}$$

with the abbreviation

$$M(r,E) = 1 + \frac{1}{2c^2}\left[E - V^{\sigma}(r)\right], \tag{B.4}$$

the speed of light c, and the spherical, spin-dependent potential $V^{\sigma}(r)$. A derivation of Eqs. (B.2) and (B.3) is discussed in detail in Refs. 182 and 183.

In order to incorporate the SRA in the MT LAPW basis the radial function $u^{a\sigma}_{l(p=1)}(r)$ $\left[u^{a\sigma}_{l}(r)\right]$ is replaced by the 2-component function

$$u^{a\sigma}_{l(p=1)}(r) \rightarrow \frac{1}{r}\begin{pmatrix} p^{a\sigma}_{l}(r) \\ q^{a\sigma}_{l}(r) \end{pmatrix} \tag{B.5}$$

which is obtained from Eqs. (B.2) and (B.3) by substituting the spherical potential $V^{\sigma}(r)$ and the energy E by the spherical, effective Kohn-Sham (KS) potential $V^{a\sigma}_{\text{eff},0}(r)$ of atom a and the energy parameter $E^{a\sigma}_l$, respectively. In analogy, the energy derivative $u^{a\sigma}_{l(p=2)}(r)\left[\dot{u}^{a\sigma}_l(r)\right]$ is replaced by the two components

$$u^{a\sigma}_{l(p=2)}(r) \to \frac{1}{r}\begin{pmatrix} \dot{p}^{a\sigma}_l(r) \\ \dot{q}^{a\sigma}_l(r) \end{pmatrix}, \tag{B.6}$$

where $\dot{p}^{a\sigma}_l(r)$ $[\dot{q}^{a\sigma}_l(r)]$ denotes the energy derivative of $p^{a\sigma}_l(r)$ $[q^{a\sigma}_l(r)]$, which is given by the set of equations

$$\frac{d\dot{p}^{a\sigma}_l(r)}{dr} = 2M(r,E^{a\sigma}_l)c\dot{q}^{a\sigma}_l(r) + \frac{1}{c}q^{a\sigma}_l(r) + \frac{\dot{p}^{a\sigma}_l(r)}{r} \tag{B.7}$$

$$\frac{d\dot{q}^{a\sigma}_l(r)}{dr} = \frac{1}{c}\left[\frac{l(l+1)}{2M(r,E^{a\sigma}_l)r^2} + V^{a\sigma}_{\text{eff},0}(r) - E^{a\sigma}_l\right]\dot{p}^{a\sigma}_l(r) - \frac{1}{c}\left[1 + \frac{l(l+1)}{4c^2M(r,E^{a\sigma}_l)^2r^2}\right]p^{a\sigma}_l(r) - \frac{\dot{q}^{a\sigma}_l(r)}{r}. \tag{B.8}$$

The matching of the scalar-relativistic two-component MT functions to the non-relativistic, one-component interstitial plane wave at the MT sphere boundary is carried out only for the large component, that corresponds to the functions $p^{a\sigma}_l(r)$ and $\dot{p}^{a\sigma}_l(r)$, while the small component remains unmatched. The notation large and small component goes back to the fact that the radial function $q^{a\sigma}_l(r)$ is connected with $p^{a\sigma}_l(r)$ according to Eq. (B.2) by

$$q^{\sigma}_l(r) = \frac{1}{2M(r,E)c}\left(\frac{d}{dr} - \frac{1}{r}\right)p^{\sigma}_l(r). \tag{B.9}$$

Thus, the function $q^{a\sigma}_l(r)$ is a factor of $1/c$ smaller than $p^{a\sigma}_l(r)$. This justifies not to match the small component at the MT sphere boundary ($r = S_a$), because it is very small, nearly zero at S_a.

We note that in the non-relativistic limit ($c \to \infty$) the set of Eqs. (B.2) and (B.3) reduces to the radial Schrödinger equation (4.2) for the large component $p^{a\sigma}_l(r)$, while the small component $q^{a\sigma}_l(r)$ is exactly zero. Accordingly $\dot{p}^{a\sigma}_l(r)$ is given in this limit by Eq. (4.10) and $\dot{q}^{a\sigma}_l(r)$ vanishes.

Due to the SRA the construction of the local orbitals changes in a similar manner.

Finite-basis set correction

The finite-basis set correction considers the response of the LAPW basis functions due to a change in the spherical effective potential explicitly. In section 6.7 we have only given the

equations to calculate the response of the radial LAPW functions in the non-relativistic limit. Here, we develop the corresponding equations in the scalar-relativistic approximation. Linearizing Eqs. (B.2) and (B.3) in the potential results in a set of differential equations for the response of the large and small component due to a given spherical perturbation $V^{a\sigma\prime}_{\text{eff},0}(r)$

$$\frac{dp^{a\sigma\prime}_l(r)}{dr} = 2M(r,E^{a\sigma}_l)cq^{a\sigma\prime}_l(r) + \frac{p^{a\sigma\prime}_l(r)}{r} + \frac{1}{c}\left[E^{a\sigma\prime}_l - V^{a\sigma\prime}_{\text{eff},0}(r)\right]q^{a\sigma}_l(r) \quad \text{(B.10)}$$

$$\frac{dq^{a\sigma\prime}_l(r)}{dr} = \frac{1}{c}\left[\frac{l(l+1)}{2M(r,E^{a\sigma}_l)r^2} + V^{a\sigma}_{\text{eff},0}(r) - E^{a\sigma}_l\right]p^{a\sigma\prime}_l(r) - \frac{q^{a\sigma\prime}_l(r)}{r} - \frac{1}{c}\left[1 + \frac{l(l+1)}{4M(r,E^{a\sigma}_l)^2r^2c^2}\right]\left[E^{a\sigma\prime}_l - V^{a\sigma\prime}_{\text{eff},0}(r)\right]p^{a\sigma}_l(r)\,. \quad \text{(B.11)}$$

While $p^{a\sigma\prime}_l(r)$ denotes the response of the large component $p^{a\sigma}_l(r)$, $q^{a\sigma\prime}_l(r)$ describes the corresponding change in the small component $q^{a\sigma}_l(r)$. $E^{a\sigma\prime}_l$ is the change in the parameter $E^{a\sigma}_l$ caused by the perturbation $V^{a\sigma\prime}_{\text{eff},0}$. It is computed according to Eq. (6.43), where $u^{a\sigma}_{p0}(r)$ has to be replaced by the two component relativistic function.

In a similar way, the differential equations for the change in the energy derivatives $\dot{p}^{a\sigma}_l(r)$ and $\dot{q}^{a\sigma}_l(r)$ are obtained from Eqs. (B.7) and (B.8)

$$\frac{d\dot{p}^{a\sigma\prime}_l(r)}{dr} = 2M(r,E^{a\sigma}_l)c\dot{q}^{a\sigma\prime}_l(r) + \frac{1}{c}\left\{\left[E^{a\sigma\prime}_l - V^{a\sigma\prime}_{\text{eff},0}(r)\right]\dot{q}^{a\sigma}_l(r) + q^{a\sigma\prime}_l(r)\right\} + \frac{\dot{p}^{a\sigma\prime}_l(r)}{r} \quad \text{(B.12)}$$

$$\frac{d\dot{q}^{a\sigma}_l(r)}{dr} = -\frac{\dot{q}^{a\sigma\prime}_l(r)}{r} + \frac{1}{c}\left[\frac{l(l+1)}{2M(r,E^{a\sigma}_l)r^2} + V^{a\sigma}_{\text{eff},0}(r) - E^{a\sigma}_l\right]\dot{p}^{a\sigma\prime}_l(r) - \frac{1}{c}\left[1 + \frac{l(l+1)}{4c^2M(r,E^{a\sigma}_l)^2r^2}\right]\left[p^{a\sigma\prime}_l(r) + \left[E^{a\sigma\prime}_l - V^{a\sigma\prime}_{\text{eff},0}(r)\right]\dot{p}^{a\sigma}_l(r)\right] + \frac{1}{c}\left[\frac{2l(l+1)}{8c^4M(r,E^{a\sigma}_l)^3r^2}\right]\left[E^{a\sigma\prime}_l - V^{a\sigma\prime}_{\text{eff},0}(r)\right]p^{a\sigma}_l(r)\,. \quad \text{(B.13)}$$

List of Abbrevations

AFM antiferromagnetic.
APW augmented plane-wave.

BZ Brillouin zone.

CI configuration interaction.

DF density functional.
DFT density-functional theory.
DOS density of states.

EXX exact exchange.

FBC finite basis correction.
FFT fast Fourier transform.
FLAPW full-potential linearized augmented-plane-wave.
FM ferromagnetic.

GGA generalized gradient approximation.
gKS generalized Kohn-Sham.

HEG homogeneous electron gas.
HF Hartree-Fock.

IBZ irreducible Brillouin zone.
IPW interstitial plane wave.
IR interstitial region.

KKR Korringa-Kohn-Rostocker.
KS Kohn-Sham.

LAPW linearized augmented-plane-wave.
LDA local-density approximation.

LMTO linearized muffin-tin orbital.

MBPT many-body perturbation theory.
MFA mean-field approximation.
MLWF maximally localized Wannier function.
MP Møller-Plesset.
MPB mixed product basis.
MT muffin-tin.
MTO muffin-tin orbital.

nn nearest neighbor.
nnn next-nearest neighbor.

OEP optimized effective potential.
OPM optimized potential method.

PAW projector augmented-wave.

RPA random-phase approximation.

SCF self-consistent field.
SRA scalar relativistic approximation.

TM transition metal.

xc exchange-correlation.

Bibliography

[1] M. Born and J. R. Oppenheimer, *Zur Quantentheorie der Molekeln*, Ann. der Physik **389**, 457 (1927)

[2] P. Hohenberg and W. Kohn, *Inhomogeneous electron gas*, Phys. Rev. **136**, B864 (1964)

[3] W. Kohn and L. J. Sham, *Self-consistent equations including exchange and correlation effects*, Phys. Rev. **140**, A1133 (1965)

[4] D. M. Ceperley and B. J. Alder, *Ground State of the Electron Gas by a Stochastic Method*, Phys. Rev. Lett. **45**, 566 (1980)

[5] S. H. Vosko, L. Wilk, and M. Nusair, *Accurate spin-dependent electron liquid correlation energies for local spin density calculations: a critical analysis*, Can. J. Phys. **58**, 1200 (1980)

[6] J. P. Perdew and Y. Wang, *Accurate and simple analytic representation of the electron-gas correlation energy*, Phys. Rev. B **45**, 13244 (1992)

[7] J. P. Perdew, K. Burke, and M. Ernzerhof, *Generalized Gradient Approximation Made Simple*, Phys. Rev. Lett. **77**, 3865 (1996)

[8] J. P. Perdew, J. A. Chevary, S. H. Vosko, K. A. Jackson, M. R. Pederson, D. J. Singh, and C. Fiolhais, *Atoms, molecules, solids, and surfaces: Applications of the generalized gradient approximation for exchange and correlation*, Phys. Rev. B **46**, 6671 (1992)

[9] J. P. Perdew and A. Zunger, *Self-interaction correction to density-functional approximations for many-electron systems*, Phys. Rev. B **23**, 5048 (1981)

[10] J. P. Perdew, *Density functional theory and the band gap problem*, Int. J. Quant. Chem. **28**, 497 (1985)

[11] R. W. Godby, M. Schlüter, and L. J. Sham, *Self-energy operators and exchange-correlation potentials in semiconductors*, Phys. Rev. B **37**, 10159 (1988)

[12] M. Grüning, A. Marini, and A. Rubio, *Density functionals from many-body perturbation theory: The band gap for semiconductors and insulators*, J. Chem. Phys. **124**, 154108 (2006)

[13] W. Kohn, Y. Meir, and D. E. Makarov, *van der Waals Energies in Density Functional Theory*, Phys. Rev. Lett. **80**, 4153 (1998)

[14] S. Kümmel and L. Kronik, *Orbital-dependent functionals: Theory and applications*, Rev. Mod. Phys. **80**, 3 (2008)

[15] A. Görling, *Orbital- and state-dependent functionals in density-functional theory*, J. Chem. Phys. **123**, 062203 (2005)

[16] A. Görling and M. Levy, *Correlation-energy functional and its high-density limit obtained from a coupling-constant perturbation expansion*, Phys. Rev. B **47**, 13105 (1993)

[17] E. Engel, A. Höck, and R. M. Dreizler, *van der Waals bonds in density-functional theory*, Phys. Rev. A **61**, 032502 (2000)

[18] J. Harris and R. O. Jones, *The surface energy of a bounded electron gas*, J. Phys. F **4**, 1170 (1974)

[19] O. Gunnarsson and B. I. Lundqvist, *Exchange and correlation in atoms, molecules, and solids by the spin-density-functional formalism* , Phys. Rev. B **13**, 4274 (1976)

[20] D. C. Langreth and J. P. Perdew, *The exchange-correlation energy of a metallic surface*, Solid State Commun. **17**, 1425 (1975)

[21] A. D. Becke, *A new mixing of Hartree-Fock and local density functional theories*, J. Chem. Phys. **98**, 1372 (1993)

[22] J. P. Perdew, M. Ernzerhof, and K. Burke, *Rationale for mixing exact exchange with density functional approximations*, J. Chem. Phys. **105**, 9982 (1996)

[23] A. Seidl, A. Görling, P. Vogl, J. A. Majewski, and M. Levy, *Generalized Kohn-Sham schemes and the band-gap problem*, Phys. Rev. B **53**, 3764 (1996)

[24] E. Wimmer, H. Krakauer, M. Weinert, and A. J. Freeman, *Full-potential self-consistent linearized-augmented-plane-wave method for calculating the electronic structure of molecules and surfaces: O_2 molecule*, Phys. Rev. B **24**, 864 (1981)

[25] M. Weinert, E. Wimmer, and A. J. Freeman, *Total-energy all-electron density functional method for bulk solids and surfaces*, Phys. Rev. B **26**, 4571 (1982)

[26] H. J. F. Jansen and A. J. Freeman, *Total-energy full-potential linearized augmented-plane-wave method for bulk solids: Electronic and structural properties of tungsten*, Phys. Rev. B **30**, 561 (1984)

[27] D. J. Singh, *Planewaves, Pseudopotentials, and the LAPW method* (Kluwer Academic Publishers, 1994)

[28] V. R. Saunders, R. Dovesi, C. Roetti, M. Causa, N. M. Harrison, R. Orlando, and C. M. Zicovich-Wilson, *CRYSTAL98 User's Manual* (University of Torino, 1998)

[29] S. Chawla and G. A. Voth, *Exact exchange in ab initio molecular dynamics: An efficient plane-wave based algorithm*, J. Chem. Phys. **108**, 4697 (1998)

[30] J. Paier, R. Hirschl, M. Marsman, and G. Kresse, *The Perdew-Burke-Ernzerhof exchange-correlation functional applied to the G2-1 test set using a plane-wave basis set*, J. Chem. Phys. **122**, 234102 (2005)

[31] P. Novak, J. Kunes, L. Chaput, and W. E. Pickett, *Exact exchange for correlated electrons*, Phys. Stat. Sol. B **243**, 559 (2006)

[32] R. T. Sharp and G. K. Horton, *A Variational Approach to the Unipotential Many-Electron Problem*, Phys. Rev. **90**, 317 (1953)

[33] A. Görling, *Exact treatment of exchange in Kohn-Sham band-structure schemes*, Phys. Rev. B **53**, 7024 (1996)

[34] A. Görling, *Erratum: Exact treatment of exchange in Kohn-Sham band-structure schemes*, Phys. Rev. B **59(E)**, 10370 (1999)

[35] T. Kotani, *Exact exchange-potential band-structure calculations by the LMTO-ASA method: MgO and CaO*, Phys. Rev. B **50**, 14816 (1994)

[36] M. Städele, J. A. Majewski, P. Vogl, and A. Görling, *Exact Kohn-Sham Exchange Potential in Semiconductors*, Phys. Rev. Lett. **79**, 2089 (1997)

[37] M. Städele, M. Moukara, J. A. Majewski, P. Vogl, and A. Görling, *Exact exchange Kohn-Sham formalism applied to semiconductors*, Phys. Rev. B **59**, 10031 (1999)

[38] A. Fleszar, *LDA, GW, and exact-exchange Kohn-Sham scheme calculations of the electronic structure of sp semiconductors*, Phys. Rev. B **64**, 245204 (2001)

[39] S. Sharma, J. K. Dewhurst, and C. Ambrosch-Draxl, *All-Electron Exact Exchange Treatment of Semiconductors: Effect of Core-Valence Interaction on Band-Gap and d-Band Position*, Phys. Rev. Lett. **95**, 136402 (2005)

[40] E. Engel, *Relevance of core-valence interaction for electronic structure calculations with exact exchange*, Phys. Rev. B **80**, 161205(R) (2009)

[41] A. Makmal, R. Armiento, E. Engel, L. Kronik, and S. Kümmel, *Examining the role of pseudopotentials in exact-exchange Kohn-Sham gaps*, Phys. Rev. B **80**, 161204(R) (2009)

[42] M. Betzinger, C. Friedrich, and S. Blügel, *Hybrid functionals within the all-electron FLAPW method: Implementation and applications of PBE0*, Phys. Rev. B **81**, 195117 (2010)

[43] M. Betzinger, C. Friedrich, S. Blügel, and A. Görling, *Local exact exchange potentials within the all-electron FLAPW method and a comparison with pseudopotential results*, Phys. Rev. B **83**, 045105 (2011)

[44] P. A. M. Dirac, *Quantum Mechanics of Many-Electron Systems*, Proc. R. Soc. Lond. A **123**, 714 (1929)

[45] D. R. Hartree, *The Wave Mechanics of an Atom with a Non-Coulomb Central Field*, Proc. Cambridge Philos. Soc. **24**, 89 (1928)

[46] J. C. Slater, *Note on Hartree's Method*, Phys. Rev. **35**, 210 (1930)

[47] V. Fock, *Näherungsmethode zur Lösung des quantenmechanischen Mehrkörperproblems*, Z. Physik **61**, 126 (1930)

[48] L. H. Thomas, *The calculation of atomic fields*, Proc. Cambridge Philos. Soc. **23**, 542 (1927)

[49] E. Fermi, *Eine statistische Methode zur Bestimmung einiger Eigenschaften des Atoms und ihre Anwendung auf die Theorie des periodischen Systems der Elemente*, Z. Phys. **48**, 73 (1928)

[50] U. von Barth and L. Hedin, *A local exchange-correlation potential for the spin polarized case: I*, Journal of Physics C: Solid State Physics **5**, 1629 (1972)

[51] R. Q. Hood, M. Y. Chou, A. J. Williamson, G. Rajagopal, and R. J. Needs, *Exchange and correlation in silicon*, Phys. Rev. B **57**, 8972 (1998)

[52] J. P. Perdew, *Accurate Density Functional for the Energy: Real-Space Cutoff of the Gradient Expansion for the Exchange Hole*, Phys. Rev. Lett. **55**, 1665 (1985)

[53] J. P. Perdew, *Density-functional approximation for the correlation energy of the inhomogeneous electron gas*, Phys. Rev. B **33**, 8822 (1986)

[54] A. D. Becke, *Density-functional exchange-energy approximation with correct asymptotic behavior*, Phys. Rev. A **38**, 3098 (1988)

[55] C. Lee, W. Yang, and R. G. Parr, *Development of the Colle-Salvetti correlation-energy formula into a functional of the electron density*, Phys. Rev. B **37**, 785 (1988)

[56] J. Kohanoff and N. I. Gidopoulos, "Handbook of Molecular Physics and Quantum Chemistry," (John Wiley & Sons, Ltd, Chichester, 2003) Chap. Density Functional Theory: Basics, New Trends, and Applications, pp. 532–568

[57] A. Dal Corso, A. Pasquarello, A. Baldereschi, and R. Car, *Generalized-gradient approximations to density-functional theory: A comparative study for atoms and solids*, Phys. Rev. B **53**, 1180 (1996)

[58] Y.-M. Juan and E. Kaxiras, *Application of gradient corrections to density-functional theory for atoms and solids*, Phys. Rev. B **48**, 14944 (1993)

[59] M. Levy and J. P. Perdew, *Hellmann-Feynman, virial, and scaling requisites for the exact universal density functionals. Shape of the correlation potential and diamagnetic susceptibility for atoms*, Phys. Rev. A **32**, 2010 (1985)

[60] K. Burke and friends, *ABC of DFT* (2007)

[61] A. D. Becke, *Density-functional thermochemistry III: The role of exact exchange*, J. Chem. Phys. **98**, 5648 (1993)

[62] P. J. Stephens, F. J. Devlin, C. F. Chabalowski, and M. J. Frisch, *Ab Initio Calculation of Vibrational Absorption and Circular Dichroism Spectra Using Density Functional Force Fields*, J. Phys. Chem. **98**, 11623 (1994)

[63] J. A. Pople, M. Head-Gordon, D. J. Fox, K. Raghavachari, and L. A. Curtiss, *Gaussian-1 theory: A general procedure for prediction of molecular energies*, J. Chem. Phys. **90**, 5622 (1989)

[64] L. A. Curtiss, C. Jones, G. W. Trucks, K. Raghavachari, and J. A. Pople, *Gaussian-1 theory of molecular energies for second-row compounds*, J. Chem. Phys. **93**, 2537 (1990)

[65] E. Engel and R. M. Dreizler, *Density Functional Theory: An Advanced Course*, 1st ed., Theoretical and Mathematical Physics (Springer, Heidelberg, 2011)

[66] E. Engel, A. Facco Bonetti, S. Keller, I. Andrejkovics, and R. M. Dreizler, *Relativistic optimized-potential method: Exact transverse exchange and Møller-Plesset-based correlation potential*, Phys. Rev. A **58**, 964 (1998)

[67] E. Engel and H. Jiang, *Orbital-dependent representation of the correlation energy functional: Properties of second-order Kohn-Sham perturbation expansion*, Int. J. Quant. Chem. **106**, 3242 (2006)

[68] M. Ernzerhof, in *Density Functionals: Theory and Applications*, Lecture Notes in Physics, Vol. 500 (Springer Berlin / Heidelberg, 1998) pp. 60–90

[69] L. J. Sham and M. Schlüter, *Density-Functional Theory of the Energy Gap*, Phys. Rev. Lett. **51**, 1888 (1983)

[70] M. E. Casida, *Generalization of the optimized-effective-potential model to include electron correlation: A variational derivation of the Sham-Schlüter equation for the exact exchange-correlation potential*, Phys. Rev. A **51**, 2005 (1995)

[71] R. W. Godby, M. Schlüter, and L. J. Sham, *Accurate Exchange-Correlation Potential for Silicon and Its Discontinuity on Addition of an Electron*, Phys. Rev. Lett. **56**, 2415 (1986)

[72] A. G. Eguiluz, M. Heinrichsmeier, A. Fleszar, and W. Hanke, *First-principles evaluation of the surface barrier for a Kohn-Sham electron at a metal surface*, Phys. Rev. Lett. **68**, 1359 (1992)

[73] J. C. Slater, *Wave Functions in a Periodic Potential*, Phys. Rev. **51**, 846 (1937)

[74] T. Loucks, *Augmented Plane Wave method* (Benjamin, New York, 1967)

[75] C. Friedrich, A. Schindlmayr, S. Blügel, and T. Kotani, *Elimination of the linearization error in GW calculations based on the linearized augmented-plane-wave method*, Phys. Rev. B **74**, 045104 (2006)

[76] M. Asato, A. Settels, T. Hoshino, T. Asada, S. Blügel, R. Zeller, and P. H. Dederichs, *Full-potential KKR calculations for metals and semiconductors*, Phys. Rev. B **60**, 5202 (1999)

[77] D. Singh, *Ground-state properties of lanthanum: Treatment of extended-core states*, Phys. Rev. B **43**, 6388 (1991)

[78] E. E. Krasovskii, A. N. Yaresko, and V. N. Antonov, *Theoretical study of ultraviolet photoemission spectra of noble metals*, J. Electron Spectrosc. Relat. Phenom. **68**, 157 (1994)

[79] E. E. Krasovskii, *Accuracy and convergence properties of the extended linear augmented-plane-wave method*, Phys. Rev. B **56**, 12866 (1997)

[80] O. K. Andersen, *Linear methods in band theory*, Phys. Rev. B **12**, 3060 (1975)

[81] N. Marzari and D. Vanderbilt, *Maximally localized generalized Wannier functions for composite energy bands*, Phys. Rev. B **56**, 12847 (1997)

[82] I. Souza, N. Marzari, and D. Vanderbilt, *Maximally localized Wannier functions for entangled energy bands*, Phys. Rev. B **65**, 035109 (2001)

[83] L. Dagens and F. Perrot, *Hartree-Fock Band Structure and Optical Gap in Solid Neon and Argon*, Phys. Rev. B **5**, 641 (1972)

[84] C. Friedrich, A. Schindlmayr, and S. Blügel, *Efficient calculation of the Coulomb matrix and its expansion around k=0 within the FLAPW method*, Comput. Phys. Comm. **180**, 347 (2009)

[85] S. K. Kim, *Group theoretical methods and applications to molecules and crystals* (Cambridge University Press, 1999)

[86] M. Betzinger, *Efficient Implementation of the Non-Local Exchange Potential within the FLAPW Method*, Master's thesis, RWTH Aachen University (2007)

[87] S. Massidda, M. Posternak, and A. Baldereschi, *Hartree-Fock LAPW approach to the electronic properties of periodic systems*, Phys. Rev. B **48**, 5058 (1993)

[88] C. G. Broyden, *A class of methods for solving nonlinear simultaneous equations*, Math. Comput. **19**, 577 (1965)

[89] C. G. Broyden, *Quasi-Newton methods and their application to function minimisation*, Math. Comput. **21**, 368 (1967)

[90] J. Paier, M. Marsman, K. Hummer, G. Kresse, I. C. Gerber, and J. G. Angyan, *Screened hybrid density functionals applied to solids*, J. Chem. Phys. **124**, 154709 (2006)

[91] T. C. Chiang and F. J. Himpsel, *Band structure and core levels of tetrahedrally-bonded semiconductors*, Landolt-Börnstein - Group III Condensed Matter Numerical Data and Functional Relationships in Science and Technology, Vol. 23 a (Springer Verlag, Berlin, 1989)

[92] S. Adachi, *Optical Properties of Crystalline and Amorphous Semiconductors: Numerical Data and Graphical Information* (Kluwer Academic, Dordrecht, 1999)

[93] R. T. Poole, J. Liesegang, R. C. G. Leckey, and J. G. Jenkin, *Electronic band structure of the alkali halides. II. Critical survey of theoretical calculations*, Phys. Rev. B **11**, 5190 (1975)

[94] M. Runne and G. Zimmerer, *Excitonic excitations and desorption from rare-gas solids*, Nuclear Instruments and Methods in Physics Research Section B: Beam Interactions with Materials and Atoms **101**, 156 (1995)

[95] A. A. Mostofi, J. R. Yates, Y.-S. Lee, I. Souza, D. Vanderbilt, and N. Marzari, *Wannier90: A Tool for Obtaining Maximally-Localised Wannier Functions*, Comput. Phys. Commun. **178**, 685 (2008)

[96] L. He and D. Vanderbilt, *Exponential Decay Properties of Wannier Functions and Related Quantities*, Phys. Rev. Lett. **86**, 5341 (2001)

[97] W. D. Grobman and D. E. Eastman, *Photoemission Valence-Band Densities of States for Si, Ge, and GaAs Using Synchrotron Radiation*, Phys. Rev. Lett. **29**, 1508 (1972)

[98] *II-VI and I-VII Compounds; Semimagnetic Compounds*, edited by O. Madelung, U. Roessler, and M. Schulz, Landolt-Börnstein - Group III Condensed Matter Numerical Data and Functional Relationships in Science and Technology, Vol. 41B (Springer Verlag, Berlin, 1999)

[99] A. Mauger and C. Godart, *The magnetic, optical, and transport properties of magnetic semiconductors*, Phys. Rep. **141**, 51 (1986)

[100] J. S. Moodera, T. S. Santos, and T. Nagahama, *The phenomena of spin-filter tunnelling*, J. Phys.: Condens. Matter **19**, 165202 (2007)

[101] M. Müller, G.-X. Miao, and J. S. Moodera, *Exchange splitting and bias-dependent transport in EuO spin filter tunnel barriers* , Europhys. Lett. **88**, 47006 (2009)

[102] Y. Shapira, S. Foner, and T. B. Reed, *EuO. I. Resistivity and Hall Effect in Fields up to 150 kOe*, Phys. Rev. B **8**, 2299 (1973)

[103] G. Petrich, S. von Molnár, and T. Penney, *Exchange-Induced Autoionization in Eu-Rich EuO*, Phys. Rev. Lett. **26**, 885 (1971)

[104] T. Penney, M. W. Shafer, and J. B. Torrance, *Insulator-Metal Transition and Long-Range Magnetic Order in EuO*, Phys. Rev. B **5**, 3669 (1972)

[105] A. Schmehl et al., *Epitaxial integration of the highly spin-polarized ferromagnetic semiconductor EuO with silicon and GaN*, Nature Mat. **6**, 882 (2007)

[106] P. G. Steeneken, L. H. Tjeng, I. Elfimov, G. A. Sawatzky, G. Ghiringhelli, N. B. Brookes, and D.-J. Huang, *Exchange Splitting and Charge Carrier Spin Polarization in EuO*, Phys. Rev. Lett. **88**, 047201 (2002)

[107] M. W. Shafer and T. R. McGuire, *Studies of Curie-Point Increases in EuO*, J. Appl. Phys. **39**, 588 (1968)

[108] P. Larson and W. R. L. Lambrecht, *Electronic structure and magnetism of europium chalcogenides in comparison with gadolinium nitride*, J. Phys.: Condens. Matter **18**, 11333 (2006)

[109] N. J. C. Ingle and I. S. Elfimov, *Influence of epitaxial strain on the ferromagnetic semiconductor EuO: First-principles calculations*, Phys. Rev. B **77**, 121202 (R) (2008)

[110] A. Rohrbach, J. Hafner, and G. Kresse, *Electronic correlation effects in transition-metal sulfides*, J. Phys.: Condens. Matter **15**, 979 (2003)

[111] M. Cococcioni and S. de Gironcoli, *Linear response approach to the calculation of the effective interaction parameters in the LDA + U method*, Phys. Rev. B **71**, 035105 (2005)

[112] E. Şaşıoğlu, C. Friedrich, and S. Blügel, *Effective Coulomb interaction in transition metals from constrained random-phase approximation*, Phys. Rev. B **83**, 121101 (2011)

[113] F. D. Murnaghan, *The Compressibility of Media under Extreme Pressures*, Proc. Nat. Acad. Sci. USA **30**, 244 (1944)

[114] F. Levy, *Effets magnétostrictifs spontanés de quelques composés des terres rares: I. Les monochalcogénures d'europium*, Phys. kondens. Materie **10**, 71 (1969)

[115] Y. Shapira and T. B. Reed, *Elastic Constants, Compressibilities and Debye Temperatures of the Eu-Chalcogenides*, AIP Conf. Proc. **5**, 837 (1972)

[116] G. Busch and P. Wachter, *Einfluß der magnetischen Ordnung auf die optische Absorption von ferro- oder antiferromagnetischen Halbleitern*, Phys. Kondens. Materie **5**, 232 (1966)

[117] M. S. Seehra and T. M. Giebultowicz, *Magnetic structures of fcc systems with nearest-neighbor and next-nearest-neighbor exchange interactions*, Phys. Rev. B **38**, 11898 (1988)

[118] L. Passell, O. W. Dietrich, and J. Als-Nielsen, *Neutron scattering from the Heisenberg ferromagnets EuO and EuS. I. The exchange interactions*, Phys. Rev. B **14**, 4897 (1976)

[119] N. W. Ashcroft and N. D. Mermin, *Festkörperphysik*, 2. ed. (Oldenbourg Wissenschaftsverlag, München, 2003)

[120] W. Nolting and A. Ramakanth, *Quantum Theory of Magnetism* (Springer, Berlin, 2009)

[121] G. Bihlmayer, "Computational Nanoscience: Do it Yourself!." (Forschungszentrum Jülich GmbH, 2006) Chap. Non-Collinearr Magnetism: Exchange parameter and T_c, pp. 447–467

[122] S. V. Tyablikov, *Lagging and anticipating greene functions in the theory of ferromagnetism*, Ukr. Mat. Zh. **11**, 287 (1959)

[123] H. Callen, *Green Function Theory of Ferromagnetism*, Phys. Rev. **130**, 890 (1963)

[124] J. Heyd, G. E. Scuseria, and M. Ernzerhof, *Hybrid functionals based on a screened Coulomb potential*, J. Chem. Phys. **118**, 8207 (2003)

[125] A. V. Krukau, O. A. Vydrov, A. F. Izmaylov, and G. E. Scuseria, *Influence of the exchange screening parameter on the performance of screened hybrid functionals*, J. Chem. Phys. **125**, 224106 (2006)

[126] M. Schlipf, M. Betzinger, C. Friedrich, M. Ležaić, and S. Blügel, *HSE hybrid functional within the FLAPW method and its application to GdN*, Phys. Rev. B **84**, 125142 (2011)

[127] V. Sahni, J. Gruenebaum, and J. P. Perdew, *Study of the density-gradient expansion for the exchange energy*, Phys. Rev. B **26**, 4371 (1982)

[128] E. Engel, S. Keller, A. Facco Bonetti, H. Müller, and R. M. Dreizler, *Local and nonlocal relativistic exchange-correlation energy functionals: Comparison to relativistic optimized-potential-model results*, Phys. Rev. A **52**, 2750 (1995)

[129] E. Engel, S. Keller, and R. M. Dreizler, *Generalized gradient approximation for the relativistic exchange-only energy functional*, Phys. Rev. A **53**, 1367 (1996)

[130] A. Görling, A. Hesselmann, M. Jones, and M. Levy, *Relation between exchange-only optimized potential and Kohn–Sham methods with finite basis sets, and effect of linearly dependent products of orbital basis functions*, J. Chem. Phys. **128**, 104104 (2008)

[131] A. Hesselmann, A. W. Götz, F. D. Sala, and A. Görling, *Numerically stable optimized effective potential method with balanced Gaussian basis sets*, J. Chem. Phys. **127**, 054102 (2007)

[132] A. Hesselmann, private communication

[133] R. J. Magyar, A. Fleszar, and E. K. U. Gross, *Exact-exchange density-functional calculations for noble-gas solids*, Phys. Rev. B **69**, 045111 (2004)

[134] J. P. Perdew, R. G. Parr, M. Levy, and J. L. Balduz, *Density-Functional Theory for Fractional Particle Number: Derivative Discontinuities of the Energy*, Phys. Rev. Lett. **49**, 1691 (1982)

[135] J. P. Perdew and M. Levy, *Physical Content of the Exact Kohn-Sham Orbital Energies: Band Gaps and Derivative Discontinuities*, Phys. Rev. Lett. **51**, 1884 (1983)

[136] A. J. Cohen, P. Mori-Sánchez, and W. Yang, *Fractional charge perspective on the band gap in density-functional theory*, Phys. Rev. B **77**, 115123 (2008)

[137] R. M. Chrenko, *Ultraviolet and infrared spectra of cubic boron nitride*, Solid State Commun. **14**, 511 (1974)

[138] M. Röppischer, R. Goldhahn, G. Rossbach, P. Schley, C. Cobet, N. Esser, T. Schupp, K. Lischka, and D. J. As, *Dielectric function of zinc-blende AlN from 1 to 20 eV: Band gap and van Hove singularities*, J. Appl. Phys. **106**, 076104 (2009)

[139] H. Okumura, K. Ohta, K. Ando, W. W. Röhle, T. Nagatomo, and S. Yoshida, *Bandgap energy of cubic GaN*, Solid-State Electron. **41**, 201 (1997)

[140] J. Schörmann, D. J. As, K. Lischka, P. Schley, R. Goldhahn, S. F. Li, W. Löffler, M. Hetterich, and H. Kalt, *Molecular beam epitaxy of phase pure cubic InN*, Appl. Phys. Lett. **89**, 261903 (2006)

[141] D. Gall, M. Städele, K. Järrendahl, I. Petrov, P. Desjardins, R. T. Haasch, T. Y. Lee, and J. E. Greene, *Electronic structure of ScN determined using optical spectroscopy, photoemission, and ab initio calculations*, Phys. Rev. B **63**, 125119 (2001)

[142] J. B. Krieger, Y. Li, and G. J. Iafrate, *Construction and application of an accurate local spin-polarized Kohn-Sham potential with integer discontinuity: Exchange-only theory*, Phys. Rev. A **45**, 101 (1992)

[143] D. Ködderitzsch, H. Ebert, and E. Engel, *Relativistic optimized potential method for open-shell systems*, Phys. Rev. B **77**, 045101 (2008)

[144] D. Ködderitzsch, H. Ebert, H. Akai, and E. Engel, *Relativistic optimized effective potential method-application to alkali metals*, J. Phys.: Condens. Matter **21**, 064208 (2009)

[145] K. Ueda, H. Yanagi, R. Noshiro, H. Hosono, and H. Kawazoe, *Vacuum ultraviolet reflectance and electron energy loss spectra of $CaTiO_3$*, J. Phys.: Condens. Matter **10**, 3669 (1998)

[146] V. Trepakov, A. Dejneka, P. Markovin, A. Lynnyk, and L. Jastrabik, *A 'soft electronic band' and the negative thermooptic effect in strontium titanate*, New J. Phys. **11**, 083024 (2009)

[147] S. G. Choi, A. M. Dattelbaum, S. T. Picraux, S. K. Srivastava, and C. J. Palmstrom, *Optical properties and critical-point energies of $BaTiO_3$ (001) from 1.5 to 5.2 eV*, J. Vac. Sci. Technol. B **26**, 1718 (2008)

[148] A. Gierlich, *All-electron GW Calculations for Perovskite Transition-Metal Oxides*, Ph.D. thesis, RWTH Aachen University (2011)

[149] B. H. Brandow, *Electronic structure of Mott insulators*, Advances in Physics **26**, 651 (1977)

[150] N. F. Mott, *Discussion of the paper by de Boer and Verwey*, Proc. Phys. Soc. **49**, 72 (1937)

[151] F. Tran, P. Blaha, K. Schwarz, and P. Novák, *Hybrid exchange-correlation energy functionals for strongly correlated electrons: Applications to transition-metal monoxides*, Phys. Rev. B **74**, 155108 (2006)

[152] W. L. Roth, *Magnetic Structures of MnO, FeO, CoO, and NiO*, Phys. Rev. **110**, 1333 (1958)

[153] J. F. Janak and A. R. Williams, *Method for calculating wave functions in a nonspherical potential*, Phys. Rev. B **23**, 6301 (1981)

[154] R. N. Iskenderov, I. A. Drabkin, L. T. Emelyanova, and Y. M. Ksendzov, Fiz. Tverd. Tela (Leningrad) **10**, 2573 (1968)

[155] J. van Elp, R. H. Potze, H. Eskes, R. Berger, and G. A. Sawatzky, *Electronic structure of MnO*, Phys. Rev. B **44**, 1530 (1991)

[156] H. K. Bowen, D. Adler, and B. H. Auker, *Electrical and optical properties of FeO*, J. Solid State Chem. **12**, 355 (1975)

[157] T. D. Kang, H. S. Lee, and H. Lee, *Optical Properties of Black NiO and CoO Single Crystals Studied with Spectroscopic Ellipsometry*, J. Korean Phys. Soc. **50**, 632 (2007)

[158] J. van Elp, J. L. Wieland, H. Eskes, P. Kuiper, G. A. Sawatzky, F. M. F. de Groot, and T. S. Turner, *Electronic structure of CoO, Li-doped CoO, and* $LiCoO_2$, Phys. Rev. B **44**, 6090 (1991)

[159] P. D. Battle and A. K. Cheetham, *The magnetic structure of non-stoichiometric ferrous oxide*, J. Phys. C **12**, 337 (1979)

[160] Z. Fang, I. V. Solovyev, H. Sawada, and K. Terakura, *First-principles study on electronic structures and phase stability of MnO and FeO under high pressure*, Phys. Rev. B **59**, 762 (1999)

[161] I. V. Solovyev, A. I. Liechtenstein, and K. Terakura, *Is Hund's Second Rule Responsible for the Orbital Magnetism in Solids?*, Phys. Rev. Lett. **80**, 5758 (1998)

[162] T. Shishidou and T. Jo, *Antiferromagnetic Structure in CoO*, J. Phys. Soc. Jpn. **67**, 2637 (1998)

[163] A. Svane and O. Gunnarsson, *Transition-metal oxides in the self-interaction–corrected density-functional formalism*, Phys. Rev. Lett. **65**, 1148 (1990)

[164] A. K. Cheetham and D. A. O. Hope, *Magnetic ordering and exchange effects in the antiferromagnetic solid solutions* $Mn_xNi_{1-x}O$, Phys. Rev. B **27**, 6964 (1983)

[165] W. L. Roth, *Magnetic Structures of MnO, FeO, CoO, and NiO*, Phys. Rev. **110**, 1333 (1958)

[166] D. C. Khan and R. A. Erickson, *Magnetic Form Factor of* Co^{++} *Ion in Cobaltous Oxide*, Phys. Rev. B **1**, 2243 (1970)

[167] W. Jauch, M. Reehuis, H. J. Bleif, F. Kubanek, and P. Pattison, *Crystallographic symmetry and magnetic structure of CoO*, Phys. Rev. B **64**, 052102 (2001)

[168] M. Methfessel and A. T. Paxton, *High-precision sampling for Brillouin-zone integration in metals*, Phys. Rev. B **40**, 3616 (1989)

[169] M. Weinert and J. W. Davenport, *Fractional occupations and density-functional energies and forces*, Phys. Rev. B **45**, 13709 (1992)

[170] C. Elsässer, M. Fähnle, C. T. Chan, and K. M. Ho, *Density-functional energies and forces with Gaussian-broadened fractional occupations*, Phys. Rev. B **49**, 13975 (1994)

[171] N. D. Mermin, *Thermal Properties of the Inhomogeneous Electron Gas*, Phys. Rev. **137**, A 1441 (1965)

[172] M. Greiner, P. Carrier, and A. Görling, *Extension of exact-exchange density functional theory of solids to finite temperatures*, Phys. Rev. B **81**, 155119 (2010)

[173] A. Görling, private communication

[174] J. A. Knapp, F. J. Himpsel, and D. E. Eastman, *Experimental energy band dispersions and lifetimes for valence and conduction bands of copper using angle-resolved photoemission*, Phys. Rev. B **19**, 4952 (1978)

[175] R. Courtes and S. Hüfner, *Photoemission experiments on copper*, Phys. Rep. **112**, 53 (1984)

[176] T. Kotani, *An optimized-effective-potential method for solids with exact exchange and random-phase approximation correlation*, J. Phys.: Condens. Matter **10**, 9241 (1998)

[177] C. Friedrich, M. C. Müller, and S. Blügel, *Band convergence and linearization error correction of all-electron GW calculations: The extreme case of zinc oxide*, Phys. Rev. B **83**, 081101 (2011)

[178] D. C. Langreth and J. P. Perdew, *The exchange-correlation energy of a metallic surface*, Solid State Communications **17**, 1425 (1975)

[179] O. Gunnarsson and B. I. Lundqvist, *Exchange and correlation in atoms, molecules, and solids by the spin-density-functional formalism*, Phys. Rev. B **13**, 4274 (1976)

[180] D. C. Langreth and J. P. Perdew, *Exchange-correlation energy of a metallic surface: Wave-vector analysis*, Phys. Rev. B **15**, 2884 (1977)

[181] A. Görling, private communication

[182] D. D. Koelling and B. N. Harmon, *A technique for relativistic spin-polarised calculations*, J. Phys. C **10**, 3107 (1977)

[183] T. Takeda, *The scalar relativistic approximation*, Z. Physik B **32**, 43 (1978)

Acknowledgement

First and foremost, I would like to thank my supervisor Prof. Dr. Stefan Blügel. He has given me the possibility to write this PhD thesis at the Forschungszentrum Jülich. His great support, encouragement, and numerous ideas essentially contribute to the success of this work.

I am truly indebted to Prof. Dr. Andreas Görling for reviewing this thesis and explaining me during a four month stay in his working group at the University Erlangen-Nuremberg the numerical nitty gritties of the EXX-OEP formalism. I will not forget the granted hospitality and pleasant inclusion in his working group.

Next, I would like to thank Prof. Dr. Carsten Honerkamp for his willingness to be the third referee of this thesis at short notice.

Furthermore, this thesis would have been impossible without the many discussions with and the steady support of my direct supervisor Dr. Christoph Friedrich. I thank Dr. Gustav Bihlmayer for his guidance concerning the FLAPW method and the FLEUR code. Moreover, I would like to thank all the members of our institute *Quantum theory of Materials*. They made my stay in Jülich in academic and personal matters unforgettable.
I am obliged to Dr. Christoph Friedrich, Dr. Ersoy Şaşıoğlu and Gregor Michalicek for proof-reading this manuscript with outmost care.

Finally, I would like to thank my family, in particular my parents, for their unbreakable faith in me and their steady support. I hope they will accompany me for a long period of time. Dinah, you had to bear numerous weekends, at which I spend more time at the desk than with you. Thank you for your inestimable patience and moral support!

Jülich, June 2011 Markus Betzinger

Publications

Parts and results of the thesis have already been published (the status of each article is indicated):

- M. Betzinger, C. Friedrich, and S. Blügel, *Hybrid functionals within the all-electron FLAPW method: Implementation and applications of PBE0*, published in Phys. Rev. B **81**, 195117 (2010)
- M. Betzinger, C. Friedrich, S. Blügel, and A. Görling, *Local exact exchange potentials within the all-electron FLAPW method and a comparison with pseudopotential results*, published in Phys. Rev. B **83**, 045105 (2011)
- M. Betzinger, C. Friedrich, A. Görling, and S. Blügel, *Precise response functions in all-electron methods: Application to the optimized-effective-potential approach,* submitted to PRB
- M. Schlipf, M. Betzinger, C. Friedrich, M. Ležaić, and S. Blügel, *HSE hybrid functional within the FLAPW method and its application to GdN,* published in Phys. Rev. B **84**, 125142 (2011)